
Aerodynamic and Propeller Performance Characteristics of a Propfan-Powered, Semispan Model

Alan D. Levin, Ronald C. Smith, and
Richard D. Wood

December 1985

Date for general release December 1987



National Aeronautics and
Space Administration

NOMENCLATURE

C_D	thrust removed drag coefficient, drag/qS
C_L	thrust removed lift coefficient, lift/qS
$C_{D_{SS}}$	slipstream interference drag coefficient
C_m	thrust removed pitching moment coefficient, pitching-moment/qS \bar{c}
C_N	normal force coefficient, normal-force/qS
C_p	pressure coefficient, $(p - p_\infty)/q$
$C_{P_{prop}}$	propeller power coefficient, power/ $\rho N^3 D^5$
$C_{T_{NET}}$	propeller net thrust coefficient, net-thrust/qS
$C_{T_{prop}}$	propeller thrust coefficient, thrust/ $\rho N^2 D^4$
C_X	axial force coefficient, axial-force/qS
C_{X_H}	hub-forebody axial force coefficient, forebody-axial-force/qS
$C_{X_{HB}}$	hub-base axial force coefficient, hub-base-axial-force/qS
\bar{c}	mean aerodynamic chord, 0.702 m
D	propeller diameter, 0.622 m
EPR	exhaust pressure ratio, p_{t_e}/p_{s_e}
J	advance ratio, $60V/ND$
HP	horsepower, W
M, MACH	Mach number
N	propeller rotational speed, rpm
p	local static pressure, kPa
p_{s_e}	average nozzle exit static pressure, kPa
p_{t_e}	average nozzle exit total pressure, kPa
p_∞	free-stream static pressure, kPa

Q torque, N-m
 q dynamic pressure, kPa
 RN Reynolds number based on \bar{c}
 S reference area, 1.434 m²
 V free-stream velocity, m/s
 x/c local chord station, fraction of chord measured from the baseline wing leading edge
 XNAC nacelle station, m
 α angle of attack, deg
 β_p propeller blade pitch angle, deg
 ΔC_D total installation drag coefficient
 ΔC_{X_N} nacelle buoyancy axial force coefficient
 θ_D droop of propeller axis, deg
 θ_T toe-in of propeller axis, deg
 η, ETA span station, fraction of semispan
 η_{NET} propeller net efficiency
 ρ density, kg/m³
 ψ nacelle azimuth station, positive clockwise (see fig. 2), deg

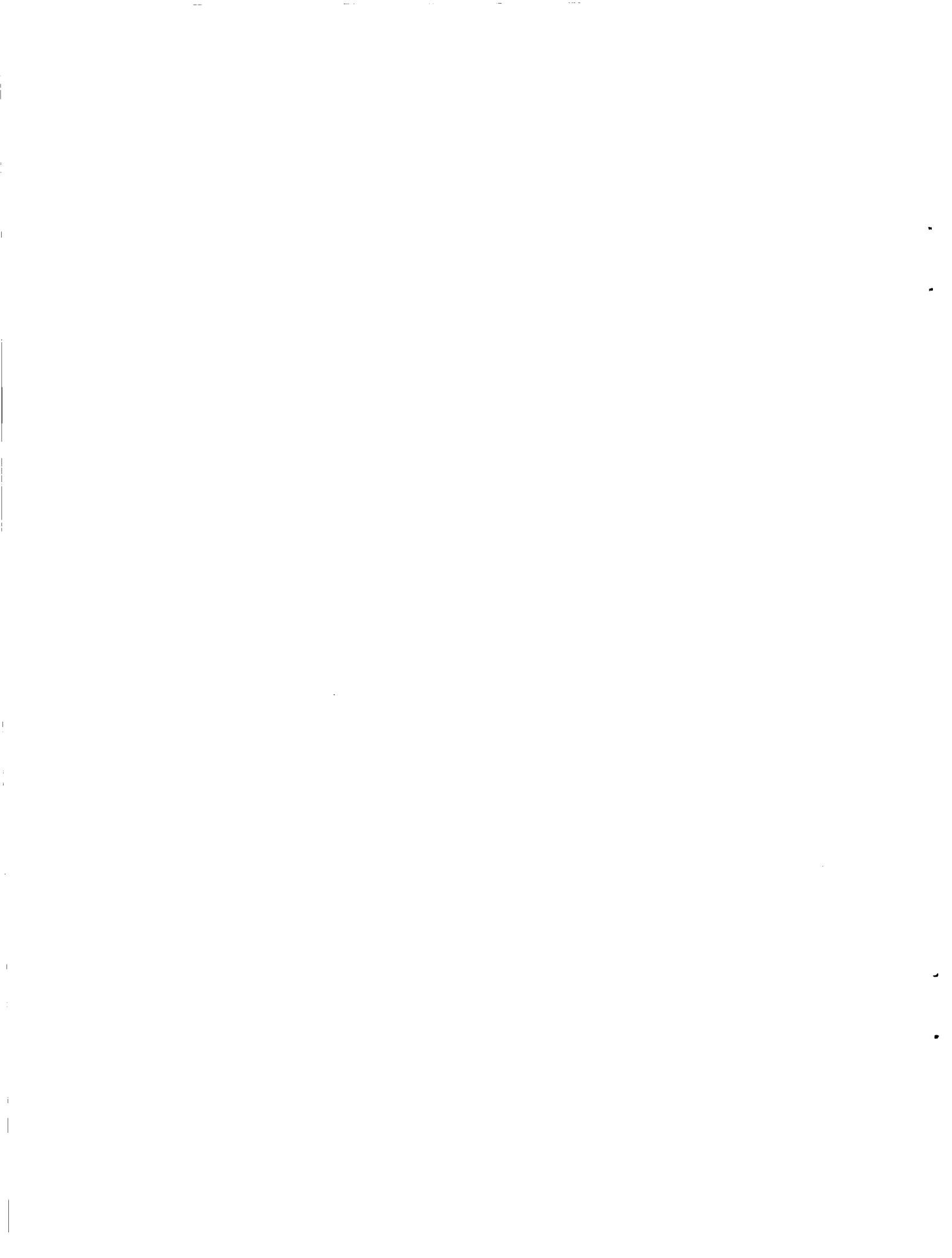
Subscripts

BAL balance
 JET jet
 TR thrust removed

Configuration codes

B body
 F3 fillet

L wing leading-edge extension (LEX)
N nacelle
P propeller
S strake
W wing



SUMMARY

A semispan wing/body model with a powered propeller has been tested to provide data on the total power plant installation drag penalty of advanced propfan-powered aircraft. The test conducted in the Ames Research Center's 11-Foot Transonic Wind Tunnel, is a part of a National Aeronautics and Space Administration (NASA) program to develop the technology for fuel efficient, high-speed, propeller-driven aircraft. The test objectives were: (1) to determine the total powerplant installation drag penalty on a representative propfan aircraft; (2) to study the effect of configuration modifications on the installed powerplant drag; and (3) to determine performance characteristics of an advanced-design propeller which was mounted on a representative nacelle in the presence of a wing.

The semispan wing/body model consisted of a swept, supercritical wing mounted low on the body. The nacelle was mated to the wing in an under-the-wing configuration. The model had instruments for measuring propeller forces, total configuration forces and moments, and pressure distributions over the wing and nacelle. Other measurements included unsteady propeller blade stresses and acoustic pressures on the body. Only the force data and pressure distributions are presented in this report. The test was conducted at angles of attack from -3° to 4° over the Mach number range 0.6 to 0.8. Tunnel total pressure was held constant at one atmosphere, resulting in Reynolds numbers between 7.8 million and 9.5 million. The test program was designed to assess jet-off and jet-on nacelle installation drag, propeller slipstream interference drag, and total powerplant installation drag.

Test results indicated that the total powerplant installation drag penalty can be as high as 77 drag counts (0.0077). However, the penalty was reduced to 18 drag counts by the addition of a wing leading edge extension, between the nacelle and body, in combination with a fillet and strake at the wing-nacelle intersections.

INTRODUCTION

Jet fuel cost has become a dominant component of the direct operating cost of transport aircraft. As a result, there is growing interest in alternate propulsion system concepts having improved fuel efficiency. One of the primary candidates is the highly loaded, high-speed propeller, typically referred to as the propfan. Several system studies (refs. 1-6) have indicated that a propfan-powered aircraft operating at $M = 0.8$ could achieve a 10% to 30% saving in fuel relative to a comparable turbofan-powered aircraft. (Near $M = 0.8$ flight speeds are being considered to ensure compatibility with existing airline operations.) At these speeds, recently developed propeller designs can provide efficient performance.

However, the fuel saving suggested by the system studies can be realized only if the propulsion system is properly integrated with the airframe.

In addition to generating the technology base from which airframe manufacturers can reliably design propfan aircraft, several technical issues must be resolved. Among these is the aerodynamic integration of the powerplant with the wing. One of the concerns about the propfan installation is the interference drag that may result from integration of the nacelle and propeller on a supercritical wing. The resultant interference effects are dependent upon the nacelle/wing interactions along with the Mach number and swirl increment generated in the slipstream. A slipstream simulator test was conducted in 1978 to experimentally evaluate these interference effects (ref. 7). A flow-through, ejector-powered nacelle located ahead of the wing was used to simulate the propeller slipstream flow. This approach permitted simulation of various propeller parameters to obtain a basic understanding of power effects on the wing. Although useful results were obtained from this investigation, a more accurate representation of the flow was required to adequately define the installed performance of these advanced propulsion systems.

Accordingly, to assess the installation drag penalties of advanced propfan-powered aircraft, tests on a semispan wing/body model of a supercritical swept-wing transport have been conducted as a part of the NASA Advanced Turboprop Program (ref. 8). Wind tunnel tests were conducted to investigate the installation losses for a wing-mounted powerplant involving interactions between the nacelle, propeller slipstream, and a swept supercritical wing. The tests reported herein were focused on the assessment of (1) the interference drag penalties of the nacelle and the propeller slipstream; (2) an understanding of the flows that cause the interference; and (3) the determination of what configuration modifications would be required to reduce the interference drag.

The test was conducted in the Ames Research Center's 11-Foot Transonic Wind Tunnel at $M = 0.6$ to $M = 0.8$. Propeller performance characteristics, pressure distributions over the wing and nacelle, powerplant installation losses, and fluorescent oil flow visualization studies were made. Only selected portions of these data are presented for discussion herein. More extensive test results are provided in graphical form on microfiche affixed to the inside back cover of this report.

MODEL DESCRIPTION AND INSTRUMENTATION

The model configuration was derived from a supercritical wing which incorporated 1975 advanced design technology for medium-range transports and which demonstrated good drag-rise characteristics near $M = 0.8$. The turboprop nacelle was mated to the wing with little attempt to blend or shape the design for optimum aerodynamic integration, such as described in reference 9.

Photographs of the semispan wing/body wing-tunnel models mounted in the Ames 11-Foot Transonic Wind Tunnel are shown in figure 1. Figures 1(a) and 1(b) show front and rear views, respectively, of the under-the-wing nacelle mated to the

supercritical wing. This configuration is hereinafter denoted as the baseline (with or without the propeller). The propeller axis was aligned downward 3.75° (droop) and inboard 2° (toe-in) to minimize the cyclic blade loads caused by wing sweep and angle of attack. The procedure used to achieve this is reported in reference 10.

Results of a previous powered test of the baseline model in the Ames 14-Foot Transonic Wind Tunnel indicated that the installation of the nacelle significantly affected the wing flow. The flow on the wing upper surface was separated near the leading edge during powered conditions. As a result of this finding, a modification to the existing wing was developed in an attempt to reduce the upper surface pressure coefficients at powered conditions. The wing modification was performed by the Douglas Aircraft Company under an Ames contract (ref. 11) and was accomplished by adding a leading edge extension (LEX) to the baseline wing. Photographs of the LEX configuration are shown in figures 1(c) through 1(e). Other modifications included the addition of a fillet and strake at the wing-nacelle junctures. These were tested as a consequence of findings from an earlier unpowered test (refs. 12 and 13). The fillet was added to the inboard wing-nacelle intersections, and the strake to the outboard, with the LEX on. A photograph of this configuration is shown in figure 1(f).

LEX Design Philosophy

A brief discussion of the design philosophy of the LEX is presented below. A more comprehensive description, and the airfoil coordinate definition of the LEX, can be found in reference 11.

The baseline wing was designed based on supercritical airfoil technology. Supercritical airfoils have a characteristic known as controlled supersonic flow. This implies that as the region of local supersonic flow develops and grows in extent over the airfoil, the shock wave terminating such a region remains weak. Integrating the nacelle with the wing caused the wing upper surface flow to separate inboard of the nacelle (ref. 12). To rectify the problem, the inboard section of the wing was redesigned with the objective of recovering the clean wing pressure distribution. The actual criteria used were that the final design, including the effects of power, should have upper surface pressure coefficients, chordwise pressure gradients, and spanwise upper surface isobar patterns similar to those exhibited by the clean wing (because the clean wing did not exhibit any flow separations and performed well).

The airfoil sections between the nacelle and the body were modified to conform to these criteria to the fullest extent permitted by the existing hardware. Because no undesirable flow phenomena were identified outboard of the nacelle, no modifications were made there. Inboard, the design constraint used to preserve wing structural integrity was that the airfoil remain unchanged except for the forward or aft 20% to 25% of the chord. Modified airfoils that fit within the existing planform which conformed to these constraints could not be found. Therefore, the use of a leading or trailing edge extension was analytically investigated. A trailing edge

extension was ruled out because it caused an undesirable unsweeping of the wing isobar pattern. Therefore, a 15% chord leading edge extension was selected.

The wing airfoil sections between the body and the nacelle for the modified planform were developed to have upper surface pressure coefficients and gradients similar to the clean wing at the transonic cruise condition ($M = 0.8$, $C_L = 0.5$), and to fair smoothly into the existing airfoil shape at the 25% chord. The airfoil shapes were developed using a two-dimensional Garabedian transonic analysis method. Then a three-dimensional analysis was used to ensure that the pressure distribution over the entire airfoil conformed to accepted design practice. The Jameson computer code, as modified by Douglas Aircraft Co. (ref. 11), restricted to wing alone, was used for the three-dimensional analysis.

The most promising design developed is denoted as MOD 3 in reference 11. MOD 3 had calculated pressure peaks near the leading edge which were about half those of the baseline wing. The transonic flow over the entire upper surface was free of shock waves even at the flow condition which corresponded to cruise power. With power, the pressure levels were less than for the clean baseline wing. Moreover, the gradients were less, and constant levels of pressure coefficient occurred at corresponding chordwise stations (constant x/c). These results indicated properly swept isobar patterns.

Model Details

The model scale was 12% based on a 180 passenger transport. The powerplant was designed for testing at 1.5 atm. Baseline model planform details are shown in figure 2(a). Fine grit was applied near the wing leading edge to produce an all turbulent boundary layer. On the wing upper surface, the grit was applied 11.7 cm (4.6 in.) from the leading edge, or at the 15% chord line, whichever was less. On the wing lower surface, it was applied 15.9 cm (6.25 in.) from the leading edge. The nacelle was scaled based on a $M = 0.8$ transport powered by two 30,000-hp engines (ref. 4). The LEX was added between the inboard side of the nacelle and the body. A fillet was added inboard of the nacelle, and a strake outboard, in an attempt to alleviate the sharp corners at the nacelle intersection with the wing. Nacelle details are shown in figure 2(b) and airfoil sections of the fillet at $\eta = 0.396$ and $\eta = 0.424$ are shown in figures 2(c) and 2(d), respectively. The coordinates of the fillet are presented in Table 1. Wing airfoil and nacelle coordinates are provided in reference 13 and the LEX coordinates are given in reference 11. Details of the strake geometry are not available at the present time.

A sectioned profile of the model powerplant is shown in figure 3. The hub contained a six-component strain gauge balance for measuring propeller forces and moments. The propeller used the Hamilton Standard SR-2 (unswept) eight-blade prop-fan geometry. Blades for this model were fabricated from molded carbon-epoxy composite and were designated SR-2C. The propeller diameter was 0.622 m (2.04 ft). Each of the eight blades was fitted with a gear sector at the end of the shank which meshed with a synchronizing ring gear in the hub. Thus, the pitch angles of all

blades were the same and could be manually changed by relocating a pin which locked the ring gear to the hub.

The six-stage axial flow turbine motor was driven by compressed air. Thrust loads from the propeller and turbine were carried by an oil-cooled, deep-race front ball bearing. A 24-channel slip ring was located at the rear of the turbine. Instrumentation signals from the hub balance were passed through a hole in the motor shaft and out through the slip rings to the nonrotating system. In addition to the propeller balance signals, the slip ring carried signals from up to four propeller-blade strain gauges for measuring blade structural response. Turbine exhaust air was ducted beneath the wing and exited the exhaust pipe at the wing midchord. Pitot probes (thrust rake) and static wall pressure taps were used to measure the exhaust thrust. A section of stainless steel honeycomb located upstream of this instrumentation removed any residual swirl from the motor exhaust. This permitted accurate calibration of the thrust rake and exhaust nozzle. Calibration of the powerplant and instrumentation was done at Fluidyne, Minneapolis, MN, using a standard ASME nozzle and thrust stand.

There was a gap of about 3.8 cm (1.5 in.) between the bottom of the body and the tunnel floor. This permitted some of the tunnel floor boundary-layer flow to pass beneath the body. A shroud was placed around the wing floor-mount to prevent this flow from impinging on the balance. A seal was placed at the wing/body juncture to prevent airflow beneath the body from passing over the wing. Throughout the test the wind-tunnel floor slots were sealed. The effect of flow passing beneath the body on the unpowered test results were described in reference 14.

Balance and Pressure Instrumentation

Total lift, drag, and pitching moment were obtained from a five-component force-moment floor balance. The balance capacity in the normal-force and axial-force directions was 53,400 N (12,000 lb) and 4,500 N (1,000 lb), respectively. Propeller forces and moments were obtained from a six-component rotating propeller balance. The balance capacity was 2,225 N (500 lb) in the normal- and side-force directions, 2,000 N (450 lb) in the axial-force direction, and 745 N-m (550 ft-lb) in rolling moment.

The coordinates of all model pressure instrumentation are given in reference 13, and consisted of the following: (1) 239 wing static orifices distributed over eight spanwise stations (fig. 2(a)); (2) 103 nacelle static orifices distributed over 12 longitudinal stations; (3) 25 hub-cavity static orifices; (4) 6 internal duct static orifices; (5) 6 nacelle-base static orifices; and (6) 21 internal duct total probes. These pressures were recorded using two 6-module Scanivalve assemblies located within a cavity in the wing. Other model instrumentation consisted of a temperature rake in the motor duct containing 10 total temperature probes, strain gauges for measuring unsteady blade stresses, 17 pressure transducers (Kulites) for measuring acoustic pressures on the wing and body, and probes to measure the motor plenum temperature and pressure. Additional instrumentation, such

as accelerometers and motor bearing temperatures, were provided to monitor the health of the turbine system for wind tunnel safety.

TEST PROCEDURE

The test variables were Mach number, angle of attack, propeller blade pitch angle, and nozzle exhaust pressure ratio (EPR). Tunnel total pressure was held constant at one atmosphere throughout the test. The Reynolds number based on mean aerodynamic chord then varied from 7.8×10^6 at $M = 0.6$ to 9.5×10^6 at $M = 0.8$. For the jet effects configurations (blades off) at each test Mach number, EPR was varied at a fixed angle of attack. EPR was varied from 1.0 to approximately 1.9 in 10 increments. Note that $EPR = 1.0$ represents a jet-off point; that is, no air was flowing through the exhaust nozzle. For the blades-on configurations, propeller speed was varied from windmill (jet-off) to 9,000 rpm in approximately 250 rpm increments, or to the maximum speed possible within power limitations, whichever occurred first. Note that propeller speed and EPR could not be varied independently.

Model angle of attack was varied from -3° to 4° throughout most of the test. Towards the end of the test, time constraints necessitated reducing the test angle of attack range to 0° to 3° . Most of the blades-on data were obtained at Mach numbers of 0.75, 0.78, and 0.8; some results were obtained at Mach numbers of 0.6 and 0.7. The measured propeller blade pitch angle was 57.2° at the 75% radius station; the design value was 57° . Limited data were also obtained at measured blade pitch angles of 55.2° and 59.2° .

DATA REDUCTION

The procedure used to obtain the total powerplant installation drag has been described in detail in reference 14. A brief description of that procedure is repeated here.

The interference drag of the various components is conceptually illustrated by the thrust removed drag polars in figure 4(a). The jet-off nacelle interference drag is the increase in drag between the nacelle-off configuration (WING-BODY), and nacelle-on configuration ($W-N_{JET-OFF}$). A jet-off drag increment is not representative of the power-on case because there is a large region of separated flow at the base of the nacelle. This separation, with resulting lift-loss, gives the appearance of an unusually large nacelle-interference drag. With the jet on, much of this lift-loss is restored, and the drag polar moves left ($W-N_{CRUISE EPR}$). The drag reduction so generated is called $C_{D_{JET}}$.

Some of the jet-on drag reduction is lost when the propeller is installed because of the interference drag caused by the propeller slipstream interaction, $C_{D_{SS}}$. This results in the drag polar $W-N-P_{CRUISE EPR}$. The total powerplant

installation drag penalty is, therefore, the increase in drag between the WING-BODY and the blades-on configurations (W-N-P_{CRUISE EPR}) evaluated at constant lift. The procedures used to obtain propeller net thrust and to adjust the floor balance measurements for both propeller and jet thrust are described in the following paragraphs.

The derivation of the net thrust obtained from balance readings and pressure measurements is illustrated in figure 4(b). The hub-base-axial-force, $C_{X_{HB}}$, is determined by integrating the pressure measurements in the hub-base cavity. The hub-forebody-axial-force, C_{X_H} , is determined from hub-balance and pressure measurements obtained with the blades removed. When a representative nacelle is placed behind the propeller a buoyancy force, ΔC_{X_N} , is induced on the propeller due to the disturbance of the flow field by the nacelle. The apparent thrust force on the blades in the presence of the nacelle is then equal to the net thrust, $C_{T_{NET}}$, plus the buoyancy force, ΔC_{X_N} . According to inviscid theory, an equal and opposite force resulting from the buoyancy effect is felt on the nacelle. The buoyancy force is determined by integrating the measured surface pressures over the nacelle for the blades-on and blades-off configurations and calculating the difference. The equation for net thrust (fig. 4(b)) has four terms representing six independent measurements, each subject to experimental uncertainty.

The derivation of the slipstream interference drag, $C_{D_{SS}}$, is illustrated in figure 4(c). The drag of the various components is shown for the clean wing, blades-off, and blades-on configurations. Also shown is the resultant drag indicated by the floor balance, $C_{D_{BAL}}$. The difference between the blades-on and blades-off expression is the slipstream interference drag, $C_{D_{SS}}$. This difference was obtained for blades-on/blades-off results at the same EPR. Where possible, the total enthalpy of the flow was matched as well as the EPR. Similarly, the equation for the slipstream interference lift is

$$C_{L_{SS}} = \left(C_{L_{BAL}} - C_{T_{JET}} \sin \alpha \sin \theta_T - C_{T_{NET}} \sin \alpha \sin \theta_T \sin \theta_D \right) \\ - C'_{L_{BAL}} - C'_{T_{JET}} \sin \alpha \sin \theta_T$$

where the prime indicates the blades-off value.

The equation for the slipstream interference drag requires 10 independent measurements, each subject to experimental uncertainty. The uncertainty in $C_{D_{SS}}$ has been estimated to be ± 0.0013 . The maximum uncertainties in the floor balance readings, based on repeatability, have been estimated to be ± 0.0020 in lift coefficient and ± 0.0002 in drag coefficient.

The equations used to obtain the net thrust, thrust removed lift, drag and pitching moment, propeller performance parameters, and propulsion interference drags are detailed below.

$$\text{Propeller-nacelle buoyancy: } \Delta C_{X_N} = C_{X_{N_{on}}} - C_{X_{N_{off}}} \quad (1)$$

$$\text{Net thrust: } C_{T_{NET}} = C_{T_{BAL}} - \Delta C_{X_N} + C_{X_H} + C_{X_{HB}} \quad (2)$$

Thrust removed lift, drag, and pitching moment:

$$C_{N_{TR}} = C_{N_{BAL}} - C_{N_{JET}} + C_{T_{NET}} \sin \theta_D \cos \theta_T$$

$$C_{X_{TR}} = C_{X_{BAL}} + C_{X_{JET}} + C_{T_{NET}} \cos \theta_D \cos \theta_T$$

$$C_L = C_{N_{TR}} \cos \alpha - C_{X_{TR}} \sin \alpha \quad (3)$$

$$C_D = C_{X_{TR}} \cos \alpha + C_{N_{TR}} \sin \alpha \quad (4)$$

$$C_m = C_{m_{BAL}} - \left(0.02261 C_{X_{JET}} + 0.20053 C_{m_{JET}} - 0.10625 C_{N_{JET}} \right) / \bar{c} \quad (5)$$

$$\text{Net efficiency: } \eta_{NET} = 9.5493 C_{T_{NET}} q_{SV}/QN \quad (6)$$

$$\text{Propeller thrust coefficient: } C_{T_{prop}} = 3600 C_{T_{NET}} qS/\rho(ND^2)^2 \quad (7)$$

$$\text{Propeller power coefficient: } C_{P_{prop}} = 0.216 \times 10^6 \text{ HP}/\rho N^3 D^5 \quad (8)$$

The equations for the interference drags are obtained by differencing the drags of two different configurations at constant values of lift coefficient and EPR.

$$\text{Jet effect: } C_{D_{JET}} = C_{D_{JET-ON}} - C_{D_{JET-OFF}} \quad (9)$$

$$\text{Slipstream drag: } C_{D_{SS}} = C_{D_{blades-on}} - C_{D_{blades-off}} \quad (10)$$

$$\text{Total installation drag: } C_D = C_{D_{blades-on}} - C_{D_{WB}} \quad (11)$$

RESULTS AND DISCUSSION

Measured results, flow visualization studies, and pressure contours are presented in figures 5 through 28. The variations of slipstream interference drag and total propulsion installation drag are shown in figures 29 through 31. A limited sample of the data are presented for discussion herein. More extensive test results are provided in graphical form on microfiche which are affixed to the inside back cover of this report. A listing of the data shown on the microfiche can be found in the appendix.

Pressure Distributions

Wing pressure distributions for three configurations are compared in figures 5 through 10. Nacelle pressures are presented as a function of azimuth in figures 11 through 15. The discussion of the pressure results is limited to the nominal cruise condition of $M = 0.8$ at an angle of attack of 2° . At this condition, the variations shown in EPR (figs. 5, 6, 10, 11 and 12) are not significant. Results at other Mach numbers and angles of attack are included on the microfiche. Note that along the nacelle centerline ($\eta = 0.481$) the nacelle pressures at $\psi = 0^\circ$ (upper surface) and $\psi = 180^\circ$ (lower surface) have been referenced to the baseline wing leading edge. At this semispan station, the pressures between $-0.194 < x/c < 0.390$ are on the nacelle centerline. A negative value for x/c represents a point ahead of the baseline wing leading edge.

Blades off- Blades-off pressure distributions at cruise EPR are compared with the wing-body in figure 5. Note that both upper and lower surface pressures are shown with the same symbol. The addition of the nacelle produced significant changes in the pressure distributions in the vicinity of the nacelle. Just inboard of the nacelle, the wing shock wave was strengthened by the nacelle as indicated by a change in the peak upper surface C_p from about -1.0 to -1.6 . In addition, a shock wave was formed on the lower surface due to the addition of the nacelle. Integration of the pressures showed that the net effect was a substantial loss in section lift. The pressure distributions further inboard ($\eta < 0.418$) indicate small separations may occur due to the nacelle installation. The upper surface pressure peaks at $\eta < 0.418$ were increased, but not to the level that would cause large flow separation. Just outboard of the nacelle ($\eta = 0.544$), both the upper and lower surface pressures were reduced slightly from the leading edge to approximately 70% of the wing chord. The effect of the nacelle on the wing pressures diminished towards the tip.

The addition of the LEX (fig. 5) reduced the upper surface pressure peak from -1.6 to about -1.2 at $\eta = 0.418$. The lower surface pressure peak has also been reduced and hence, the strength of the shock wave has diminished. The pressures outboard of the nacelle were unaffected by the LEX, as would be expected.

Blades on- A comparison of wing pressure distributions at cruise power are shown in figure 6 for the three test configurations. The direction of propeller rotation was up-inboard, which increased the local angle of attack of the inboard airfoil sections and decreased the local angle outboard. At $\eta = 0.418$, the addition of the LEX did not affect the magnitude of upper surface suction peak. The location of the pressure peak on the LEX was approximately the same distance behind the LEX leading edge as the wing peak was behind the wing leading edge. The addition of the LEX has not affected the upper surface pressure peak because the flow is separated. However, the lower surface suction peak has been eliminated. Addition of the fillet and strake reduced the upper surface suction peak from about -1.6 to about -1.1 at $\eta = 0.418$. This indicates that adding the fillet eliminated the flow separation as indicated by the steep pressure gradient. Further inboard, the fillet increased the suction peak and moved the peak pressure location slightly behind that for the LEX configuration. The fillet and strake had a small effect on the lower surface pressures. Outboard of the nacelle ($\eta > 0.481$) there were only small differences among the configurations. The fillet and strake significantly reduced the installation drag penalty, which will be discussed later. Because of this drag reduction, it is suggested that the LEX and fillet may work as a more efficient stator for recovering some of the energy lost in the form of slipstream angular momentum. The removal of a portion of the slipstream swirl indicates it may be desirable to allow the wing to depart from an elliptic span load distribution.

Power effects- The effect of power on the wing pressures of the baseline configuration (WBNP) is shown in figure 7. An $EPR = 1.0$ represents the propeller at windmill speed (jet-off); an $EPR = 1.257$ represents an intermediate power setting; and an $EPR = 1.774$ is near cruise power. Inboard of the nacelle, within the propeller slipstream, increased power tends to increase regions of separated flow because of propeller swirl. Because the wing cannot support the large pressure gradients, the flow separates. On the lower surface, there was generally an increase in C_p with increasing power. The net effect of the increase in power was a small increase in section lift inboard from the nacelle. Just outboard of the nacelle, the effect of power was to decrease the upper and lower surface pressures forward of the 60% chord station. The effects shown are consistent with the changes in local section angle of attack due to propeller rotation. Outboard of the propeller slipstream ($\eta > 0.597$) the effects of power were not significant.

The effect of power on the WBNLP and WBNLF3SP configurations are shown in figures 8 and 9, respectively. The trends resulting from power are similar to those described for the baseline configuration. Inboard, additional power decreases the upper surface pressure coefficients and increases them on the lower surface. Outboard, additional power increases the upper surface C_p and decreases the lower surface C_p . These results are consistent with an up-inboard propeller rotation.

Figure 10 compares blades on/off pressure distributions at cruise power for the LEX configuration. Inboard of the nacelle, the upper surface pressures decrease with blades on, caused by the increase in local section angle of attack due to the propeller slipstream swirl. The slipstream changes the nature of the flow at $\eta = 0.418$ as follows: (1) on the upper surface the blades-off shock wave has been

replaced by a region of separated flow ($0 < x/c < 0.3$); and (2) on the lower surface the weak shock wave has been eliminated. Outboard of the nacelle ($\eta > 0.481$), the effect of the slipstream is generally consistent with a decreased angle of attack.

Nacelle pressures- The variation of nacelle surface pressures with an azimuth at each of the 12 nacelle stations is shown in figures 11 through 15. The values of XNAC indicated on the figures is the nacelle station in meters. The zero-degree-azimuth position is at the top of the nacelle, increasing clockwise when viewed from the front. The first nacelle station (XNAC = 0.254 m) is 1.27 cm (0.5 in.) behind the hub. The inboard wing, leading-edge/nacelle intersection is located at approximately XNAC = 0.597 m for the baseline configuration and at approximately XNAC = 0.521 m for the LEX configuration. With blades-off (fig. 11), there were only small differences in C_p between the baseline and LEX configurations, except near the wing/nacelle intersection (XNAC = 0.444 to 0.597 m). At these stations, there was an increase in the negative pressure peak with the LEX caused by the wing upwash field. Behind the leading-edge intersection there were again only minor changes caused by the LEX. The effects of the LEX with blades on are similar to those with blades off. Near the wing/nacelle juncture, the variation in C_p was greatest with LEX on. Further downstream, the differences between blades on and blades off were about the same for the LEX configuration as for the baseline. Although slight, the effect of the slipstream extends over the entire length of the nacelle.

The effect of the fillet and strake on the nacelle pressures is presented in figure 12. The nacelle pressures were affected more by the fillet ($\psi = 270^\circ$) than by the strake ($\psi = 90^\circ$), probably as a consequence of the greater spanwise extent of the fillet. It was shown in reference 13 that with blades off the drag improvement from the strake was about equal to the increment provided by the inboard fillet. The reason for this is not apparent from either the nacelle or wing pressure distributions.

The effect of power on the nacelle pressures for the WBNP, WBNLP, and WBNLF3SP configurations is shown in figures 13 through 15, respectively. Applying cruise power slightly increased the surface pressures over the nacelle when compared with the windmilling propeller. The pressures generally decreased downstream from the wing/nacelle juncture. The effect of power on the WBNLF3SP configuration was less than for the other two configurations.

Flow Visualization Studies

Several configurations were studied using fluorescent oil to visualize the flow in the boundary layer. Photographs taken under ultraviolet light are presented in figure 16.

Figure 16(a) shows the wing (alone) upper surface. The effect of adding the nacelle with propeller off and jet off is shown in figure 16(b). This photograph shows the strong inward sidewash behind the nacelle and the strong normal shock adjacent to the inboard side of the nacelle. The shock location agrees with that

indicated on the pressure distributions (fig. 5). A small separation bubble can be seen just downstream of this shock. Figure 16(c) shows the effect of the LEX on the upper surface boundary layer flow. The normal shock wave on the inboard side of the nacelle has been almost completely eliminated. A reduction in shock strength would be expected because the increased chord has effectively thinned the wing section, increasing the drag rise Mach number. The LEX had little effect on the strong inward sidewash or the small region of trailing edge separation behind the nacelle. Figure 16(d) is a photograph of the underside of the WBNLP with jet off (propeller at windmill). It shows the separation behind the nacelle exhaust pipe which is primarily responsible for the jet-off lift loss described in reference 12. The effect of the jet (propeller off) is shown in figure 16(e). It is evident that the large separated flow region behind the exhaust pipe has been greatly reduced. With the jet on, much of the wing lower surface lift is restored, the major contribution to the "jet effect" benefit.

The effect of a windmilling propeller (power off) on the wing upper surface boundary layer flow is shown in figure 16(f). Comparison of this photograph with the propeller- and jet-off case (fig. 16(b)) shows little or no effect of the windmilling propeller. The upper surface flow with the propeller at cruise thrust is shown in figure 16(g). The inboard upper surface flow curves sharply forward in a highly irregular separated flow region. Across the top of the nacelle, the sidewash in the boundary layer has been greatly increased from the windmill condition (fig. 16(f)), indicating the presence of strong spanwise pressure gradients. This is supported by the pressure distributions (fig. 8) and the pressure contours described in the next section. The lower surface boundary layer flow, with the propeller at cruise thrust, is shown in figure 16(h). Comparison of this photograph with the propeller-off, jet-on case (fig. 16(e)), shows little or no effect of the propeller on the lower surface flow. For this under-the-wing nacelle configuration, the lower surface flow appears to be dominated by nacelle geometry rather than by the propeller. Based on these findings, it would be expected that for an over-the-wing nacelle configuration, the wing lower surface boundary layer flow would be affected more by the propeller rather than by the nacelle.

Pressure Contours

Pressure contours (isobars) for the upper and lower wing surfaces are presented in figures 17 through 19. The outline enclosing the contours on the figures extends from $\eta = 0.250$ to $\eta = 0.849$, the range for the rows of pressure taps. For those configurations that include the nacelle, the pressures on the nacelle at $\psi = 0^\circ$ are used for the upper surface and $\psi = 180^\circ$ for the lower surface. Only those nacelle pressures which lie at or behind the wing leading edge were used to obtain the isobars.

Isobar patterns serve as a useful guide to study configuration modifications and slipstream effects on the wing. Figures 17(a) and 17(b) show the isobars for the wing-body upper and lower surfaces, respectively. Note that the benefits of sweep are maintained over most of the wing planform. No undesirable features are

evident, such as unnecessarily high suction peaks or steep adverse pressure gradients. Adding the nacelle (figs. 17(c) and 17(d)) causes a concentration of the isobars inboard of the nacelle and toward the wing leading edge. Upper surface suction peaks are increased and the effectiveness of wing sweep is lost in this region. This indicates the presence of strong pressure gradients caused by a shock wave as shown by the oil flow visualization studies. The isobar patterns for the WBNL are shown in figures 17(e) and 17(f). They show an improvement due to adding the LEX. The suction peaks have been reduced, the pressure gradients are less severe, and effectiveness of wing sweep has been restored to some extent.

For the WBNP configuration, in the presence of the slipstream (figs. 18(a) and 18(b)), there is an unsweeping of the isobars. Also, the beneficial effects of wing sweep are lost when compared to the blades-off configuration (fig. 17(c)). Inboard, the wing local angle of attack is increased and the pressure peak moved forward. Toward the center of the propeller, the low-pressure isobars increase slightly (less negative C_p) compared to the blades-off configuration (fig. 17(c)). This causes the isobar pattern to be less severely unswept. Further outboard, within the propeller slipstream, the wing local angle of attack is decreased. Outside the slipstream, the isobars tend to assume a pattern similar to the wing alone. When the LEX was installed (figs. 18(c) and 18(d)), there was a significant improvement in the isobars inboard from the nacelle compared to the baseline configuration.

The addition of the fillet and strake (figs. 19(a) and 19(b)) increases the suction pressure peak and gradients on the LEX. The strake causes the outboard isobars to be less densely spaced (reduced gradients) and thereby restores sweep effectiveness. Unfortunately, a motor bearing failure prevented obtaining boundary layer flow visualization photographs for the fillet-strake configuration. However, oil flow studies of an unpowered wing-nacelle-fillet configuration were made during a previous test (ref. 13). The boundary layer flow visualization studies from that test showed the inboard shock wave had moved inward and was not normal to the flow as was the shock on the baseline configuration. Behind the shock, the flow had the appearance of being similar to the flow around a flat plate with stationary vortices rolled up at the edges. Because of the vortices, the flow behind the shock appeared to be quickly returned to the uniform streamwise flow. It is felt that the flow with the propeller on would be similar to that with the propeller off in those regions outboard of the slipstream.

Longitudinal Aerodynamic Characteristics

The effects of Reynolds number and power on the thrust-removed longitudinal aerodynamic parameters are presented in figures 20 through 22. The longitudinal force and moment coefficients for all configurations are referenced to the trapezoidal wing area of the baseline configuration.

Wing-body characteristics- Reynolds number effects on the longitudinal aerodynamic parameters of the wing/body configuration are shown in figure 20. At all test

Mach numbers, both lift and pitching moment are affected only slightly by variations in Reynolds number. The variation in drag is caused by the effect of Reynolds number on skin friction. The differences shown are generally less than the differences in calculated skin friction drag, assuming an all turbulent boundary layer. Note that for semispan configurations the absolute drag levels are not representative of a full span configuration. Additional contributions to the drag are caused by the tunnel-floor boundary layer acting on the underside of the body and possibly altering the reflection plane by the crossflow boundary layer with changes in angle of attack. However, it should be emphasized that reliable increments can be obtained from semispan testing.

Baseline characteristics- The effects of jet exhaust on the thrust-removed aerodynamic parameters of the baseline configuration are compared with the wing-body parameters in figure 21. An $EPR = 1.0$ represents jet-off; an $EPR = 1.75$ is near cruise. With jet-off, the lift coefficient at all angles of attack was reduced without significant effect on the lift curve slope, the stability was reduced, and the drag coefficient increased significantly at all lift coefficients. The lift loss with jet-off was caused by flow separation at the base of the nacelle, evidenced by the flow visualization photograph (fig. 16(d)). Turning on the jet restored much of the lift loss caused by this flow separation; the stability was slightly increased and the drag was reduced. For instance, at $C_L = 0.5$, the jet-off nacelle drag penalty, indicated by the difference between the circles and squares, is about 71 counts (0.0071). Turning on the jet reduced the installed nacelle drag penalty to about 38 counts. The difference between the two (33 counts) is the jet effect, $\Delta C_{D_{JET}}$, discussed previously.

When the nacelle was installed, the angle of attack had to be increased approximately 0.5° to maintain a $C_L = 0.5$. With jet on, the angle of attack had to be increased only 0.15° to maintain this C_L . This confirms the results described in reference 13 that the high jet-off nacelle drag and lift loss was caused primarily by separated flow at the base of the nacelle. Therefore, the jet-off nacelle drag increments do not represent the nacelle installed drag.

LEX characteristics- The effect of the LEX on the thrust-removed longitudinal parameters at $M = 0.8$ is shown in figure 22. Adding the LEX had a negligible effect on the lift when compared with the baseline (WBN). However, adding the LEX had a significant destabilizing effect due to an increase in area forward of the moment reference. The pressure distributions with LEX on (fig. 5) confirm the forward movement of the wing chordwise loading. The LEX reduced the drag at all lift coefficients when compared with the baseline wing-body-nacelle configuration. At $C_L = 0.5$, the drag with LEX on was about 10 counts less than the baseline. The net jet-on nacelle installation drag penalty was about 23 counts at $C_L = 0.5$ for the LEX configuration (circles vs. diamonds). The primary benefit of adding the LEX was to restore the inboard wing sections drag divergence characteristics to more nearly resemble the wing alone. The 23-count installed drag includes a friction drag increment for the LEX. Adding the LEX has reduced the nacelle installation drag penalty close to that of the isolated nacelle (20 counts), as reported in reference 12.

Propeller performance- The variation in propeller power coefficient, and net efficiency as a function of advance ratio is shown in figure 23. Results are shown for two propeller blade pitch angles at angles of attack from 0° to 4°. Propeller power and thrust coefficient increase with increased blade pitch angle because of the expected decrease in windmill speed with increased blade pitch. These characteristics were affected only slightly by changes in angle of attack. The maximum value of net efficiency increased slightly with increased blade pitch angle; the maximum occurred at a higher advance ratio (lower propeller speed). Note that the highest value of advance ratio represents the propeller at windmill. The lowest value represents a point beyond the estimated cruise condition.

The effects of configuration modifications on propeller performance at the cruise condition are shown in figure 24. The power and thrust for a constant advance ratio are lower with LEX on than for the baseline. At a constant value of propeller thrust coefficient, configuration modifications cause a decrease in the advance ratio. The largest incremental decrease in advance ratio (J) occurred when the LEX was added. The difference in J due to configuration modifications is equivalent to an increase of 0.25° in blade pitch angle (for a fixed configuration). The net efficiency is less for the LEX configuration than for the baseline, with a further reduction when the fillet and strake are added. The net efficiency varies according to the relation $\eta_{NET} = J C_{T_{prop}} / C_{P_{prop}}$. For a given thrust coefficient, the decrease in J resulting from configuration modifications results in a reduced net efficiency. From these data it appears that configuration geometry has a significant effect on propeller efficiency. It is not clear why the addition of the LEX, fillet, and strake have such an effect on propeller performance.

The effect of Reynolds number on propeller performance for the baseline configuration is shown in figure 25. At the lower Reynolds number, less power was required for the same propeller speed and less thrust was generated. At low advance ratios (J < 3.2) the net efficiency shows no significant Reynolds number effect. There appears to be a greater effect of Reynolds number at the lower rpm. However, at high advance ratio and low Reynolds number the data is more uncertain because the balance was so lightly loaded. A small Reynolds number effect would be expected as a consequence of a slight change in the flow characteristics over the propeller. The 87% efficiency point (J = 3.43) at the low Reynolds number was due to the power being somewhat low, and the point is suspect. It was not known whether this was due to an error in the torque measurement or in the propeller speed.

Thrust-removed characteristics- The thrust-removed longitudinal aerodynamic parameters are shown as a function of net thrust in figures 26 through 28. Figure 26 shows the variation for several angles of attack and blade pitch angles for the baseline configuration; figure 27 presents similar data for the LEX configuration; and figure 28 compares results for different configurations. Note that a negative net thrust coefficient occurs when the propeller is windmilling. At this condition the propeller actually produces drag.

In general, the data show a significant increase in lift with net thrust at low thrust levels. Only a small thrust (EPR about 1.05) was required to restore the

lift-loss due to separation at the nacelle base. This was obtained at a low propeller speed, close to windmill. Approximately 80% of the increase in C_L from the jet-off value was achieved at an $EPR = 1.05$ or $C_{T_{NET}} = 0.0080$ ($EPR = 1.75$ is required for cruise), and further increases in thrust produced little improvement in lift. The drag generally increased with increasing thrust and at a faster rate at higher angles of attack. Even as the lift remained relatively constant with increasing thrust, the slipstream interference drag continued to increase. Initially, nose-down pitching moment increases at low thrust levels because of the restoration of the lift near the wing trailing edge. Further increases in thrust generally had only small effects on the moment.

A comparison of the three configurations at an angle of attack of 2° is shown in figure 28. At moderate and high thrust levels the LEX-fillet-strake configuration had the highest lift, and at all thrust levels had the lowest drag. The low drag levels with the fillet and strake are believed to be caused by a combination of configuration features. First, the strake may have reduced the strong inward cross flow around the nacelle, although this was not apparent from the pressure distributions. Because oil flow photographs were not available, this effect could not be confirmed. Second, the addition of the fillet eliminated the sharp corner at the wing-nacelle intersection and effectively reduced the local thickness-to-chord ratio as well. The effectively thinner wing reduces the compressibility drag, supported by the pressure distributions previously described. This reduction in compressibility drag was apparently much greater than the slight drag increase caused by an increase in surface area. It is expected that the LEX-fillet-strake configuration would have the least slipstream interference drag because the reduced thickness perturbation permits higher lifting pressures without separation. However, jet effects data on this configuration were not obtained, and therefore the slipstream interference drag could not be determined.

Installation Drag Increments

The variation of slipstream interference drag with propeller power coefficient is presented in figure 29 for a constant angle of attack of 2° . Each point represents the difference between blades-on and blades-off drag polars evaluated at the EPR and C_L for the blades-on configuration. When presented in this manner, therefore, a portion of the slipstream drag includes a small drag increment caused by an increase in lift with power. The lift coefficients caused by power at constant angle of attack may differ by up to 0.03 in the range of net thrust coefficients of interest. The slipstream interference drag coefficient increases linearly with increasing power. The addition of the LEX (fig. 29(b)) substantially reduced the slipstream drag (note change in scale). In general, the slipstream drag for the LEX configuration was approximately half the value for the baseline.

The variation of slipstream interference drag with Mach number at $C_L = 0.5$ and cruise thrust is shown in figure 30(a) for LEX off, and figure 30(b) for LEX on. At $M = 0.80$, adding the LEX reduced the slipstream drag to approximately 25% of the value for the baseline configuration. The addition of the LEX has

effectively thinned the inboard wing sections thereby increasing the drag divergence Mach number.

The variation of total powerplant installation drag as a function of Mach number is presented in figure 31. For the baseline configuration (fig. 31(a)), the installation drag generally increased with increasing Mach number; increased with increasing C_L ; and had a greater variation with Mach number at the high C_L 's. At $M = 0.8$ and $C_L = 0.5$, the total installation drag of 77 counts is approximately 24% of a typical airplane cruise drag coefficient (estimated from $C_L = 0.5$ and a lift-drag ratio of about 16).

The effect of adding the LEX on the total installation drag is shown in figure 31(b). The total installation drag again increased with increasing Mach number, but in contrast to the LEX-off results, generally decreased with increasing C_L . The LEX was designed to provide best performance, in the presence of the slipstream, at the cruise condition. These results clearly indicate that the design approach used (ref. 11) was quite successful. At the cruise condition, the installation drag was reduced from 77 counts for the baseline configuration to 36 counts with the LEX. Thus, adding the LEX (WBNLP) reduced the installation drag from 24% (WBNP) to about 11% of a typical airplane cruise drag.

The effect of adding the fillet and strake on the total powerplant installation drag is shown in figure 31(c). Eliminating the sharp corners at the wing-nacelle intersections reduced the installation drag to 18 counts at the cruise condition. This represents less than 6% of a typical airplane cruise drag and compares favorably with current turbofan installations. At the lowest test Mach number and C_L , the data indicate that there is favorable interference. However, the result is within the experimental uncertainty of the measurements, and further testing is required to substantiate these values.

CONCLUSIONS

Tests were conducted on a semispan wing/body model with a powered propeller in the Ames 11-Foot Transonic Wind Tunnel. The swept supercritical wing was tested with an under-the-wing nacelle at Mach numbers from 0.6 to 0.8 and angles of attack from -3° to 4° . The test was conducted at a constant total pressure of one atmosphere. The test results indicated the following conclusions:

1. The addition of the nacelle caused a strong acceleration of the flow, resulting in stronger shock waves on both the upper and lower wing surface. Addition of a LEX between the nacelle and body reduced the strength of the shock waves.
2. The propeller increased the suction pressure peaks inboard from the nacelle because the up-inboard propeller rotation increased the local angle of attack of the wing. Adding the LEX had a negligible effect on the upper surface suction peaks, but eliminated the lower surface suction peak. The addition of a fillet and strake significantly reduced the upper surface suction peak at the wing-nacelle juncture.

3. Low values of exhaust pressure ratio (about 1.05) restored much of the lift-loss that was caused by flow separation at the base of the nacelle when the jet was off.

4. The LEX-fillet-strake configuration had the highest lift at moderate thrust levels; it had the lowest drag at all thrust levels.

5. The total powerplant installation drag penalty ($M = 0.8$, $C_L = 0.5$) for the baseline configuration was about 77 drag counts (24% of a typical airplane cruise drag). Adding the LEX reduced the drag penalty to about 36 drag counts (11% of the cruise drag). The LEX-fillet-strake configuration had the lowest installation drag penalty of 18 drag counts (less than 6% of the cruise drag).

APPENDIX

MICROFICHE DATA ORGANIZATION

On the microfiche affixed to the inside back cover of this report, the data are presented in graphical format. The data cover the test Mach number range 0.6 to 0.8, and angles of attack from -3° to 4° . The pressure data are on microfiche pages 1 through 11, and force data are on pages 12 and 13.

A page of microfiche contains a frame matrix of 7 rows, and up to 9 columns. On each page, the first frame (upper left corner) is intentionally left blank. The figures are arranged sequentially by column. Letting "I" denote the *i*th row and "J" the *j*th column, then the figure order on any page is given by:

$$A_{11}, A_{11}, \dots, A_{71}, A_{12}, \dots, A_{72}, \dots, A_{19}, A_{2J}, \dots, A_{79}$$

The following list of figures shows the microfiche location of each figure by page, row, and column. For example, 7,3,6 indicates that the figure is located on microfiche page 7, row 3, column 6.

FIG. NO.	BRIEF TITLE	MACH NUMBER				
		0.60	0.70	0.75	0.78	0.80
	<u>Wing Pressure Data</u>					
5	Blades-off, Cruise Power	1,3,1	1,2,4	1,1,7	1,7,9	2,7,3
6	Blades-on, Cruise Power			2,6,6	2,1,9	3,4,2
7	Power Effects - WBNP			3,6,4	3,5,7	4,5,1
8	Power Effects - WBNLP			4,4,4	4,6,6	4,1,9
9	Power Effects - WBNLF3SP				5,4,2	5,2,4
10	Blades-off vs Blades-on	5,7,5	5,6,8			6,6,2
	<u>Nacelle Pressure Data</u>					
11	WBN,WBNL,WBNP,WBNLP			6,1,5	6,4,8	7,1,3
12	Effect of Fillet and Strake				7,4,6	7,1,9
13	Power Effects - WBNP			8,6,2	8,1,7	9,4,2
14	Power Effects - WBNLP			9,6,6	10,3,1	10,6,4
15	Power Effects - WBNLF3SP				10,2,8	11,7,1
	<u>Thrust Removed Characteristics</u>					
20	Reynolds Number Effects	12,3,1	12,5,1			12,7,1
21	Nacelle and Jet Effects	12,2,2	12,4,2	12,6,2	12,1,3	12,3,3
22	Lex-on vs Lex-off	12,5,3	12,7,3	12,2,4	12,4,4	12,6,4
	<u>Propeller Performance</u>					
23(A)	$\alpha = 0^\circ$	12,1,5	12,3,5	12,5,5	12,7,5	12,2,6
23(B)	$\alpha = 1^\circ$	12,4,6	12,6,6	12,1,7	12,3,7	12,5,7
23(C)	$\alpha = 2^\circ$	12,7,7	12,2,8	12,4,8	12,6,8	12,1,9
23(D)	$\alpha = 3^\circ$	12,3,9	12,5,9	12,7,9	13,3,1	13,5,1
23(E)	$\alpha = 4^\circ$	13,7,1	13,2,2			13,4,2

**ORIGINAL PAGE IS
OF POOR QUALITY**

FIG. NO.	BRIEF TITLE	MACH NUMBER				
		0.60	0.70	0.75	0.78	0.80
24	Configuration Effects			13,6,2	13,1,3	13,3,3
25	Effect of Reynolds Number					13,5,3
<u>Variation with Net Thrust</u>						
26	WBNP, PITCH=55°					13,7,3
	WBNP, PITCH=57°			13,1,4	13,2,4	13,3,4
	WBNP, PITCH=59°					13,4,4
27	WBNLP, PITCH=55°			13,5,4	13,6,4	
	WBNLP, PITCH=57°	13,7,4	13,1,5	13,2,5	13,3,5	13,4,5
	WBNLP, PITCH=59°					13,5,5
28	Configuration Effects			13,6,5	13,7,5	13,1,5
<u>Slipstream Drag</u>						
29(A)	Power Effect, $\alpha=0^\circ$, WBNP	13,2,6	$e \beta_p=57^\circ$	13,3,6	$e \beta_p=55^\circ$	
	Power Effect, $\alpha=1^\circ$, WBNP	13,4,6		13,5,6		
	Power Effect, $\alpha=2^\circ$, WBNP	13,6,6		13,7,6		
	Power Effect, $\alpha=3^\circ$, WBNP	13,1,7		13,2,7		
29(B)	Power Effect, $\alpha=0^\circ$, WBNLP	13,3,7		13,4,7		
	Power Effect, $\alpha=1^\circ$, WBNLP	13,5,7				
	Power Effect, $\alpha=2^\circ$, WBNLP	13,6,7		13,7,7		
	Power Effect, $\alpha=3^\circ$, WBNLP	13,1,8				
30(A)	Mach Variation, $C_L=0.5$, WBNP					13,2,8
30(B)	Mach Variation, $C_L=0.5$, WBNLP		13,3,8			
<u>Total Installation Drag</u>						
31(A)	Mach Variation, WBNP					13,4,8
31(B)	Mach Variation, WBNLP			13,5,8		
31(C)	Mach Variation, WBNLF3SP					13,6,8

REFERENCES

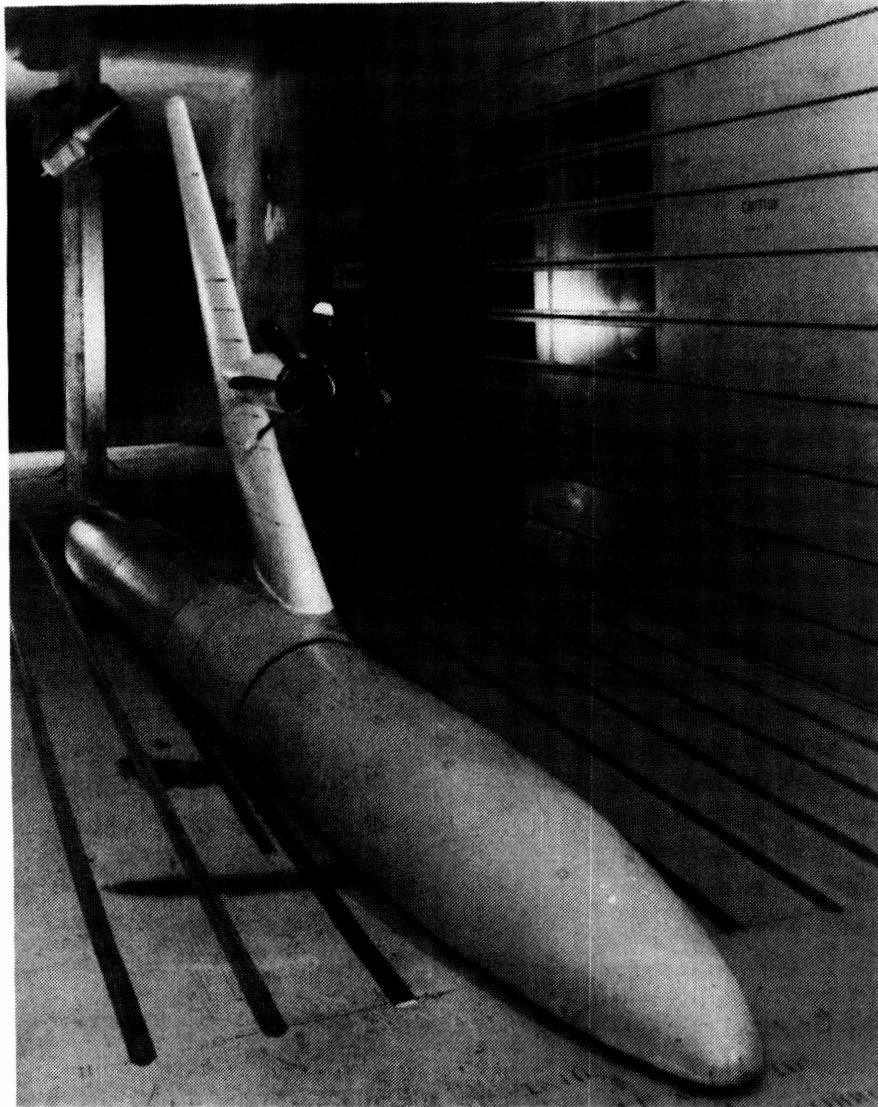
1. Hopkins, J. P.; and Wharton, H. E.: Study of the Cost/Benefit Tradeoffs for Reducing the Energy Consumption of the Commercial Air Transportation System, Lockheed-California Co. NASA CR-137927, 1976.
2. Kraus, E. F.; and Van Abkoude, J. C.: Cost/Benefit Tradeoffs for Reducing the Energy Consumption of the Commercial Air Transportation System, Vol. I: Technical Analysis, Douglas Aircraft Co. NASA CR-137923, 1976.
3. Hopkins, J. P.: Study of the Cost/Benefit Tradeoffs for Reducing the Energy Consumption of the Commercial Air Transportation System, Lockheed-California Co. NASA CR-137926, 1976.
4. Staff Paper, Energy Consumption Characteristics of Transports Using the Prop-Fan Concept, Boeing Commercial Airplane Co. NASA CR-137938, 1976.
5. Goldsmith, I. M.: A Study to Define the Research and Technology Requirements for Advanced Turbo/Propfan Transport Aircraft, Douglas Aircraft Co. NASA CR-166138, 1981.
6. Dugan, J. F.; Bencze, D. P.; and Williams, L. J.: Advanced Turboprop Technology Development. AIAA Paper 77-1223, 1977.
7. Welge, H. R.; and Crowder, J. P.: Simulated Propeller Slipstream Effects on a Supercritical Wing, Douglas Aircraft Co. NASA CR-152138, 1978.
8. Dugan, James F.: The NASA High Speed Turboprop Program. SAE Paper 80-1120, 1980.
9. Welge, H. Robert: Prop-Fan Integration at Cruise Speeds, AGARD Paper 33, presented at AGARD Symposium on Aerodynamics of Power Plant Installation, Toulouse, France, May 11-14, 1981.
10. Mendoza, J. P.: Interference Effects of Aircraft Components on the Local Blade Angle of Attack of a Wing Mounted Propeller. NASA TM 78587, 1979.
11. Welge, H. Robert; Newhart, Dan H.; and Dahlin, John A.: Analysis of Mach Number 0.8 Turboprop Slipstream Wing/Nacelle Interactions, Douglas Aircraft Co. NASA CR-166216, 1981.
12. Smith, Ronald C.; and Levin, Alan D.: Propfan Installation Aerodynamics of a Supercritical Swept Wing Transport Configuration. AIAA Paper 81-1563, 1981.

13. Levin, Alan D.; and Smith, Ronald C.: Installed Nacelle Drag-Improvement Tests of a $M = 0.8$ Turboprop Transport Configuration. NASA TM 84302, 1983.
14. Levin, Alan D.; and Smith, Ronald C.: Propfan Propulsion Integration Test Techniques. AIAA Paper 82-0577, 1982.

TABLE 1.- FILLET COORDINATES

y = 88.80 cm ($\eta = 0.396$)			y = 95.07 cm ($\eta = 0.424$)		
x, cm	z, cm upper	z, cm lower	x, cm	z, cm upper	z, cm lower
284.25	-12.09	-12.09	279.83	-13.64	-13.64
284.48	-11.63	-12.40	279.81	-13.46	-13.72
285.12	-11.30	-12.57	280.04	-13.31	-13.89
285.75	-11.07	-12.65	280.67	-12.95	-13.84
286.39	-10.95	-12.73	281.31	-12.83	-13.71
287.02	-10.80	-12.80	281.94	-12.57	-13.69
287.66	-10.67	-12.90	283.21	-12.24	-13.64
288.29	-10.52	-12.98	284.48	-11.86	-13.56
288.93	-10.31	-13.06	285.75	-11.58	-13.49
289.56	-10.13	-13.11	287.02	-11.33	-13.41
290.20	-9.98	-13.16	288.29	-11.05	-13.36
290.83	-9.83	-13.20	289.56	-10.75	-13.34
291.47	-9.73	-13.26	290.83	-10.46	-13.34
292.10	-9.58	-13.34	292.10	-10.21	-13.36
292.74	-9.45	-13.39	293.37	-9.96	-13.39
293.37	-9.32	-13.46	294.64	-9.80	-13.41
294.01	-9.19	-13.51	295.91	-9.58	-13.46
294.64	-9.09	-13.56	297.18	-9.37	-13.49
295.28	-9.02	-13.59	298.45	-9.19	-13.51
295.91	-8.89	-13.64	299.72	-9.04	-13.56
296.55	-8.81	-13.72	300.35	-8.92	-13.59
			300.99	-8.86	-13.61
			301.63	-8.69	-13.64
Fairs tangent to LEX			Fairs tangent to LEX		
x is in the wing reference plane					

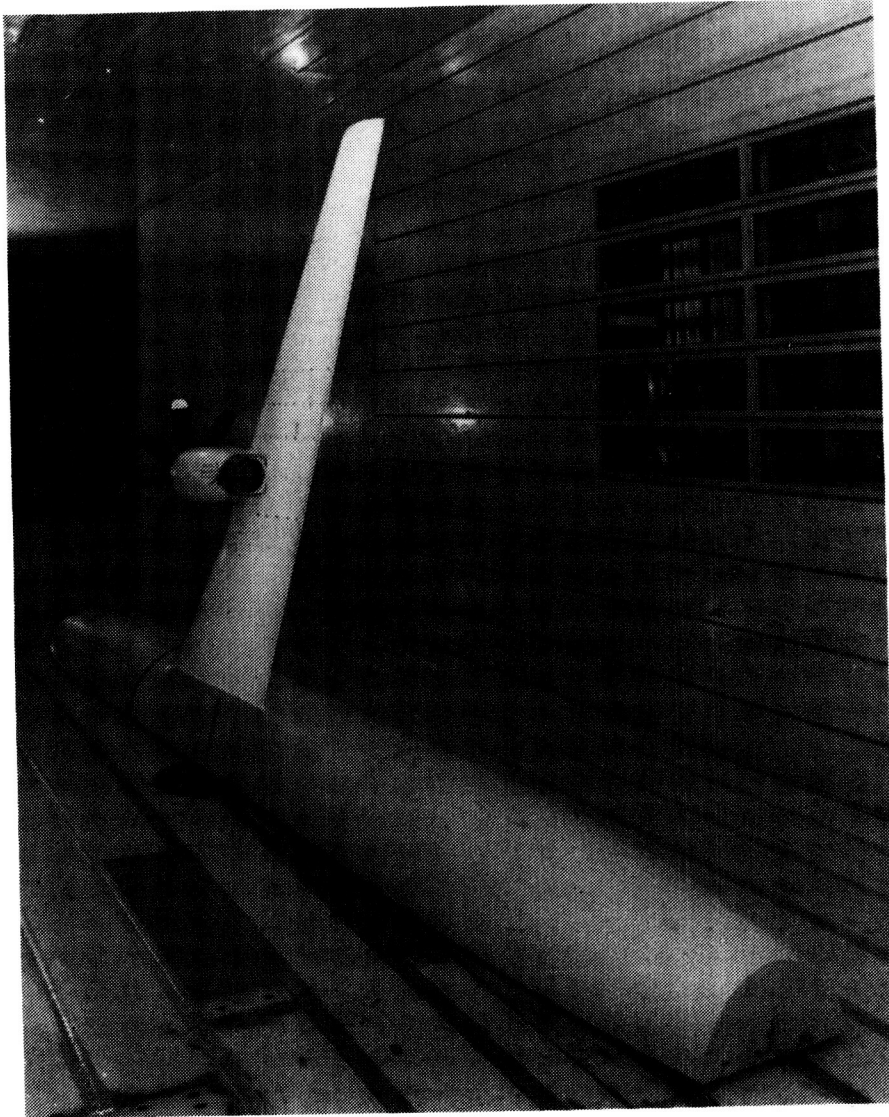
ORIGINAL PAGE IS
OF POOR QUALITY



(a) Baseline, front view.

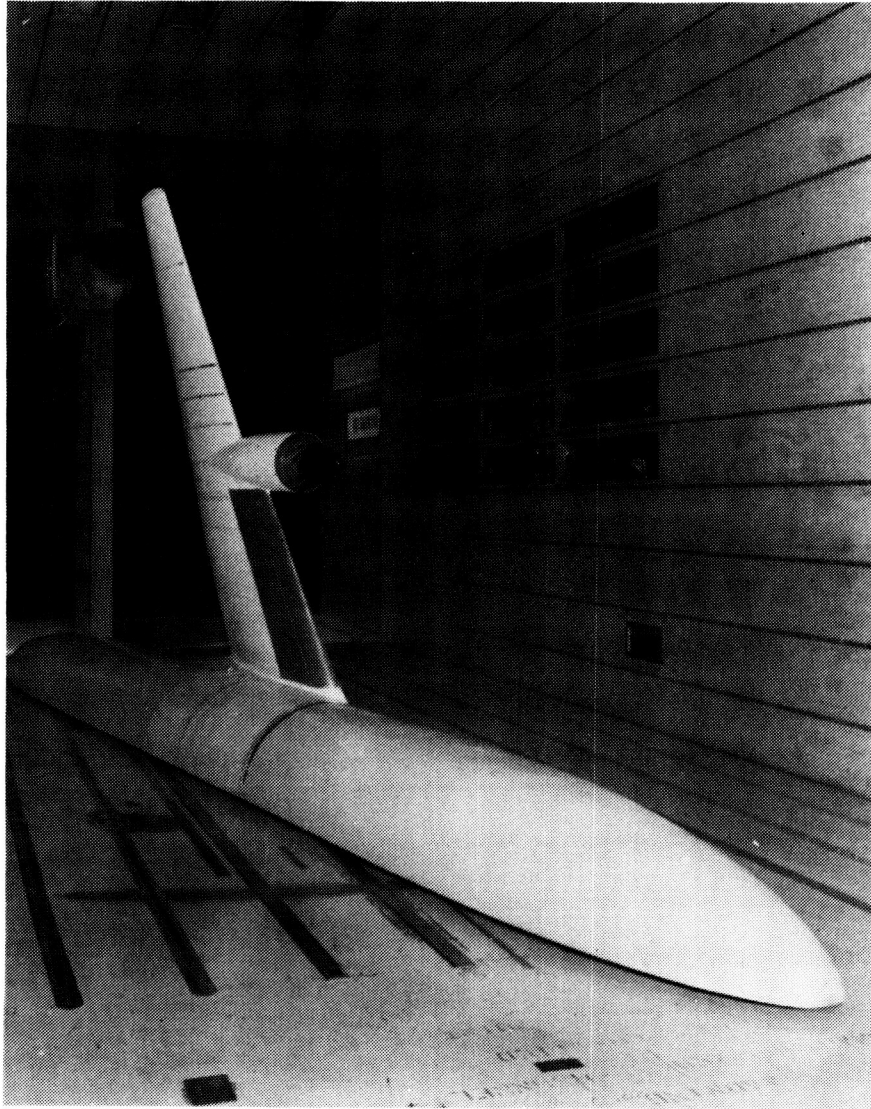
Figure 1.- Model installed in the 11-ft wind tunnel.

ORIGINAL PAGE IS
OF POOR QUALITY



(b) Baseline, rear view.

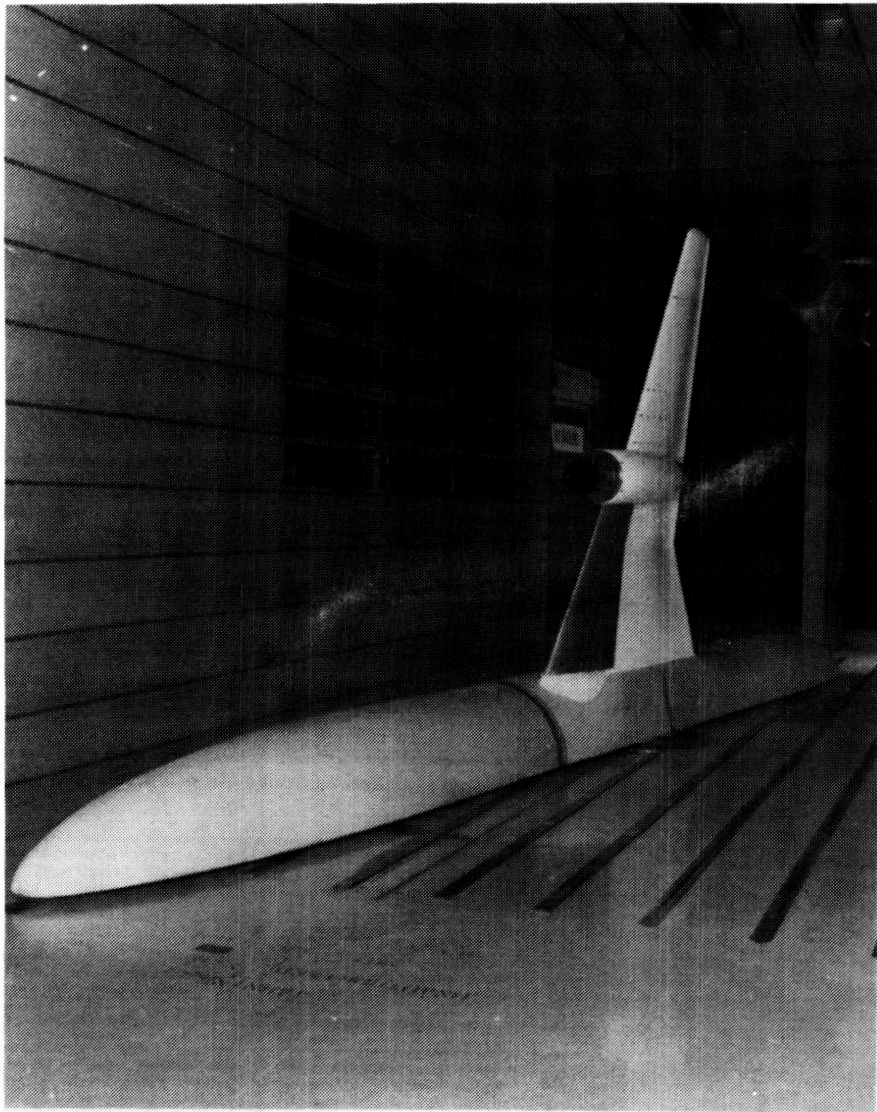
Figure 1.- Continued.



(c) LEX configuration, upper surface.

Figure 1.- Continued.

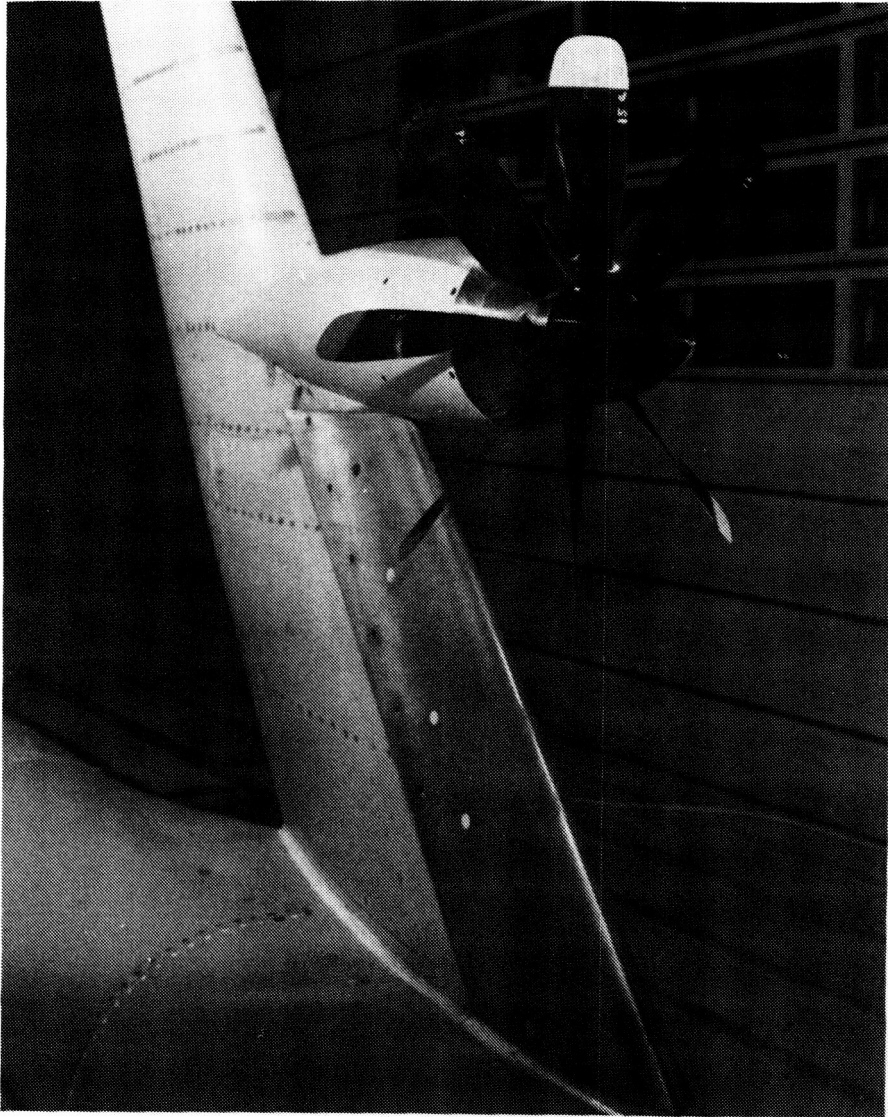
ORIGINAL PAGE IS
OF POOR QUALITY



(d) LEX configuration, lower surface.

Figure 1.- Continued.

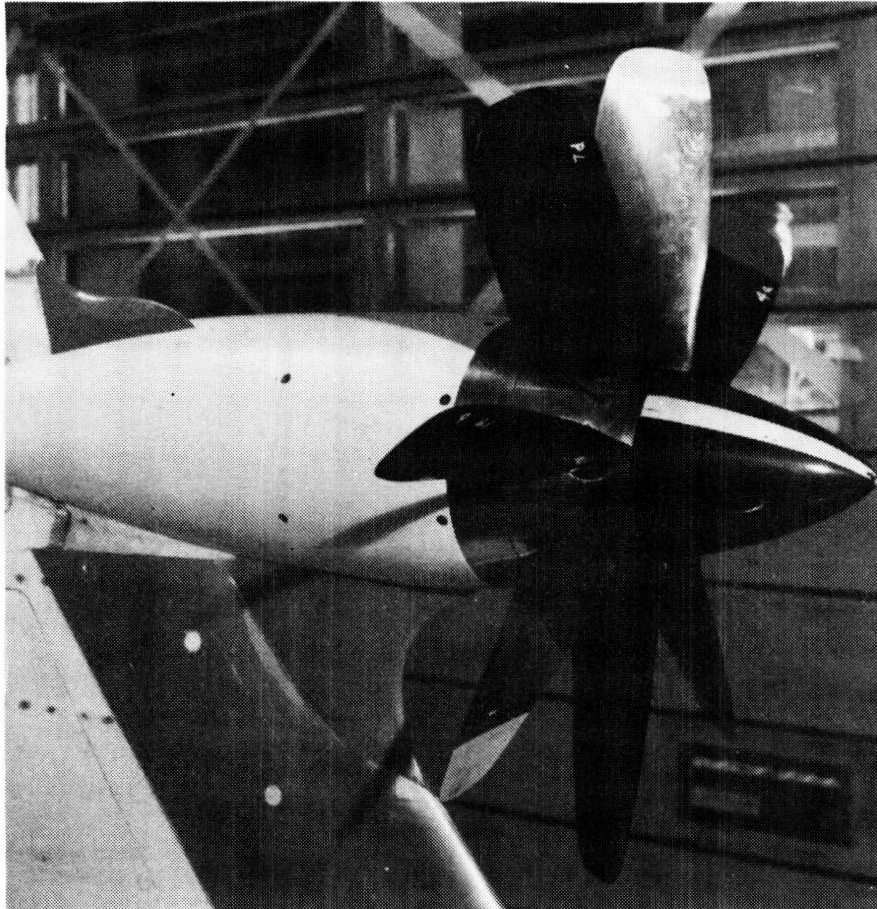
ORIGINAL PAGE IS
OF POOR QUALITY



(e) Close-up of LEX, upper surface.

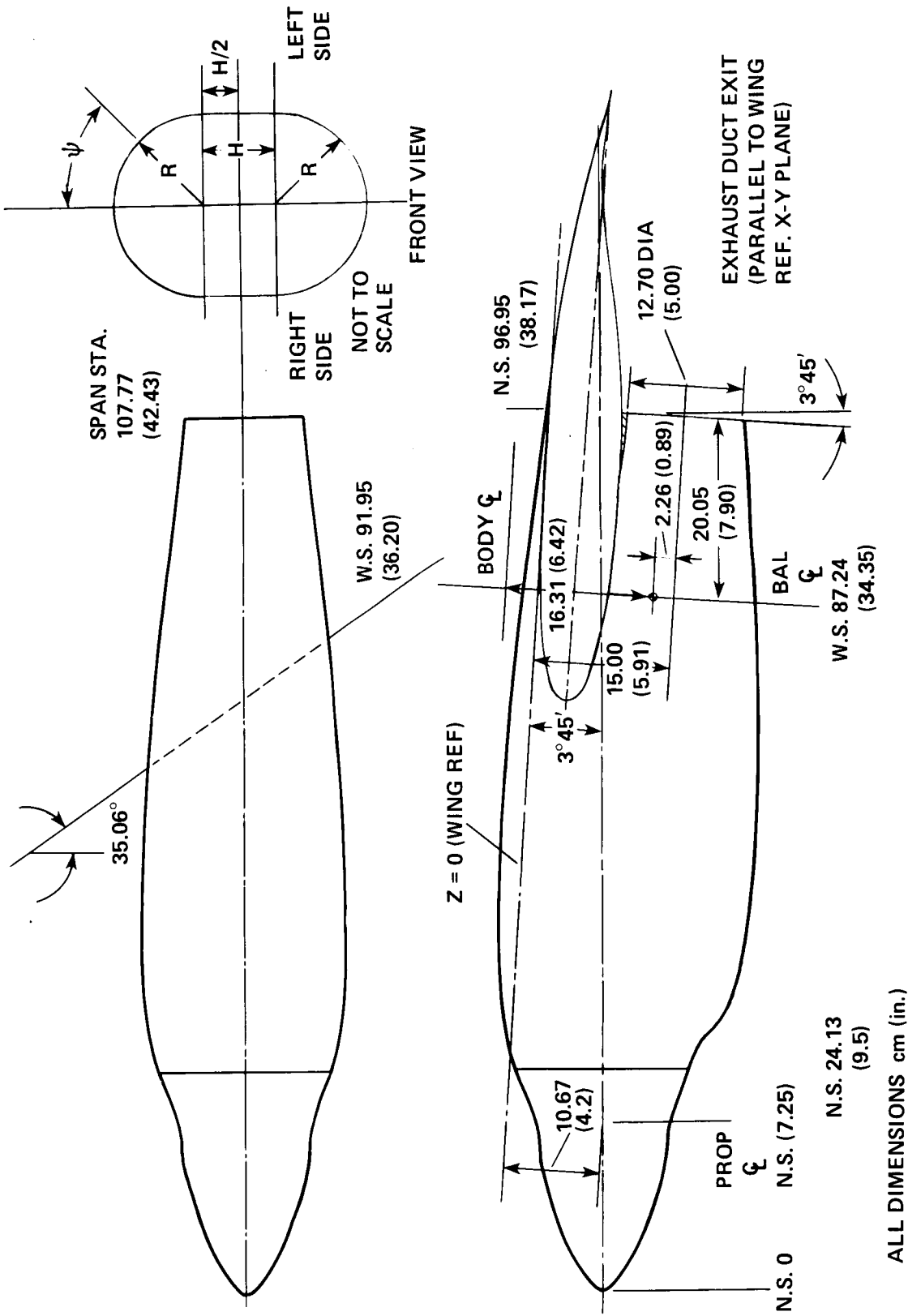
Figure 1.- Continued.

ORIGINAL PAGE IS
OF POOR QUALITY



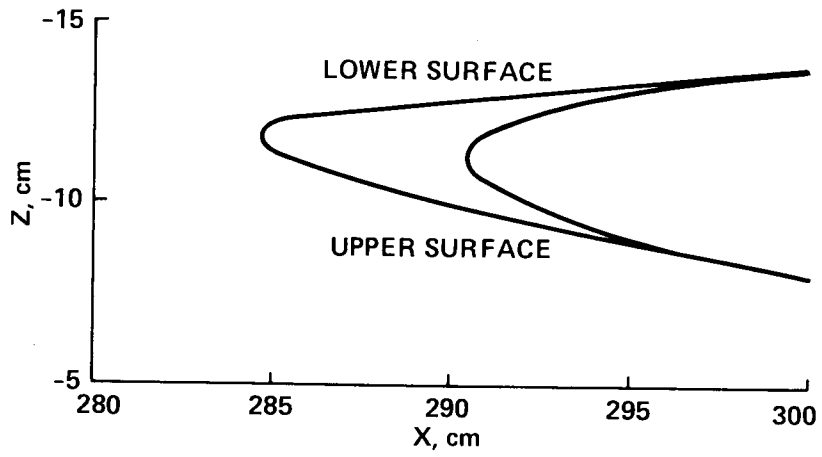
(f) LEX, fillet, strake configuration.

Figure 1.- Concluded.



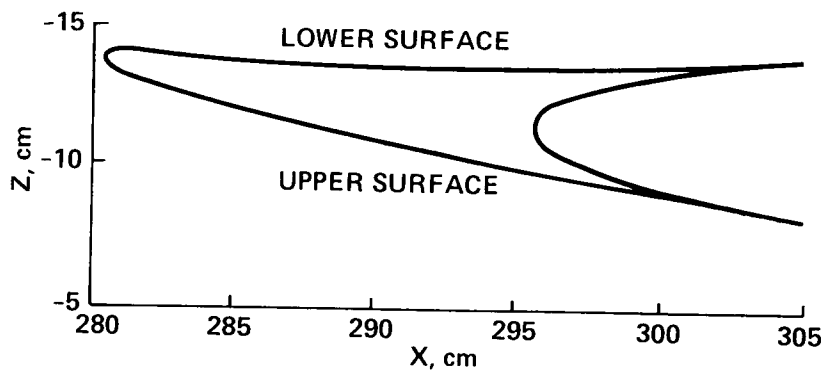
(b) Nacelle geometry.

Figure 2.- Continued.



(c) Fillet geometry at $\eta = 0.396$.

Figure 2.- Continued.



(d) Fillet geometry at $\eta = 0.424$.

Figure 2.- Concluded.

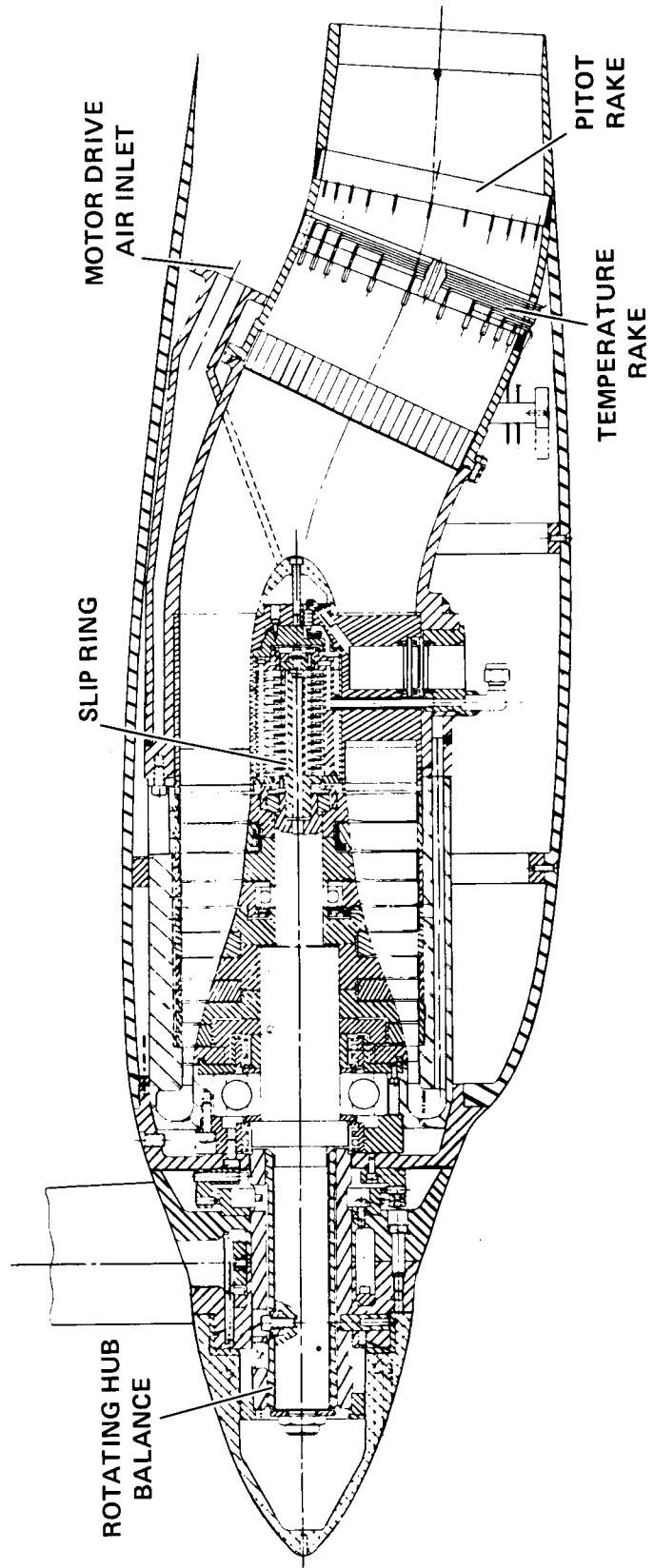
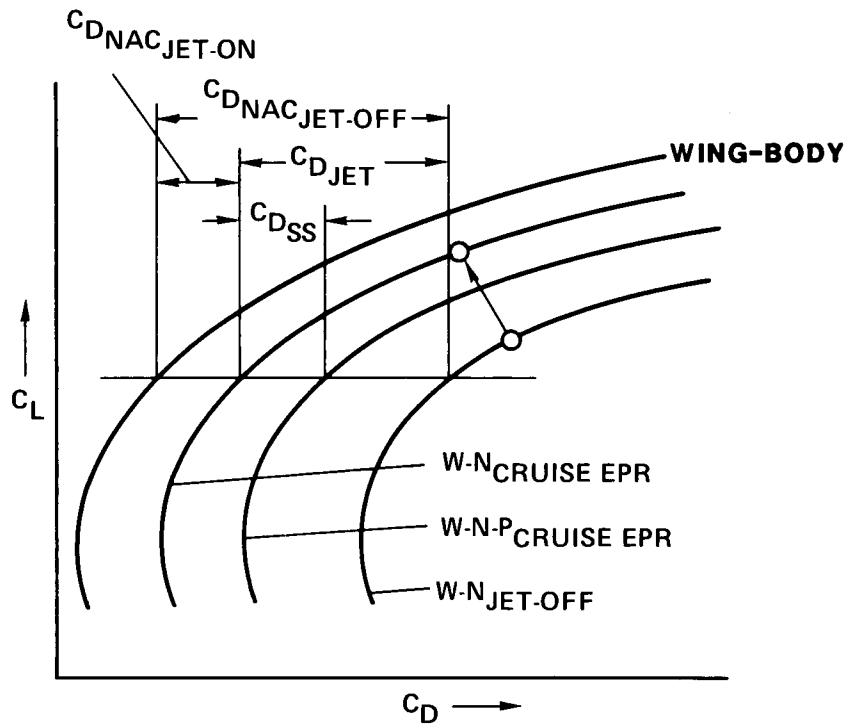
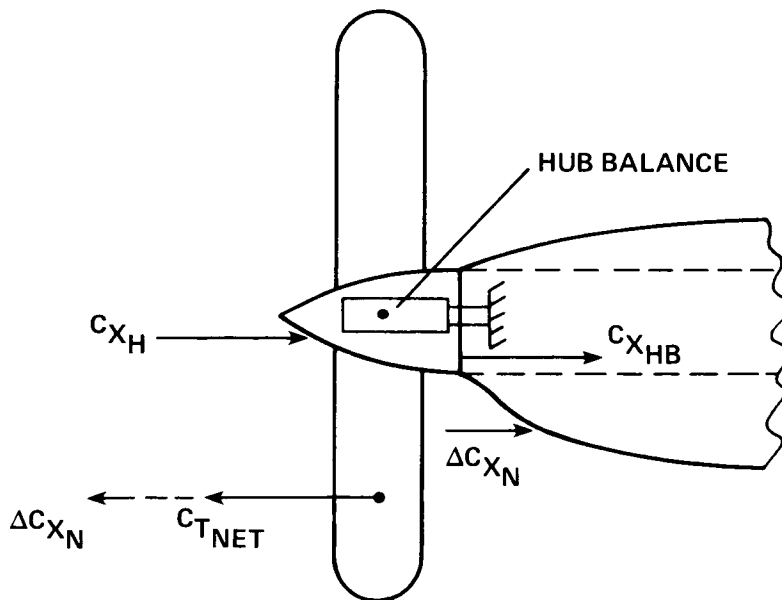


Figure 3.- Powerplant details.



(a) Interference drag increments.

Figure 4.- Illustration of drag and thrust determination.

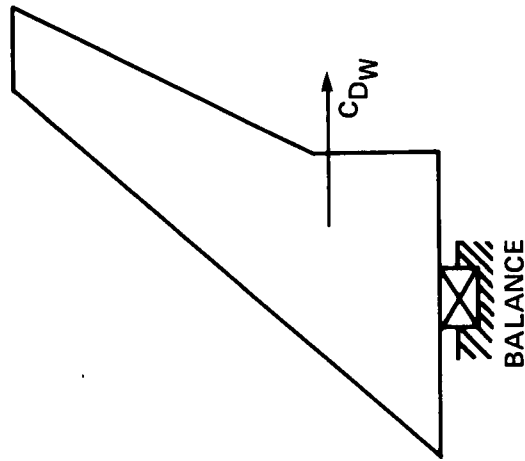


$$C_{T_{NET}} = C_{T_{BAL}} - \Delta C_{X_N} + C_{X_{HB}} + C_{X_H}$$

(b) Derivation of net thrust.

Figure 4.- Continued.

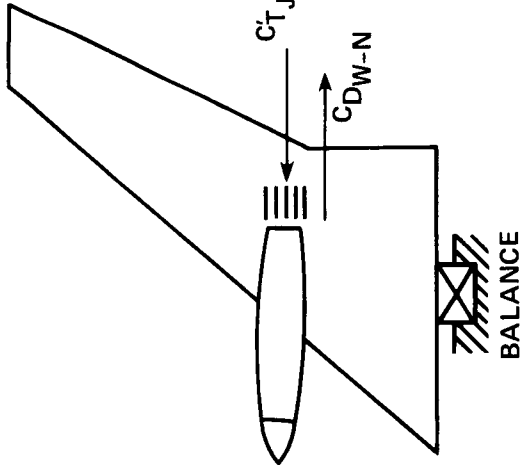
CLEAN WING



$$C_{D\text{BAL}} = C_{D\text{W}}$$

$$\Delta C_{D\text{NAC}} = C_{D\text{W-N}} - C_{D\text{W}}$$

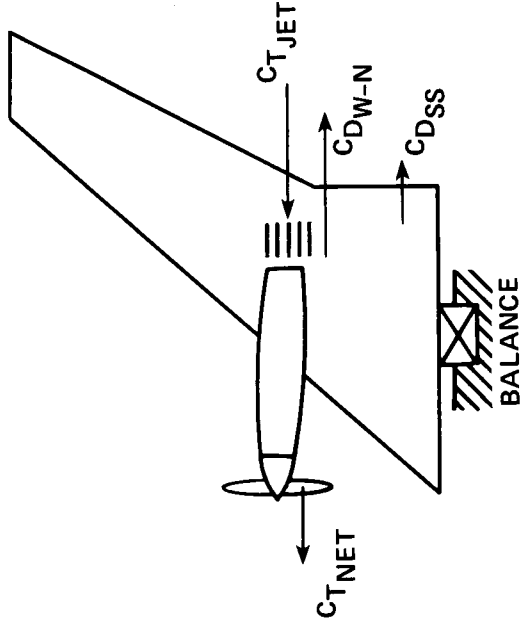
BLADES-OFF



$$C'_{D\text{BAL}} = C_{D\text{W-N}} - C'_{T\text{JET}} \cos \alpha \cos \theta_T$$

$$C_{D\text{SS}} = [C''_{D\text{BAL}} + C_{T\text{JET}} \cos \alpha \cos \theta_T + C_{T\text{NET}} \cos \alpha \cos \theta_T \cos \theta_D] - [C'_{D\text{BAL}} + C'_{T\text{JET}} \cos \alpha \cos \theta_T]$$

BLADES-ON



$$C''_{D\text{BAL}} = C_{D\text{W-N}} - C_{T\text{JET}} \cos \alpha \cos \theta_T - C_{T\text{NET}} \cos \alpha \cos \theta_D \cos \theta_T + C_{D\text{SS}}$$

(c) Derivation of slipstream interference drag.

Figure 4.- Concluded.

SYMBOL CONFIGURATION DESCRIPTION

○ HB
 □ HB
 ◻ HB
 ◊ HB

EPR ALPHA

.000 1.987
 .000 1.987
 1.682 1.946
 1.682 1.946
 1.728 1.963

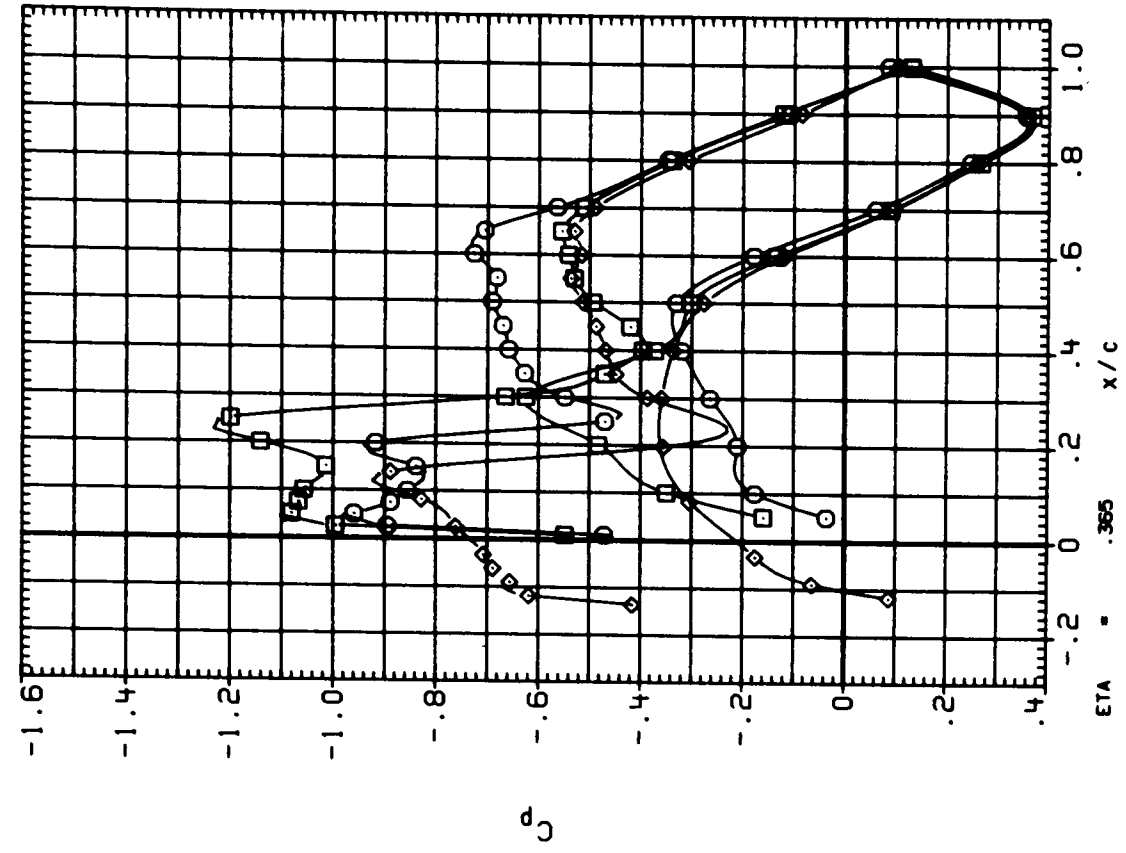
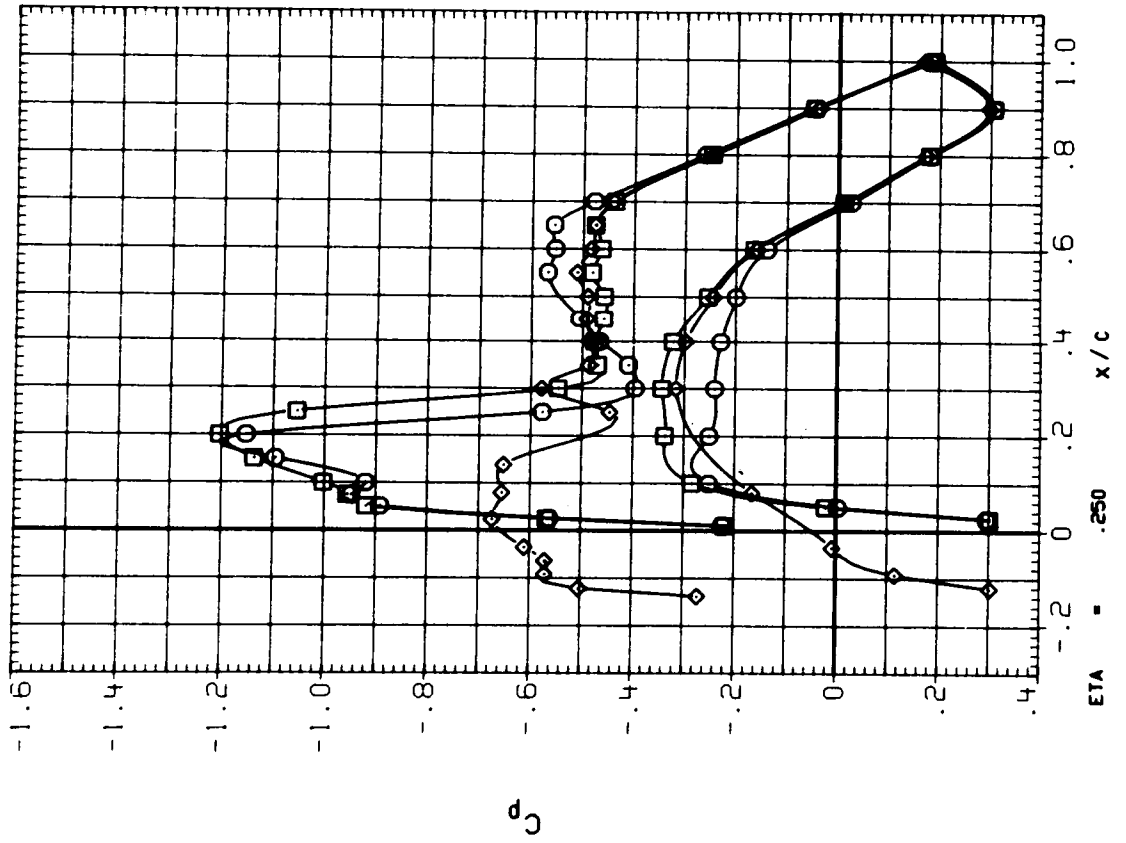


Figure 5.- Blades-off pressure distributions at cruise power; M = 0.803.

SYMBOL CONFIGURATION DESCRIPTION

- WB
- WB
- ◇ WBN
- ◇ WBNL
- ◇ WBNL

EPR ALPHA

.000	1.987
.000	1.987
1.682	1.946
1.682	1.946
1.728	1.963
1.728	1.963

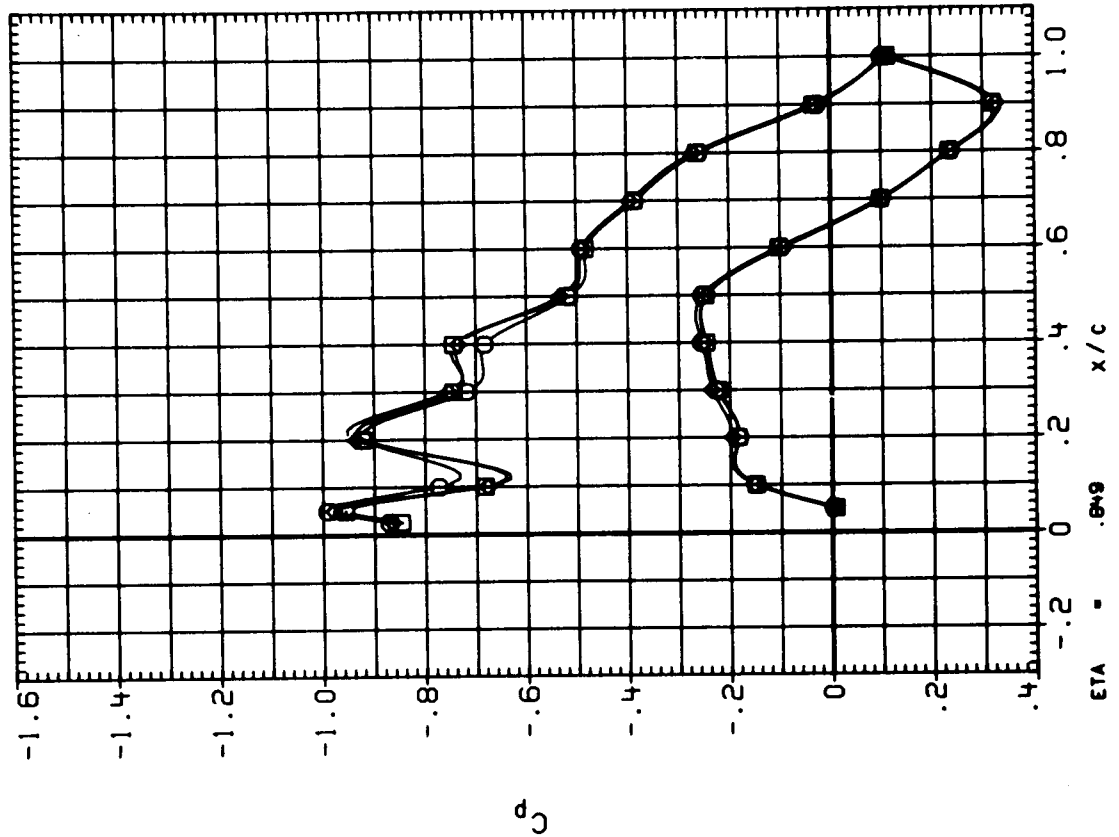
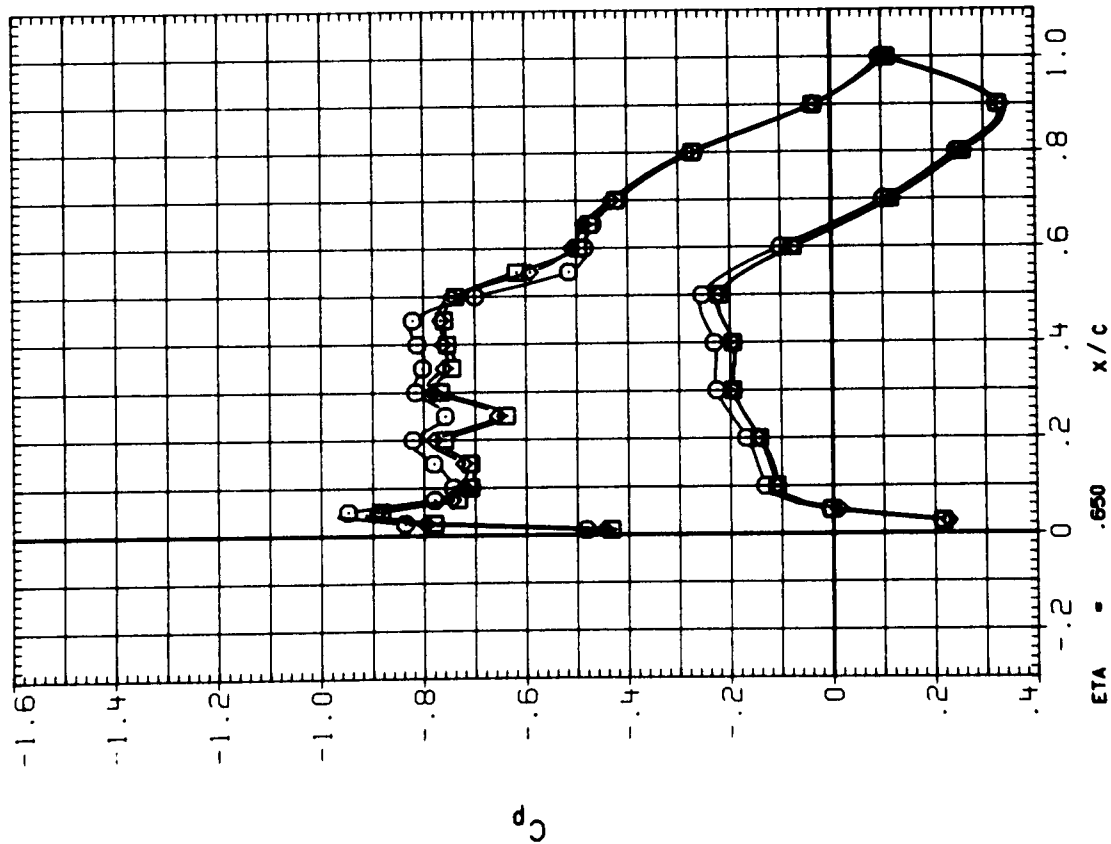
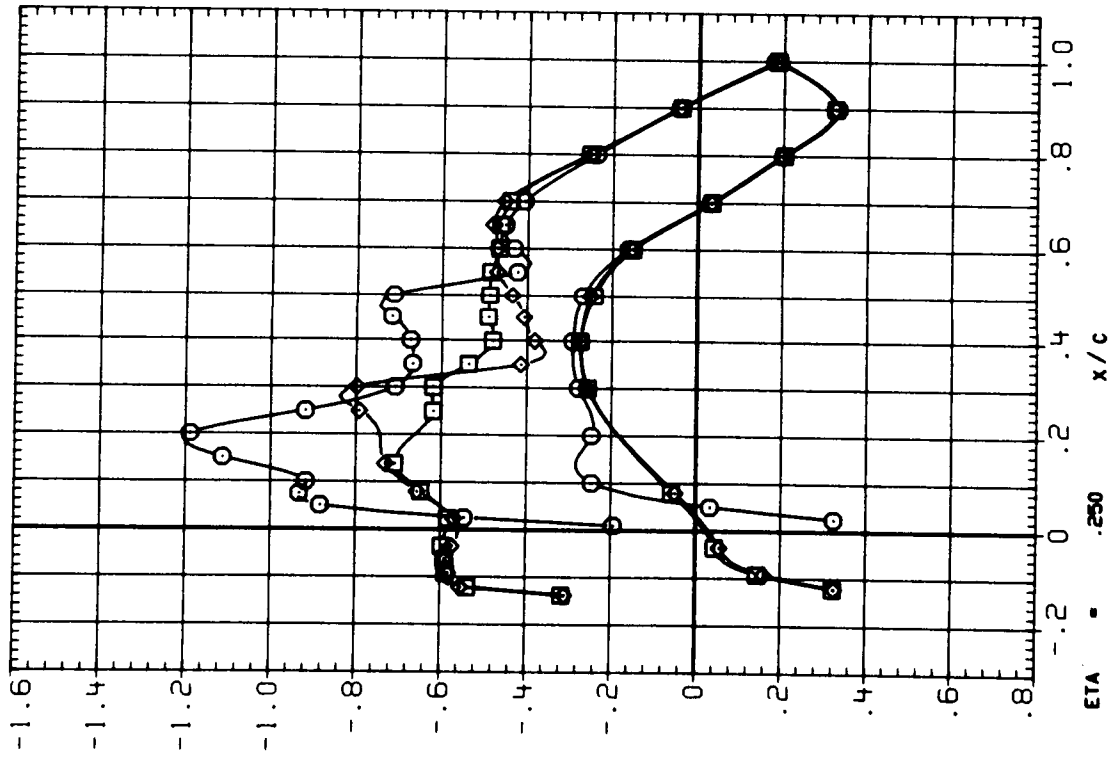


Figure 5.- Concluded.

SYMBOL CONFIGURATION DESCRIPTION
 ○ WBNP
 □ WBNP
 ◇ WBNL P
 ○ WBNL P
 ◇ WBNL F 3SP
 ◇ WBNL F 3SP



EPR RPM ALPHA PITCH
 1.774 8471 1.938 57.2
 1.774 8471 1.938 57.2
 1.770 8494 1.963 57.2
 1.770 8494 1.963 57.2
 1.725 8486 1.945 57.2
 1.725 8486 1.945 57.2

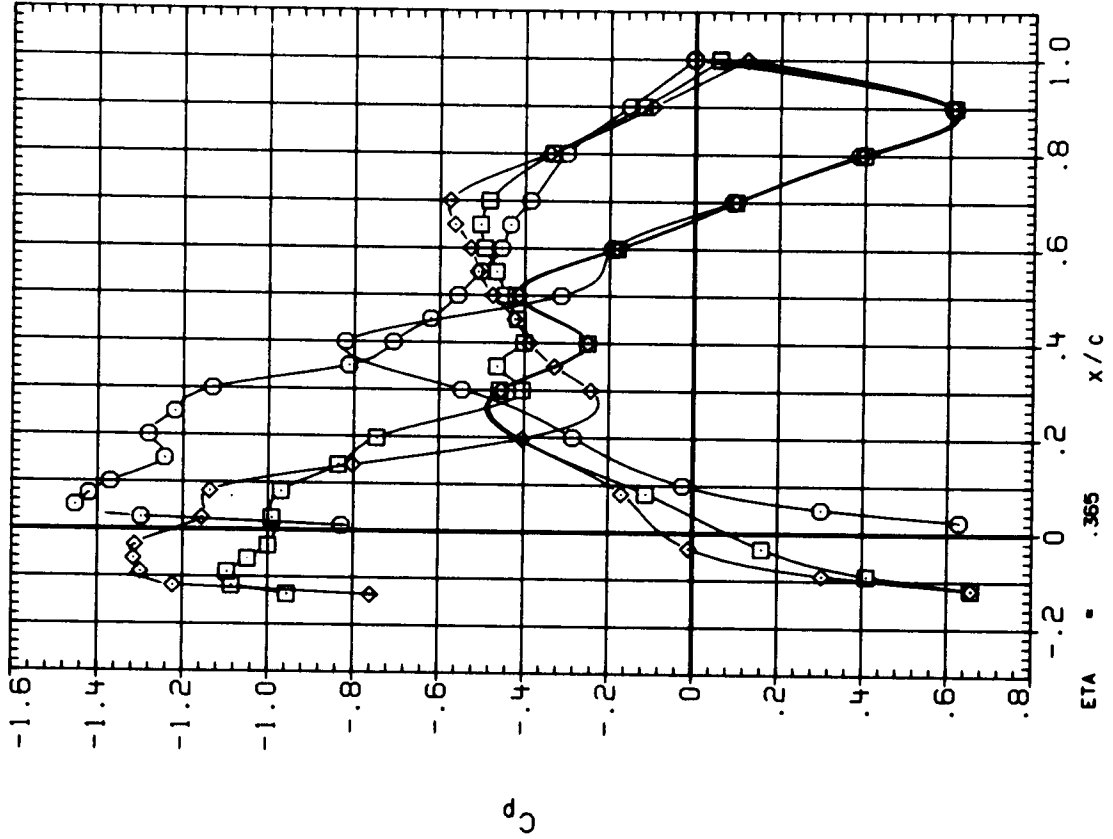


Figure 6.- Blades-on pressure distributions at cruise power; M = 0.809.

SYMBOL CONFIGURATION DESCRIPTION
 ○ WBNP
 □ WBNP
 ◇ WBNLP
 ○ WBNLP
 ◇ WBNLF 3SP
 ◇ WBNLF 3SP

EPR RPM ALPHA PITCH
 1.774 8471 1.938 57.2
 1.774 8471 1.938 57.2
 1.770 8494 1.963 57.2
 1.770 8494 1.963 57.2
 1.725 8485 1.945 57.2
 1.725 8486 1.945 57.2

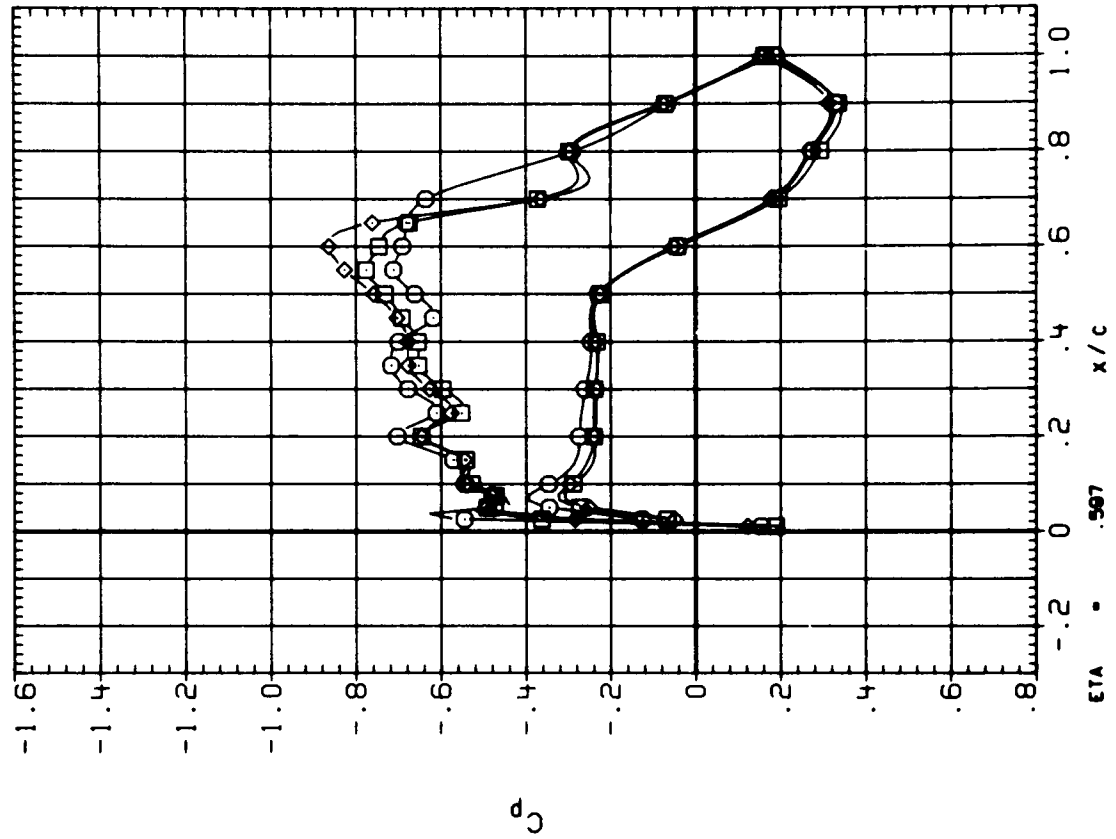
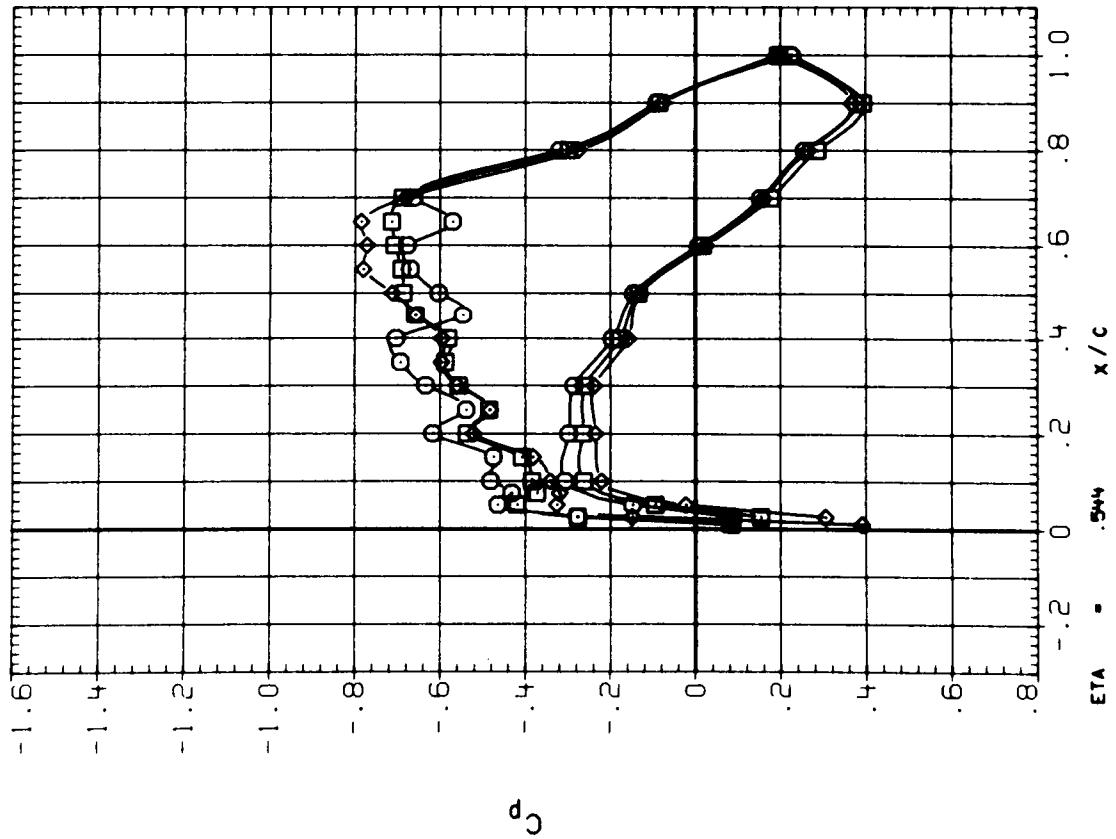


Figure 6.- Continued.

SYMBOL CONFIGURATION DESCRIPTION

○ ○ ○ ○ WBNP

□ □ □ □ WBNP

◇ ◇ ◇ ◇ WBNLP

 WBNLP

 WBNLF 3SP

 WBNLF 3SP

EPR RPM ALPHA PITCH

1.774 8471 1.938 57.2

1.774 8471 1.938 57.2

1.770 8494 1.963 57.2

1.770 8494 1.963 57.2

1.725 8486 1.945 57.2

1.725 8486 1.945 57.2

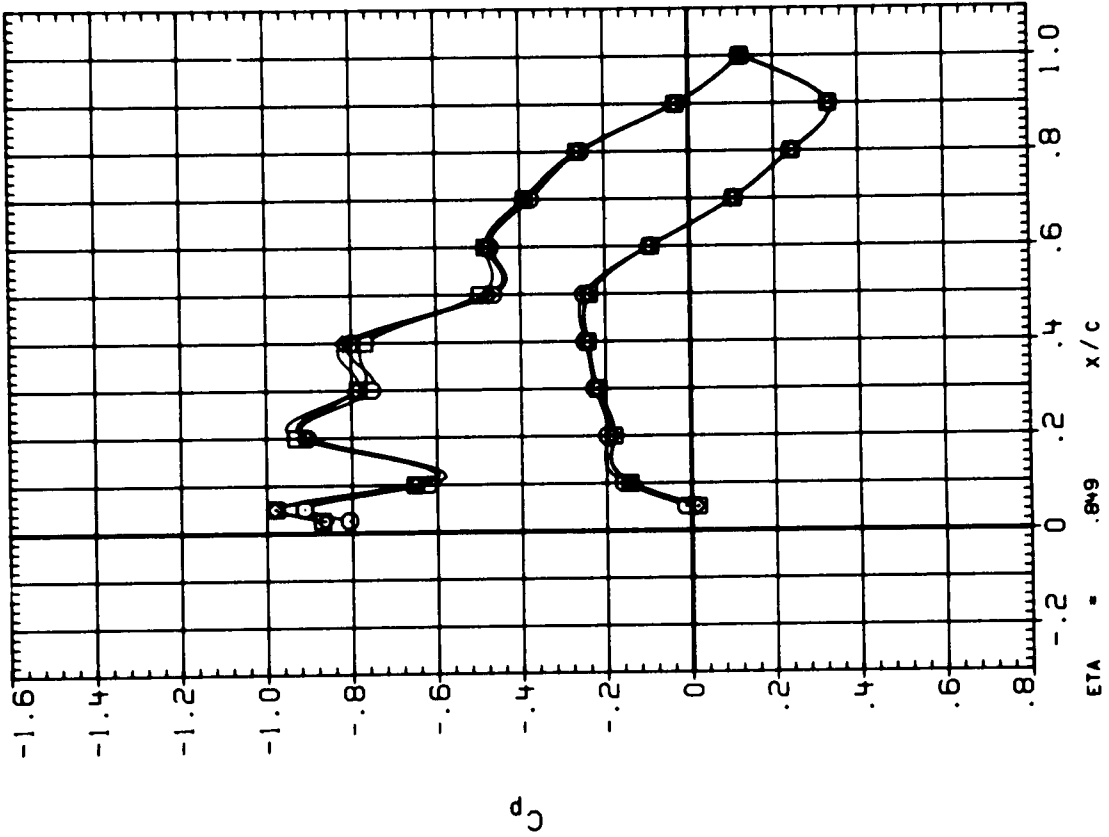
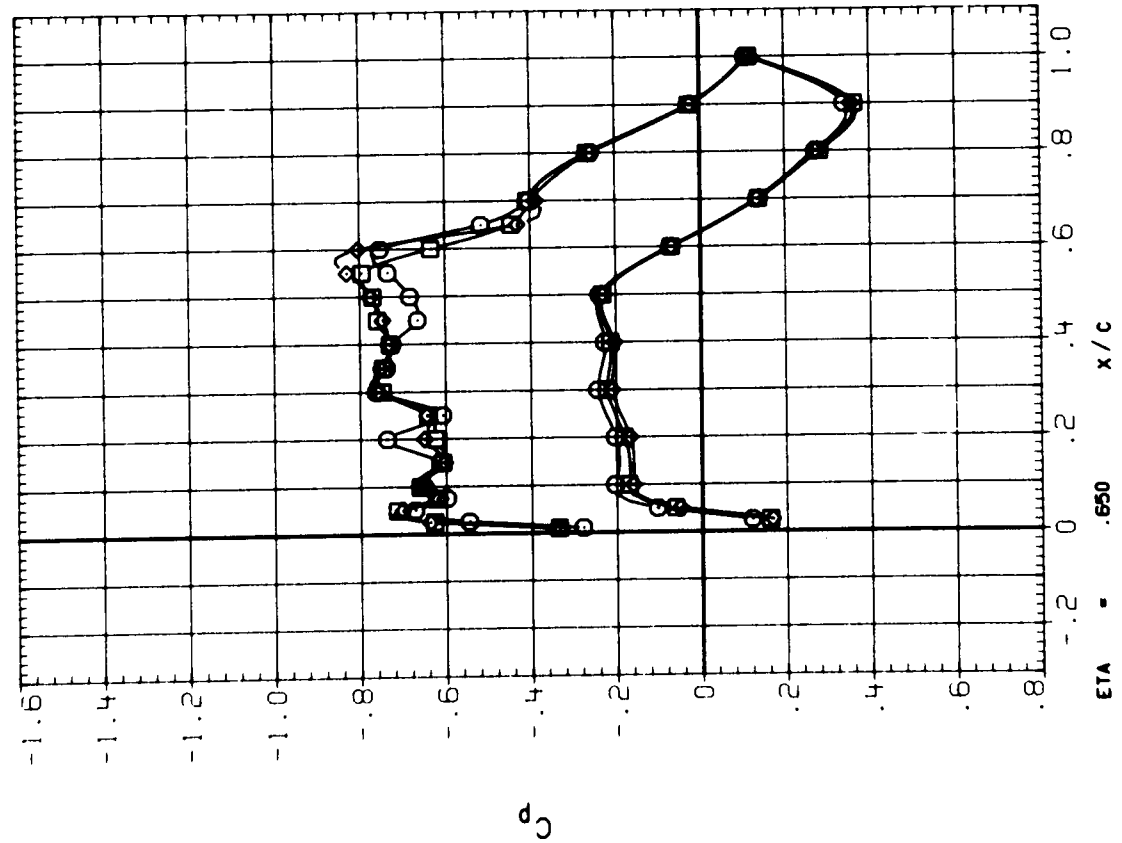


Figure 6.- Concluded.

SYMBOL CONFIGURATION DESCRIPTION

○ ○ ○ ○ HBNP

□ □ □ □ HBNP

◇ ◇ ◇ ◇ HBNP

EPR RPM ALPHA PITCH

1.000 6381 1.954 57.2

1.000 6381 1.954 57.2

1.257 7599 1.936 57.2

1.257 7599 1.936 57.2

1.774 8471 1.938 57.2

1.774 8471 1.938 57.2

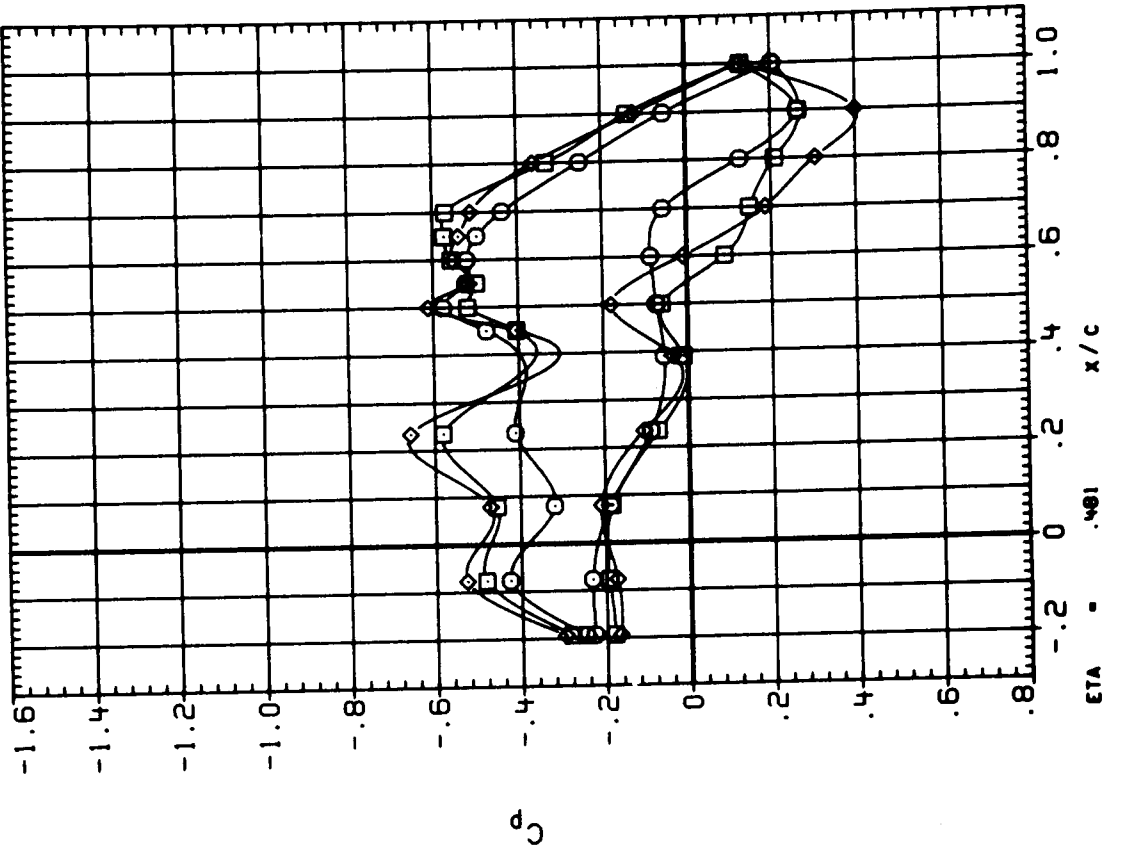
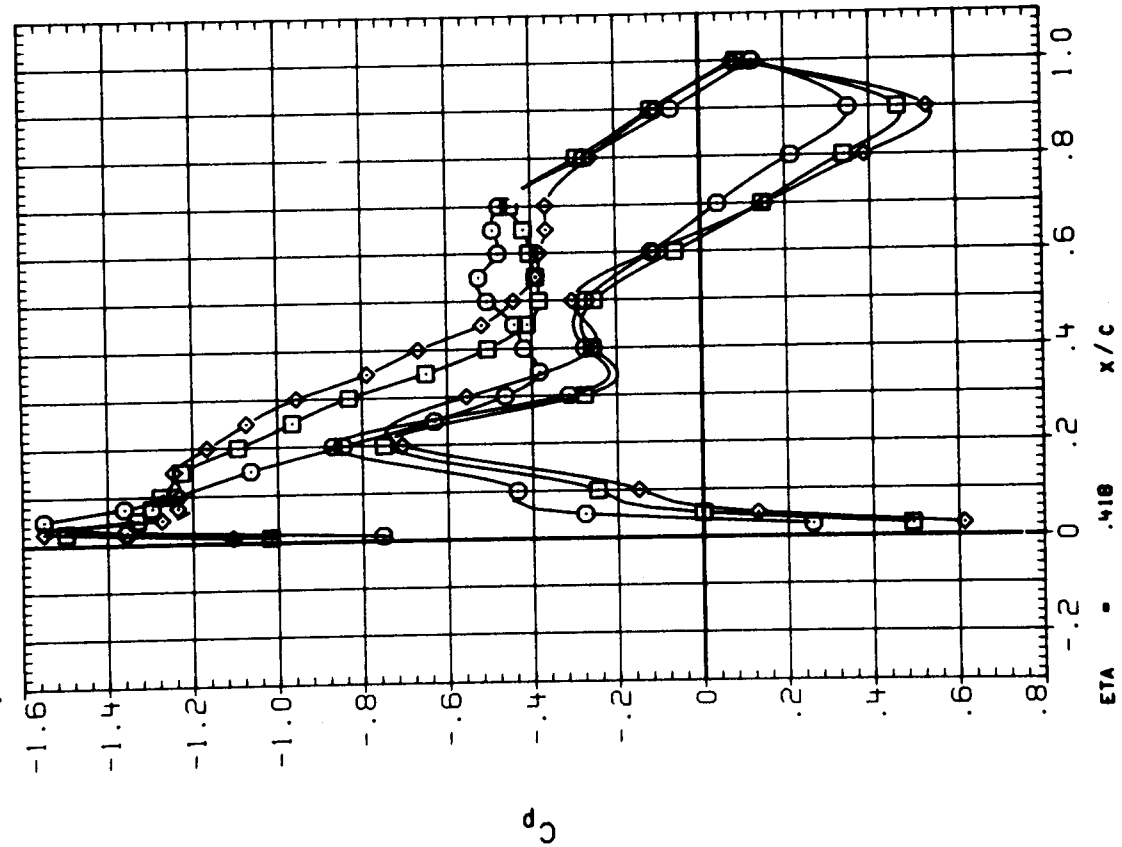


Figure 7.- Continued.

SYMBOL CONFIGURATION DESCRIPTION

○ WBNP

□ WBNP

◇ WBNP

EPR RPM ALPHA PITCH

1.000 6381 1.954 57.2

1.000 6381 1.954 57.2

1.257 7599 1.936 57.2

1.257 7599 1.936 57.2

1.774 8471 1.938 57.2

1.774 8471 1.938 57.2

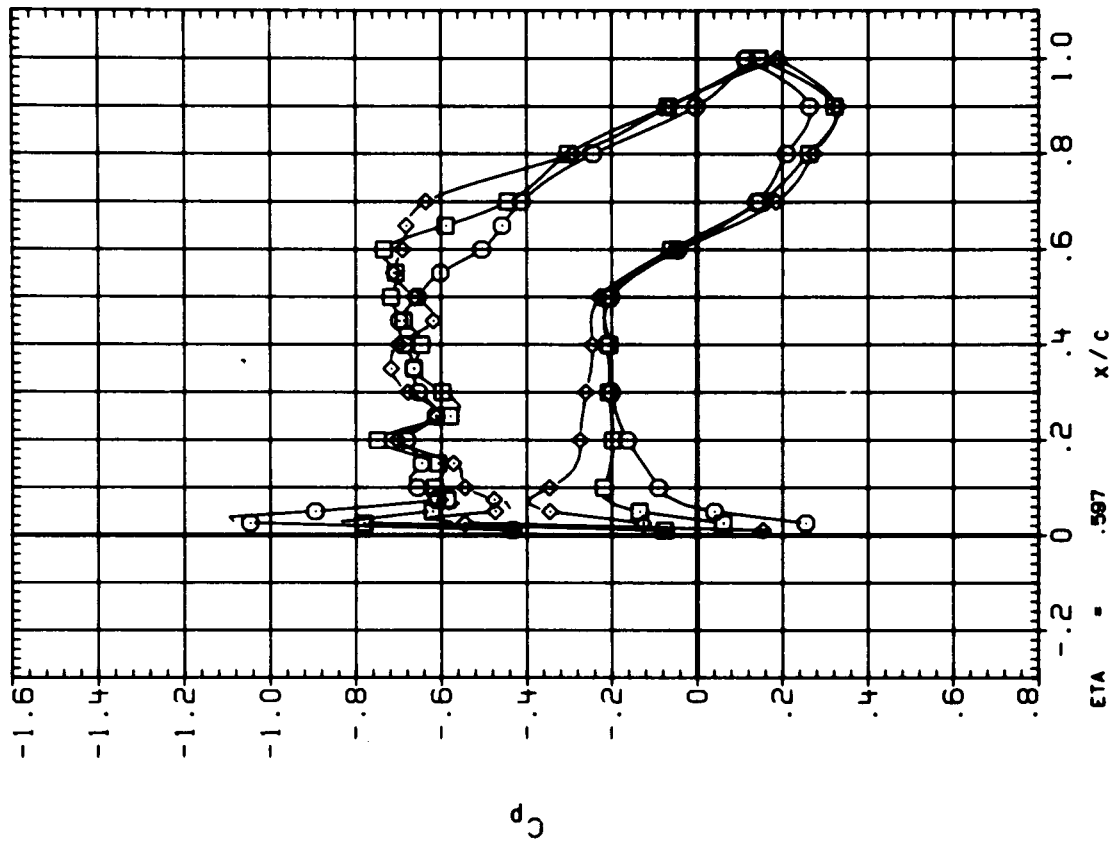
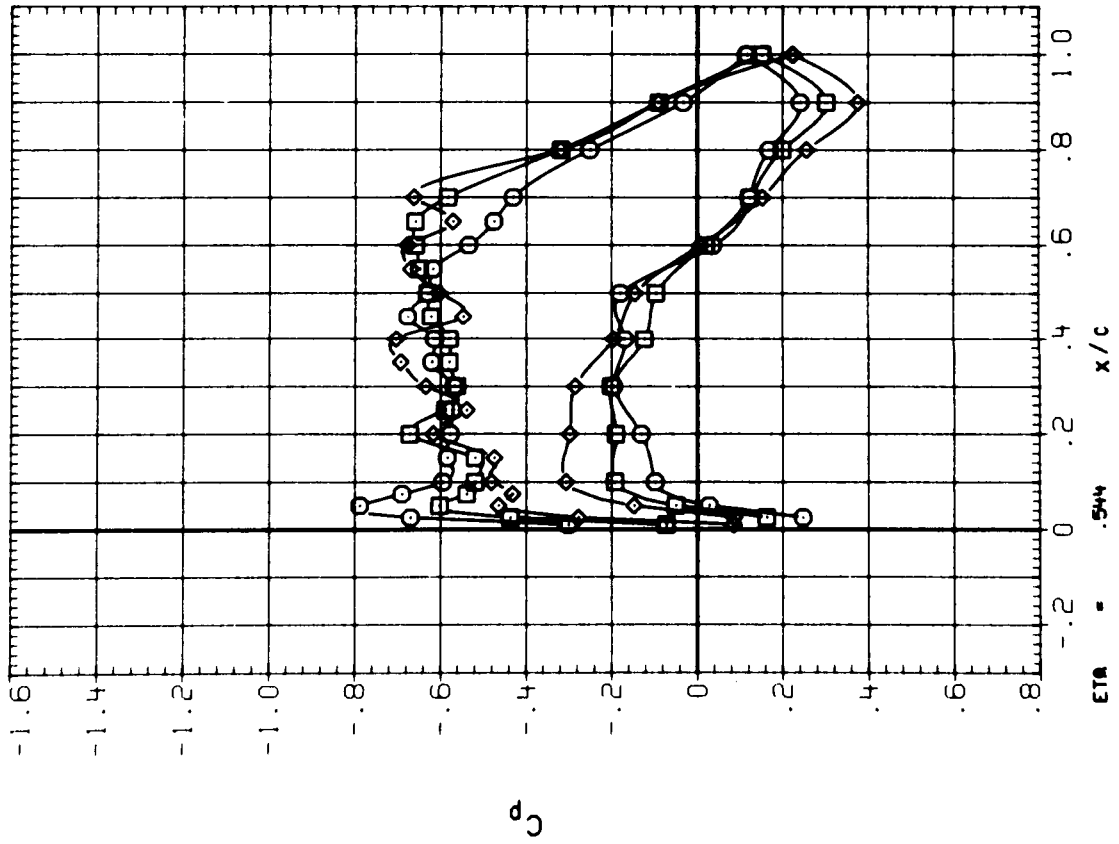


Figure 7.- Continued.

SYMBOL CONFIGURATION DESCRIPTION

- WB/NLP
- WB/NLP
- ◇ WB/NLP

EPR	RPM	ALPHA	PITCH
1.003	6494	1.967	57.2
1.003	6494	1.967	57.2
1.196	7483	1.962	57.2
1.770	8494	1.963	57.2
1.770	8494	1.963	57.2

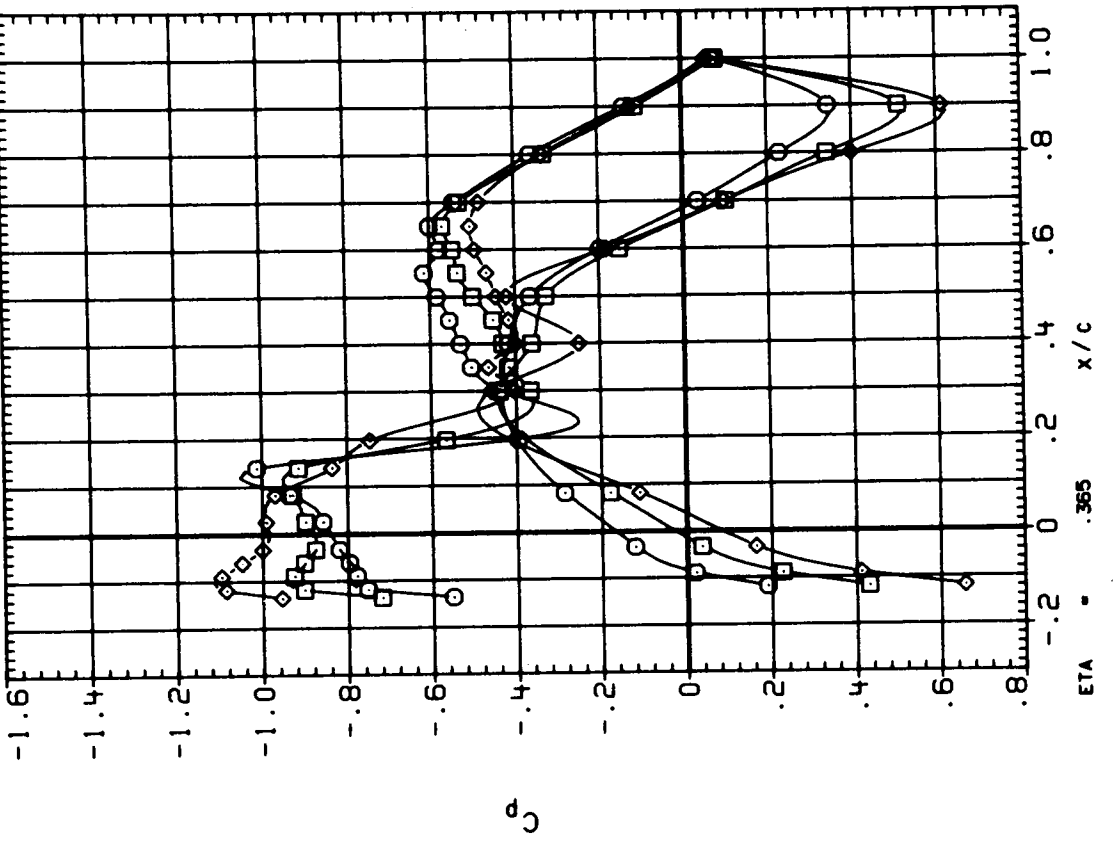
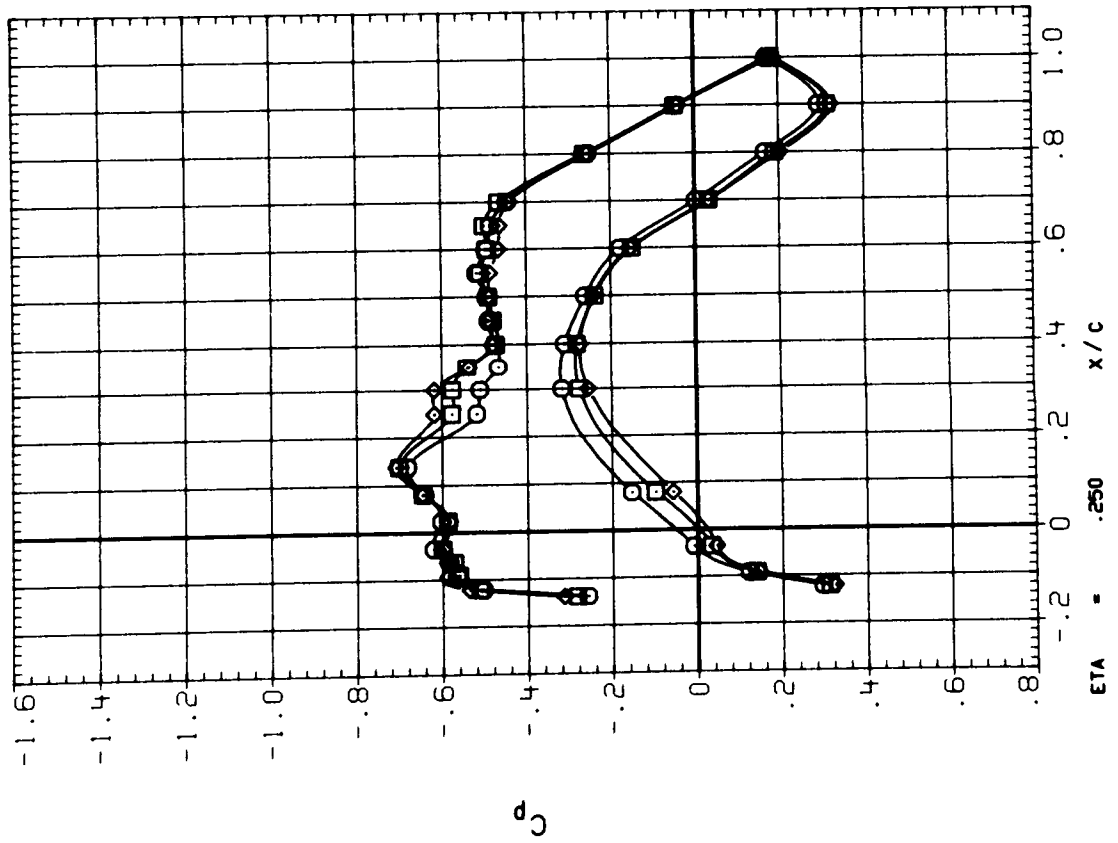
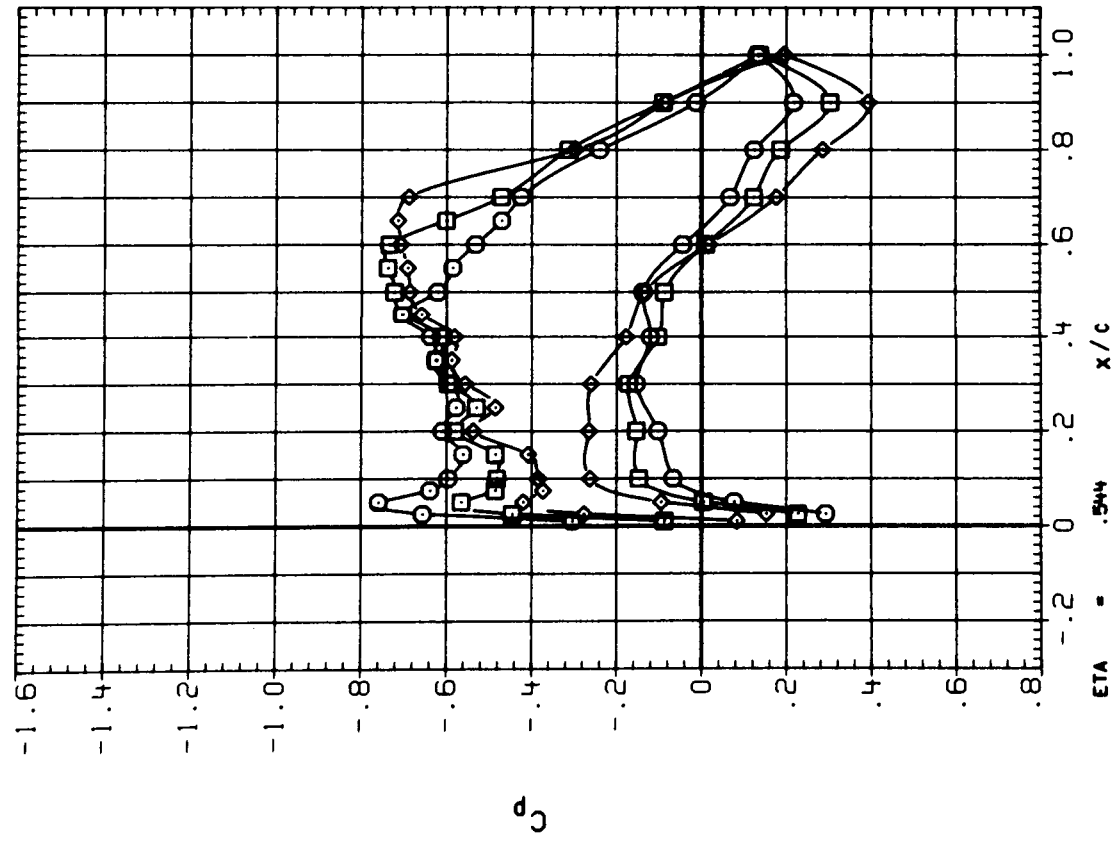


Figure 8.- Effect of power on wing pressures--baseline + LEX configuration;
M = 0.800.

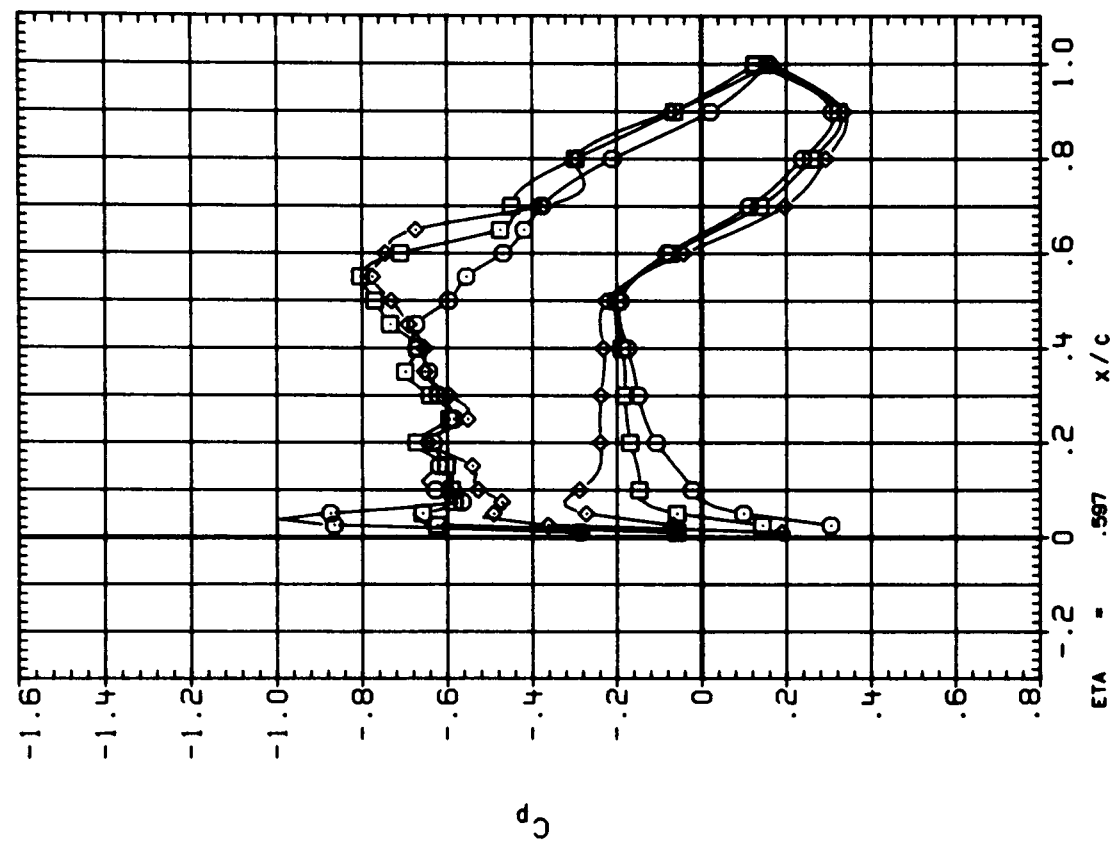
SYMBOL CONFIGURATION DESCRIPTION

- MBNLP
- MBNLP
- ◇ MBNLP
- ◇ MBNLP



ETA = .544

EPR	RPM	ALPHA	PITCH
1.003	6494	1.967	57.2
1.003	6494	1.967	57.2
1.196	7483	1.962	57.2
1.196	7483	1.962	57.2
1.770	8494	1.963	57.2
1.770	8494	1.963	57.2



ETA = .597

Figure 8.- Continued.

SYMBOL CONFIGURATION DESCRIPTION

○ ○ ○ ○ ○

□ □ □ □ □

◇ ◇ ◇ ◇ ◇

EPR RPM ALPHA PITCH

1.000 6446 1.972 57.2

1.000 6446 1.972 57.2

1.188 7483 1.966 57.2

1.188 7483 1.966 57.2

1.725 8486 1.945 57.2

1.725 8486 1.945 57.2

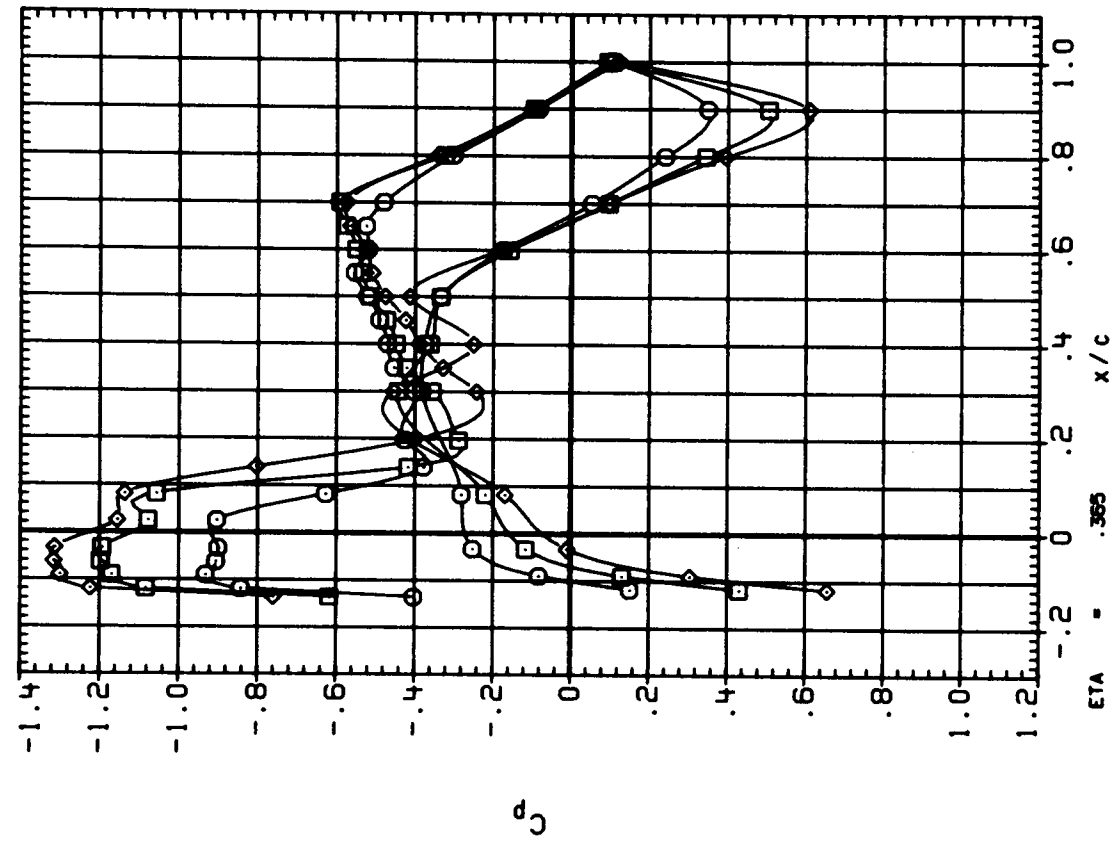
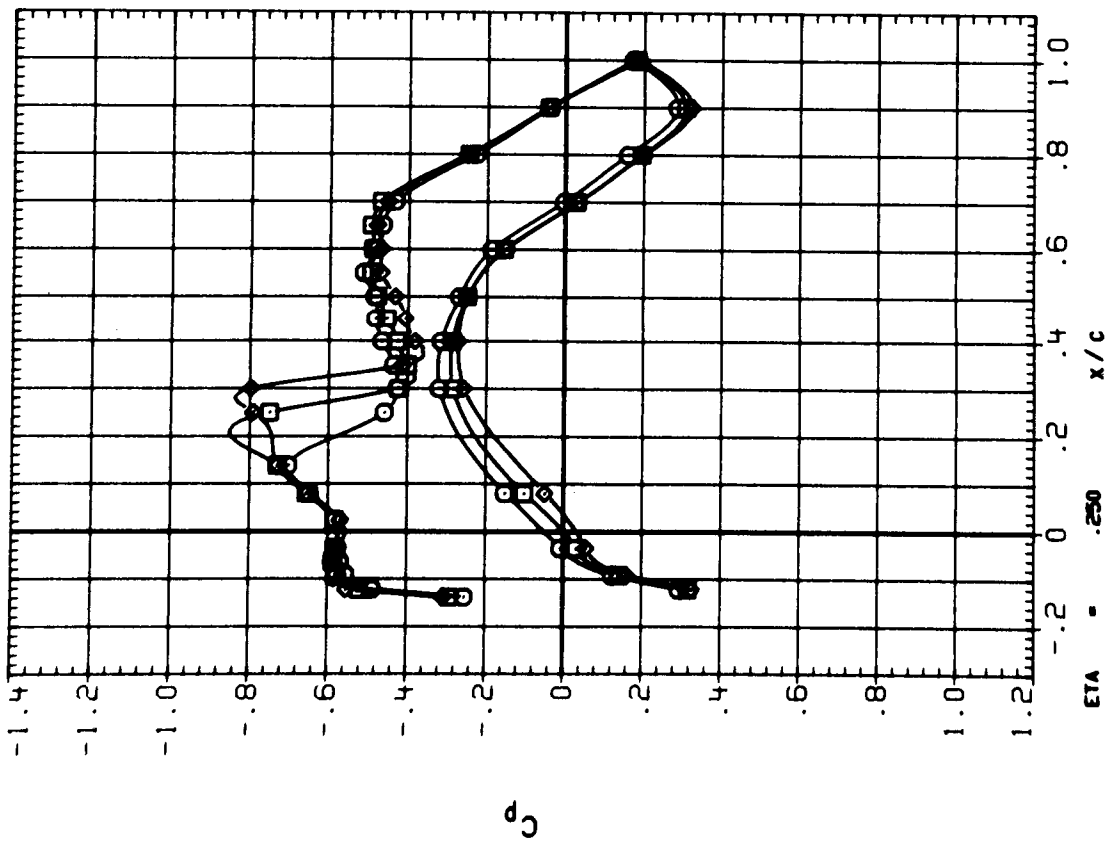


Figure 9.- Effect of power on wing pressures --baseline + LEX, fillet, and stroke configuration; M = 0.808.

SYMBOL CONFIGURATION DESCRIPTION
 ○ WBNLF3SP
 □ WBNLF3SP
 ◇ WBNLF3SP

EPR RPM ALPHA PITCH
 1.000 6446 1.972 57.2
 1.000 6446 1.972 57.2
 1.188 7483 1.966 57.2
 1.188 7483 1.966 57.2
 1.725 8486 1.945 57.2
 1.725 8486 1.945 57.2

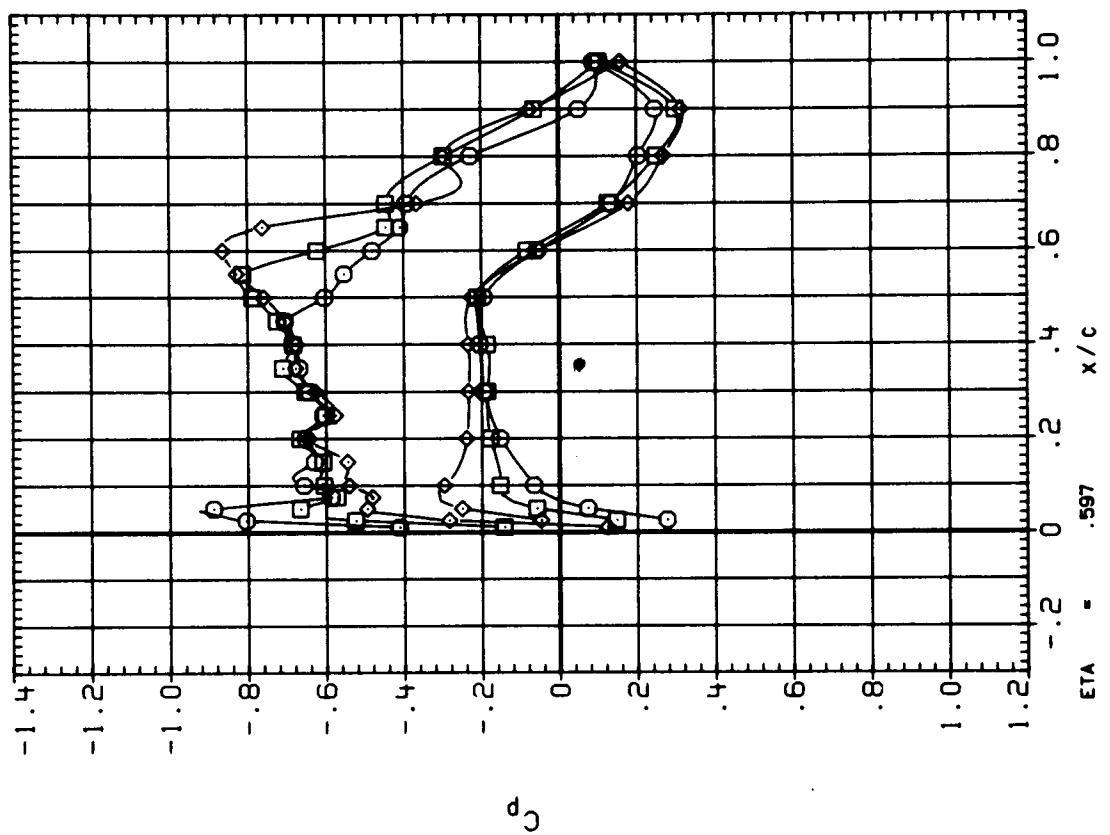
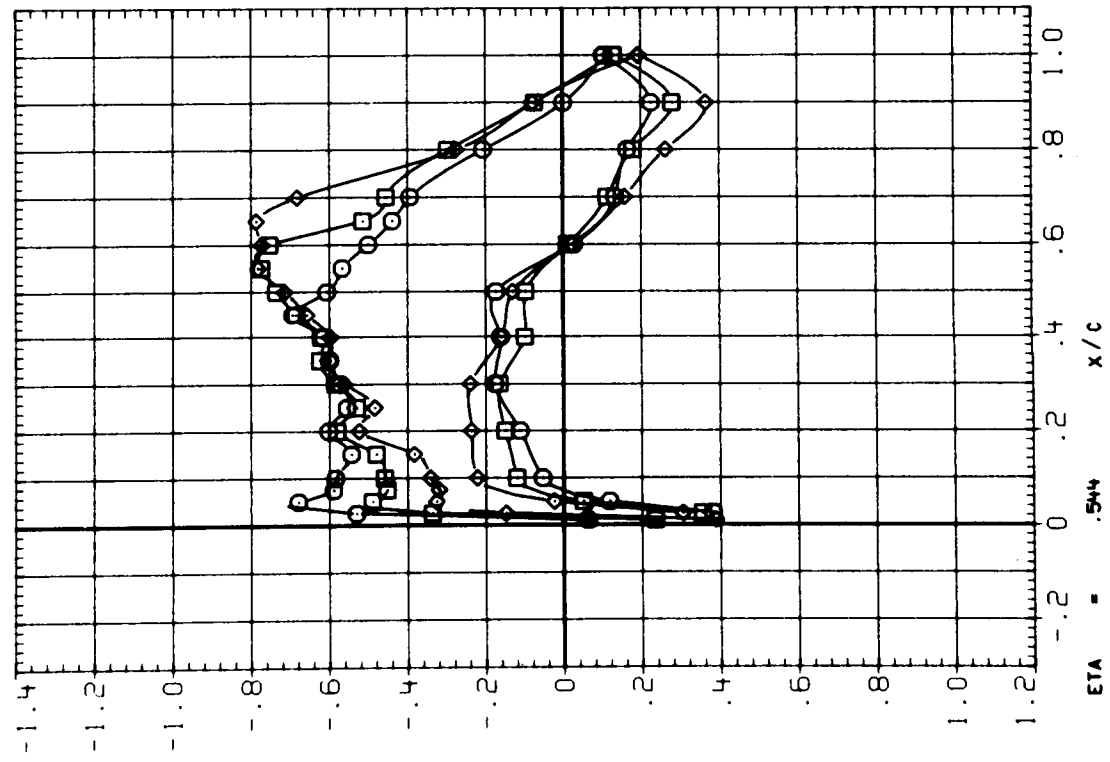


Figure 9.- Continued.

SYMBOL CONFIGURATION DESCRIPTION
 ○ ○ ○ ○ WBNL
 □ □ □ □ WBNL
 ○ ○ ○ ○ WBNL
 □ □ □ □ WBNL

EPR RPM ALPHA PITCH
 1.728 8494 1.963 57.2
 1.728 8494 1.963 57.2
 1.770 8494 1.963 57.2

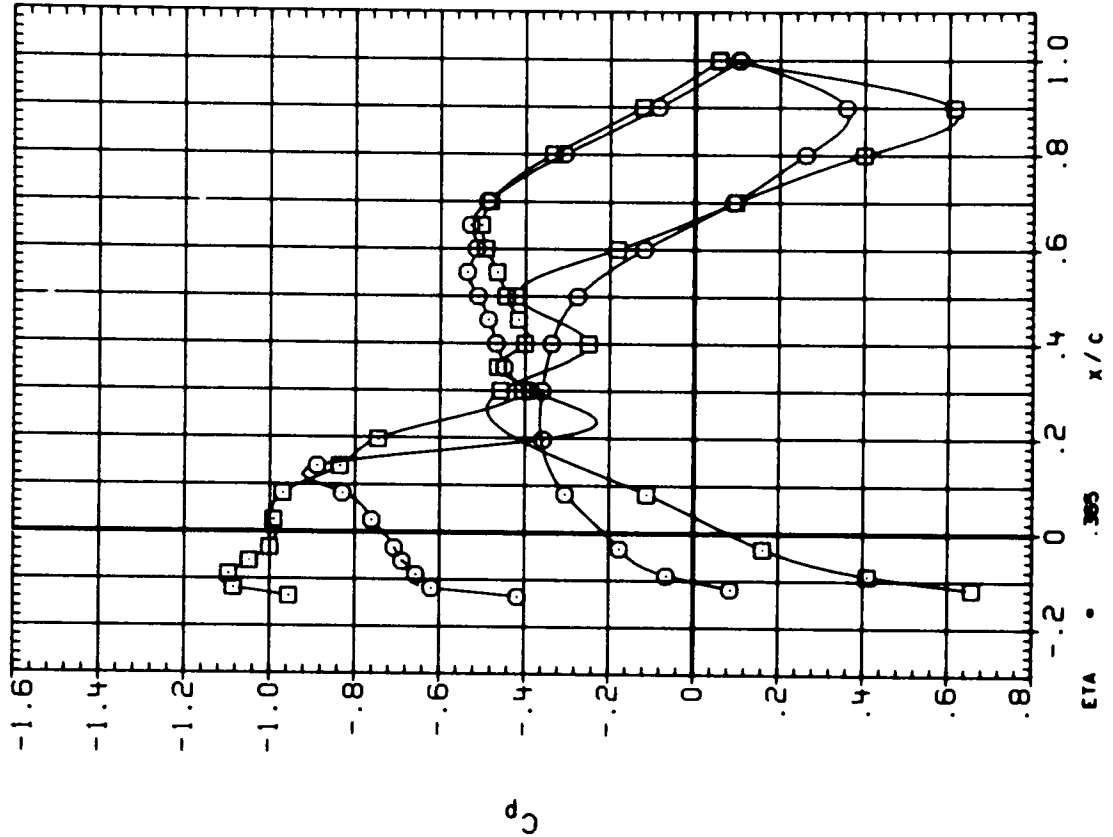
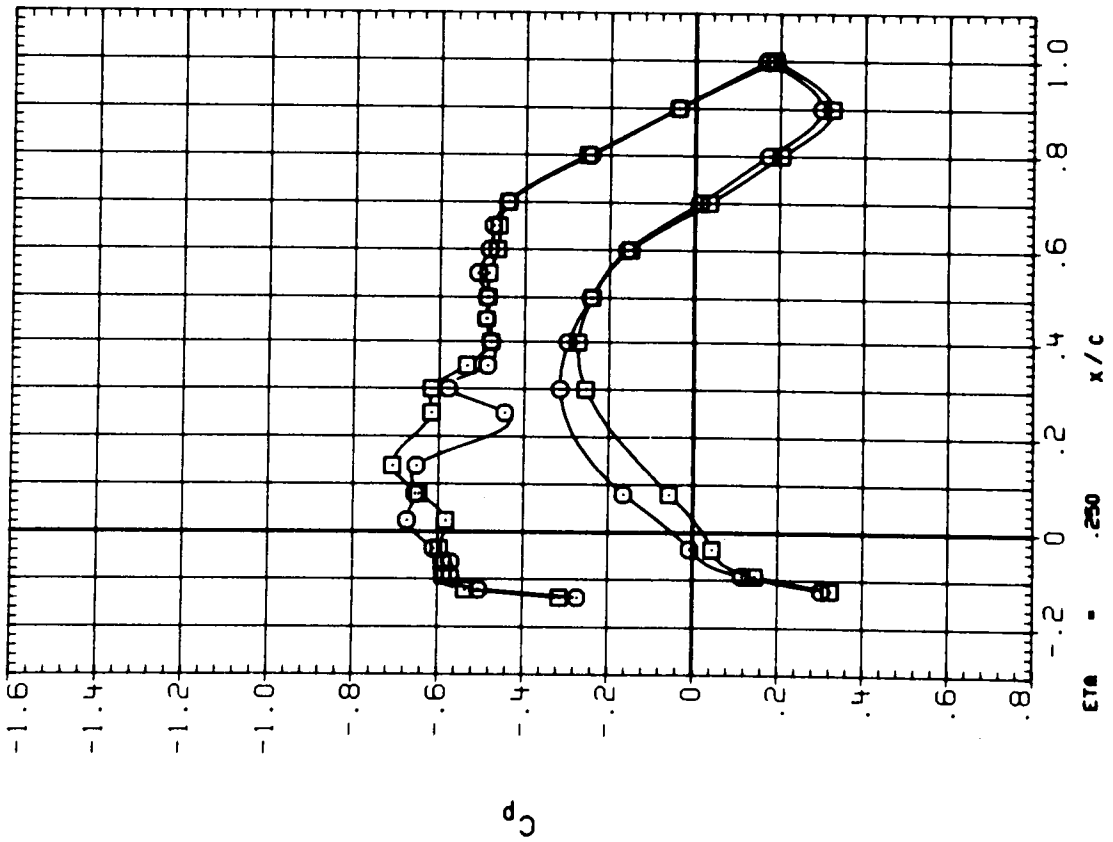


Figure 10.- Comparison of blades-on with blades-off; M = 0.803.

SYMBOL CONFIGURATION DESCRIPTION
 ○ ○ ○ ○ MBNL
 □ □ □ □ MBNL P

EPR RPM ALPHA PITCH
 1.728 8494 1.963 57.2
 1.728 8494 1.963 57.2
 1.770 8494 1.963 57.2
 1.770 8494 1.963 57.2

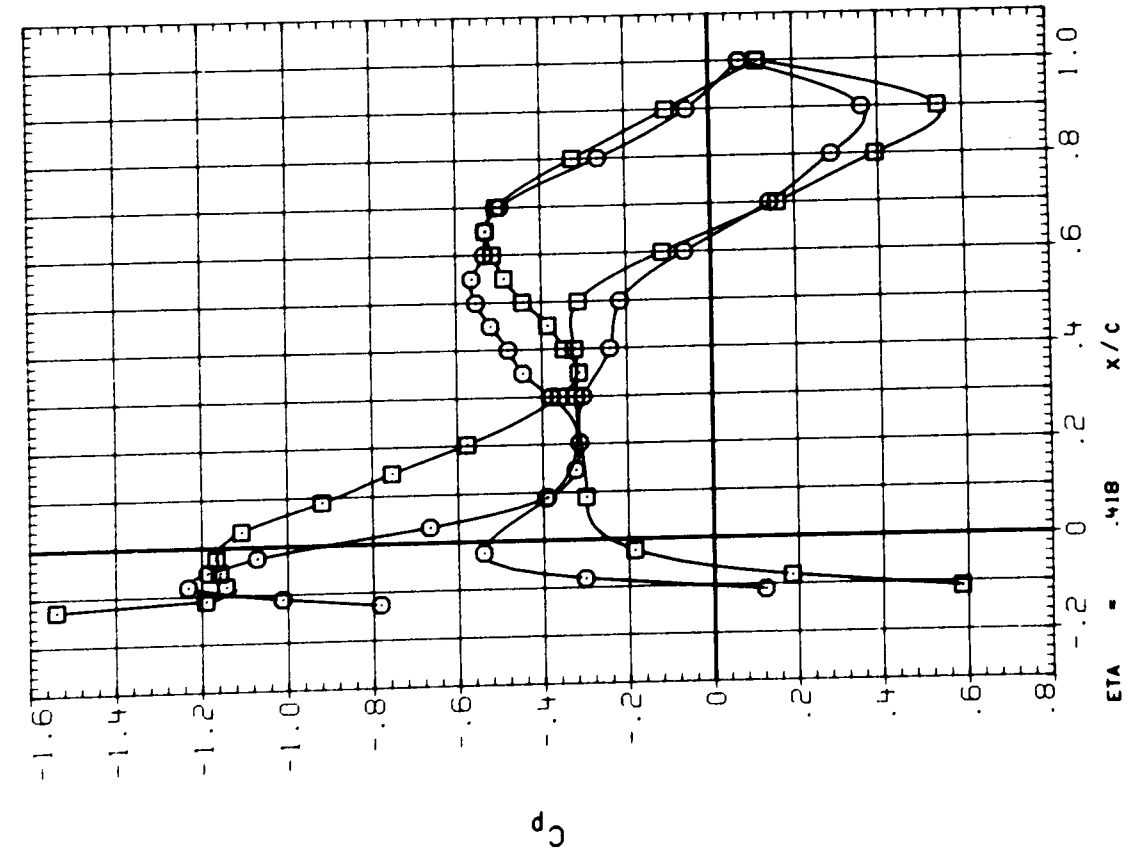
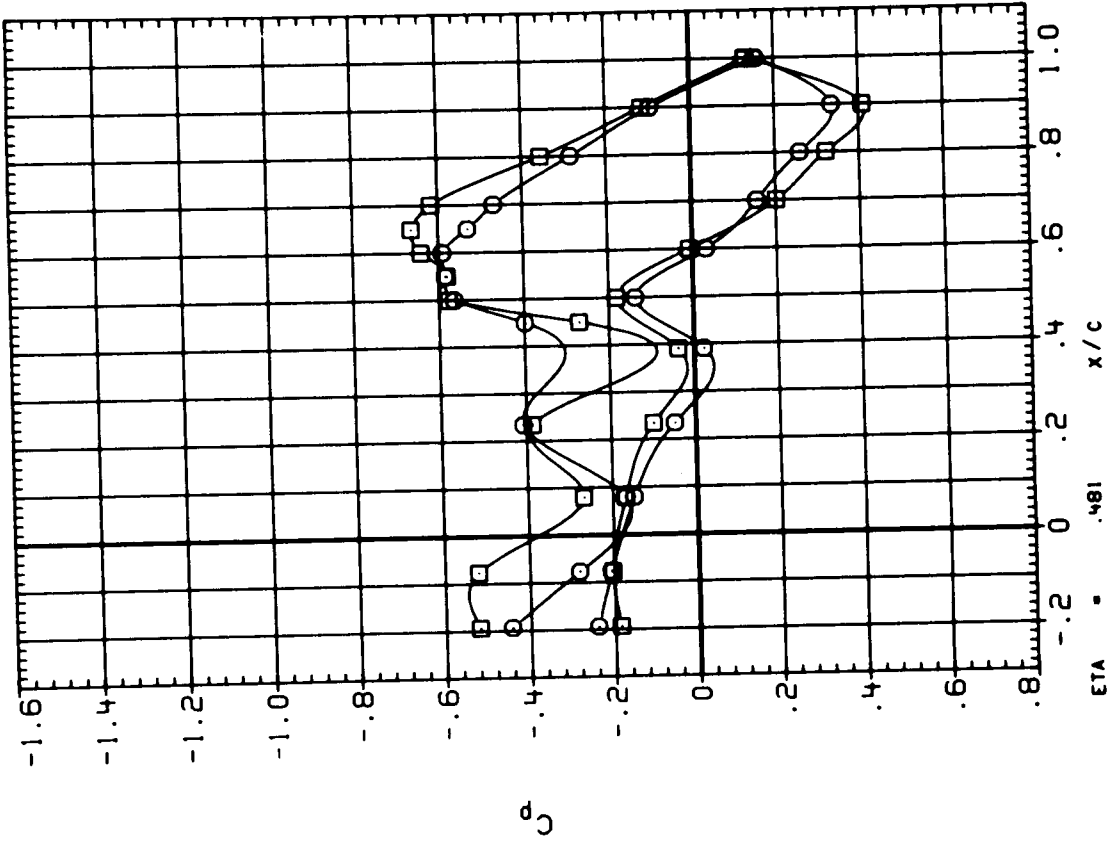


Figure 10.- Continued.

SYMBOL CONFIGURATION DESCRIPTION
 ○ ○ ○ ○ MBNL
 ○ ○ ○ ○ MBNL
 □ □ □ □ MBNL P
 □ □ □ □ MBNL F

EPR RPM ALPHA PITCH
 1.728 1.963
 1.728 1.963
 1.770 8494 57.2
 1.770 8494 57.2

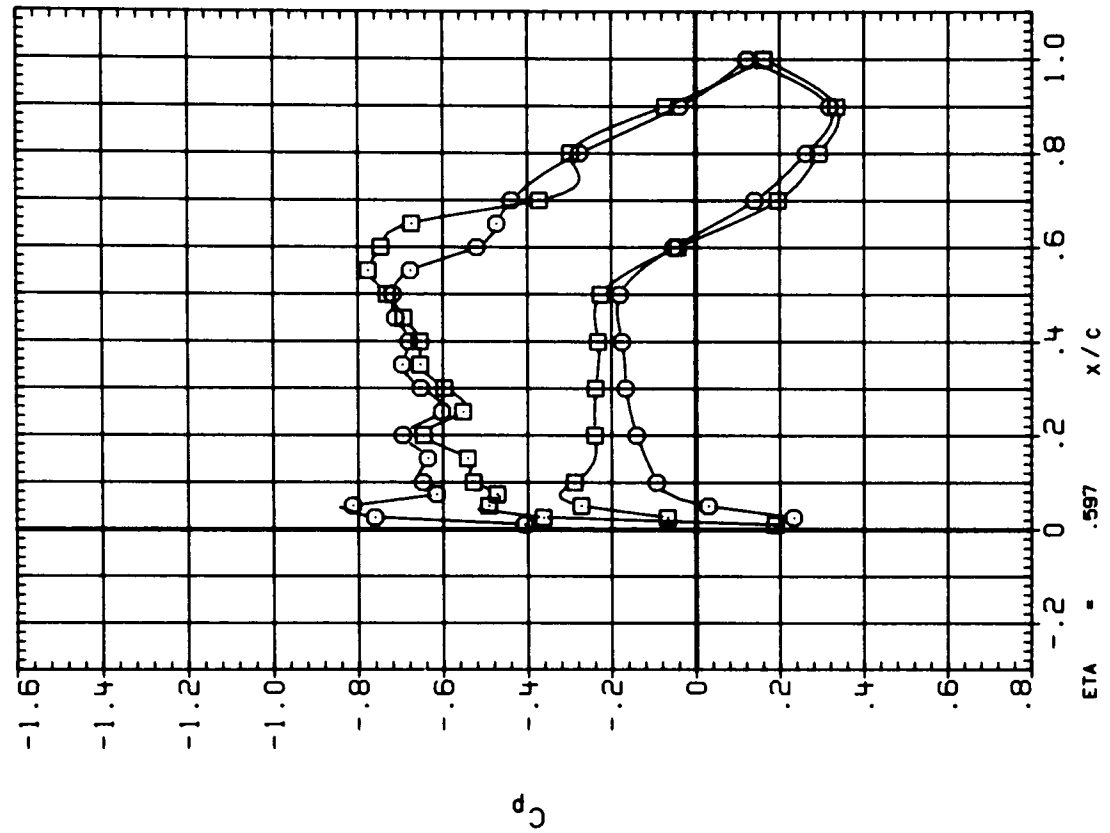
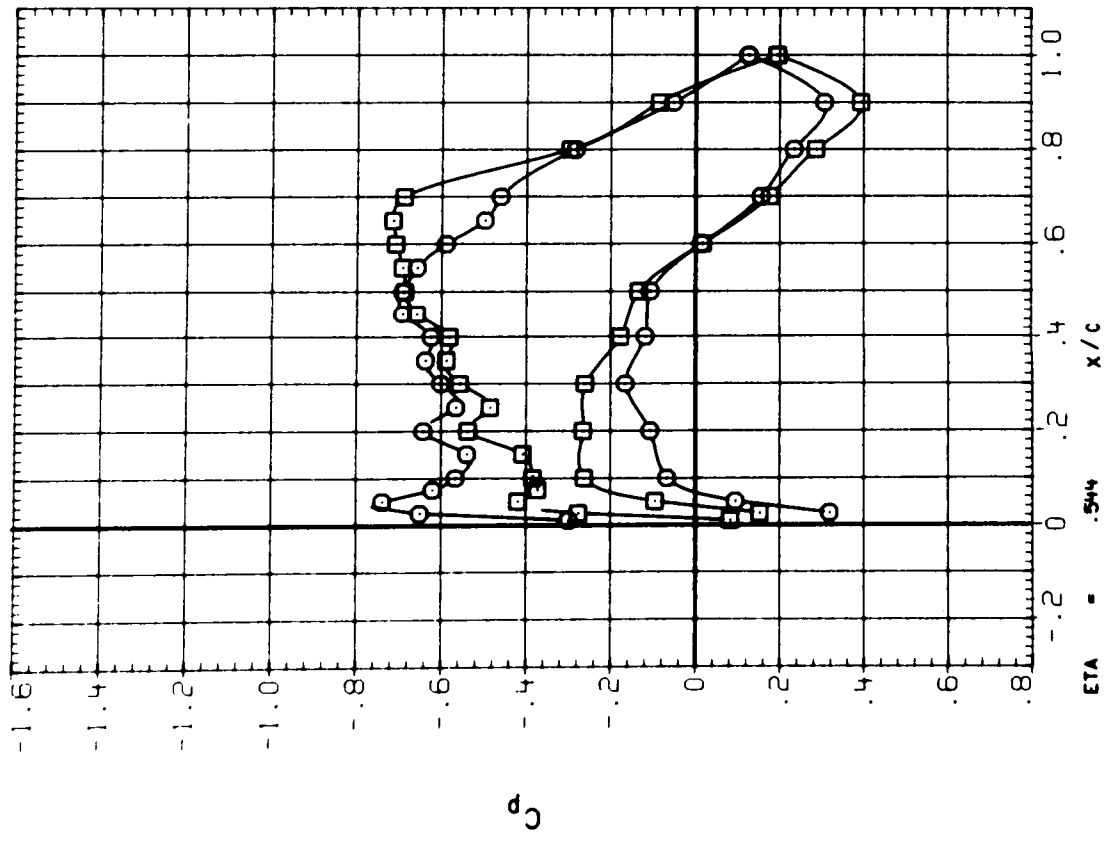


Figure 10.- Continued.

SYMBOL CONFIGURATION DESCRIPTION
 ○ WBNL
 □ WBNL P

EPR RPM ALPHA PITCH
 1.728 8494 1.963 57.2
 1.728 8494 1.963 57.2
 1.770 8494 1.963 57.2
 1.770 8494 1.963 57.2

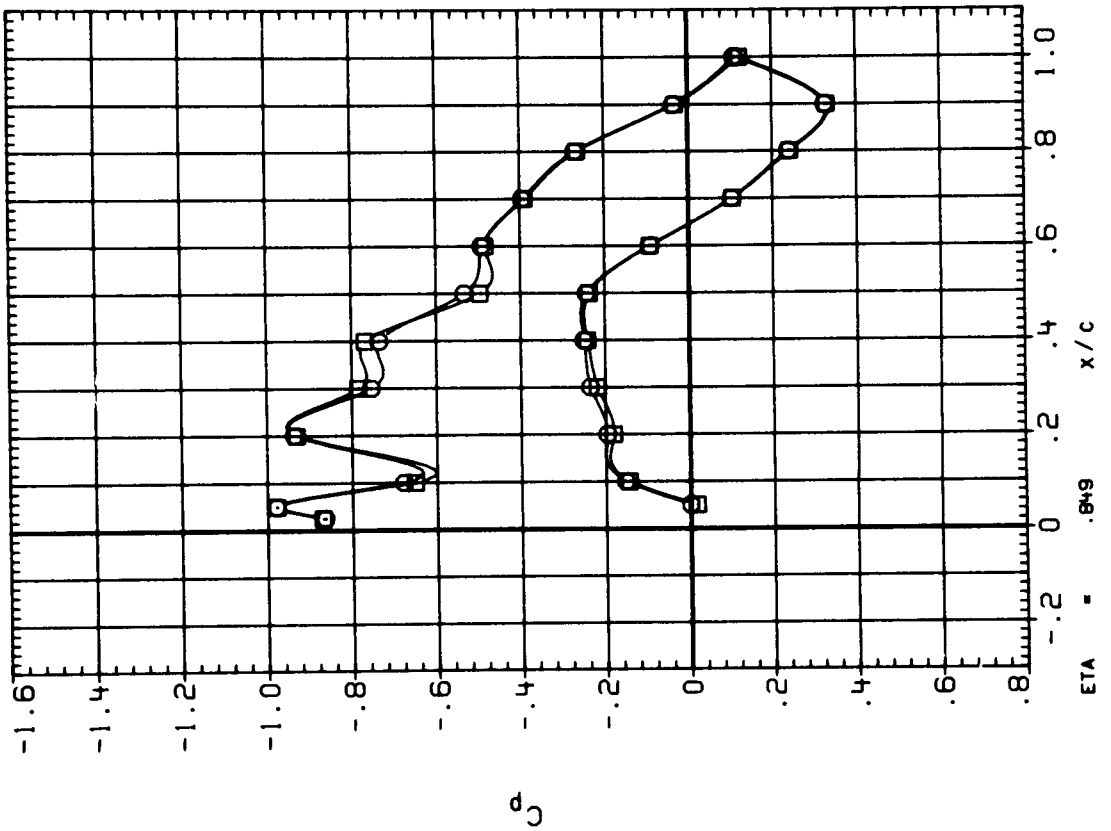
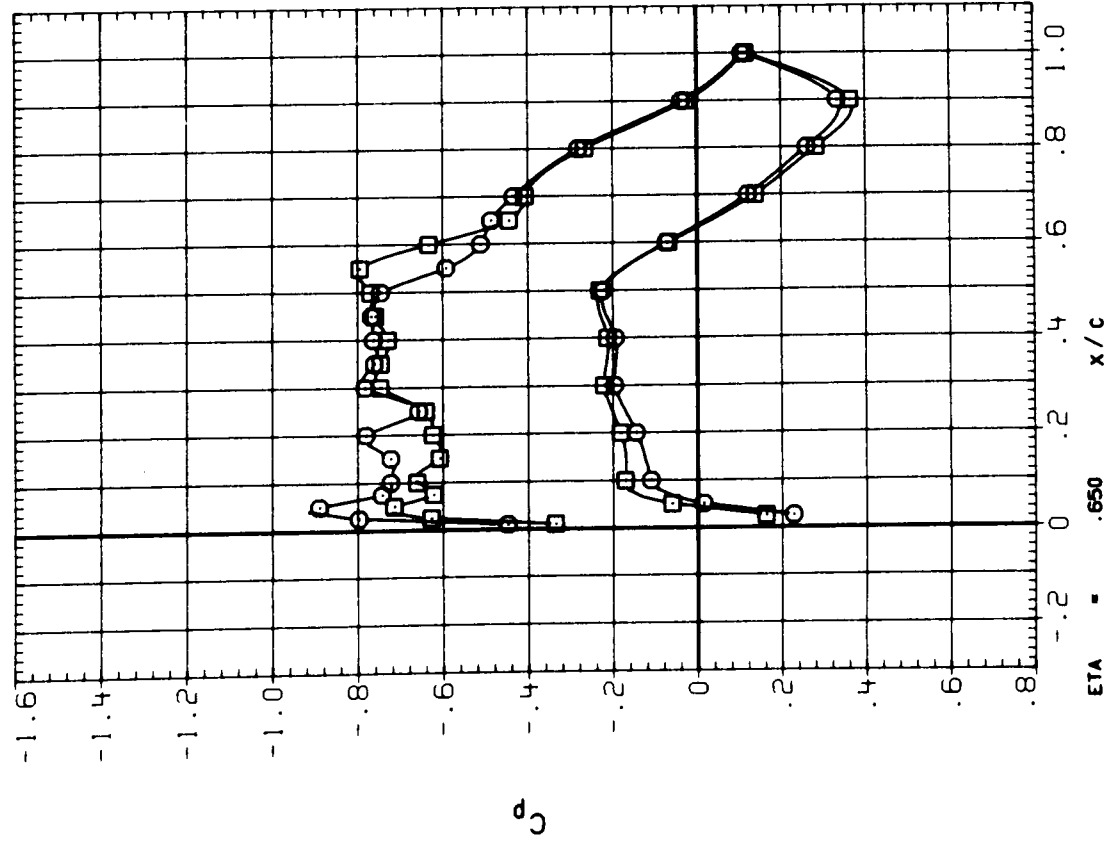


Figure 10.- Concluded.

SYMBOL CONFIGURATION DESCRIPTION

○ MBNP

□ MBN

◇ MBNLP

△ MBNL

EPR ALPHA PITCH

1.774 1.938 57.2

1.682 1.946 57.2

1.770 1.963 57.2

1.728 1.963 57.2

RPM 8471

8494

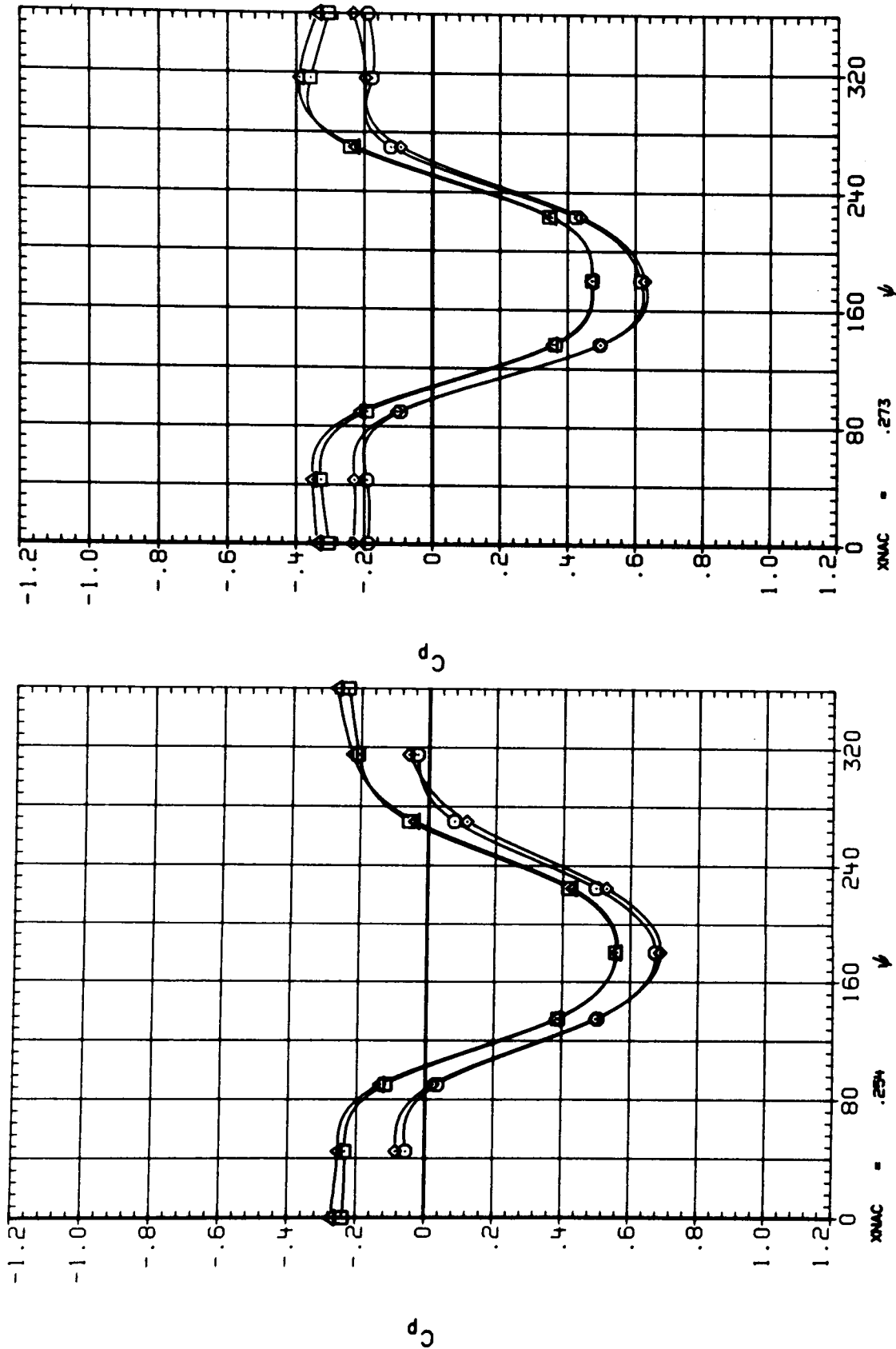


Figure 11.- Nacelle pressure distributions at cruise power; M = 0.809.

SYMBOL CONFIGURATION DESCRIPTION

○ MBNP
 □ MBN
 △ MBNLP
 ◇ MBNL

EPR 8471 ALPHA 57.2
 1.774 1.938
 1.682 1.946
 1.770 1.963
 1.728 1.963

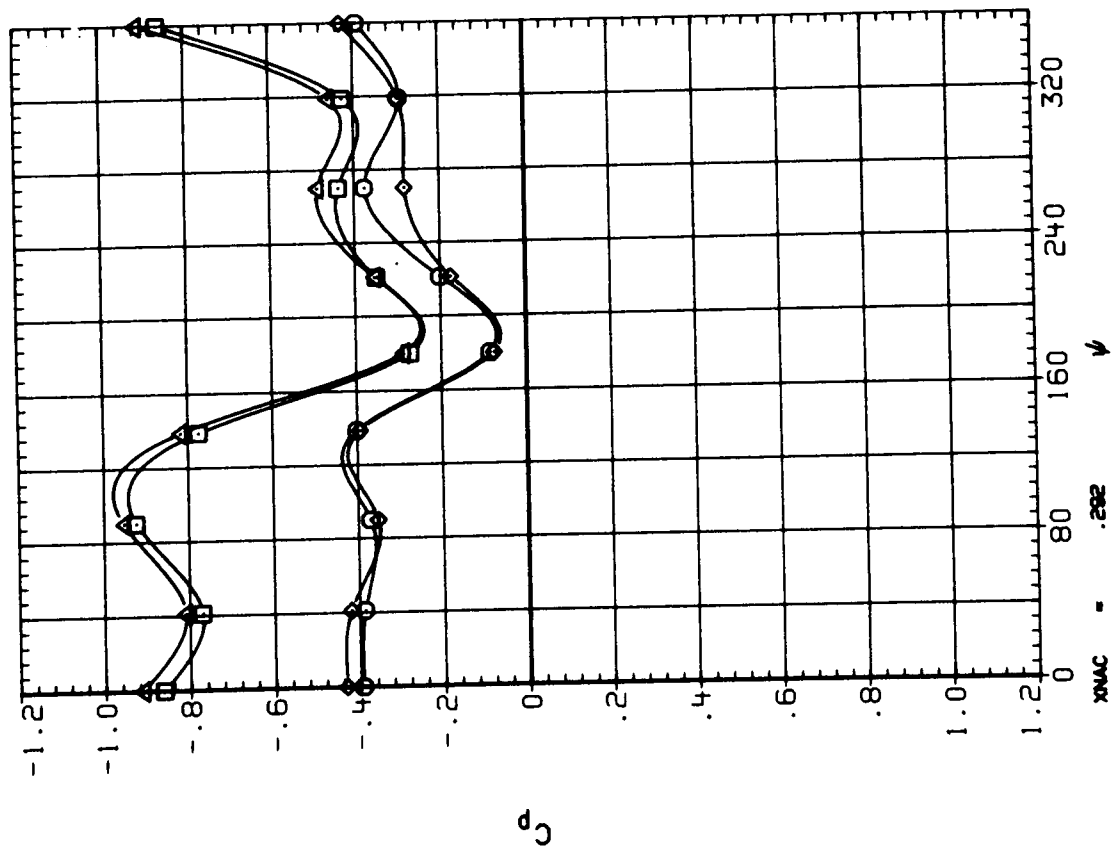
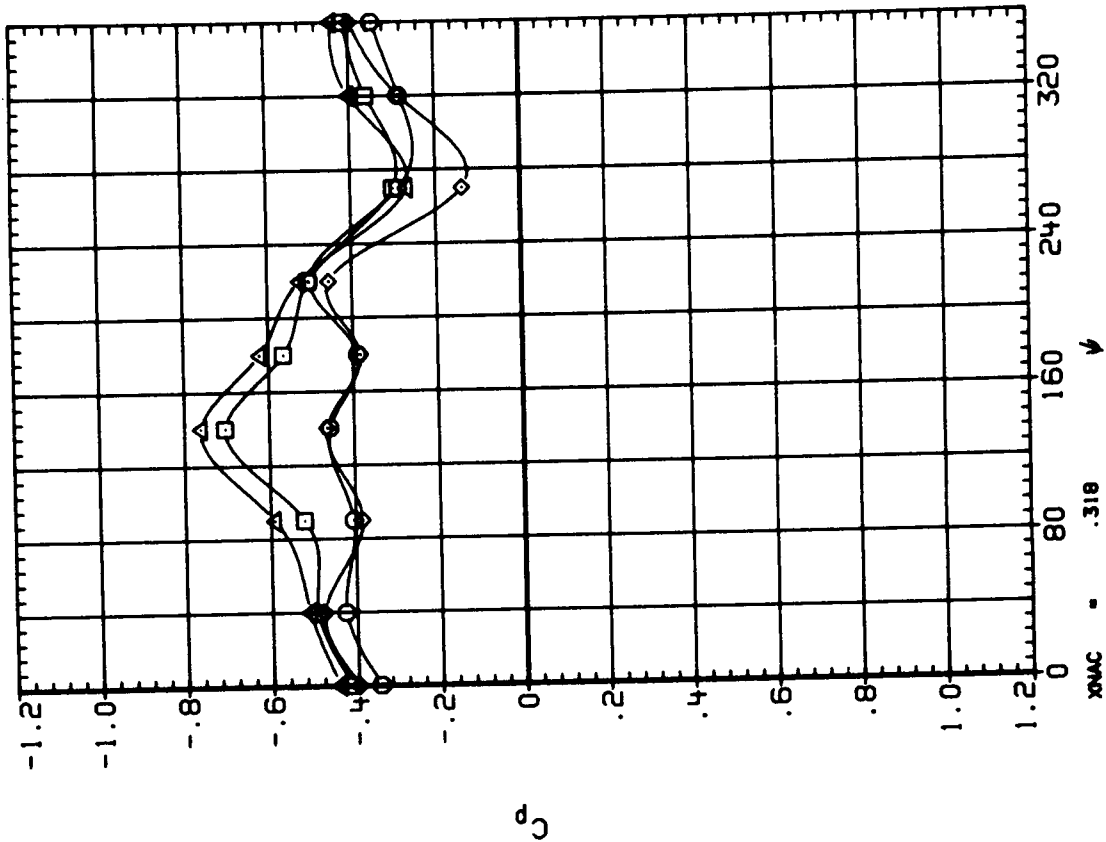


Figure 11.- Continued.

SYMBOL CONFIGURATION DESCRIPTION

- WBNP
- WBN
- ◇ WBNLP
- △ WBNL

EPR	RPM	ALPHA	PITCH
1.774	8471	1.938	57.2
1.682	8494	1.946	57.2
1.770		1.963	
1.728		1.963	

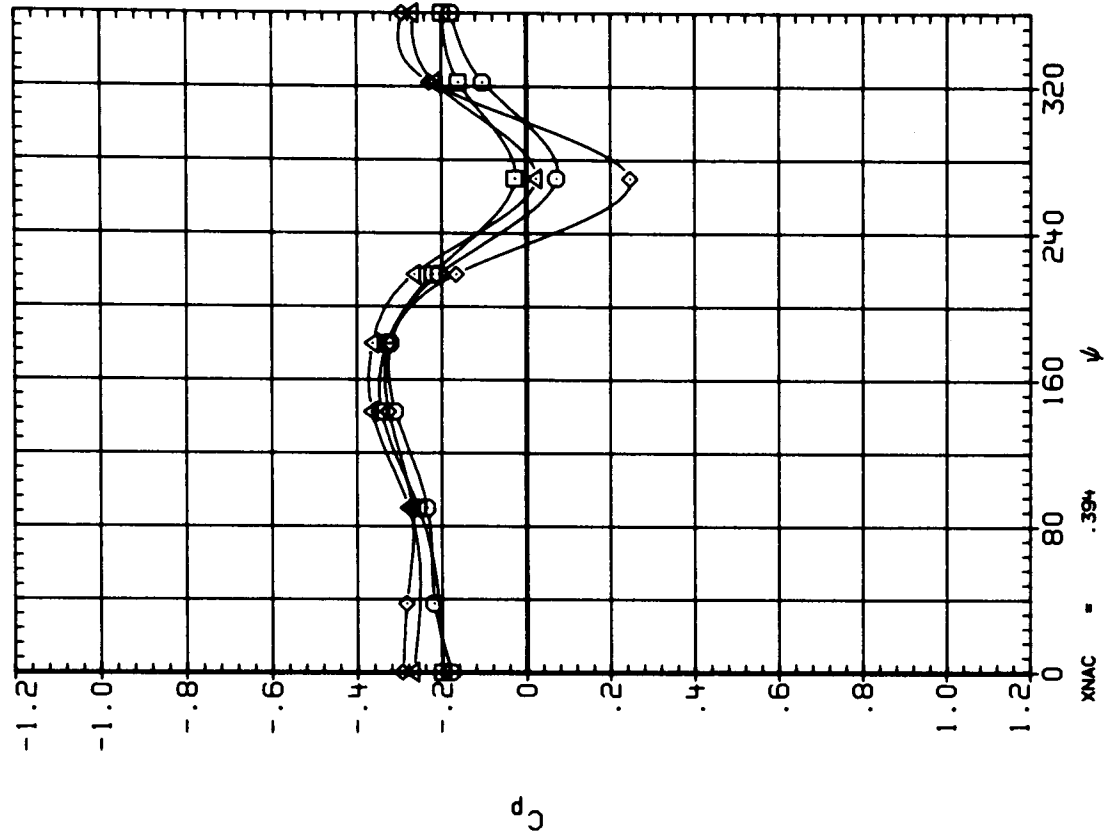
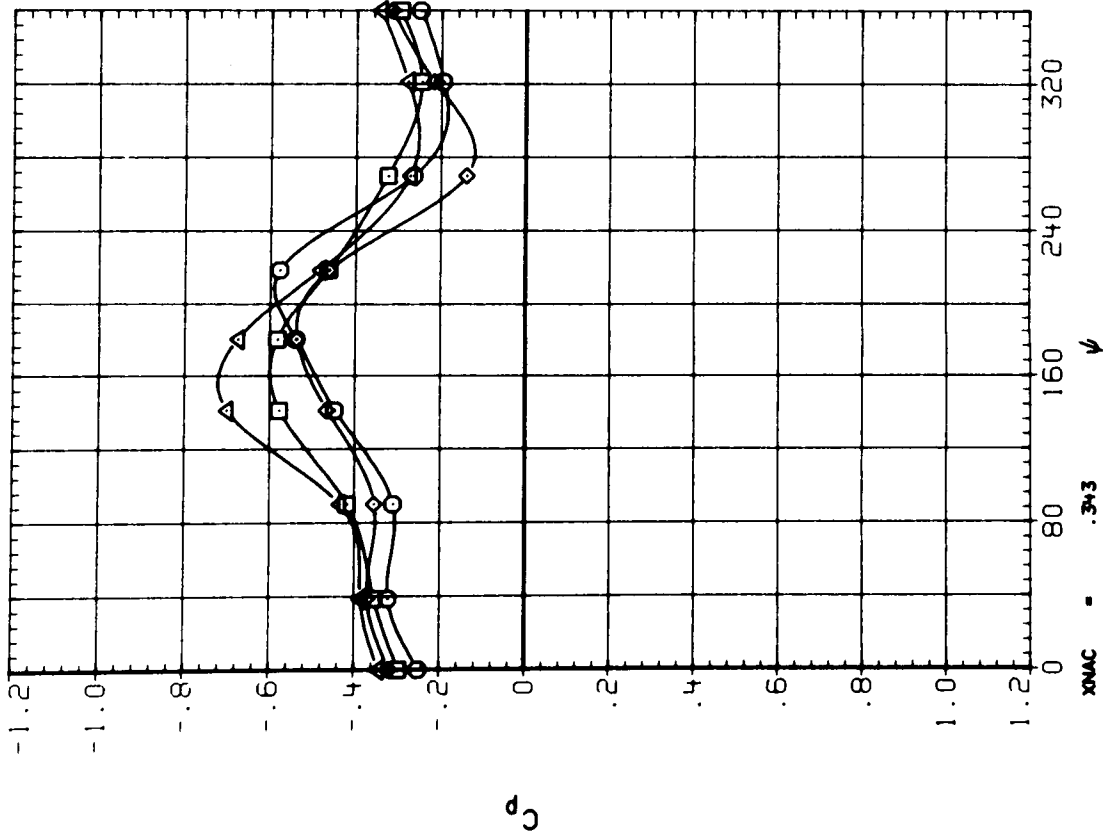


Figure 11.- Continued.

SYMBOL CONFIGURATION DESCRIPTION

□ WBNP
 ○ WBN
 ◇ WBNLP
 △ WBNL

EPR RPM ALPHA PITCH

1.774 8471 1.938 57.2
 1.682 8494 1.946 57.2
 1.770 8494 1.963 57.2
 1.728 8494 1.963 57.2

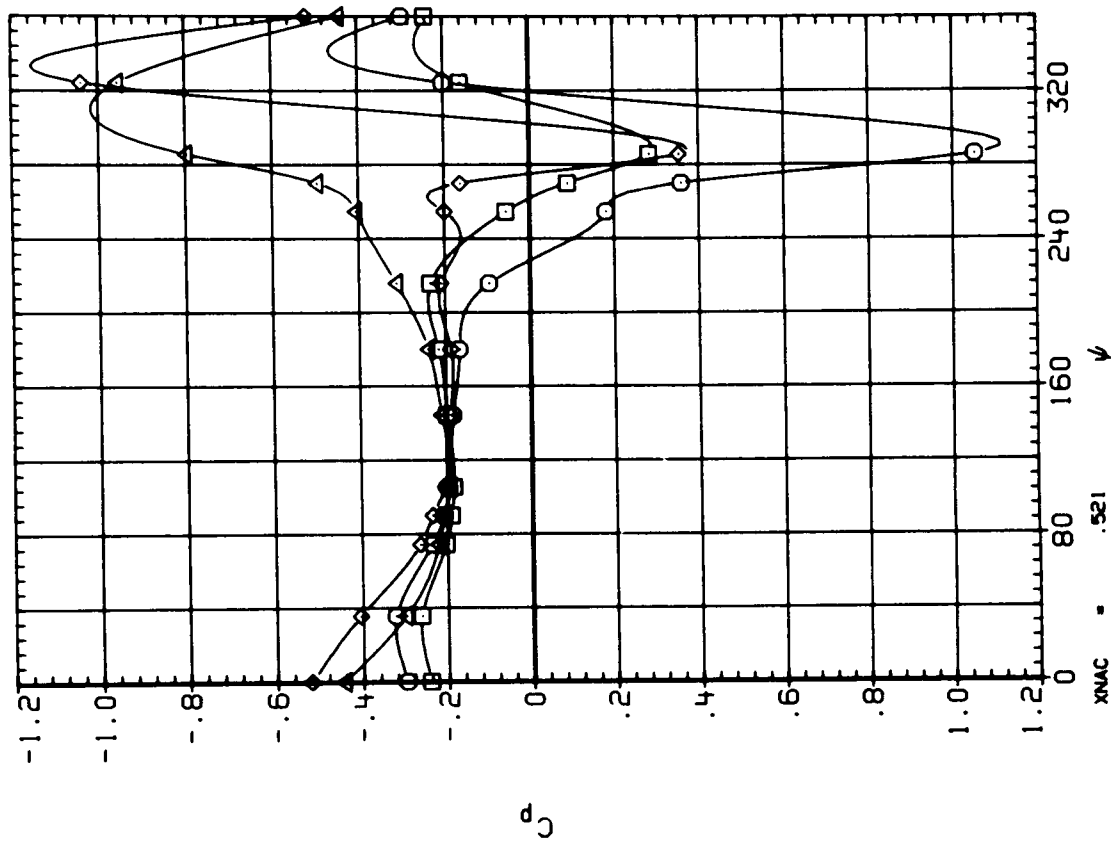
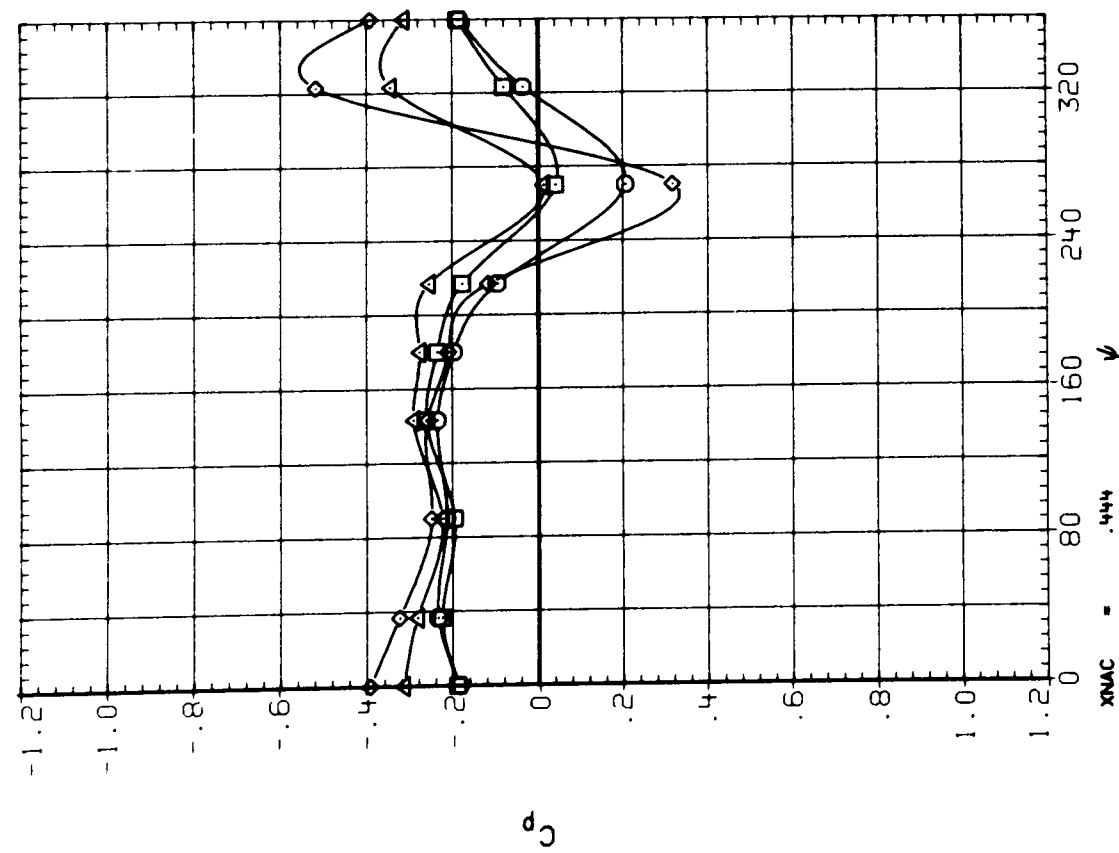


Figure 11.- Continued.

SYMBOL CONFIGURATION DESCRIPTION

- MBNP
- MBN
- ◇ MBNLP
- △ MBNL

EPR	RPM	ALPHA	PITCH
1.774	8471	1.938	57.2
1.682	8494	1.946	57.2
1.770		1.963	
1.728		1.963	

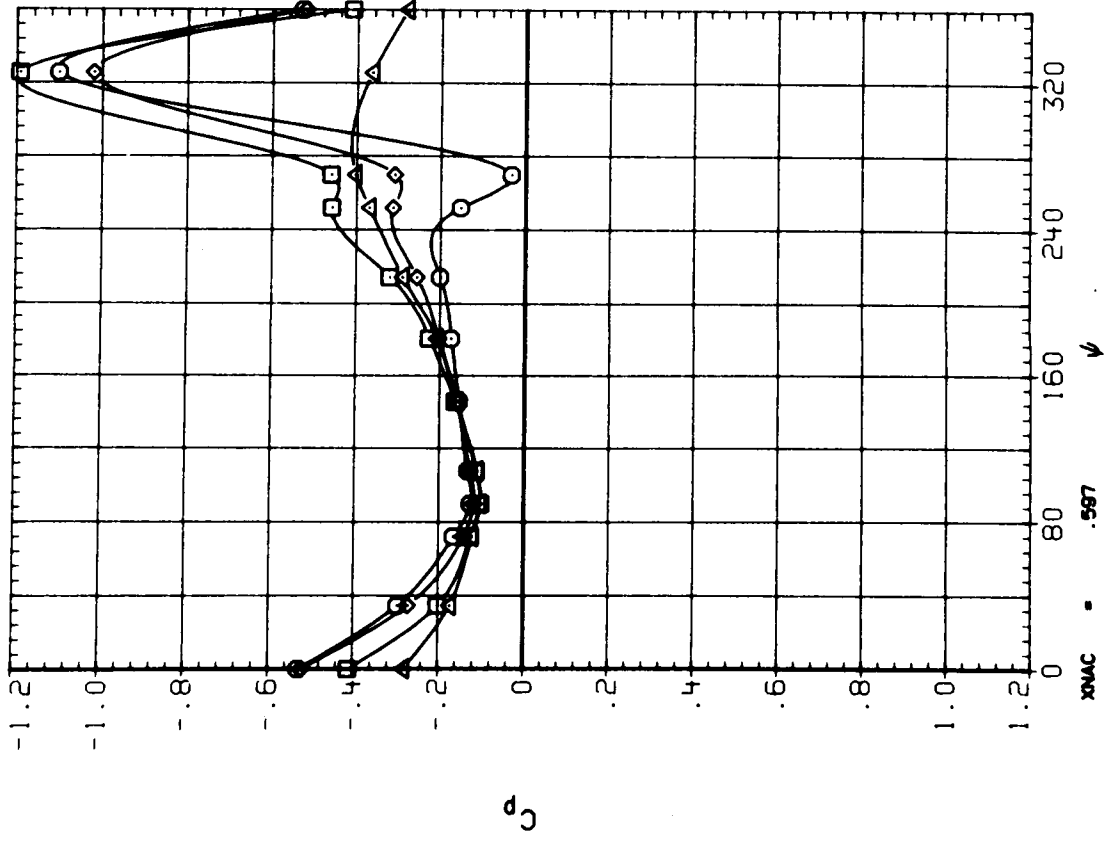
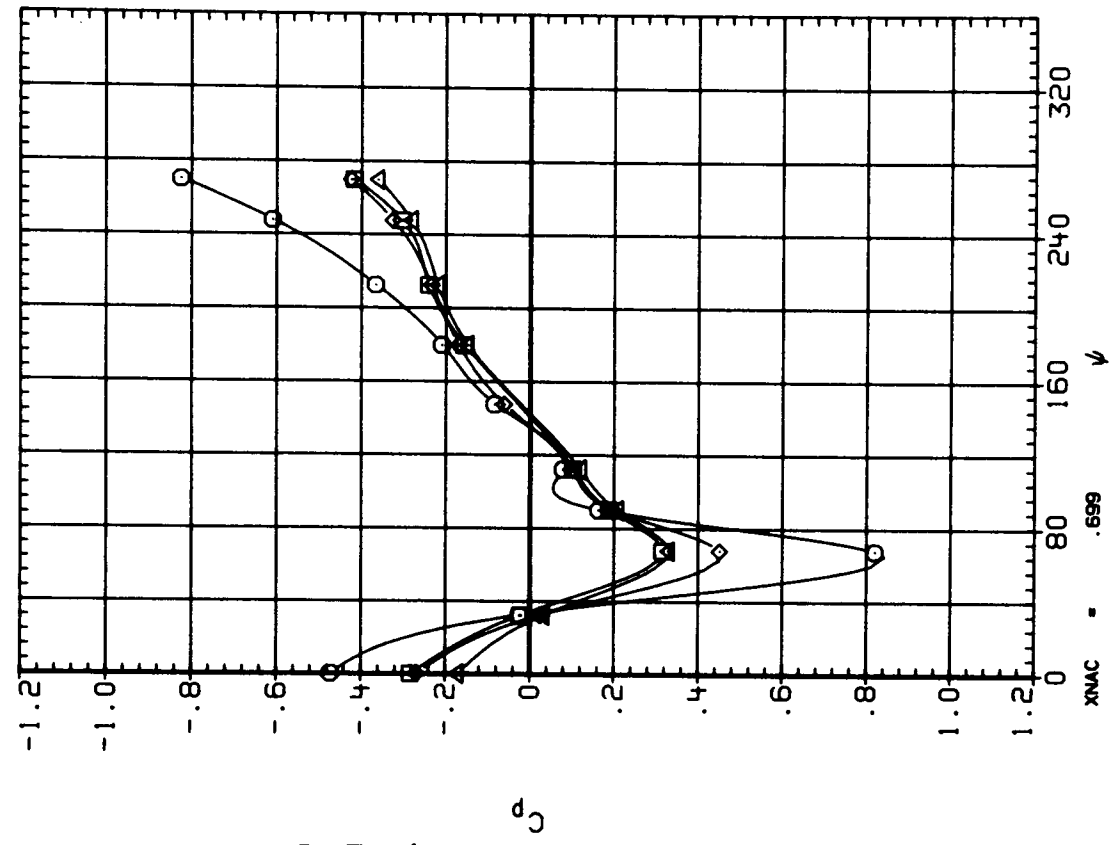


Figure 11.- Continued.

SYMBOL CONFIGURATION DESCRIPTION

○ MBNP
 □ MBN
 △ MBNLP
 ◇ MBNL

EPR RPM ALPHA PITCH

1.774 8471 1.938 57.2
 1.682 8494 1.946 57.2
 1.770 8494 1.963 57.2
 1.728 8494 1.963 57.2

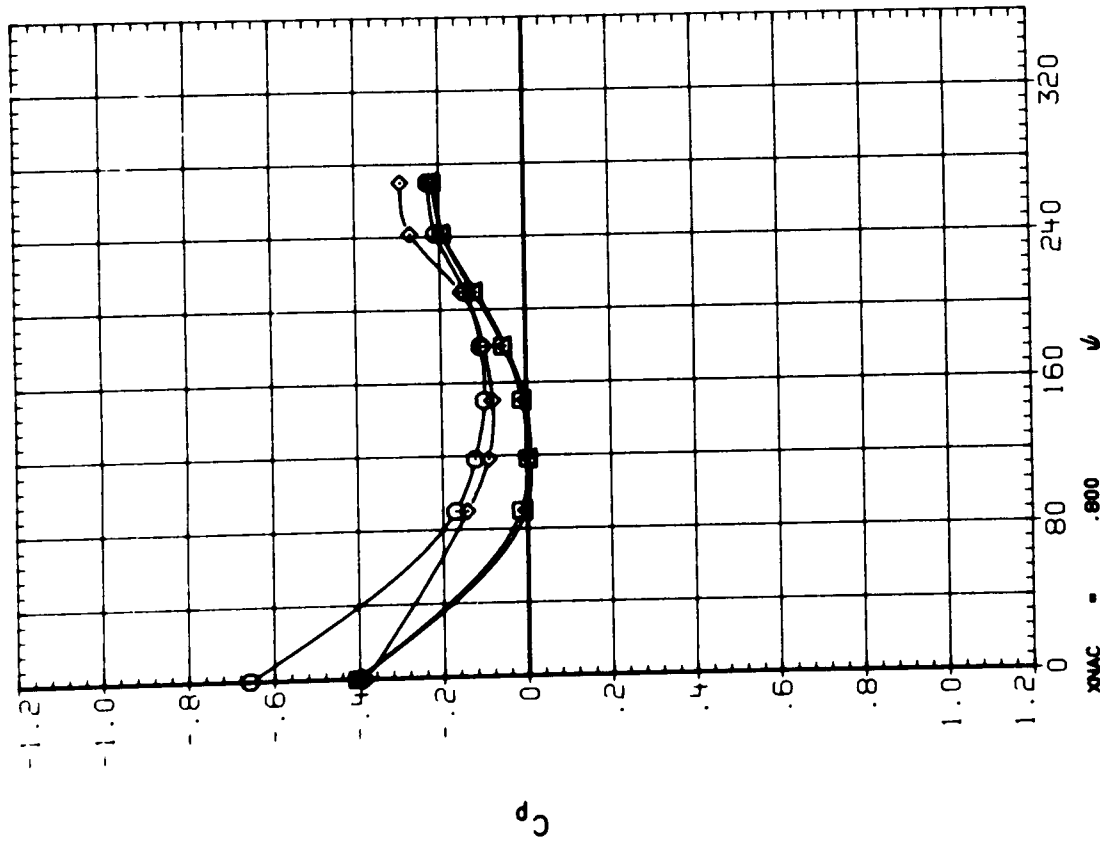
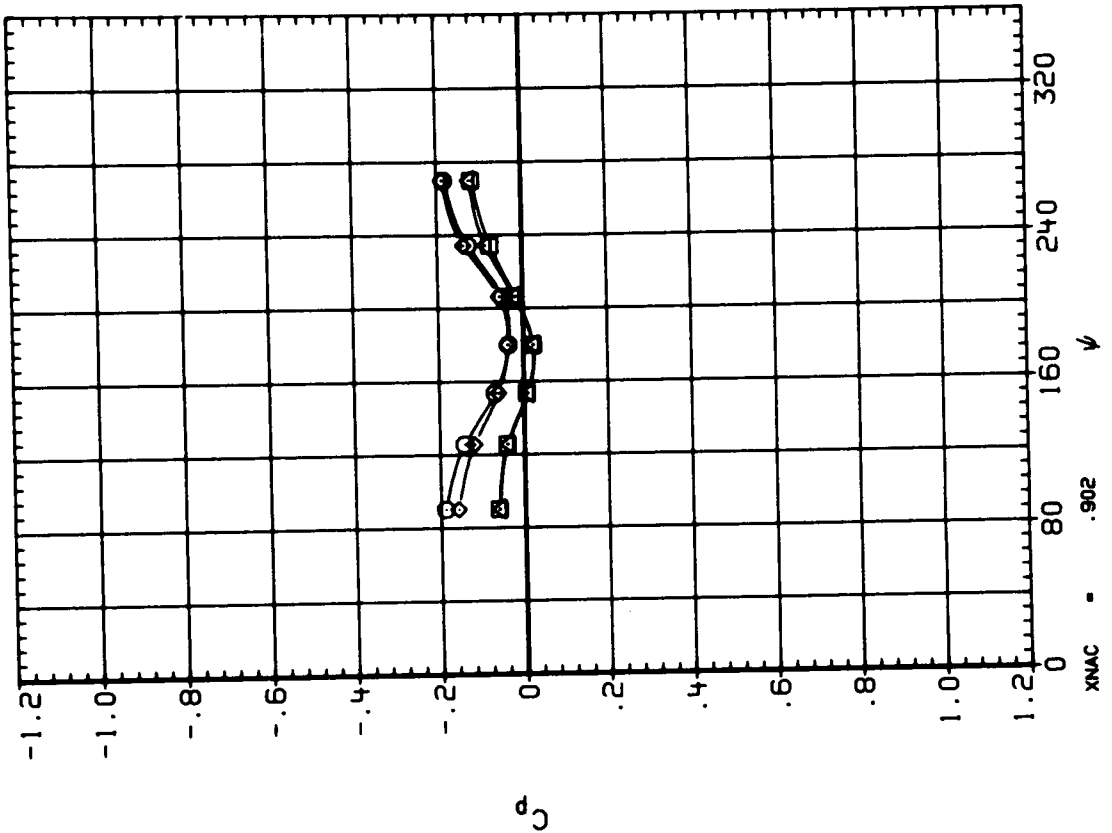


Figure 11.- Concluded.

SYMBOL CONFIGURATION DESCRIPTION
 ○ WBNLF
 □ WBNLF 3SP

EPR RPM ALPHA PITCH
 1.770 8494 1.963 57.2
 1.725 9486 1.945 57.2

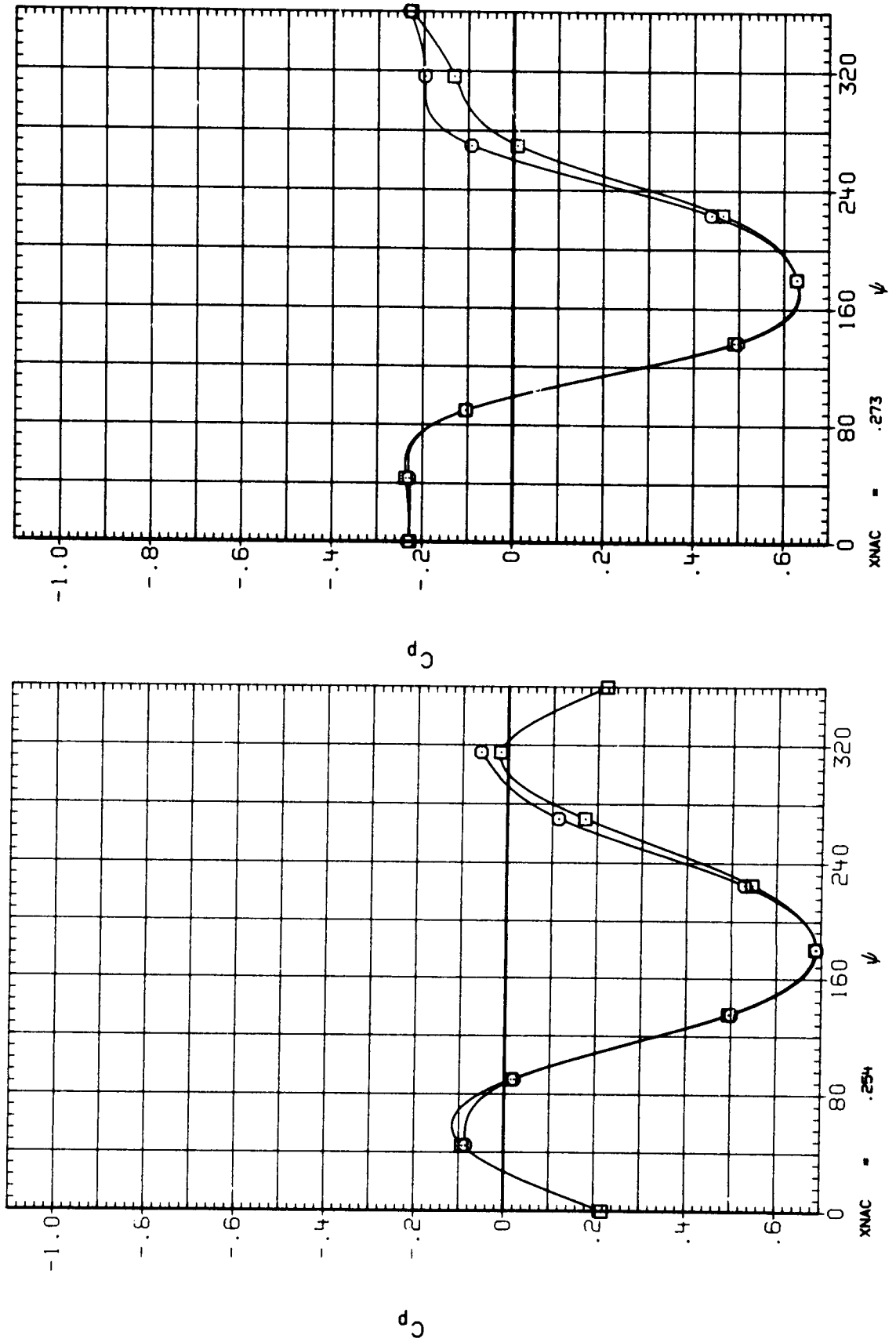


Figure 12.- Effect of fillet and strake on nacelle pressures; $M = 0.802$.

SYMBOL CONFIGURATION DESCRIPTION
 ○ WBNL P
 □ WBNL F3SP

EPR RPM ALPHA PITCH
 1.770 8494 1.963 57.2
 1.725 8486 1.945 57.2

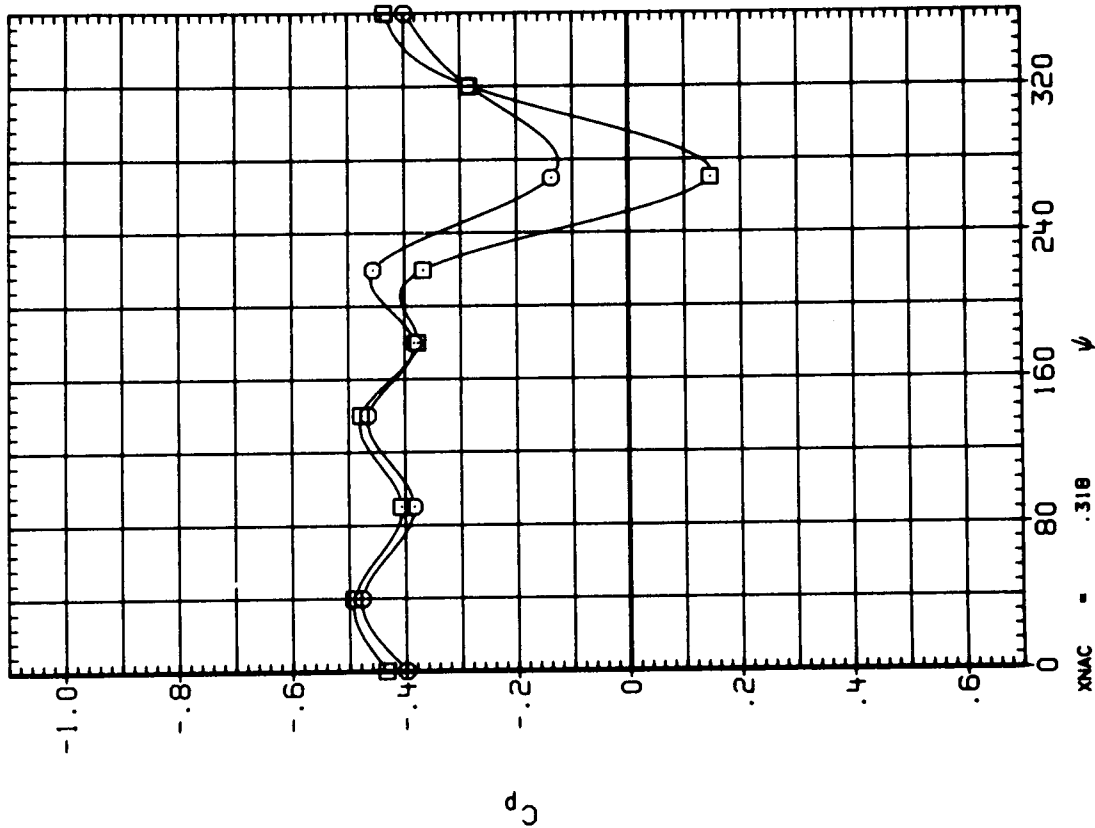
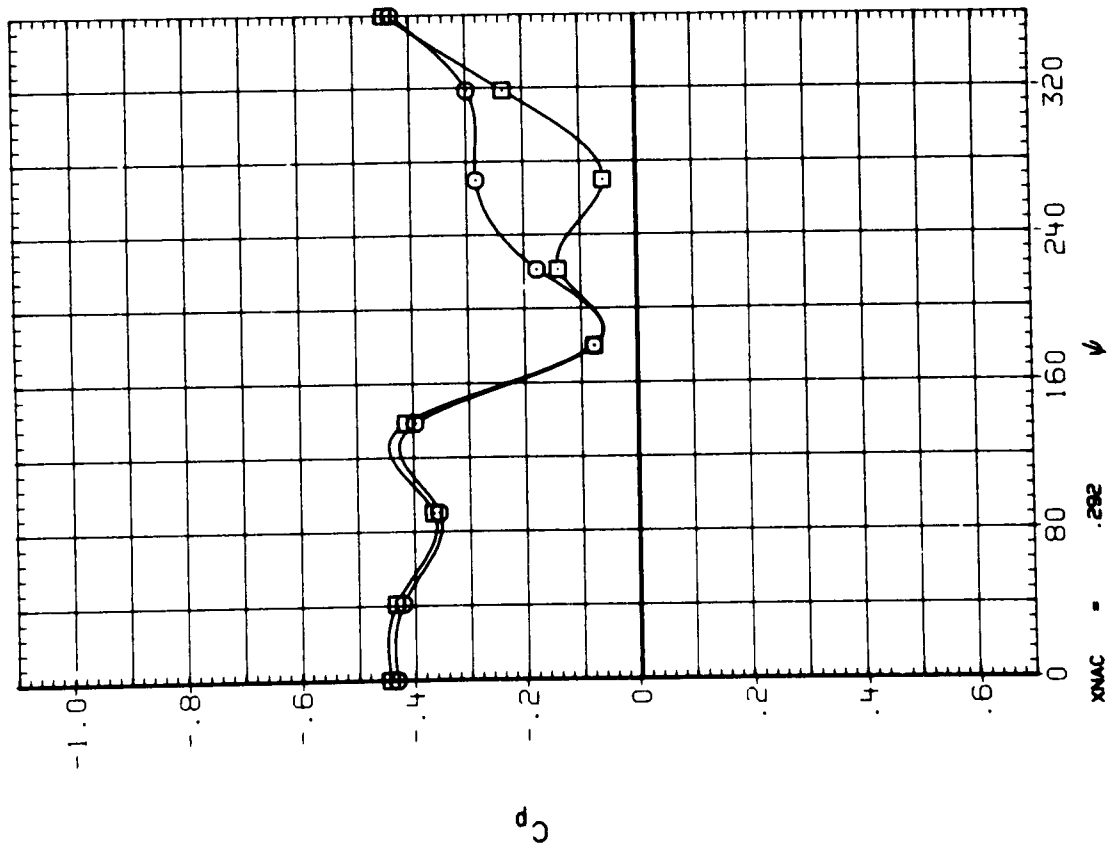


Figure 12.- Continued.

SYMBOL CONFIGURATION DESCRIPTION
 ○ WBNLP
 □ WBNLF3SP

EPR RPM ALPHA PITCH
 1.770 8494 1.963 57.2
 1.725 8486 1.945 57.2

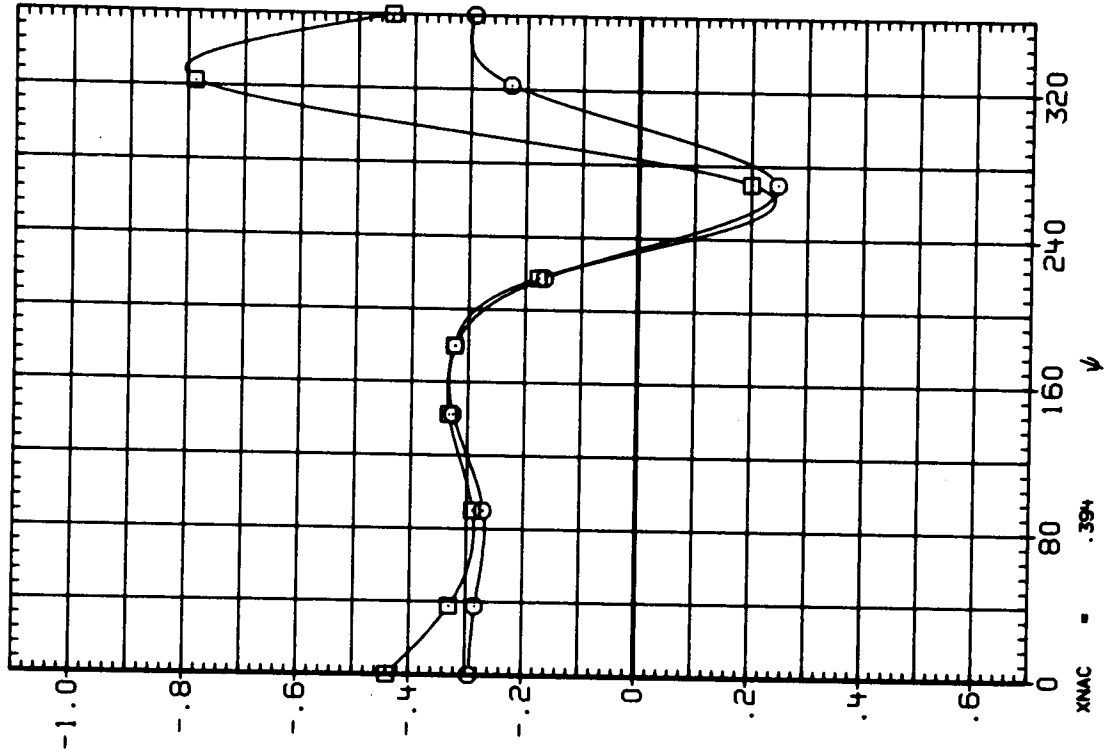
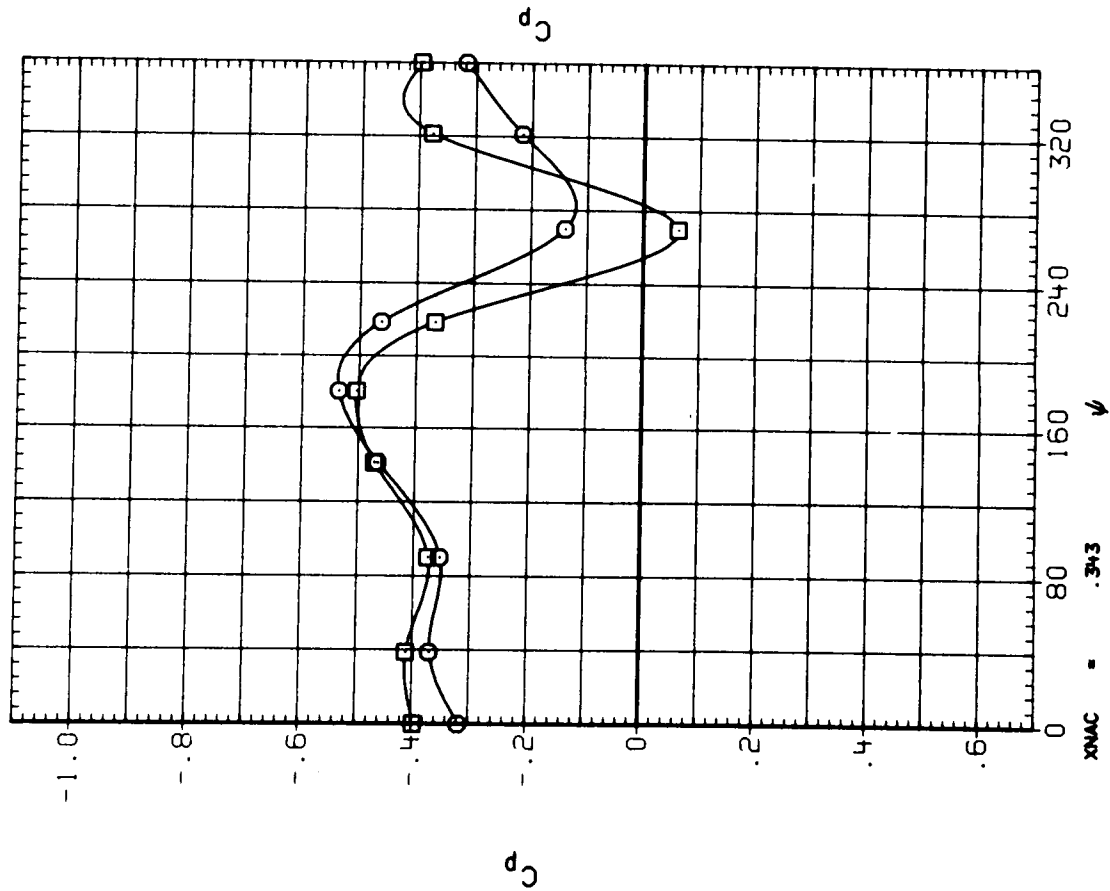


Figure 12.- Continued.

SYMBOL CONFIGURATION DESCRIPTION
 ○ HBNLP
 □ HBNLF3SP

EPR RPM ALPHA PITCH
 1.770 8494 1.963 57.2
 1.725 8486 1.945 57.2

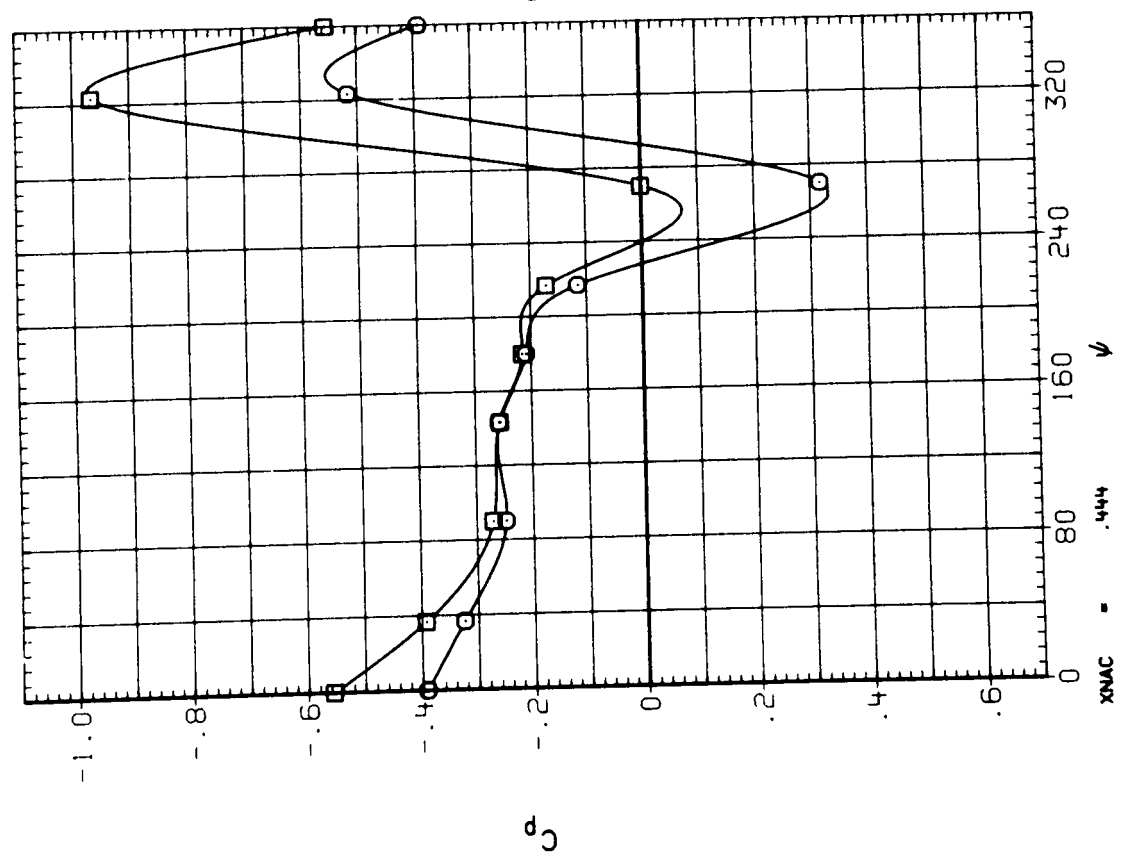
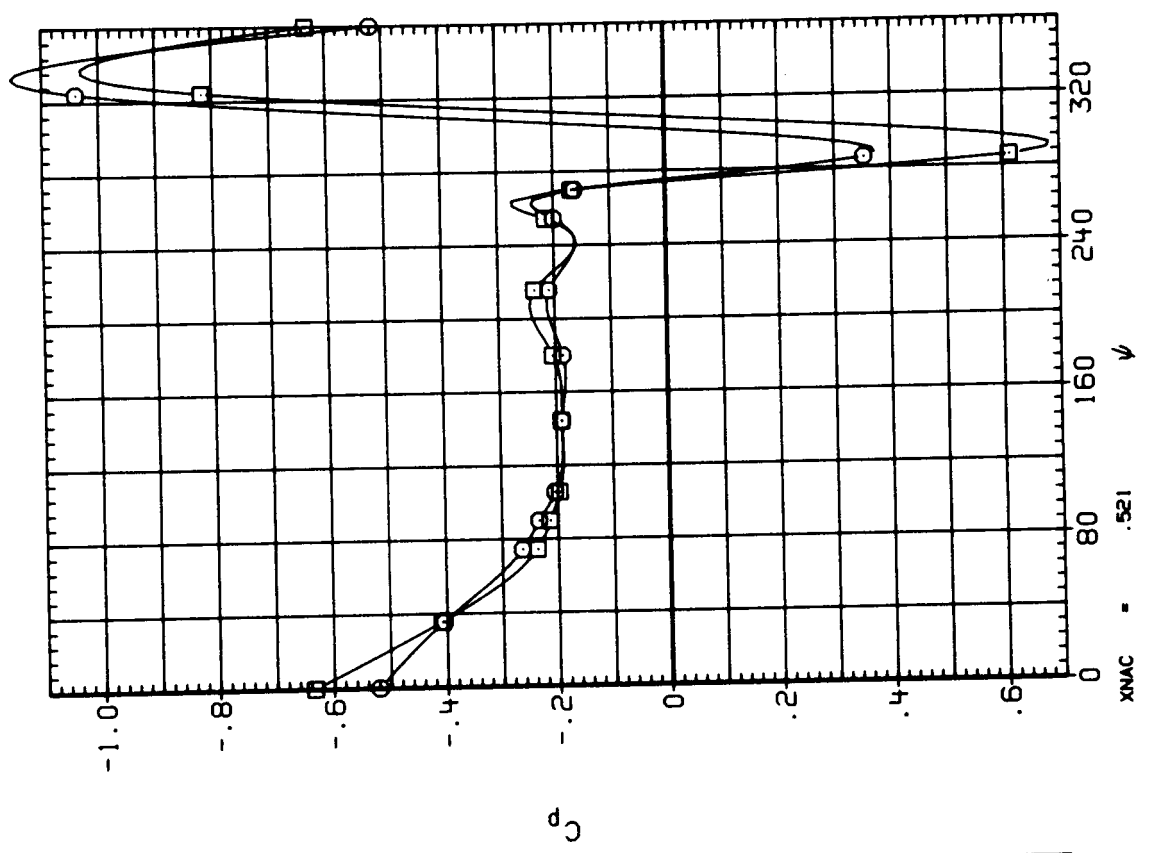


Figure 12.- Continued.

SYMBOL CONFIGURATION DESCRIPTION
 ○ HBNLP
 □ HBNLF3SP

EPR RPM ALPHA PITCH
 1.770 8494 1.963 57.2
 1.725 8486 1.945 57.2

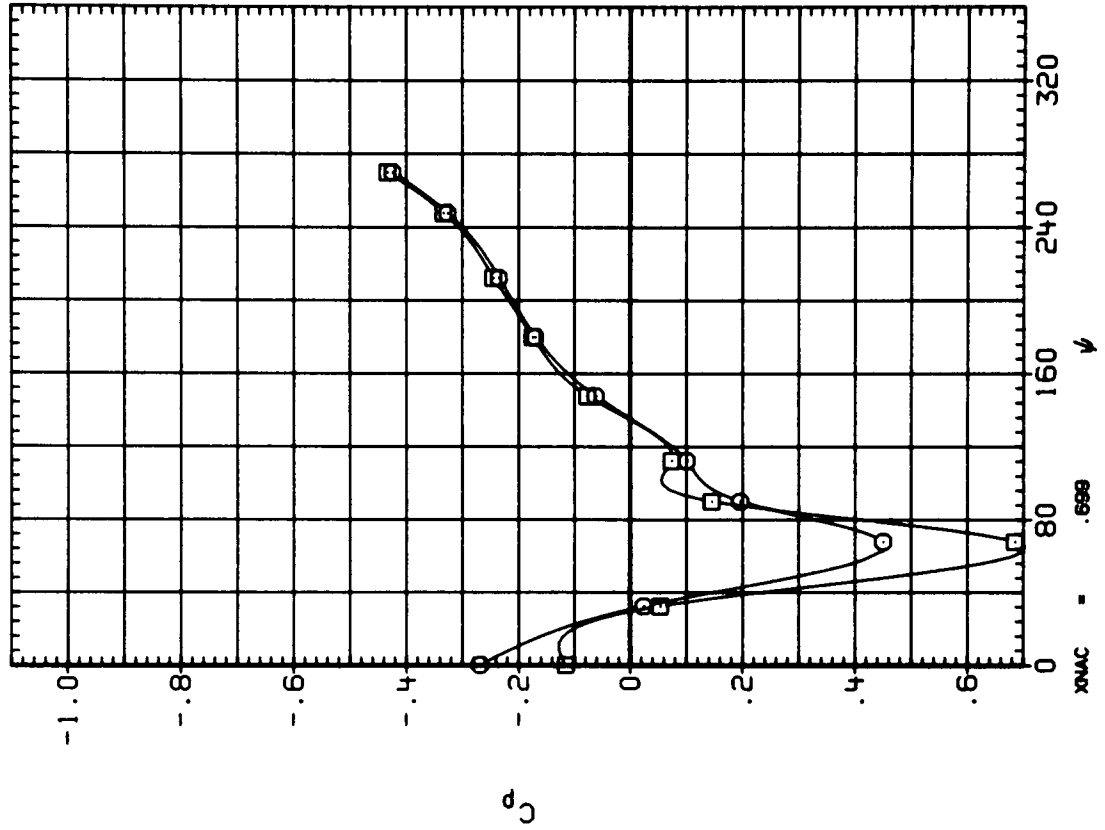
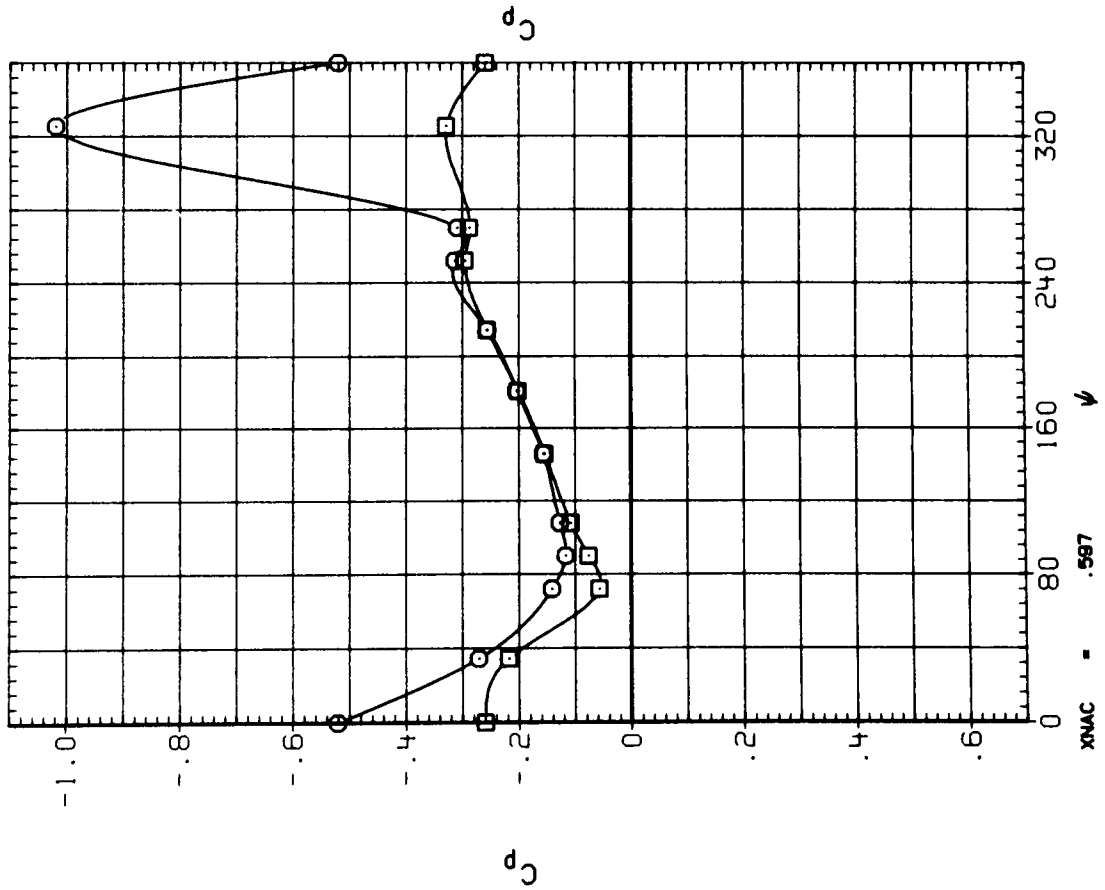


Figure 12.- Continued.

SYMBOL CONFIGURATION DESCRIPTION
 ○ MENLP
 □ MENLF3SP

EPR RPM ALPHA PITCH
 1.770 8494 1.963 57.2
 1.725 8486 1.945 57.2

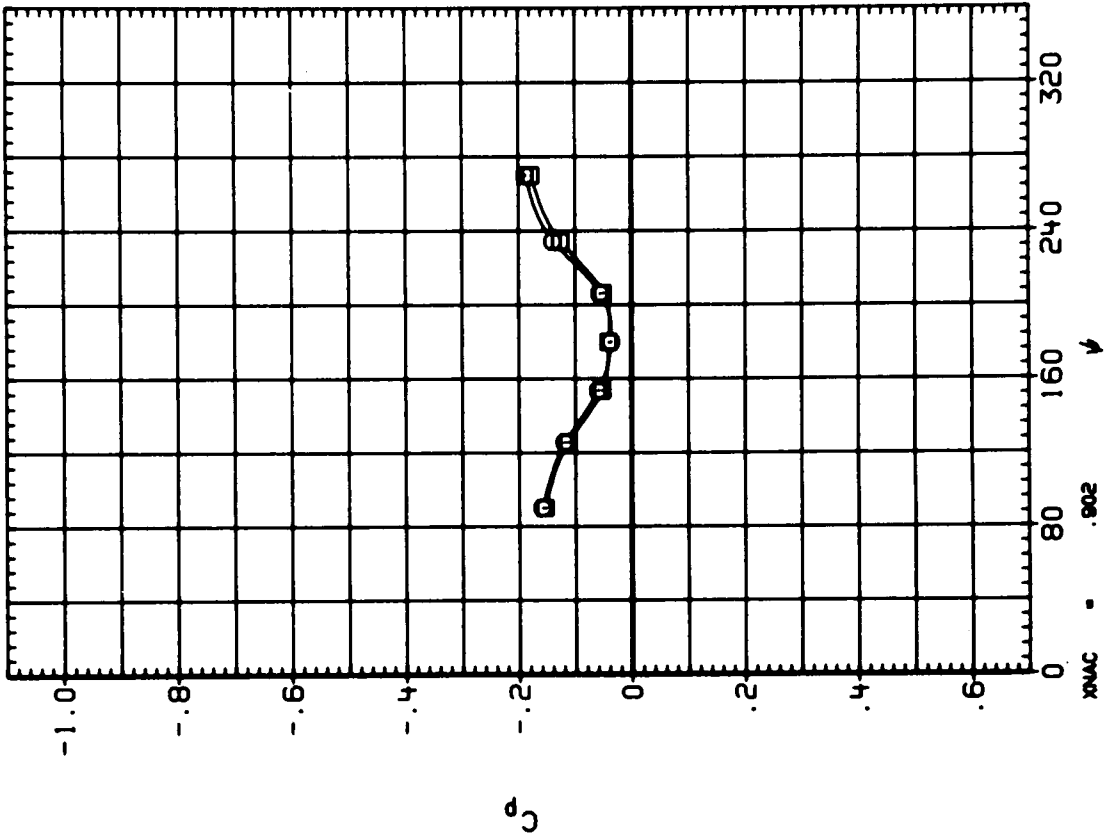
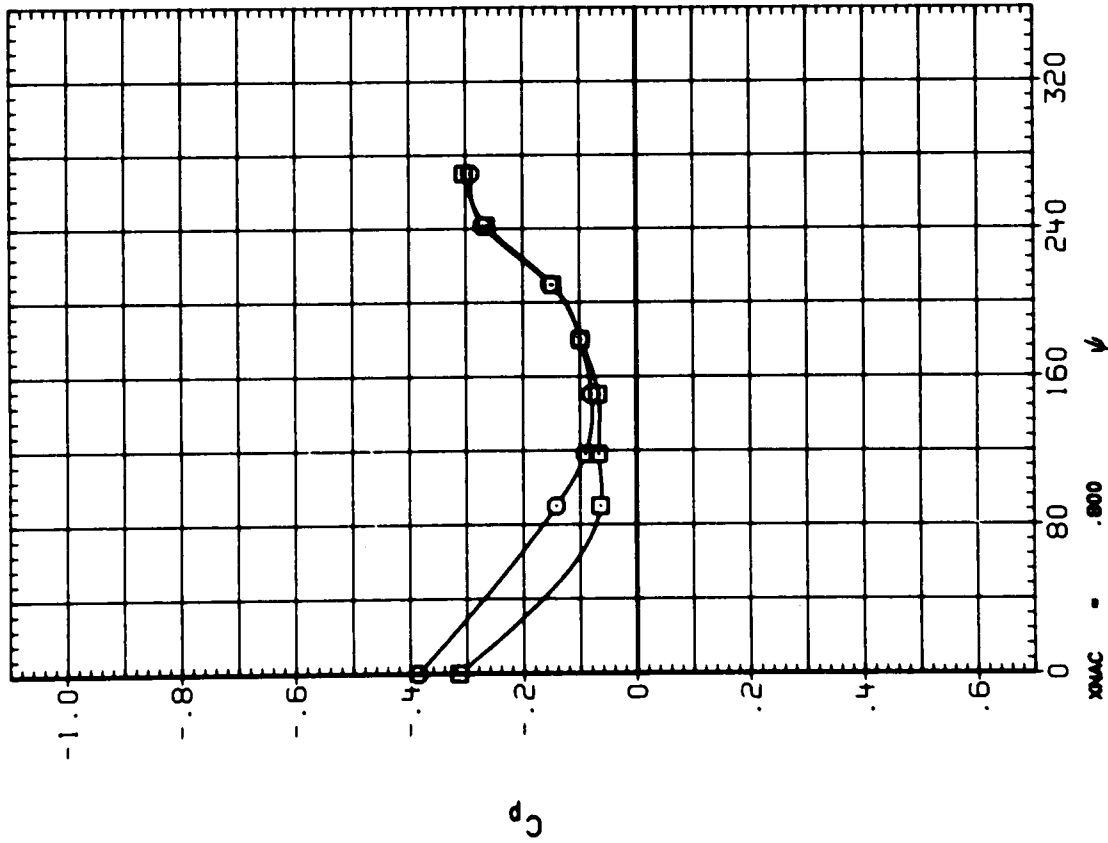


Figure 12.- Concluded.

SYMBOL CONFIGURATION DESCRIPTION
 ○ WENF
 □ WENF

EPR RPM ALPHA PITCH
 1.000 5381 1.954 57.2
 1.774 8471 1.938 57.2

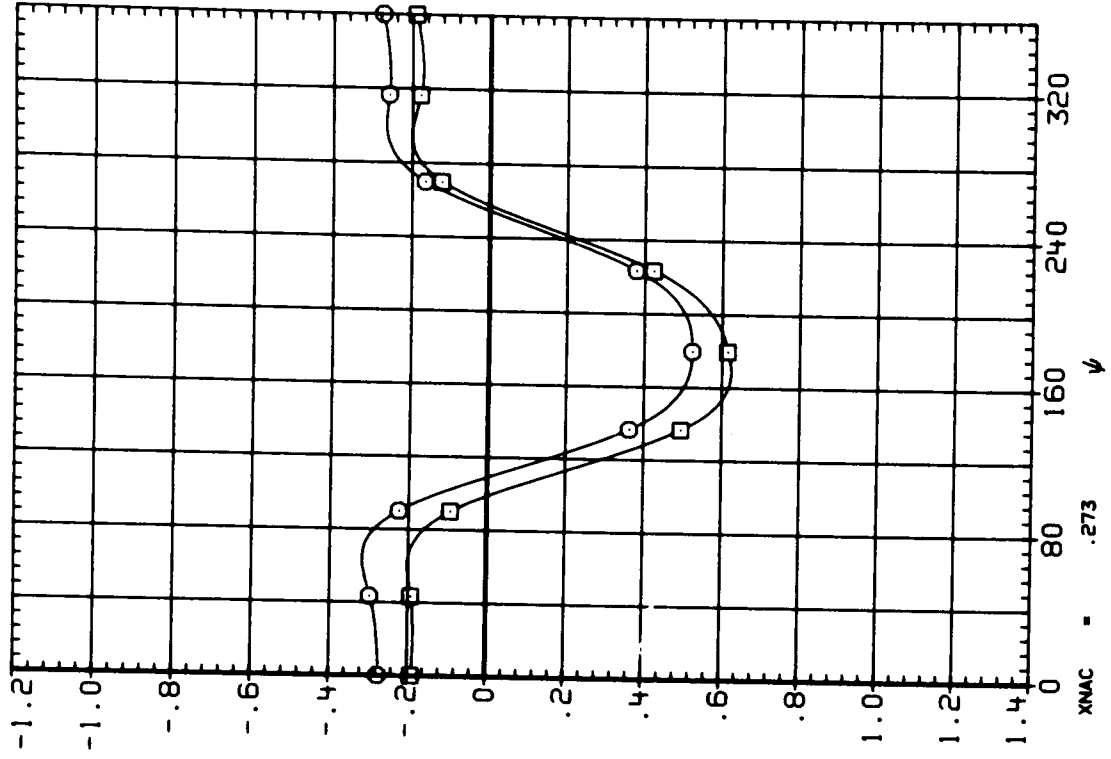
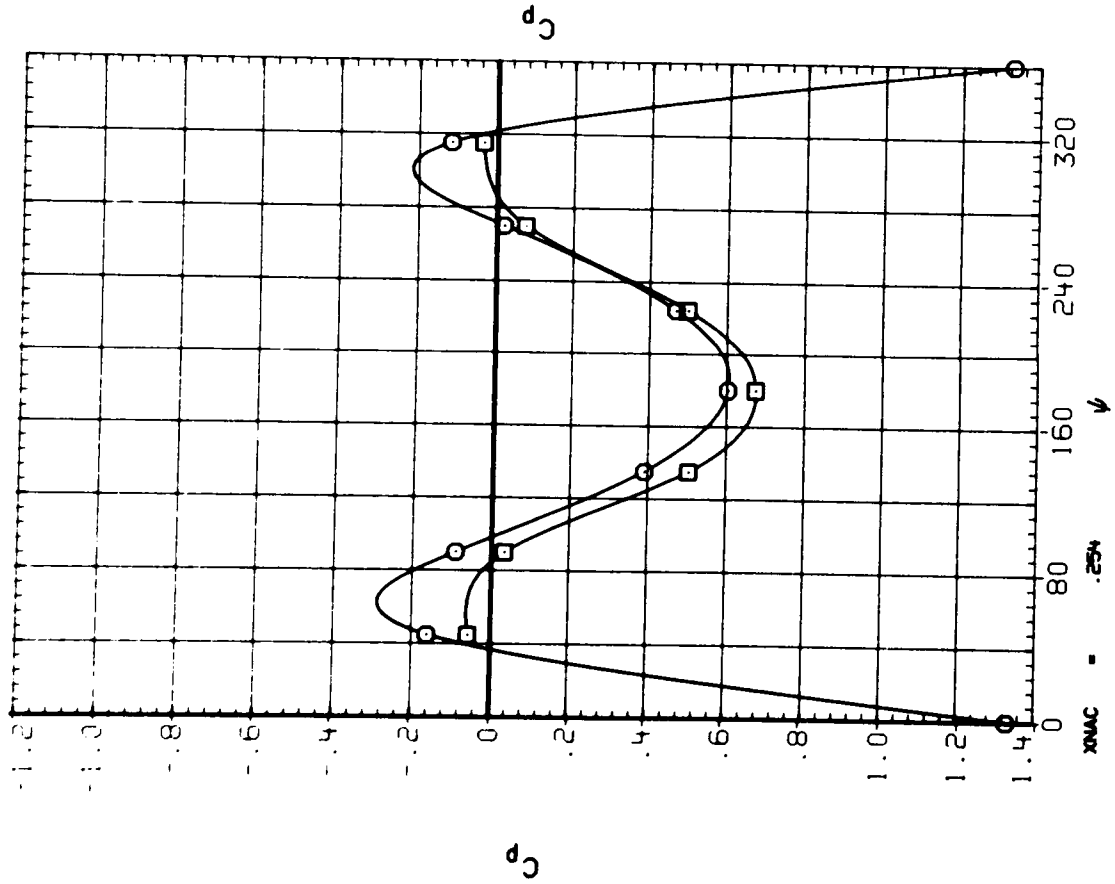


Figure 13.- Effect of power on nacelle pressures--baseline configuration;
 M = 0.803.

SYMBOL CONFIGURATION DESCRIPTION
 ○ WBNP
 □ WBNP

EPR RPM ALPHA PITCH
 1.000 6381 1.954 57.2
 1.774 8471 1.938 57.2

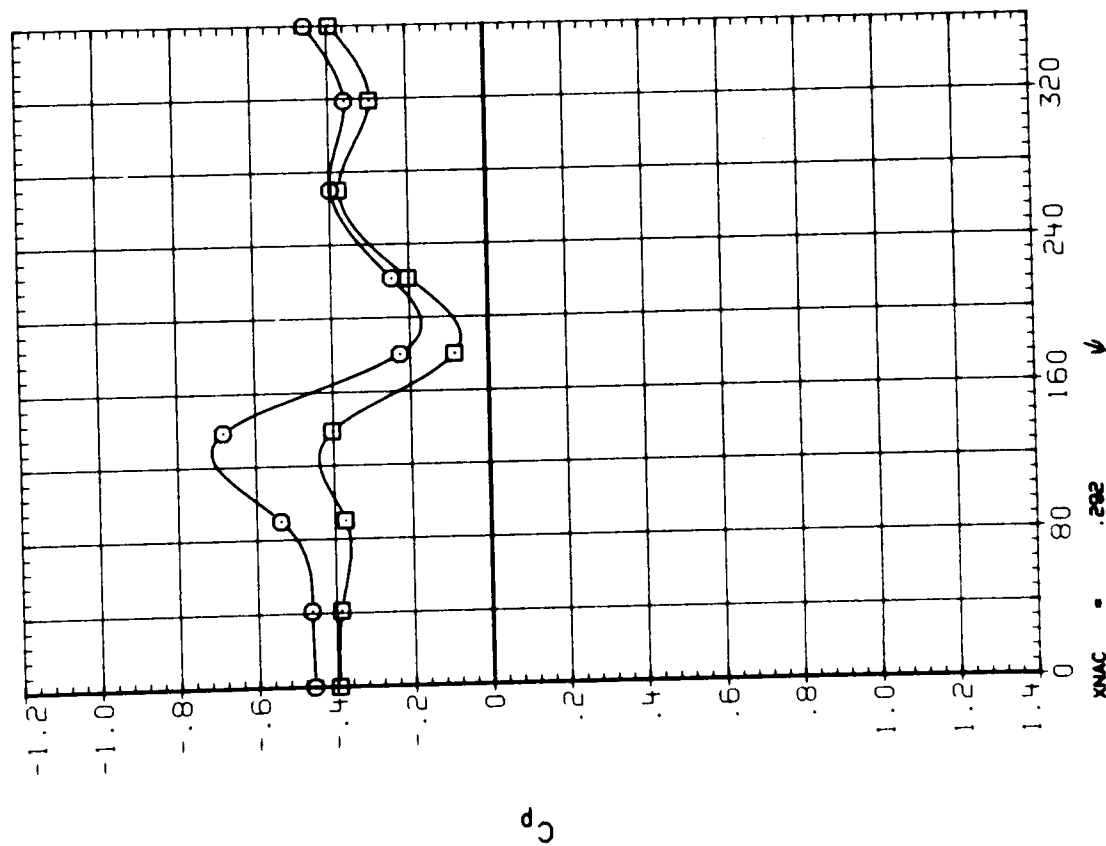
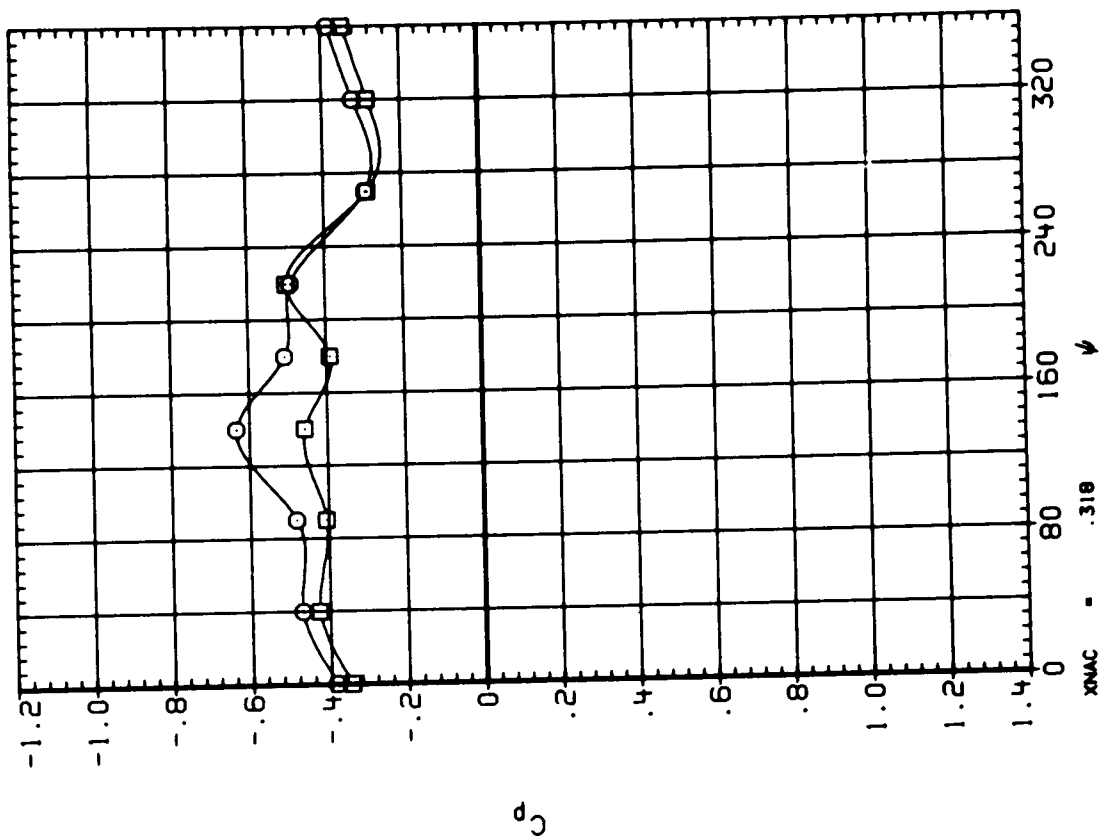


Figure 13.- Continued.

SYMBOL CONFIGURATION DESCRIPTION
 ○ HBNP
 □ HBNP

EPR RPM ALPHA PITCH
 1.000 6381 1.954 57.2
 1.774 8471 1.938 57.2

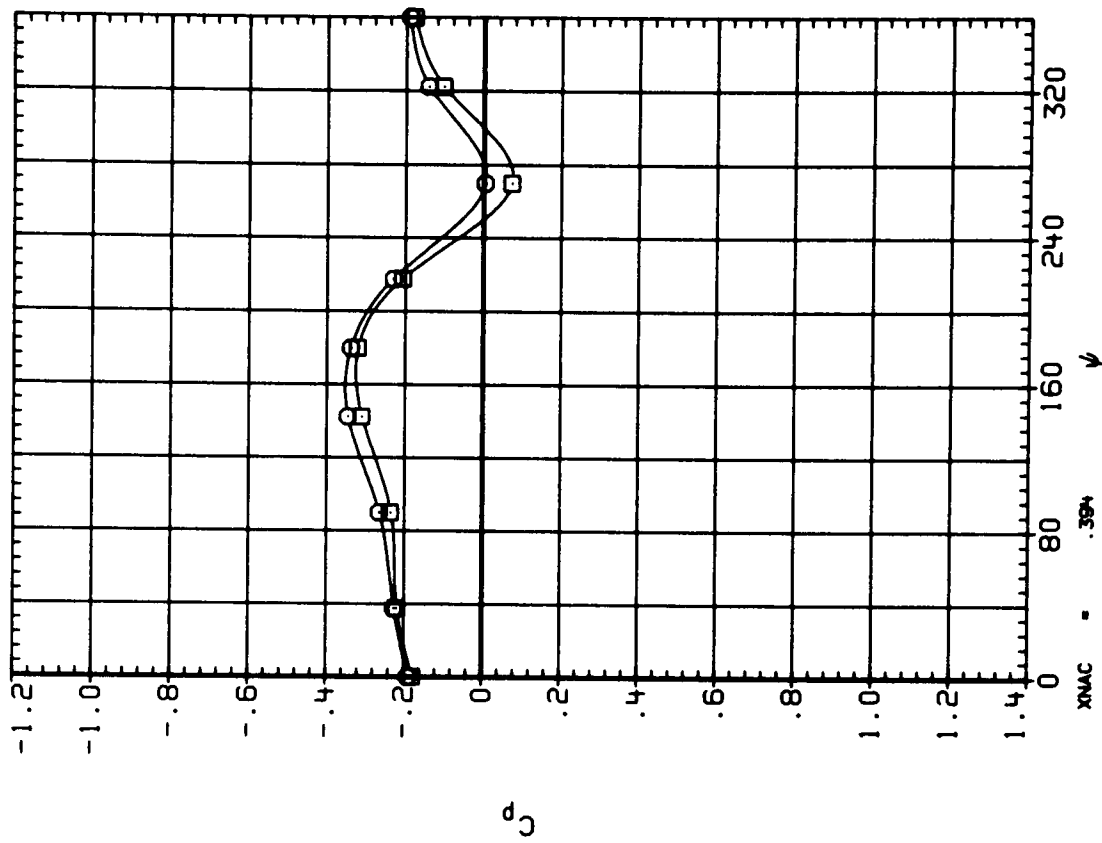
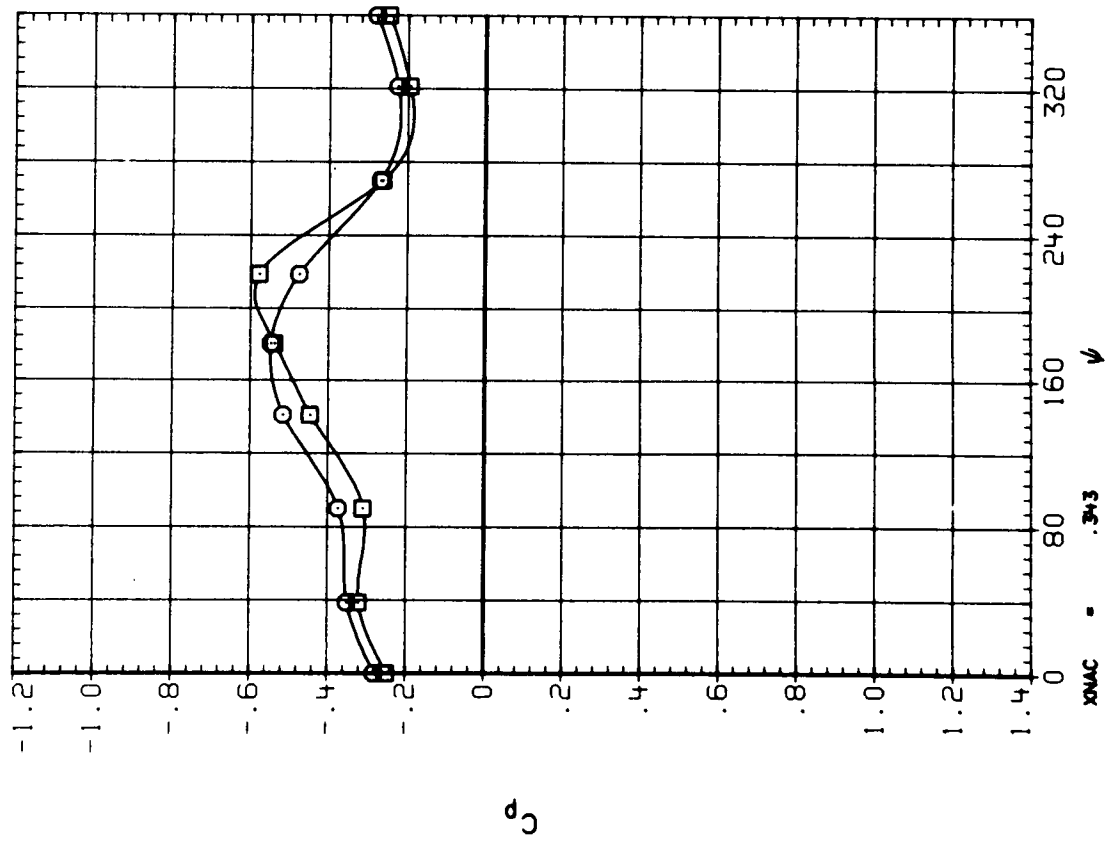


Figure 13.- Continued.

SYMBOL CONFIGURATION DESCRIPTION
 ○ HBNP
 □ HBNP

EPR RPM ALPHA PITCH
 1.000 5381 1.954 57.2
 1.774 8471 1.938 57.2

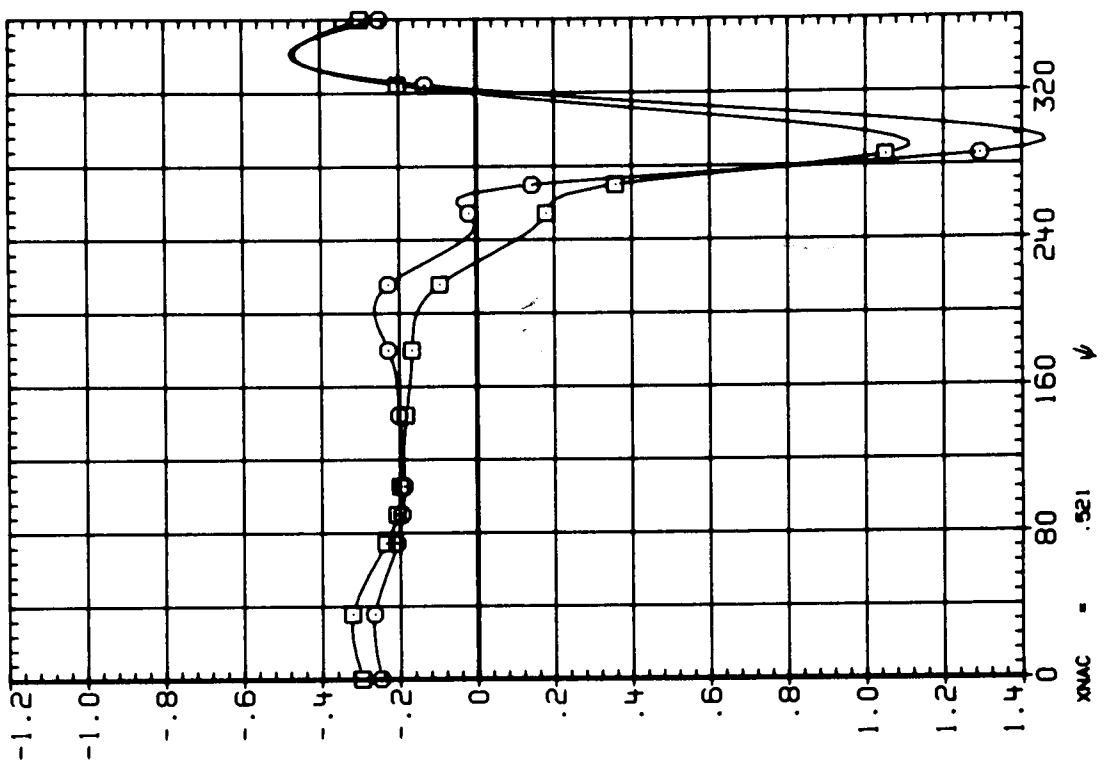
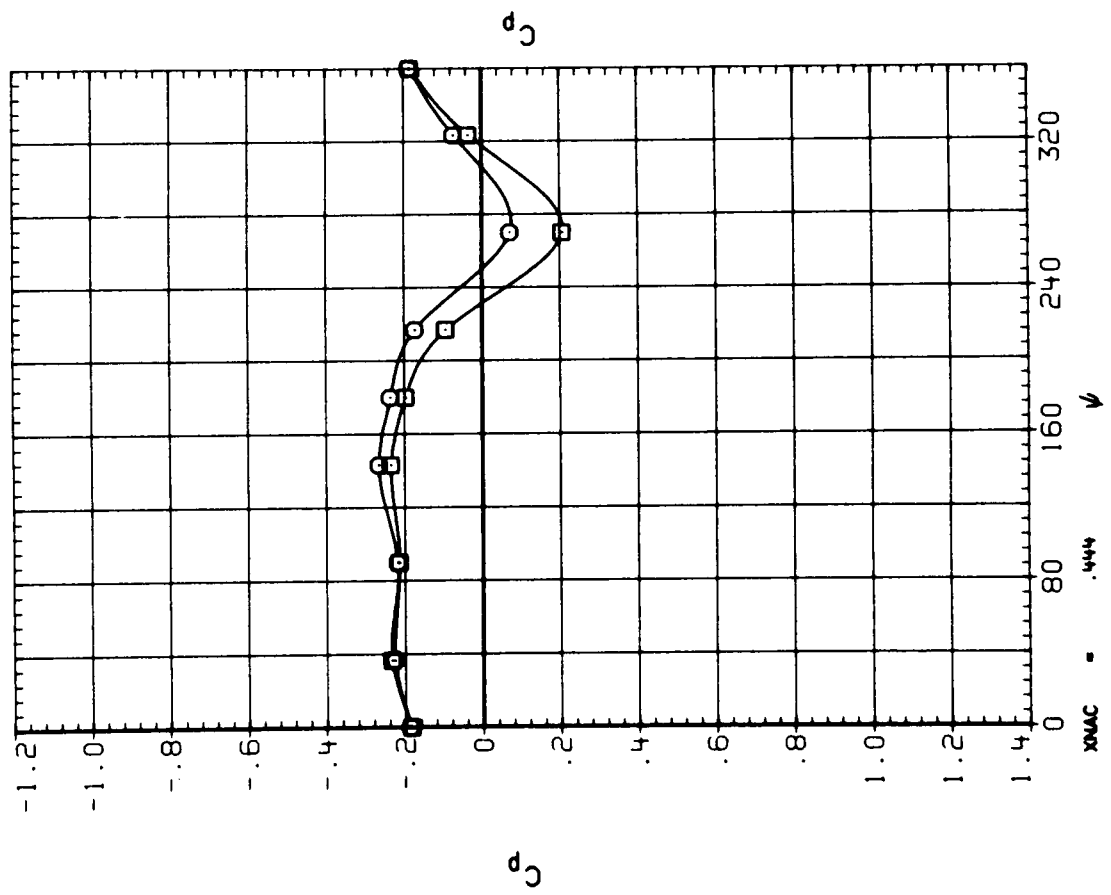


Figure 13.- Continued.

SYMBOL CONFIGURATION DESCRIPTION
 ○ HBNP
 □ HBNP

EPR RPM ALPHA PITCH
 1.000 6381 1.954 57.2
 1.774 8471 1.938 57.2

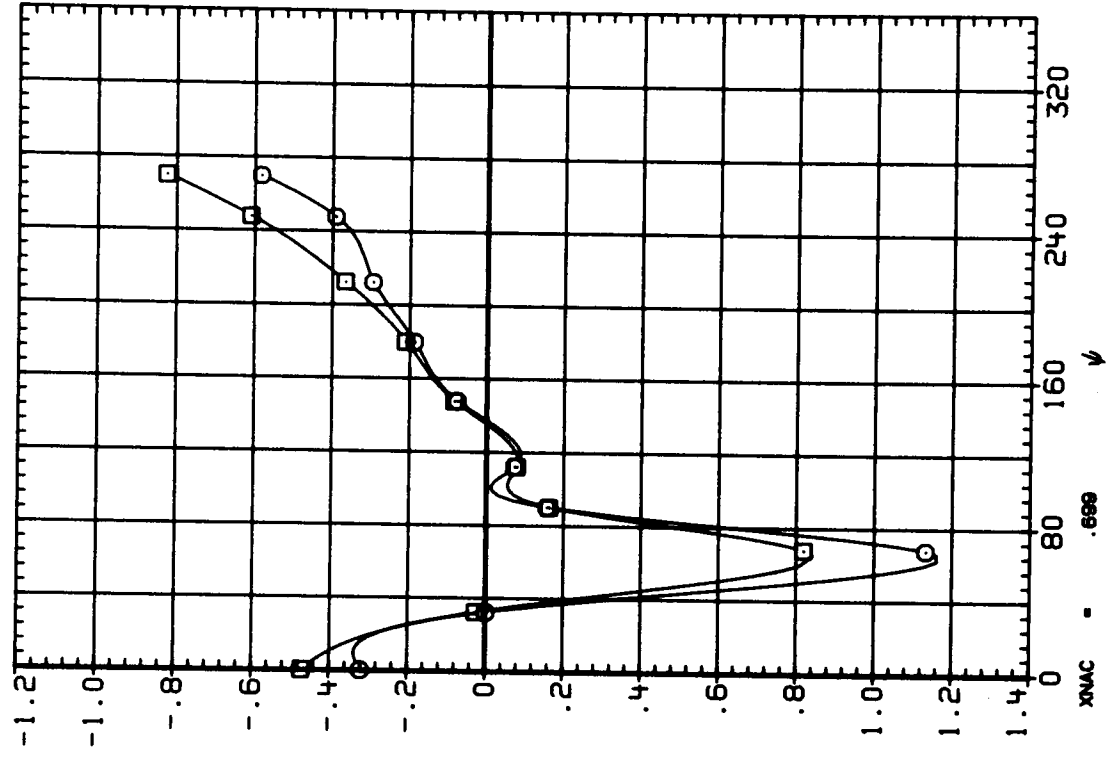
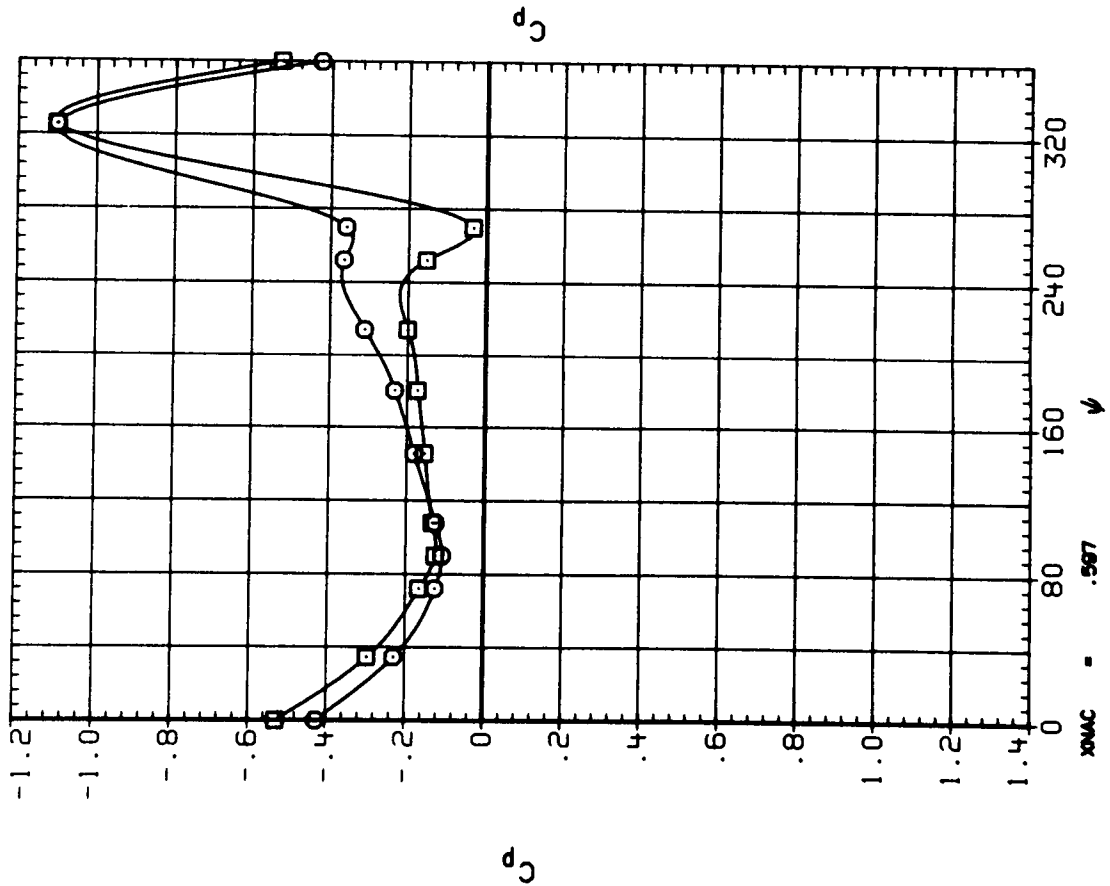


Figure 13.- Continued.

SYMBOL CONFIGURATION DESCRIPTION
 ○ HBSP
 □ HBSP

EPR RPM ALPHA PITCH
 1.000 6381 1.954 57.2
 1.774 8471 1.938 57.2

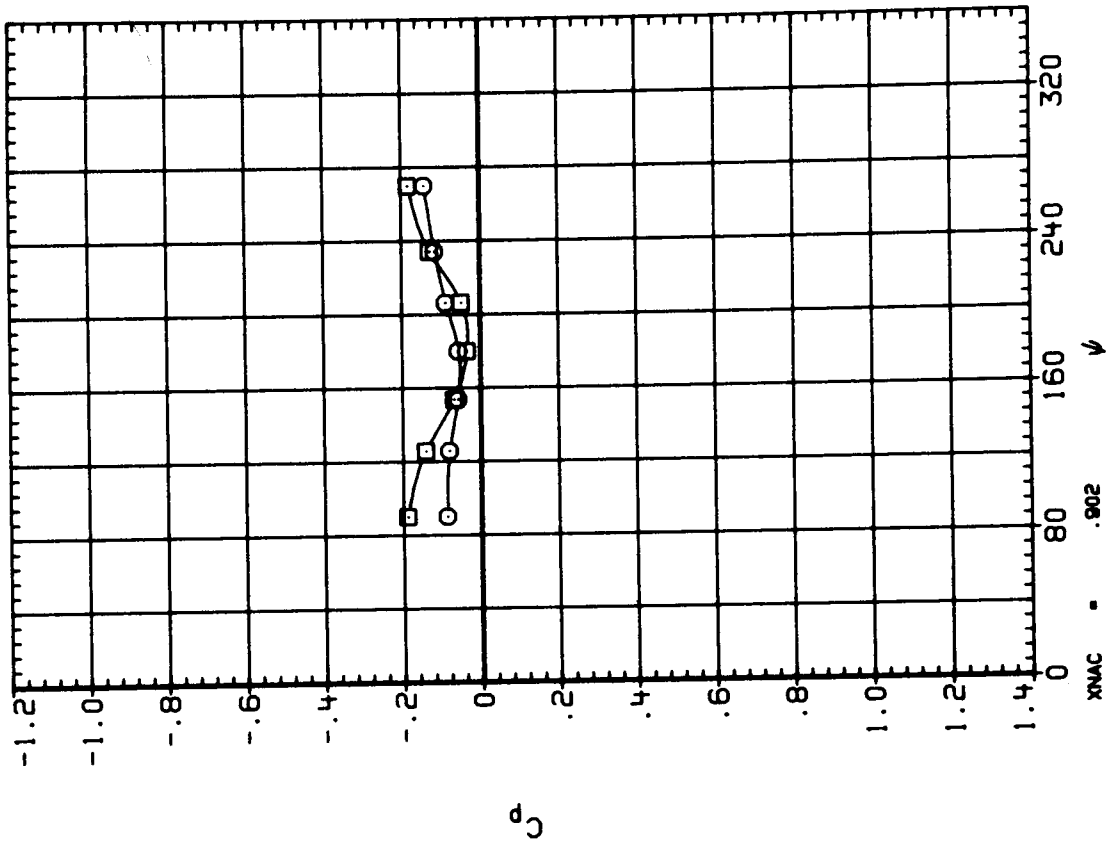
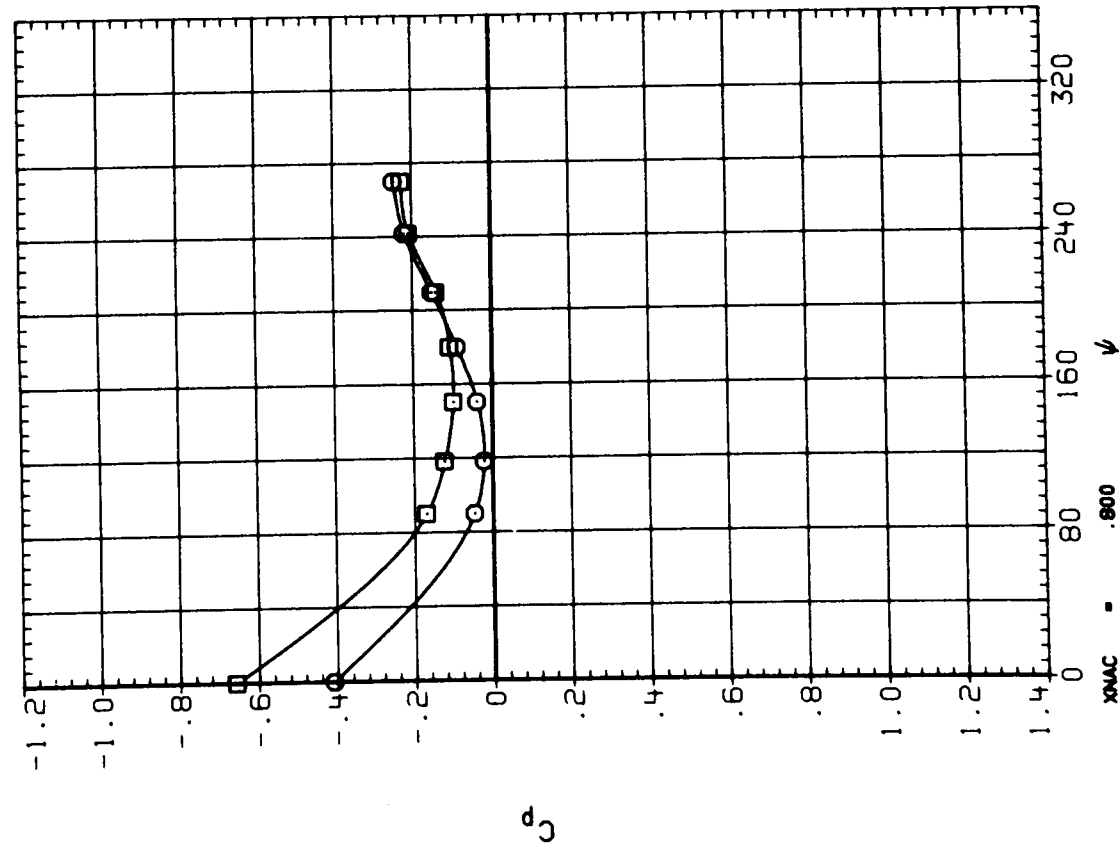


Figure 13.- Concluded.

SYMBOL CONFIGURATION DESCRIPTION

○ WBNLP
□ WBNLP

EPR 1.003 6494 ALPHA 1.967 57.2
1.770 8494 1.963 57.2

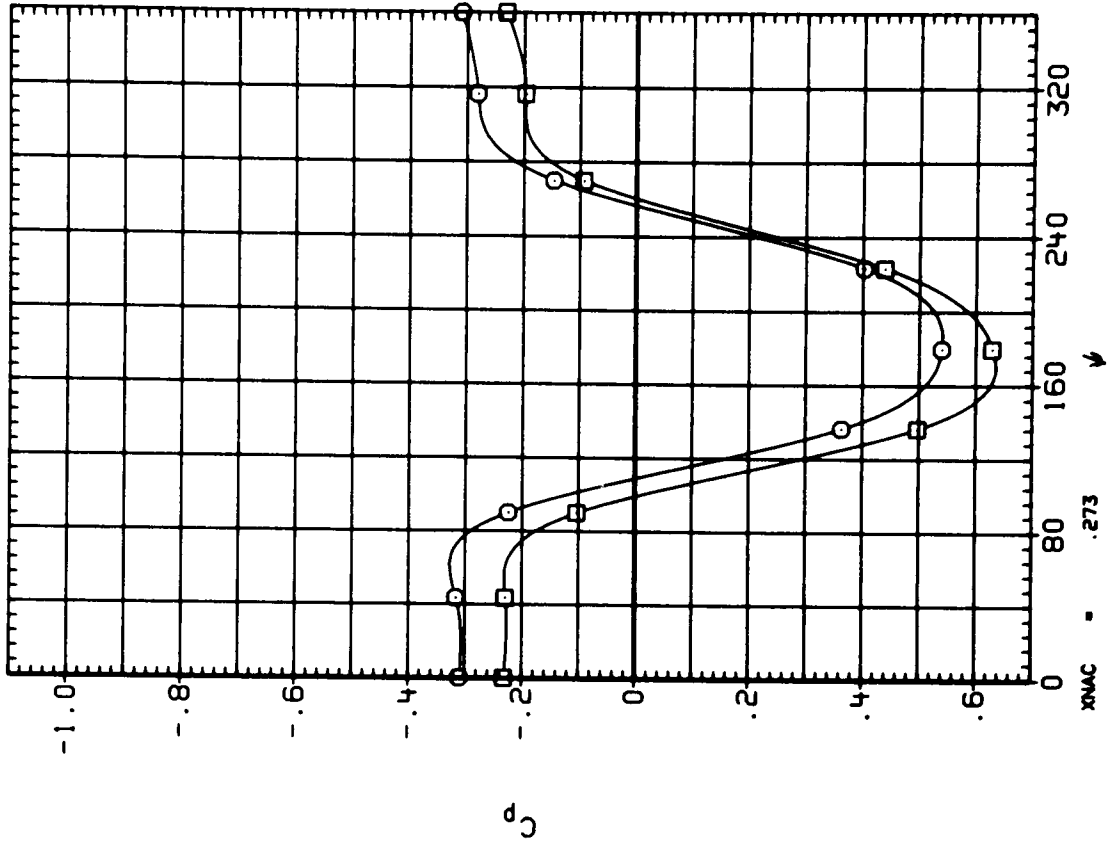
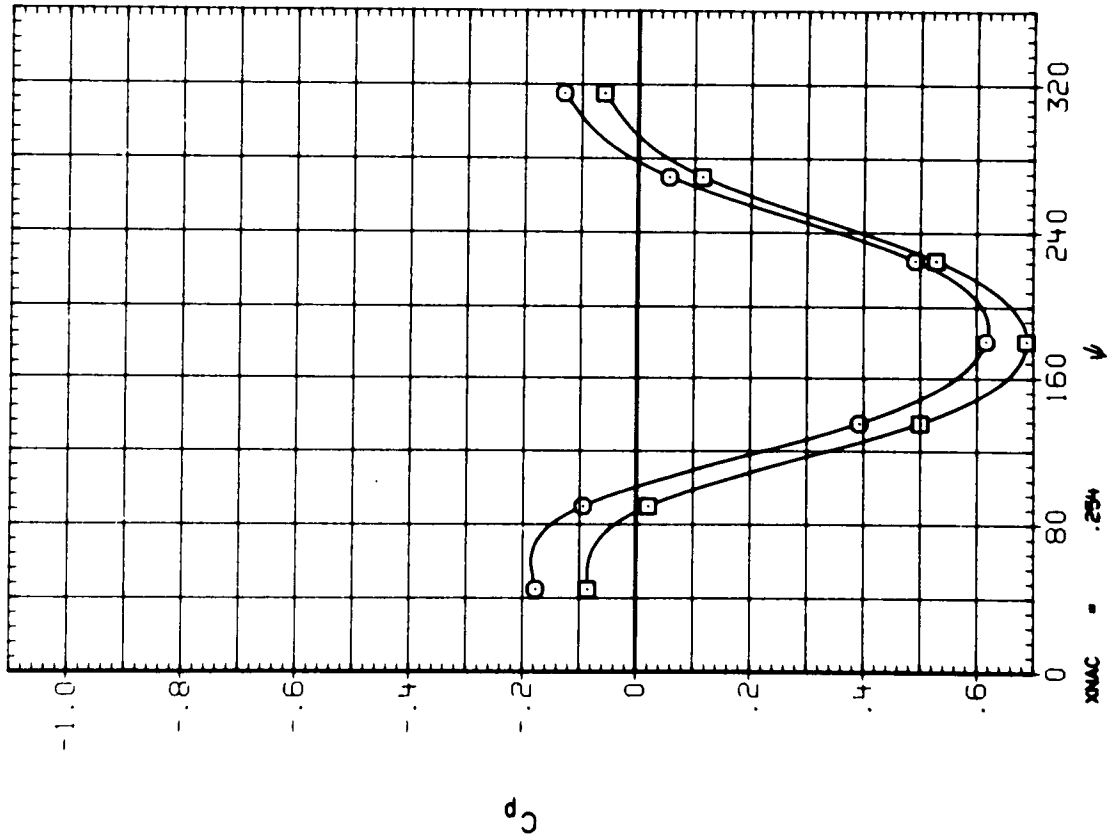


Figure 14.- Effect of power on nacelle pressures--baseline + LEX configuration;
M = 0.800.

SYMBOL CONFIGURATION DESCRIPTION

- HE/NLP
- HE/NLP

EPR	RPM	ALPHA	PITCH
1.003	6494	1.967	57.2
1.770	8494	1.963	57.2

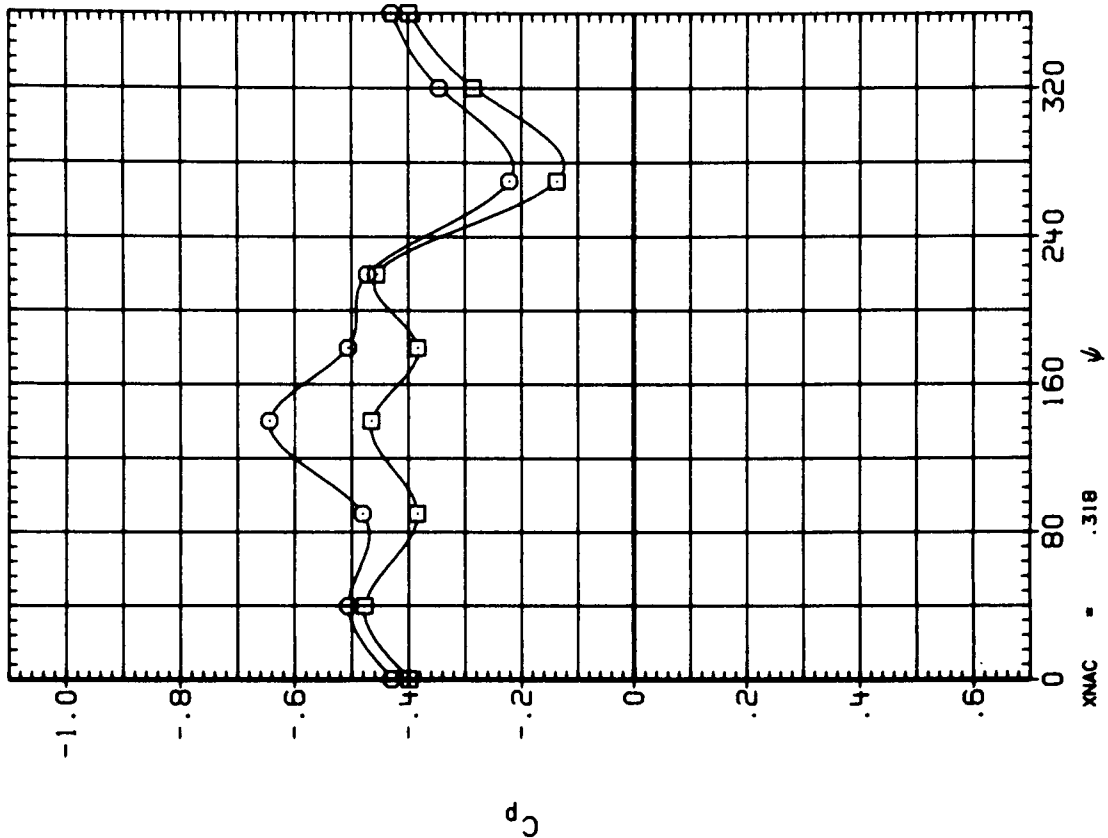
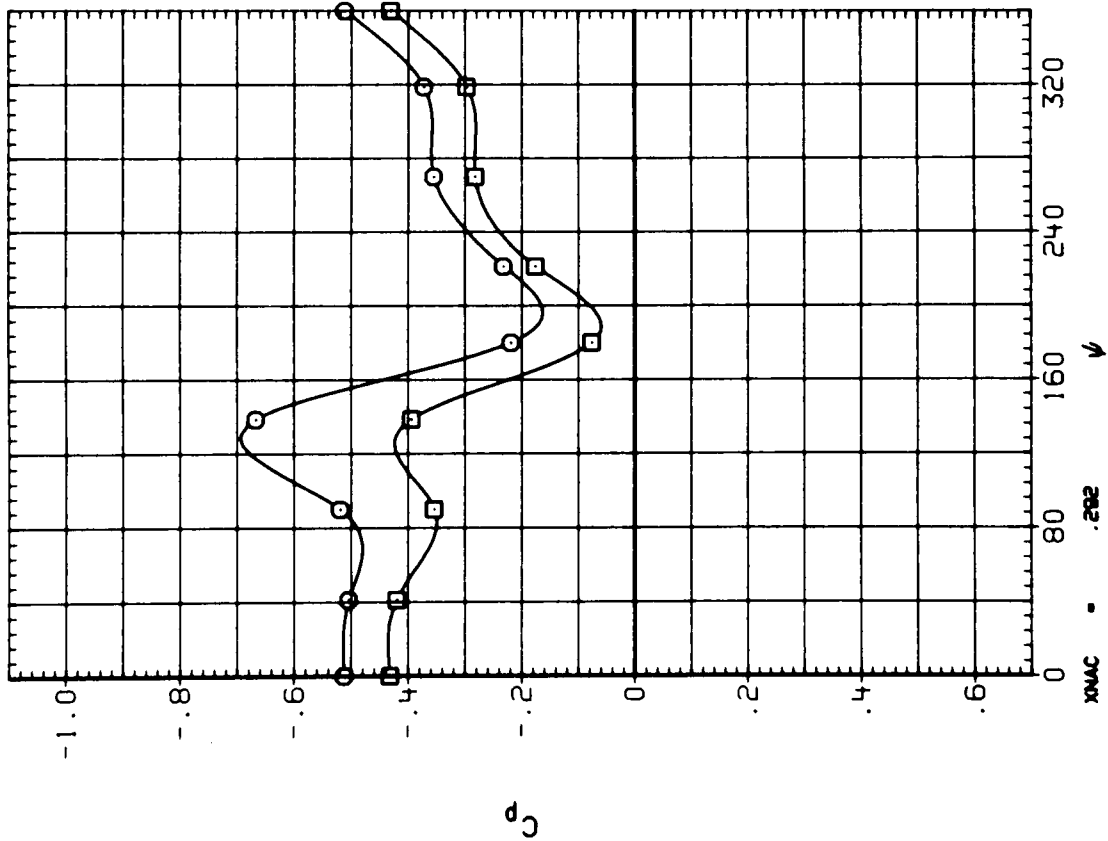


Figure 14.- Continued.

SYMBOL CONFIGURATION DESCRIPTION
 ○ HENLP
 □ HENLP

EPR 1.003 ALPHA 1.967 PITCH 57.2
 1.770 1.963 57.2

RPM 6494 6494

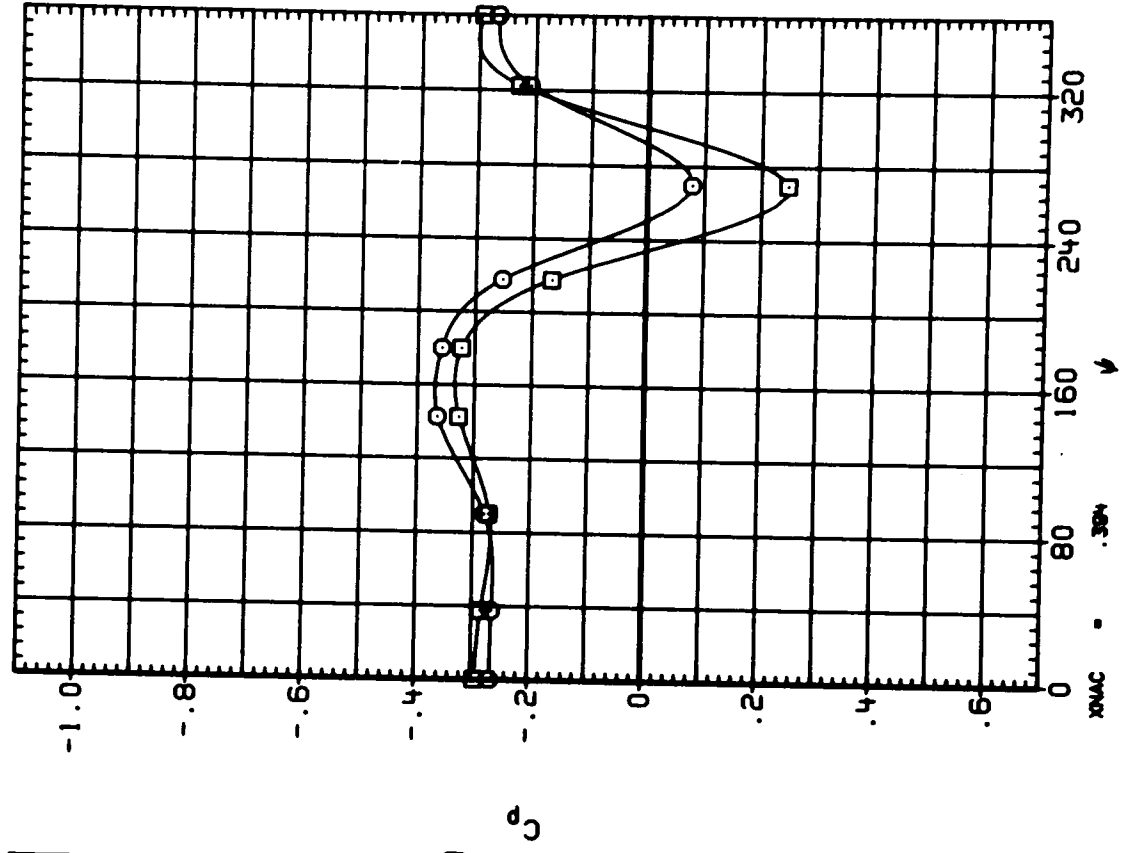
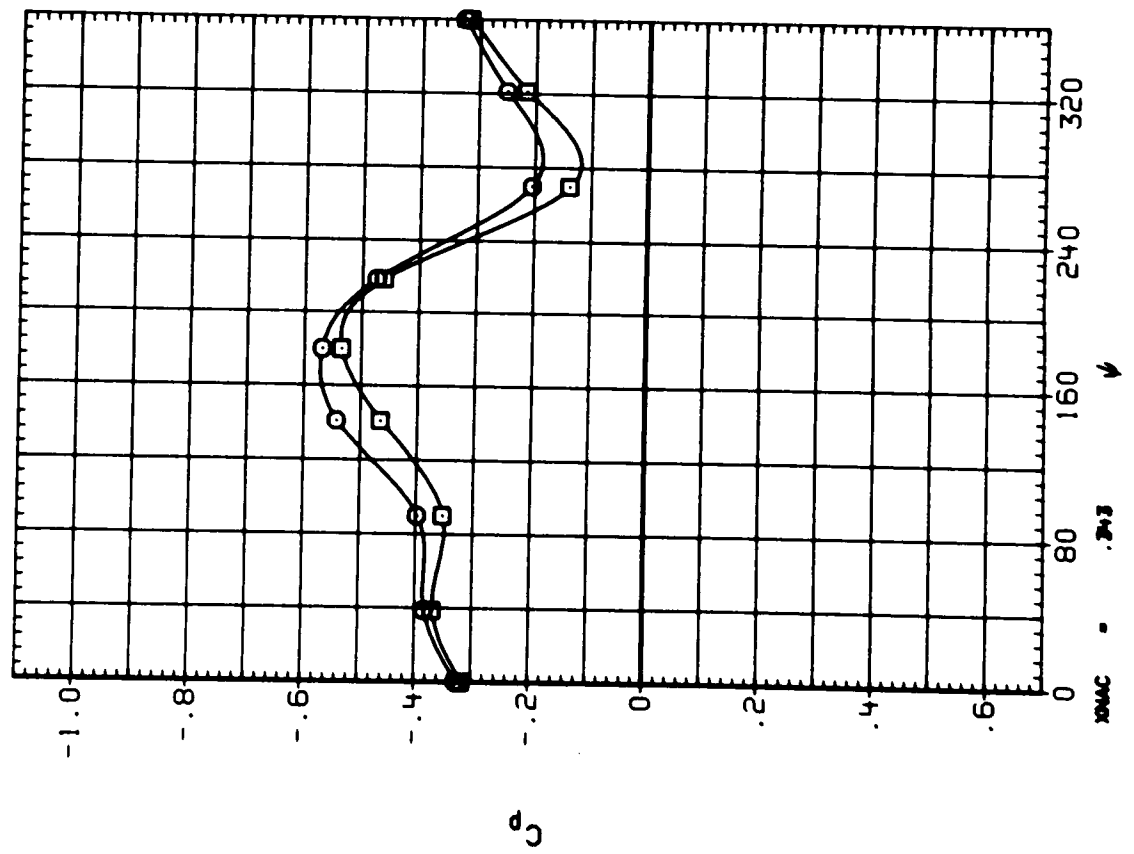


Figure 14.- Continued.

SYMBOL CONFIGURATION DESCRIPTION
 ○ HENLP
 □ HENLP

EPR RPM ALPHA PITCH
 1.003 8494 1.967 57.2
 1.770 8494 1.963 57.2

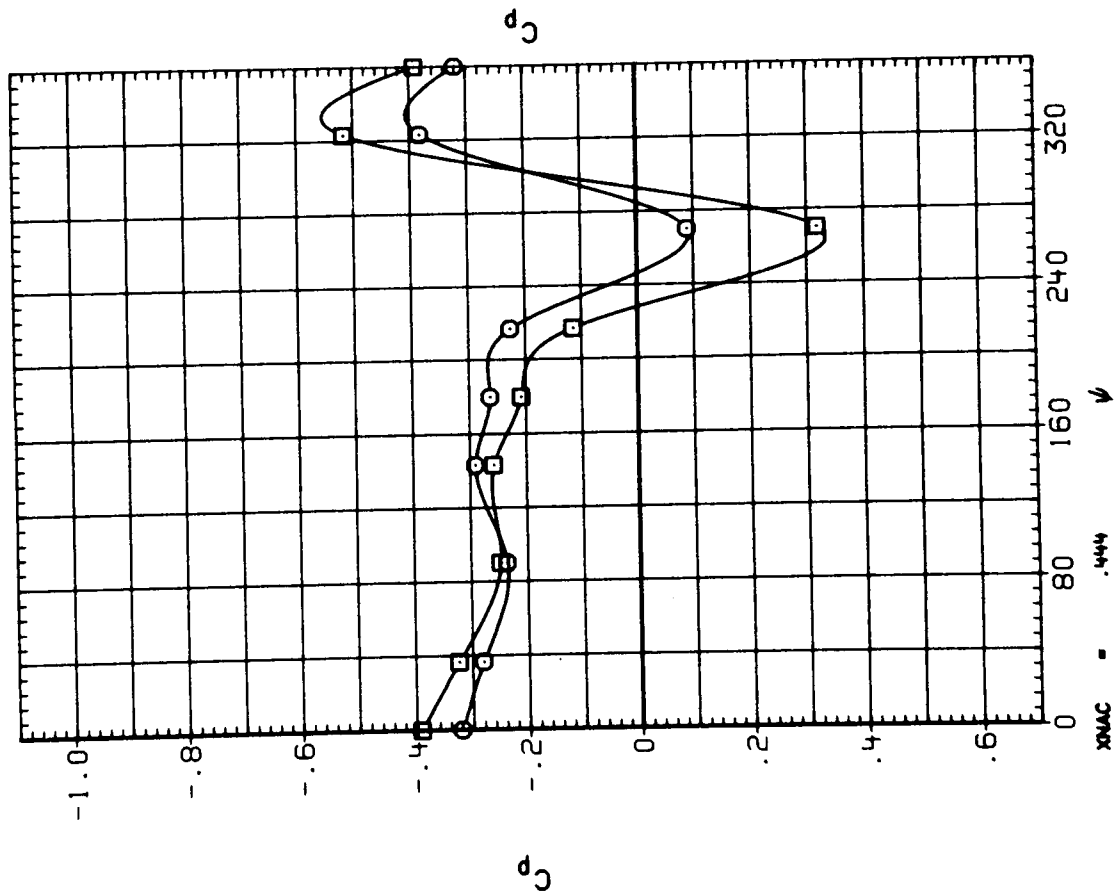
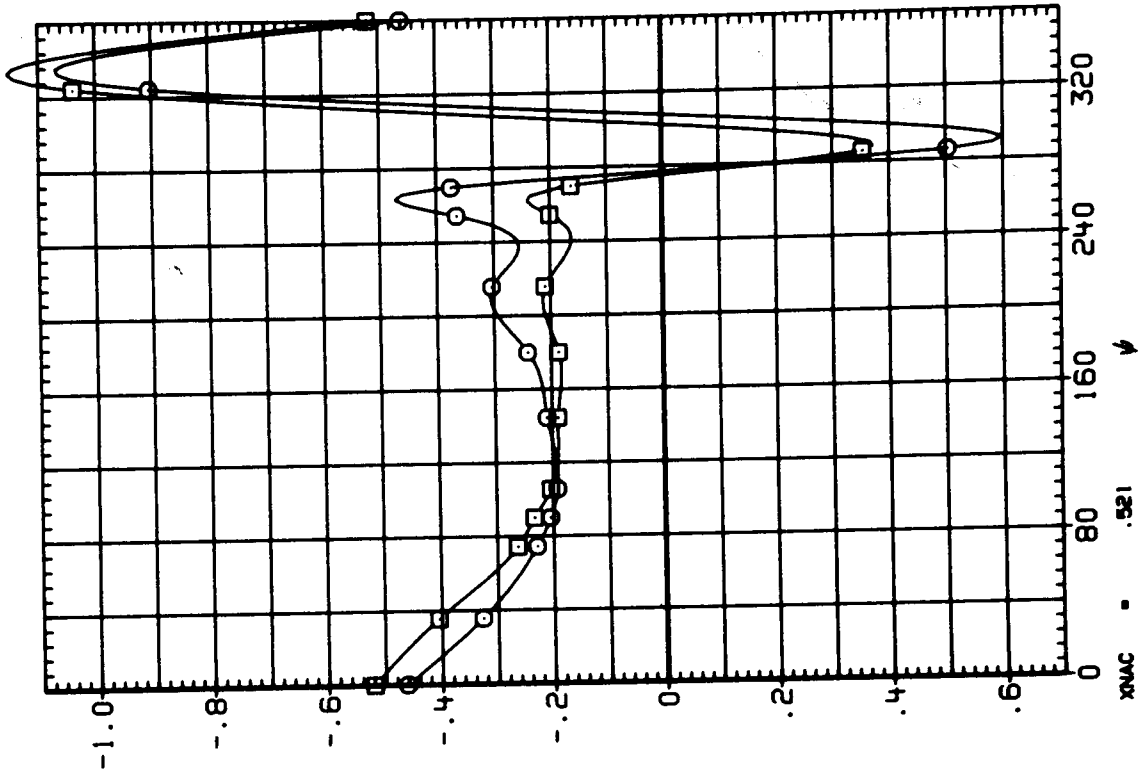


Figure 14.- Continued.

SYMBOL CONFIGURATION DESCRIPTION

- MBNLP
- MBNLP

EPR 1.003
1.770

RPM 6494
8494

ALPHA 1.967
1.963

PITCH 57.2
57.2

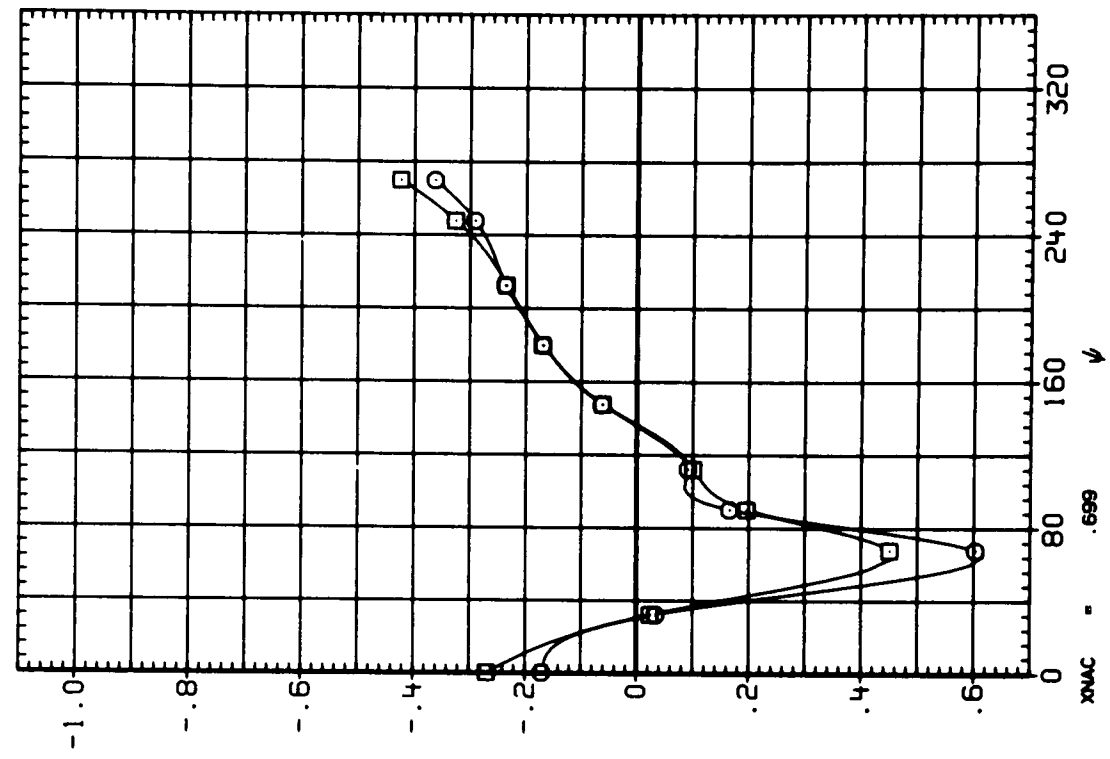
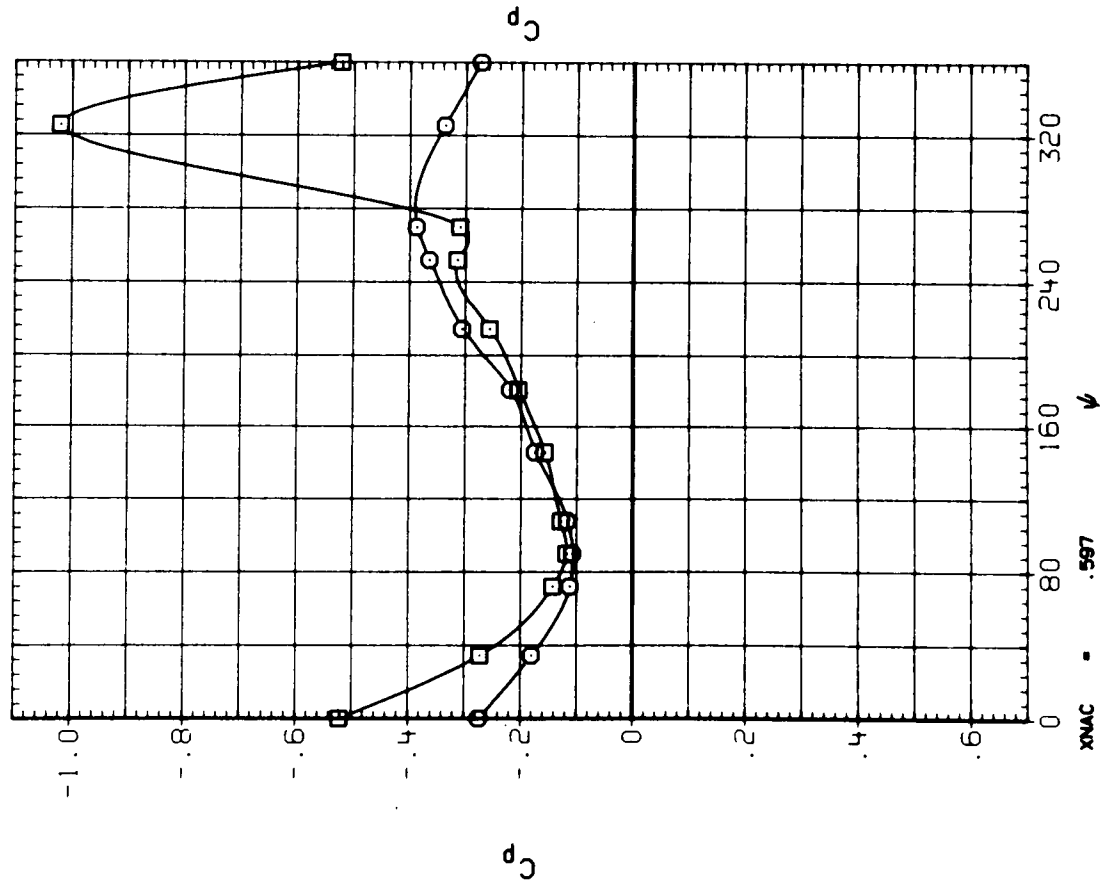


Figure 14.- Continued.

SYMBOL CONFIGURATION DESCRIPTION
 ○ HB/NLP
 □ HB/NLP

EPR RPM ALPHA PITCH
 1.003 8494 1.967 57.2
 1.770 8494 1.963 57.2

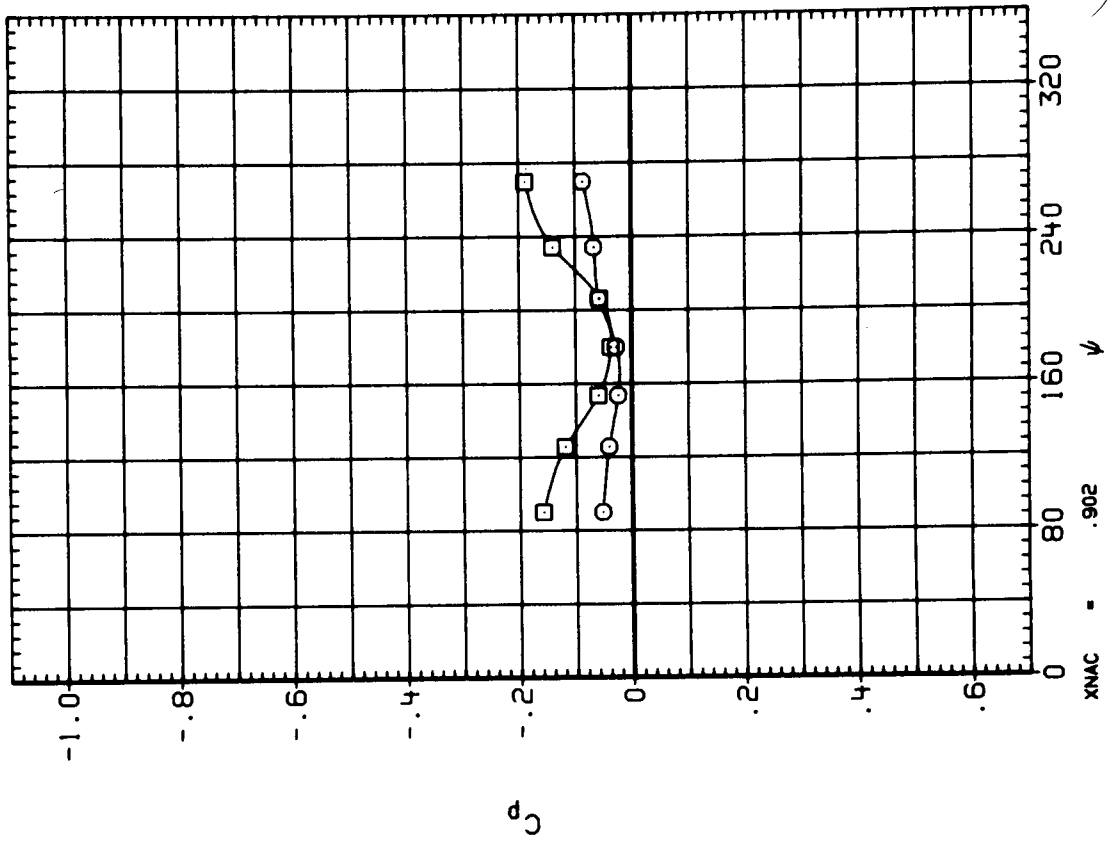
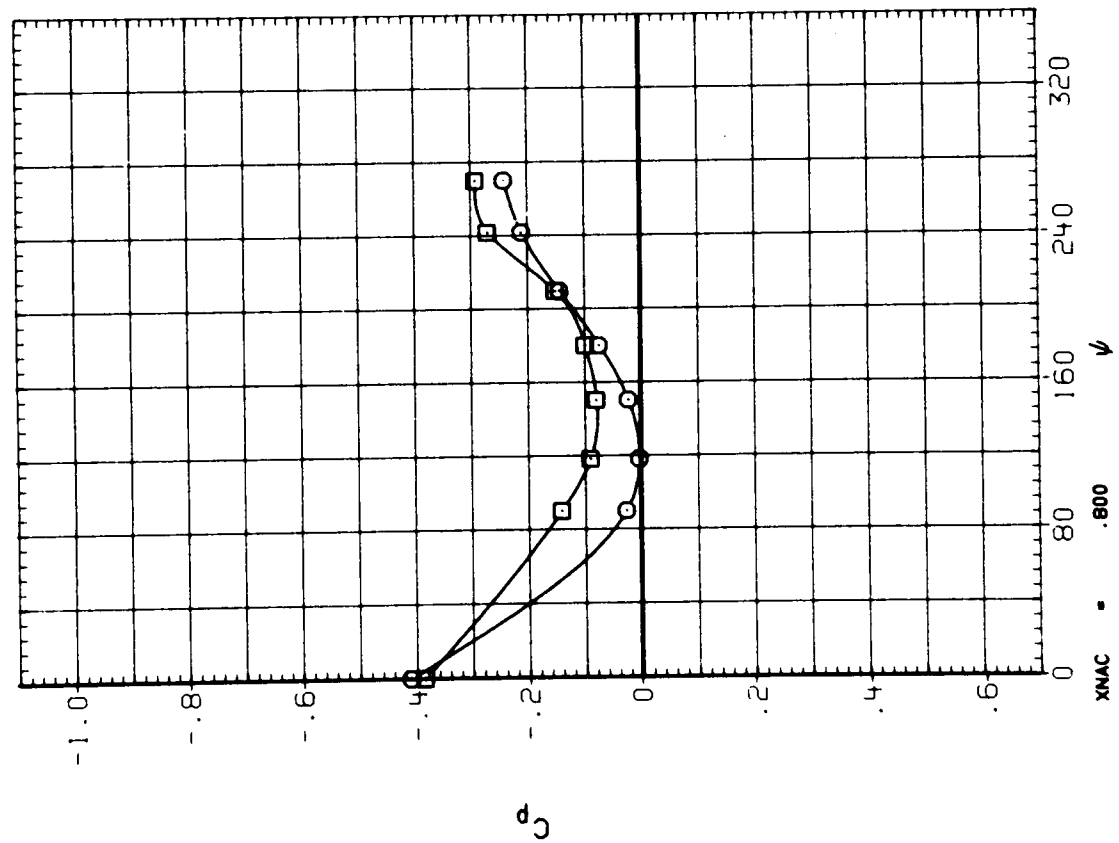


Figure 14.- Concluded.

SYMBOL CONFIGURATION DESCRIPTION
 ○ MBNLF3SP
 □ MBNLF3P

EPR 1.000 ALPHA 1.972 PITCH 57.2
 1.725 1.945 57.2

RPM 6446
 8466

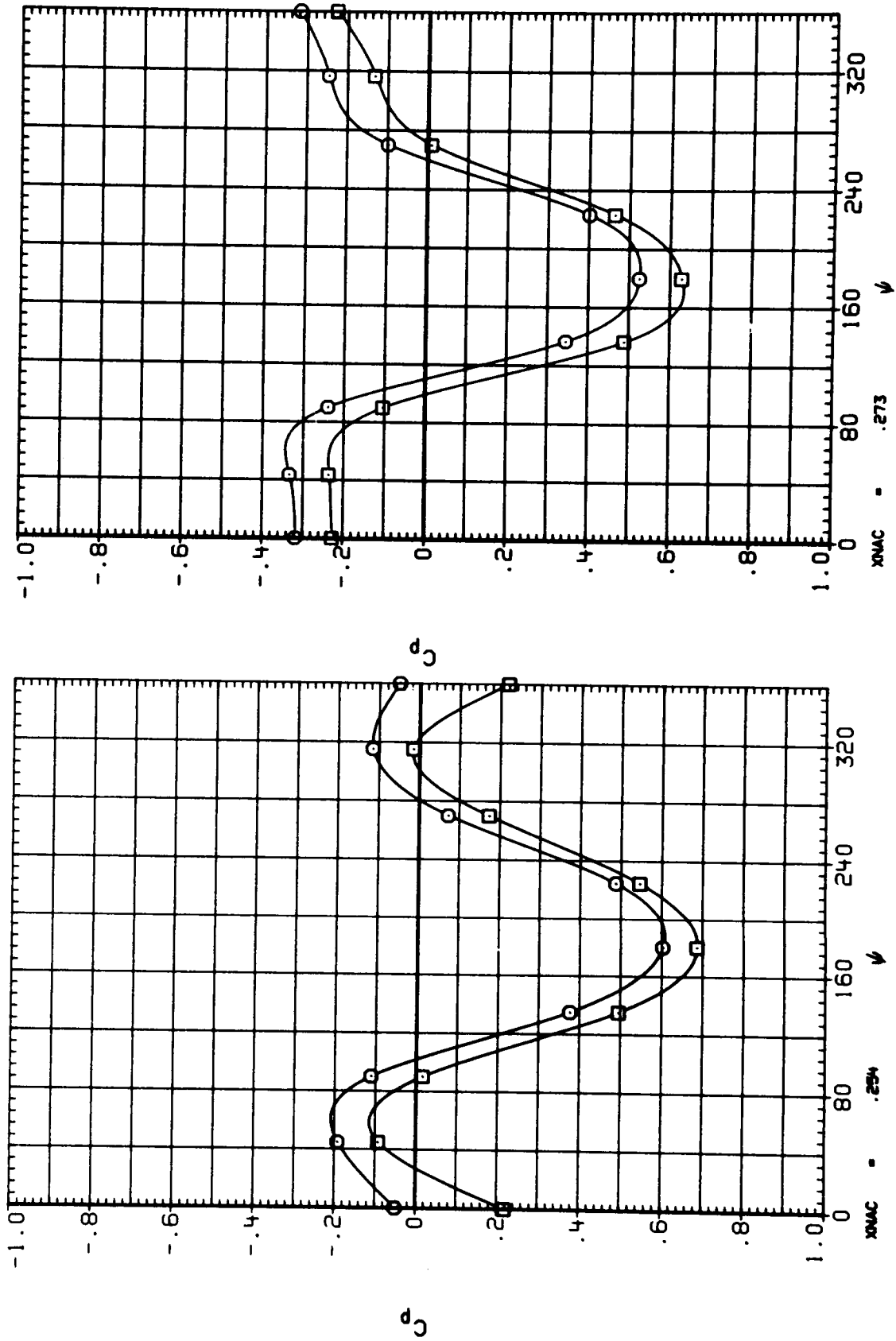


Figure 15.- Effect of power on nacelle pressures--baseline + LEX, fillet, and strake configuration; $M = 0.808$.

SYMBOL CONFIGURATION DESCRIPTION
 ○ HEALF3SP
 □ HEALF3SP

EPR RPM ALPHA PITCH
 1.000 6446 1.972 57.2
 1.725 8486 1.945 57.2

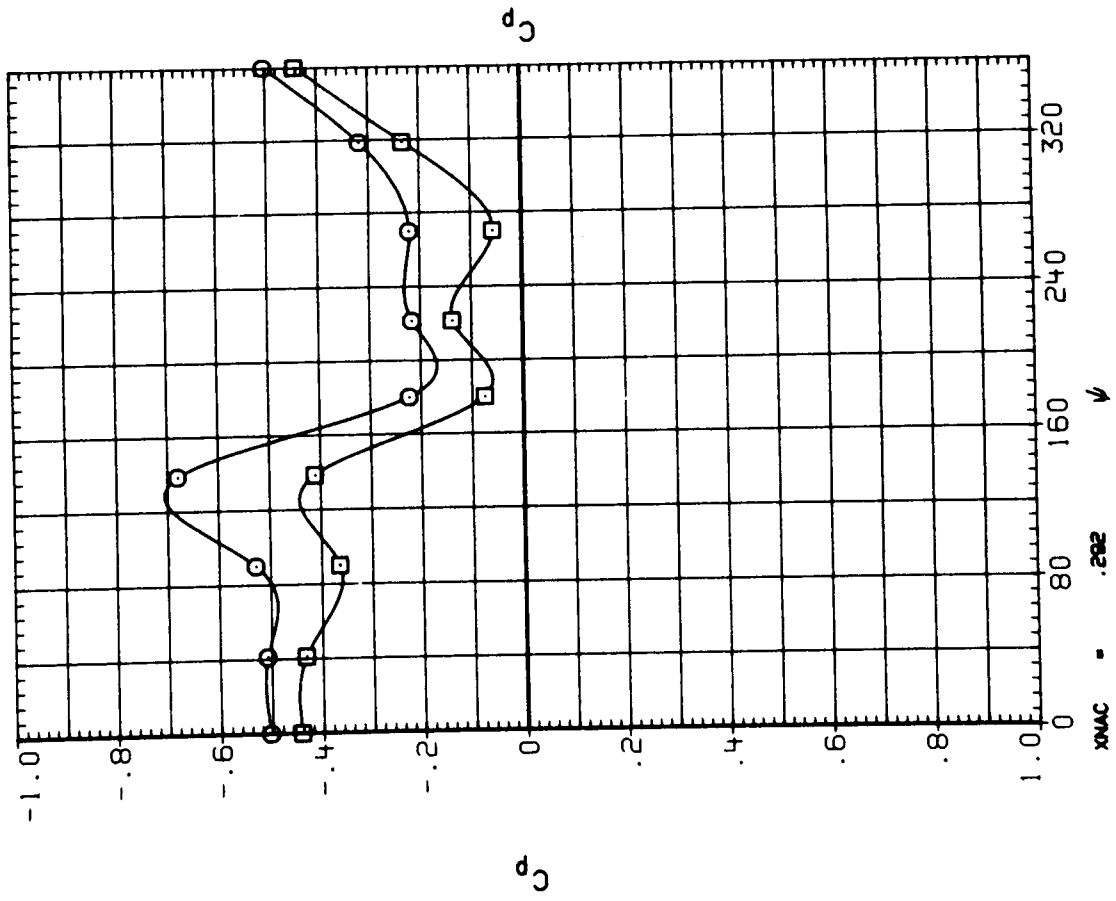
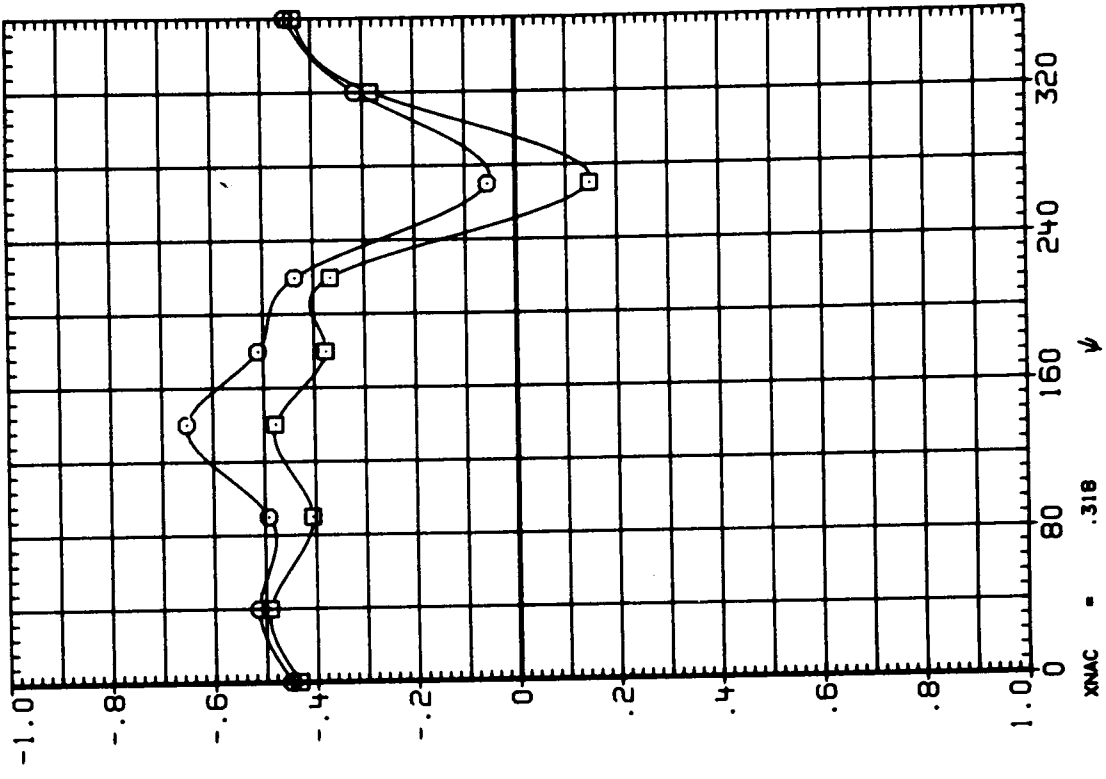


Figure 15.- Continued.

SYMBOL CONFIGURATION DESCRIPTION
 ○ WBNLF3SP
 □ WBNLF3SP

EPR RPM ALPHA PITCH
 1.000 8446 1.972 57.2
 1.725 8486 1.945 57.2

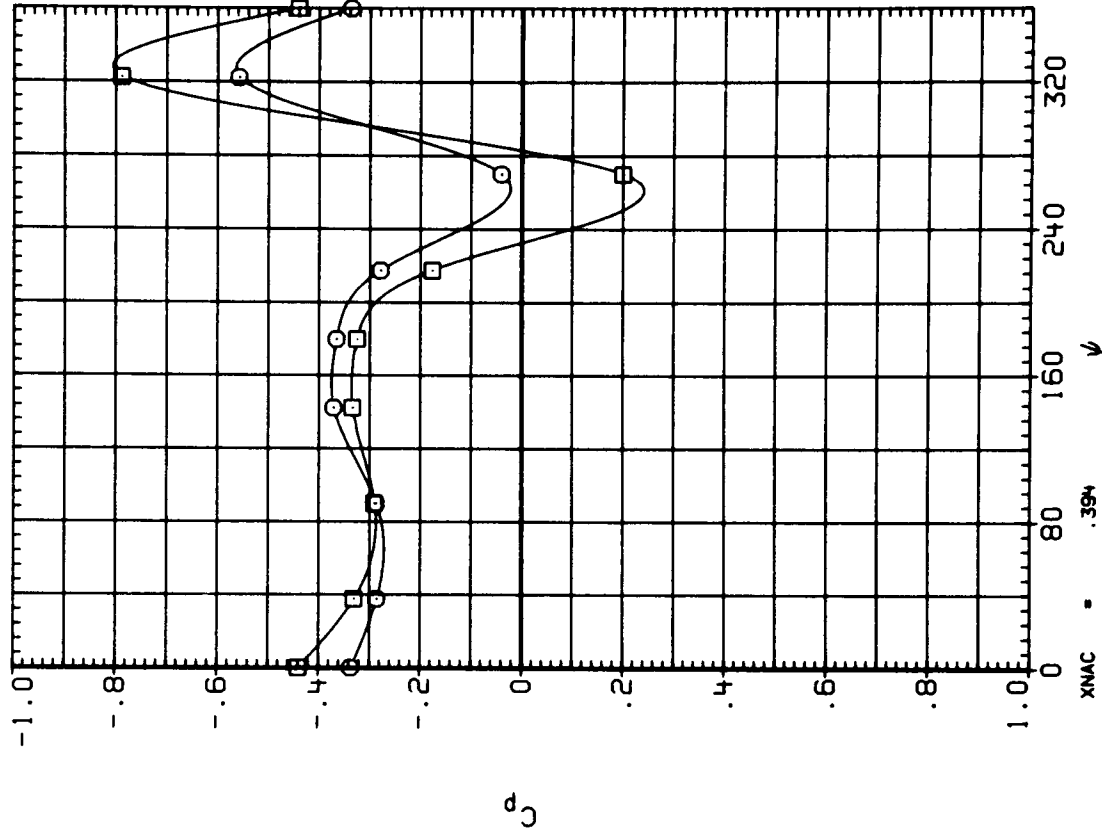
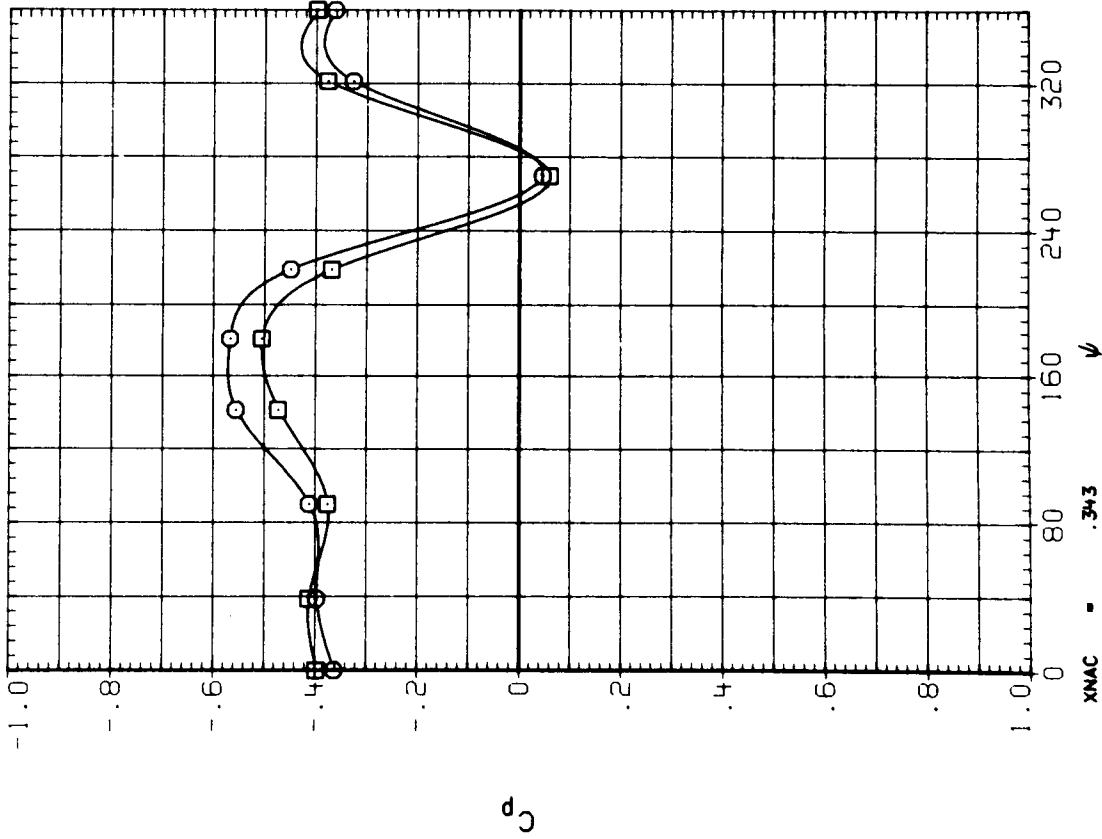


Figure 15.- Continued.

SYMBOL CONFIGURATION DESCRIPTION
 ○ WBNLF 3SP
 □ WBNLF 3SP

EPR RPM ALPHA PITCH
 1.000 6446 1.972 57.2
 1.725 8486 1.945 57.2

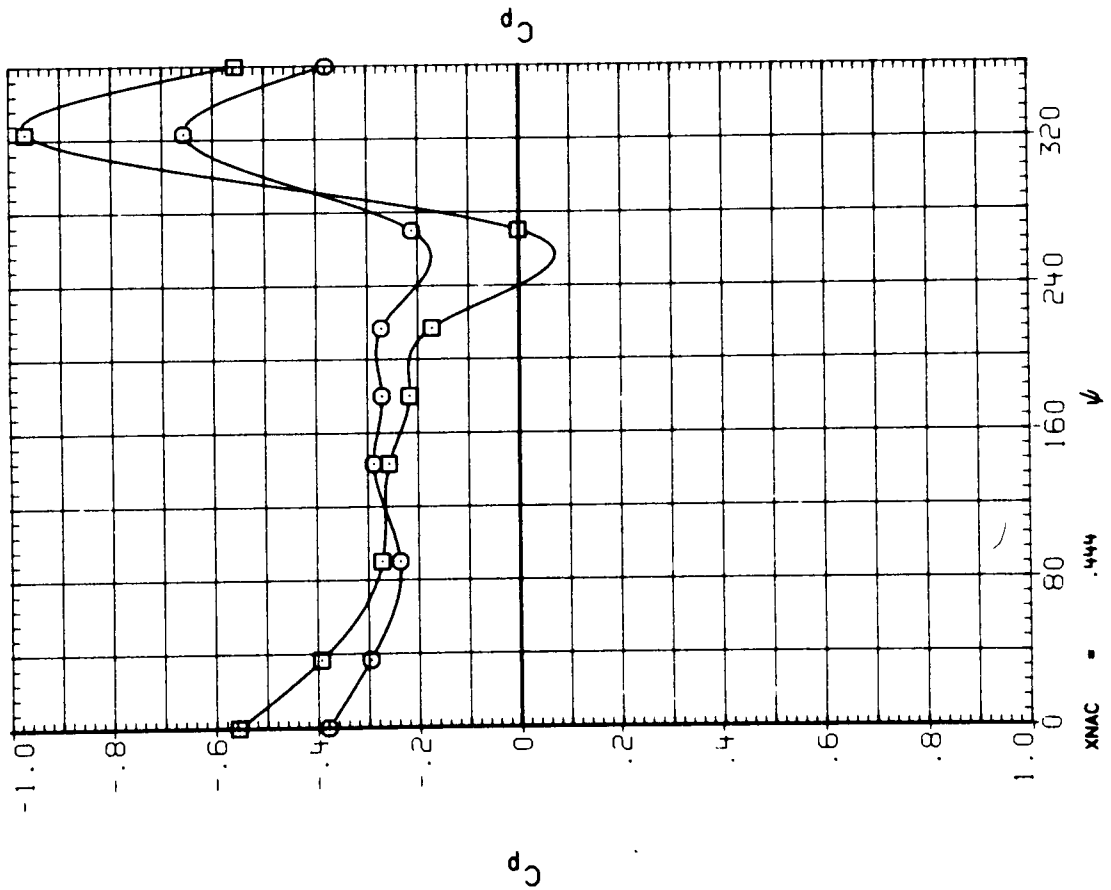
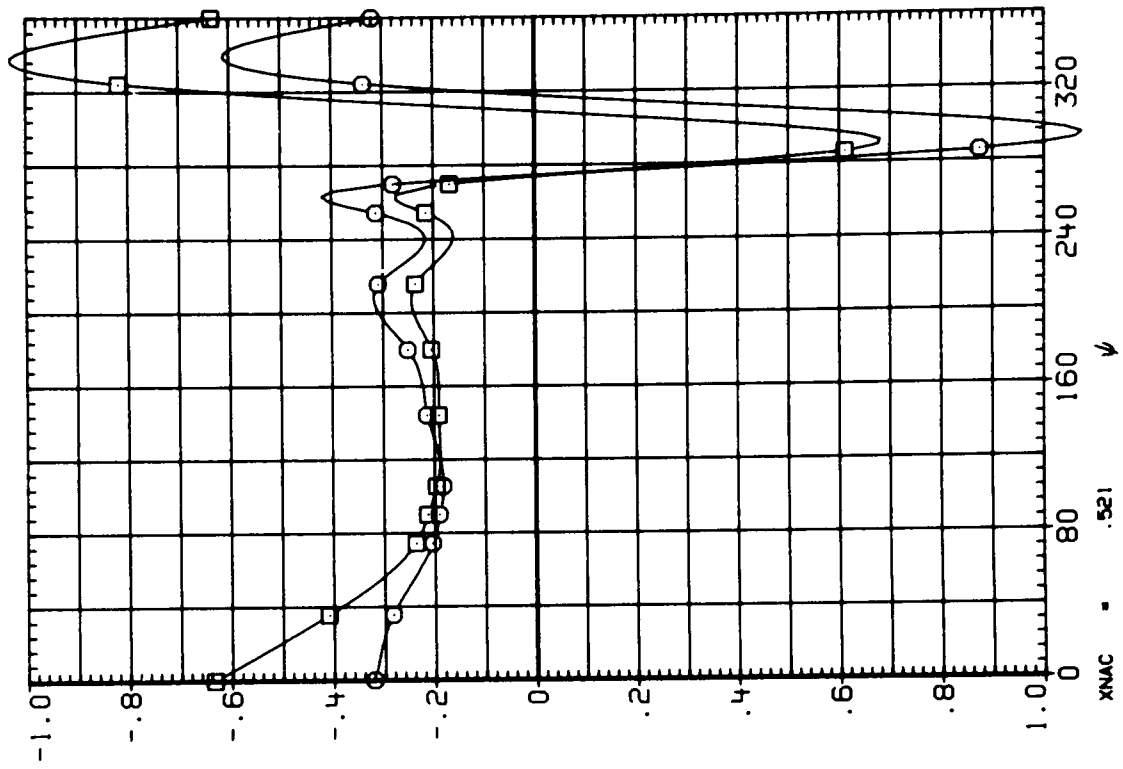


Figure 15.- Continued.

SYMBOL CONFIGURATION DESCRIPTION
 ○ HBNLF33P
 □ HBNLF33P

EPR RPM ALPHA PITCH
 1.000 6446 1.972 57.2
 1.725 8486 1.945 57.2

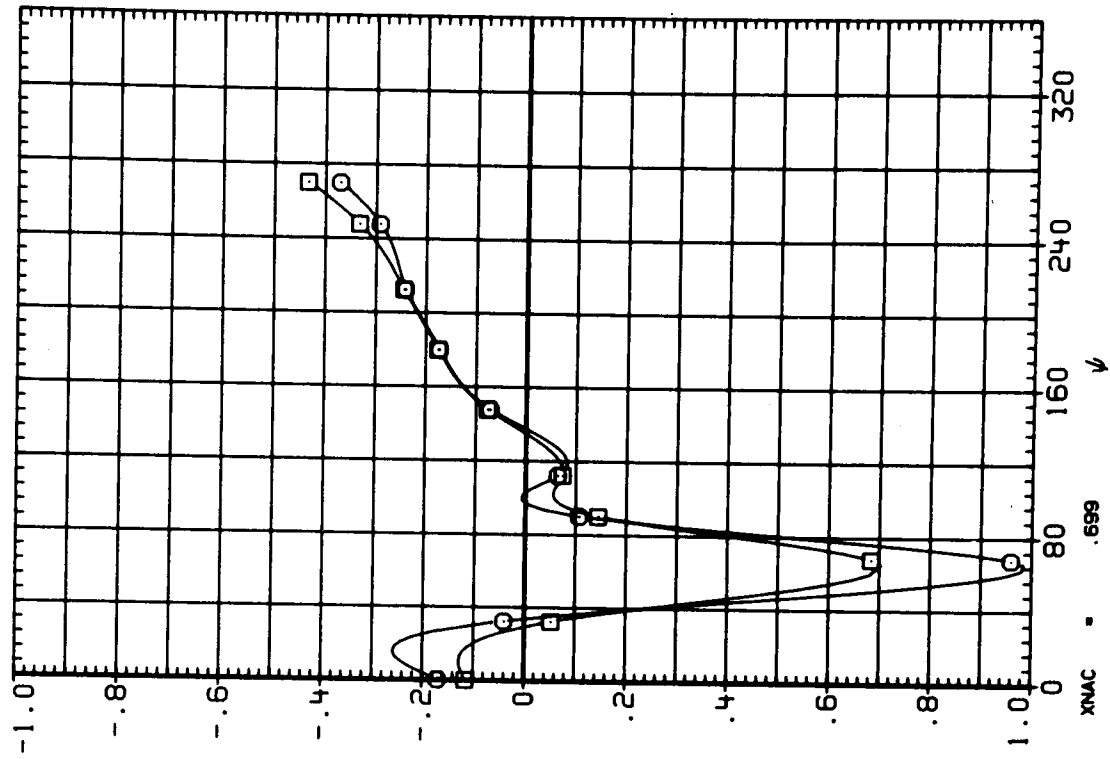
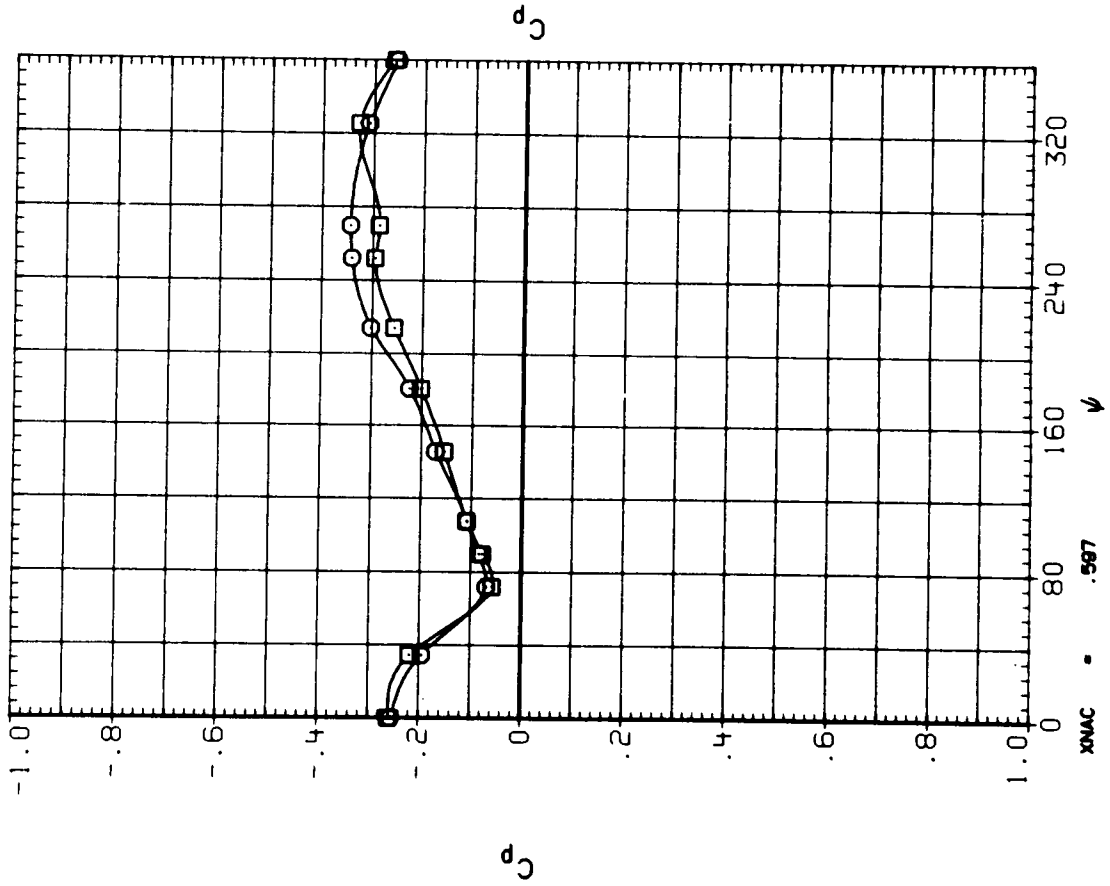


Figure 15.- Continued.

SYMBOL CONFIGURATION DESCRIPTION
 ○ HBNLF 3SP
 □ HBNLF 3SP

EPR 1.000 1.725
 RPM 6446 8486
 ALPHA 1.972 1.945
 PITCH 57.2 57.2

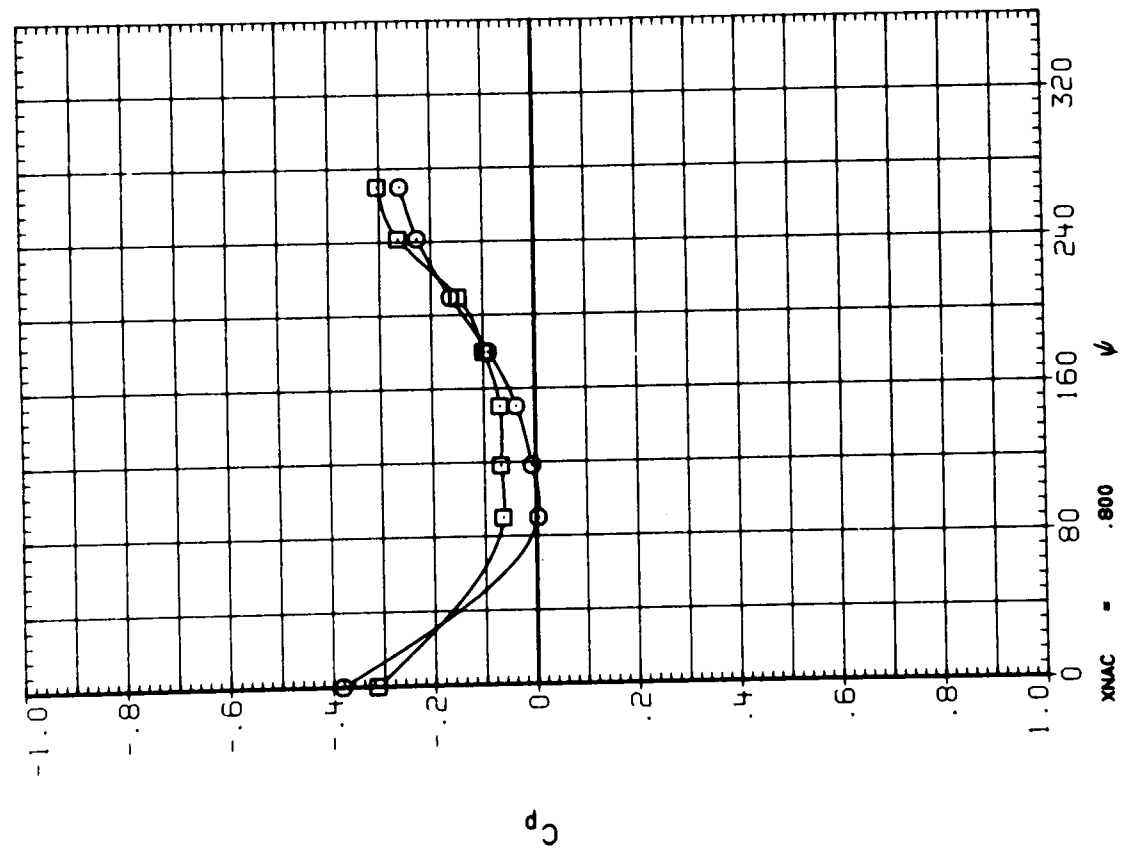
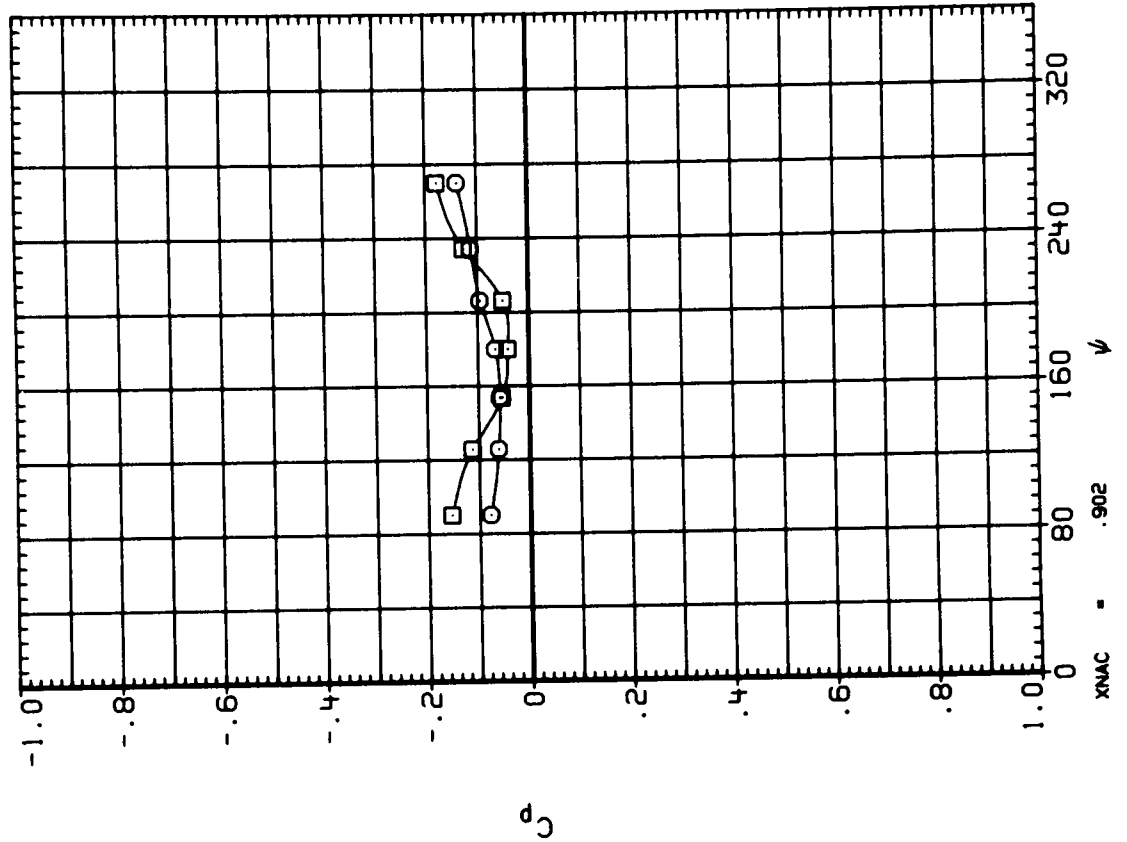
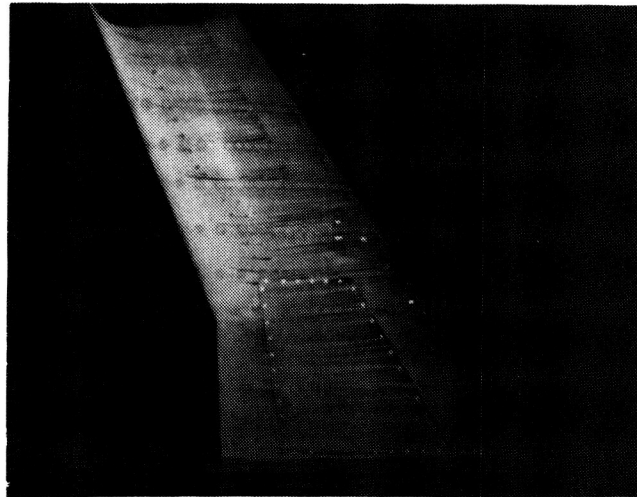


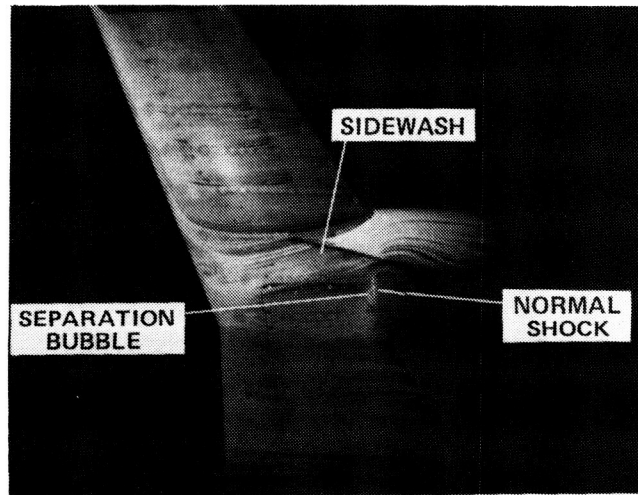
Figure 15.- Concluded.

ORIGINAL PAGE IS
OF POOR QUALITY

ORIGINAL PAGE IS
OF POOR QUALITY



(a) Wing; upper surface.

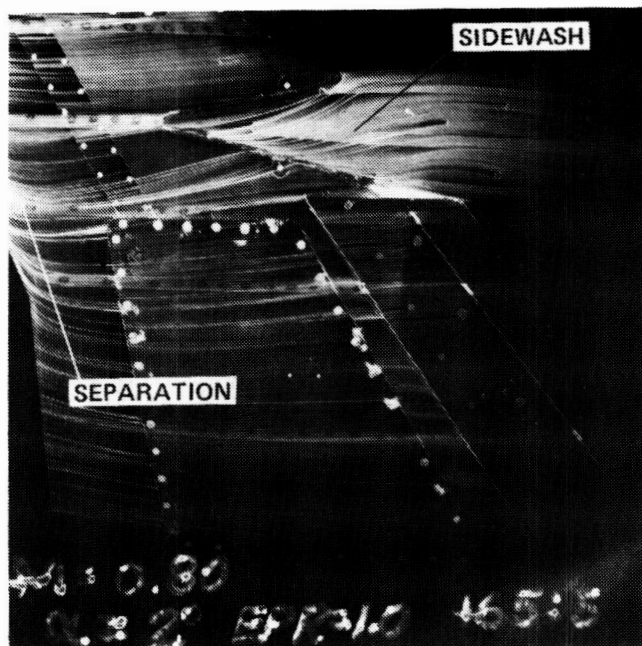


(b) Wing/nacelle; upper surface.

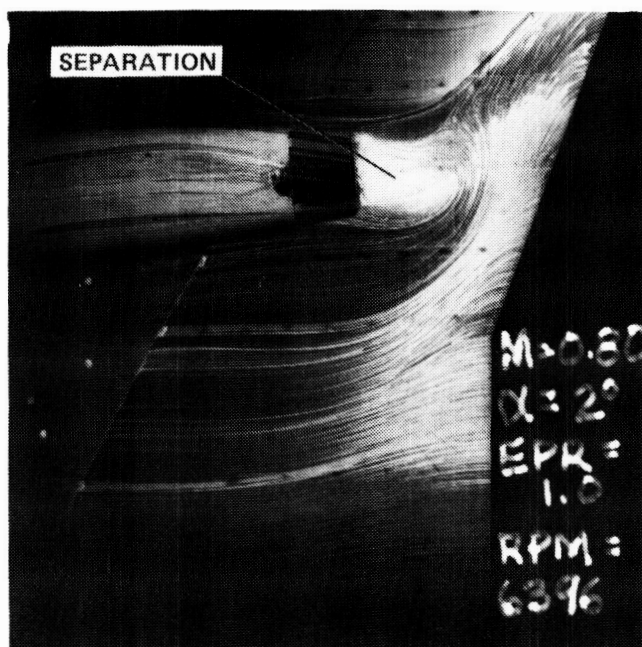
Figure 16.- Oil flow visualization; $M = 0.8$, $\alpha = 2^\circ$.



ORIGINAL PAGE IS
OF POOR QUALITY



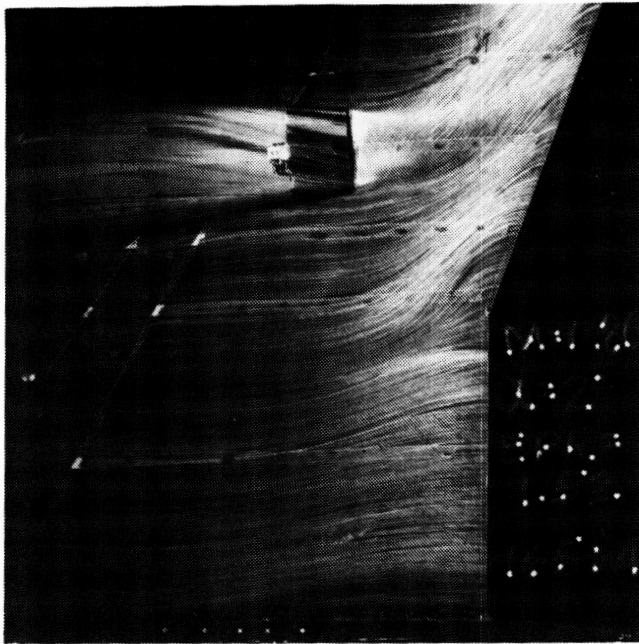
(c) WBNL; upper surface, jet off.



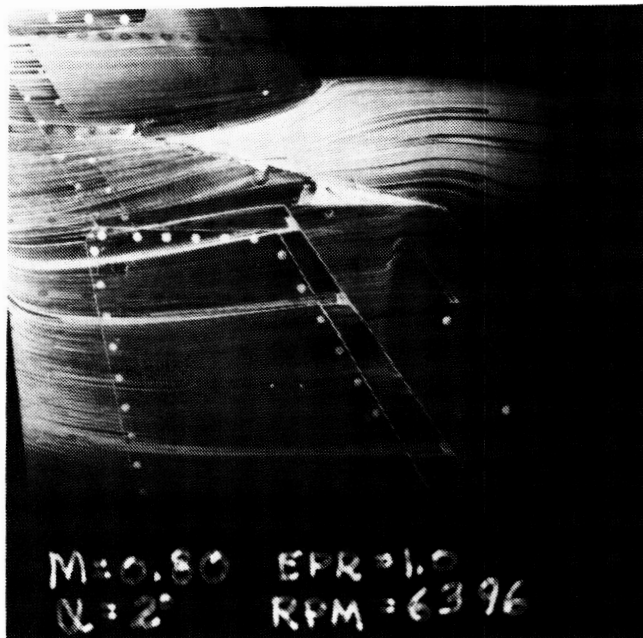
(d) WBNLP; lower surface, jet off.

Figure 16.- Continued.

ORIGINAL PAGE IS
OF POOR QUALITY

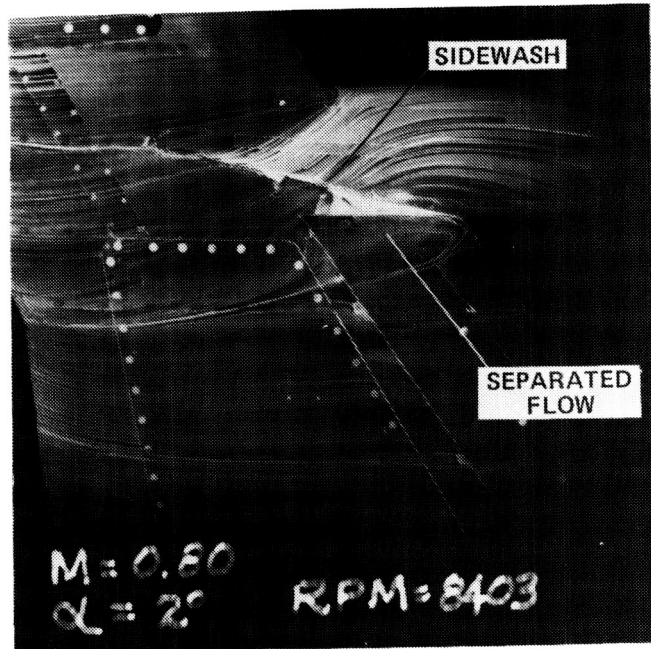


(e) WBNL; lower surface, jet on.

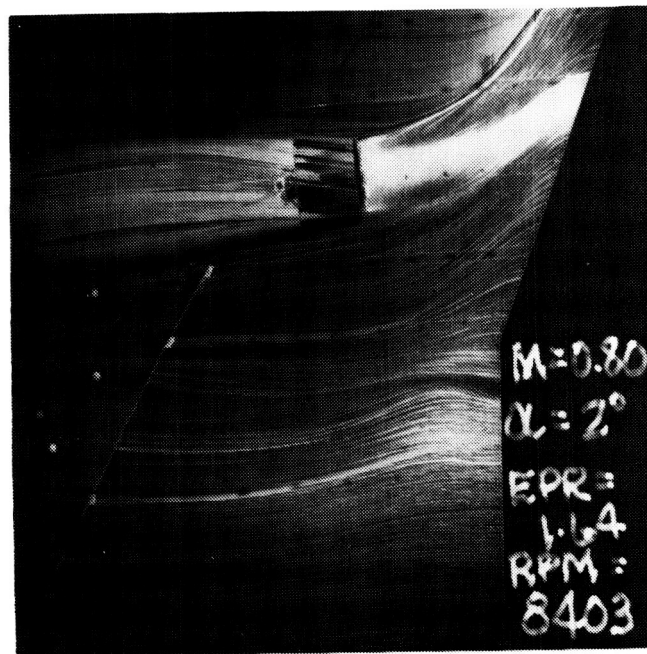


(f) WBNLP; upper surface, windmill.

Figure 16.- Continued.

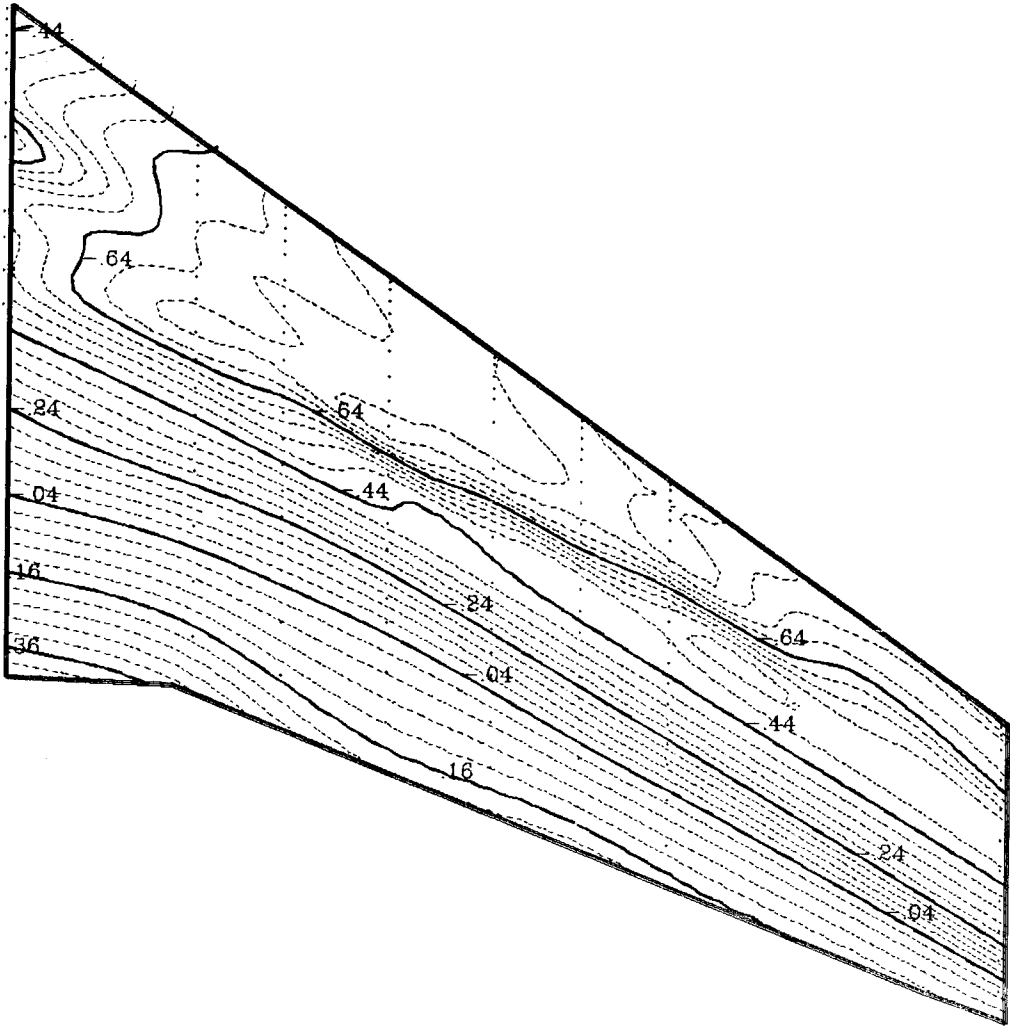


(g) WBNLP; upper surface, cruise power.



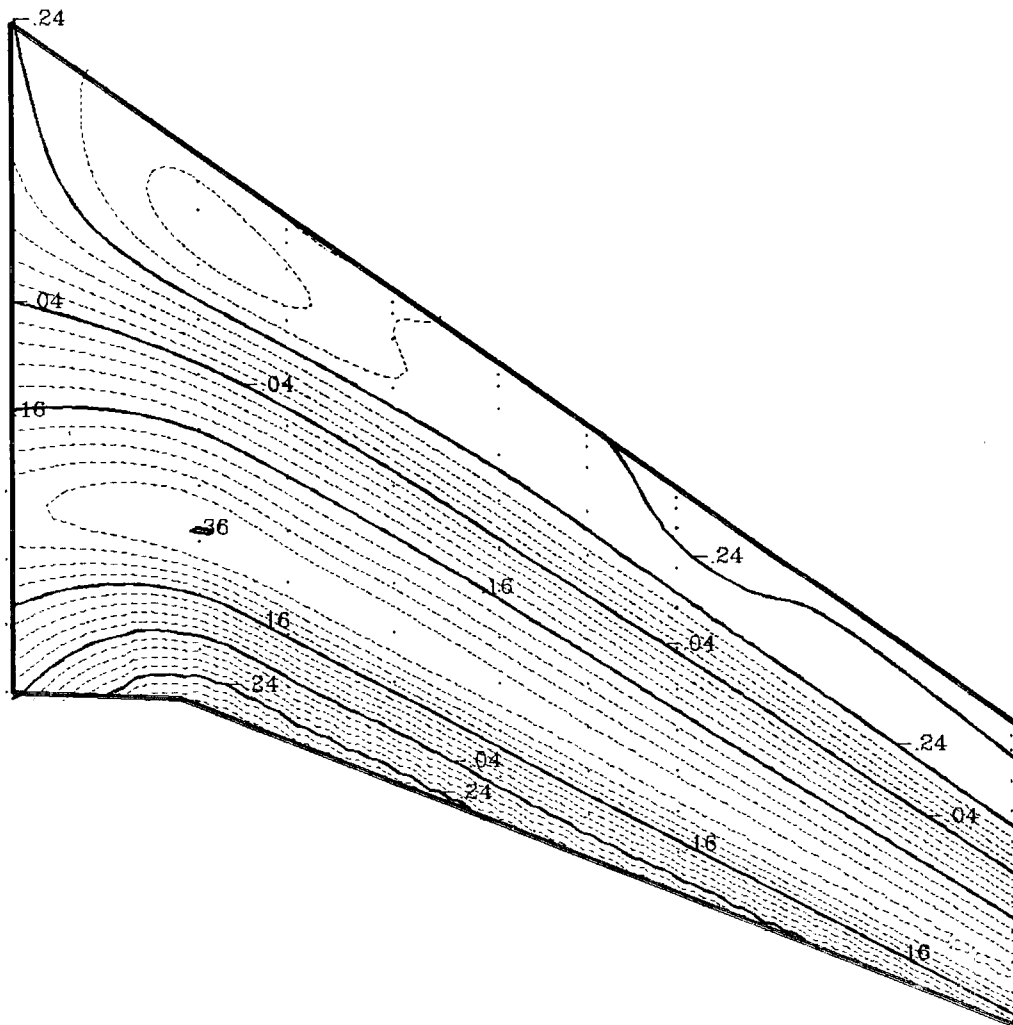
(h) WBNLP; lower surface, cruise power.

Figure 16.- Concluded.



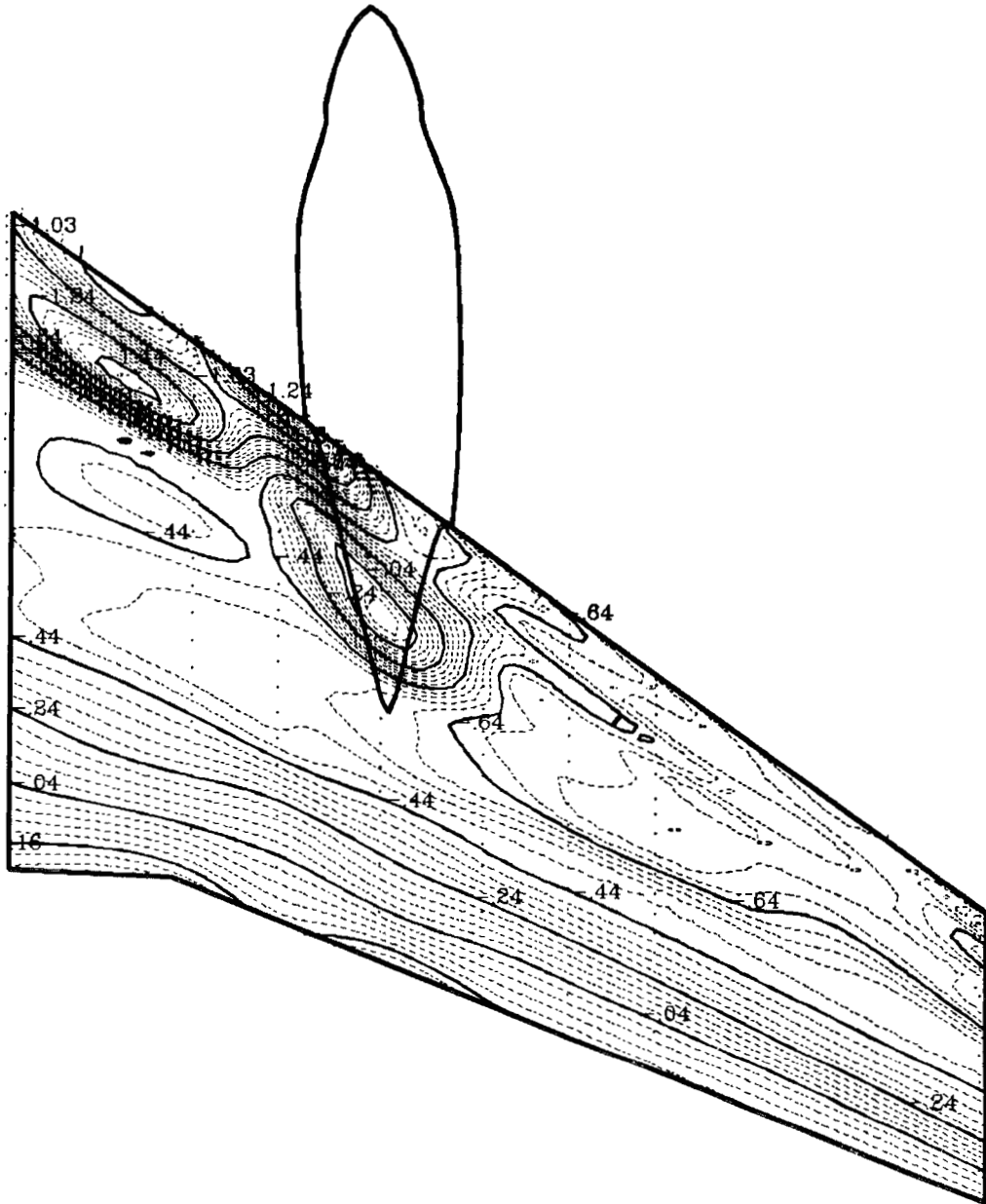
(a) Wing-body, upper surface; $M = 0.80$, $\alpha = 1.99^\circ$.

Figure 17.- Propeller-off pressure isobars.



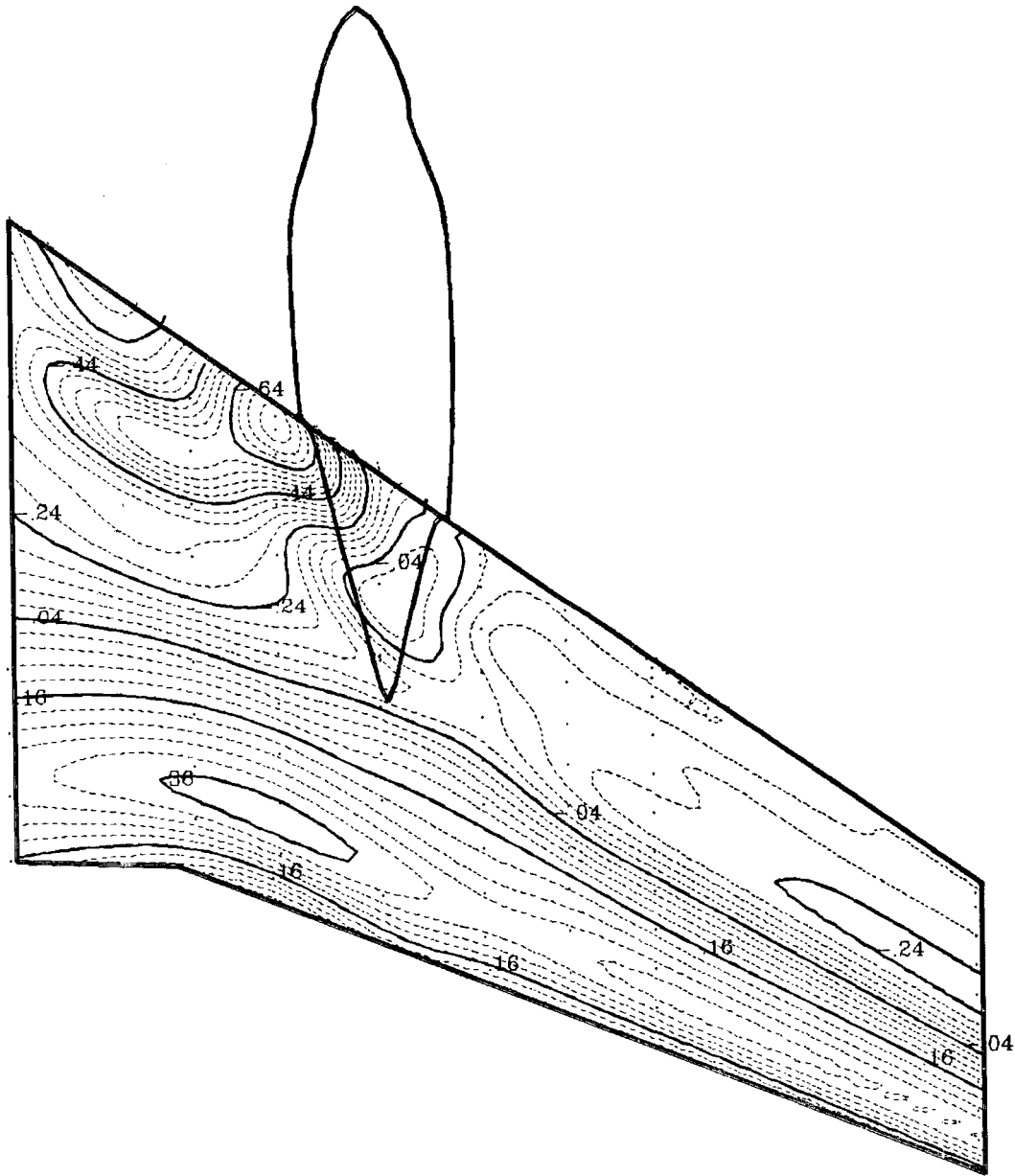
(b) Wing-body, lower surface; $M = 0.80$, $\alpha = 1.99^\circ$.

Figure 17.- Continued.



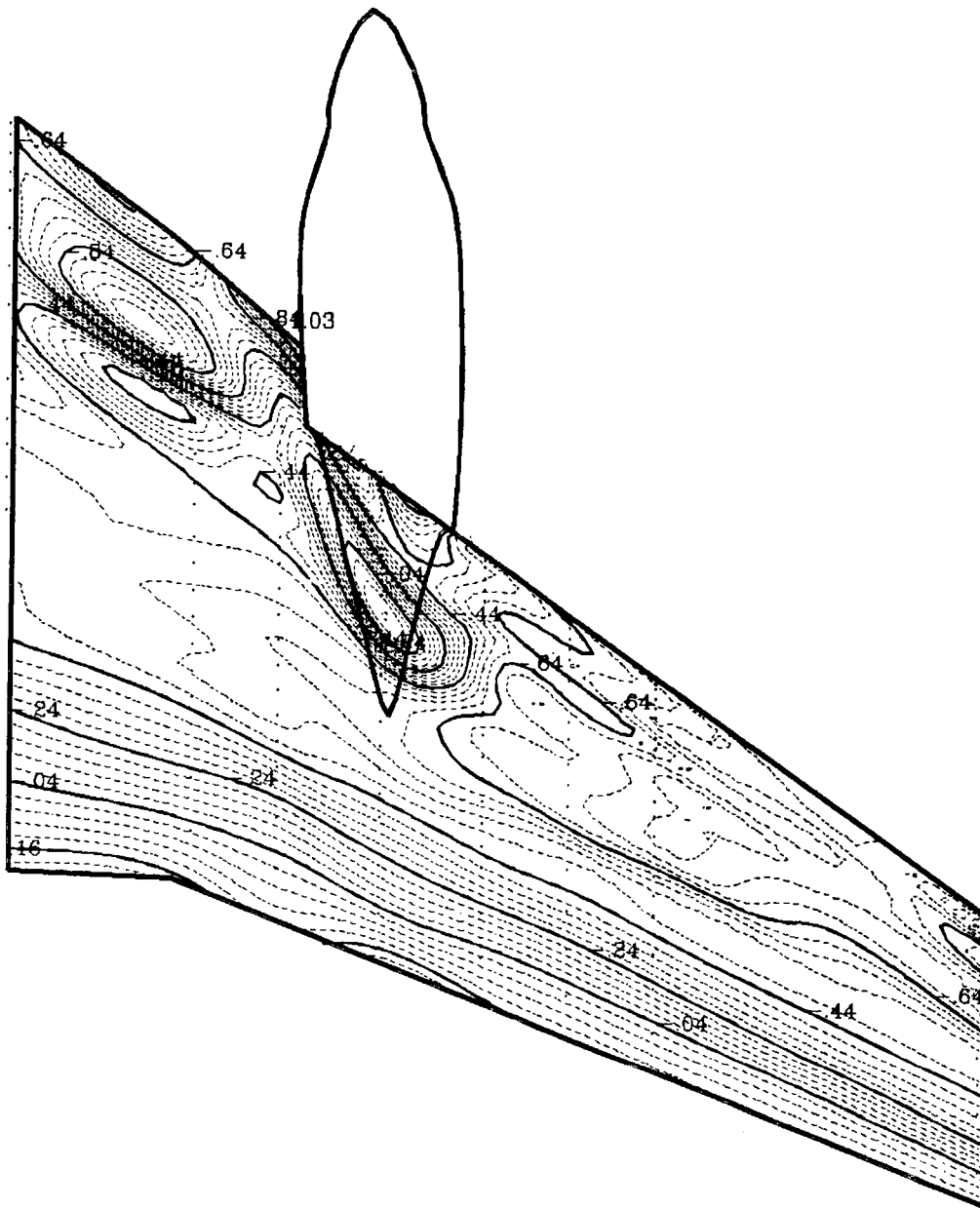
(c) Wing-body-nacelle, upper surface; $M = 0.80$, $\alpha = 1.95^\circ$, $EPR = 1.68$.

Figure 17.- Continued.



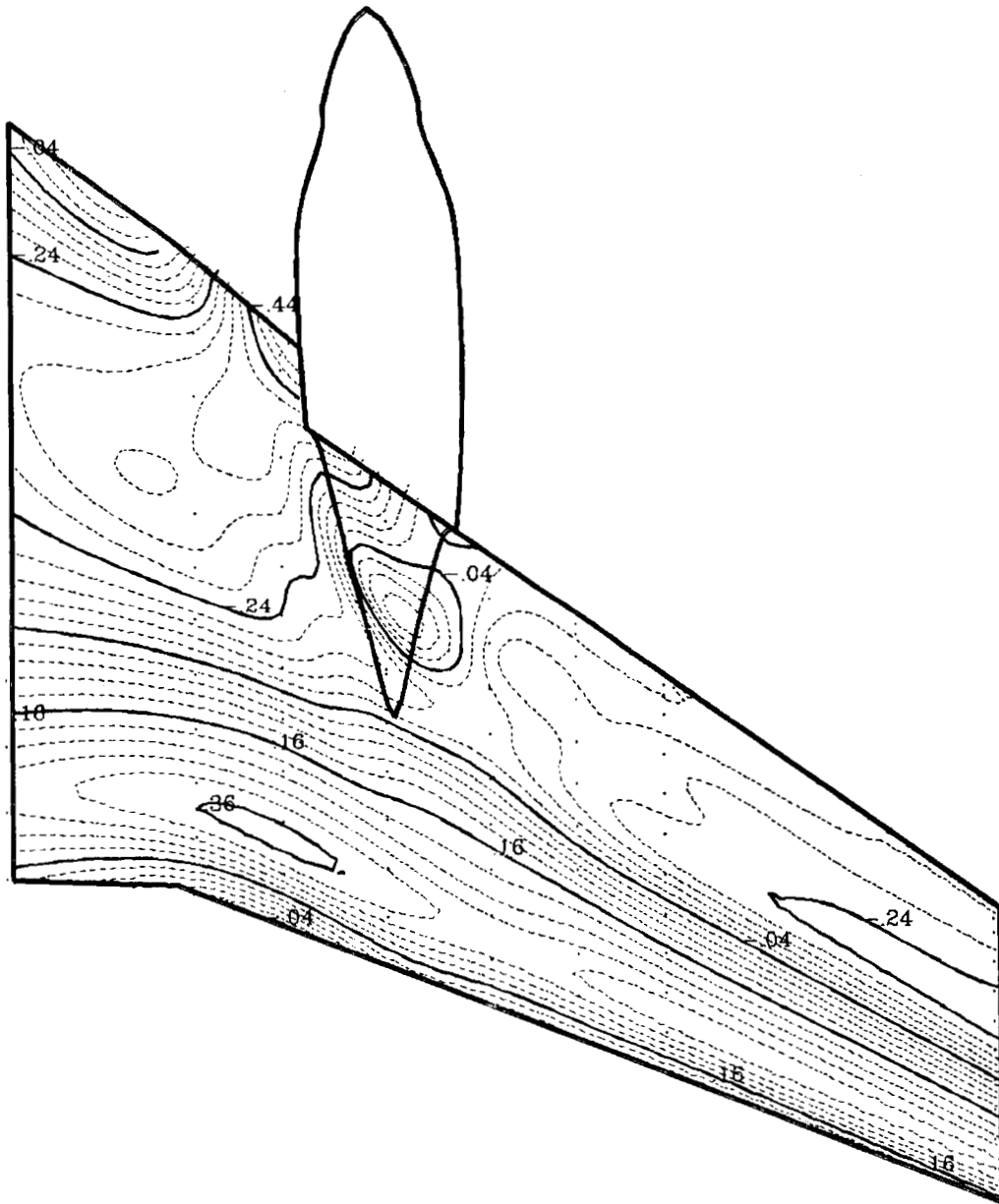
(d) Wing-body-nacelle, lower surface; $M = 0.80$, $\alpha = 1.95^\circ$, $EPR = 1.68$.

Figure 17.- Continued.



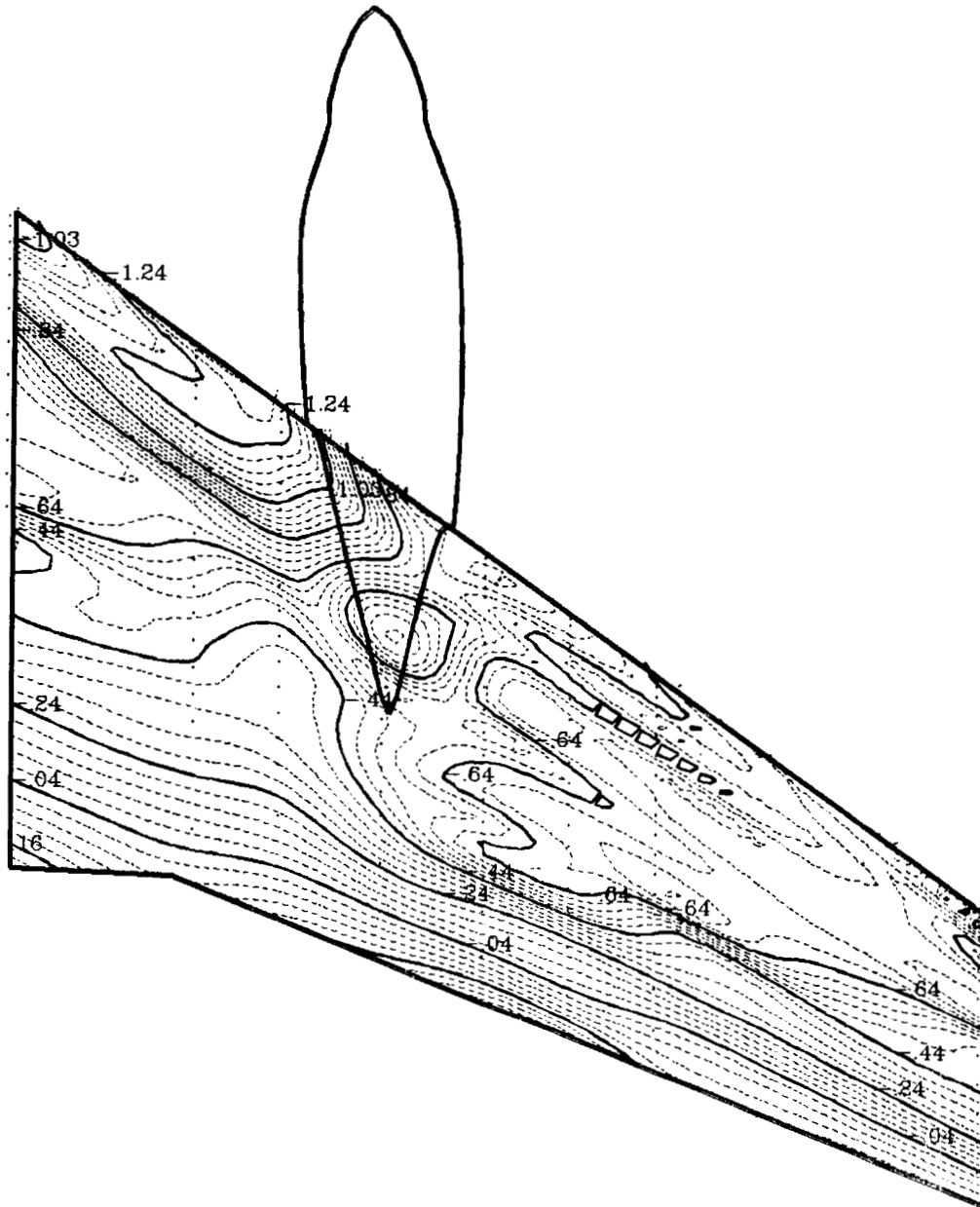
(e) Wing-body-nacelle LEX, upper surface; $M = 0.80$, $\alpha = 1.96^\circ$, $EPR = 1.73$.

Figure 17.- Continued.



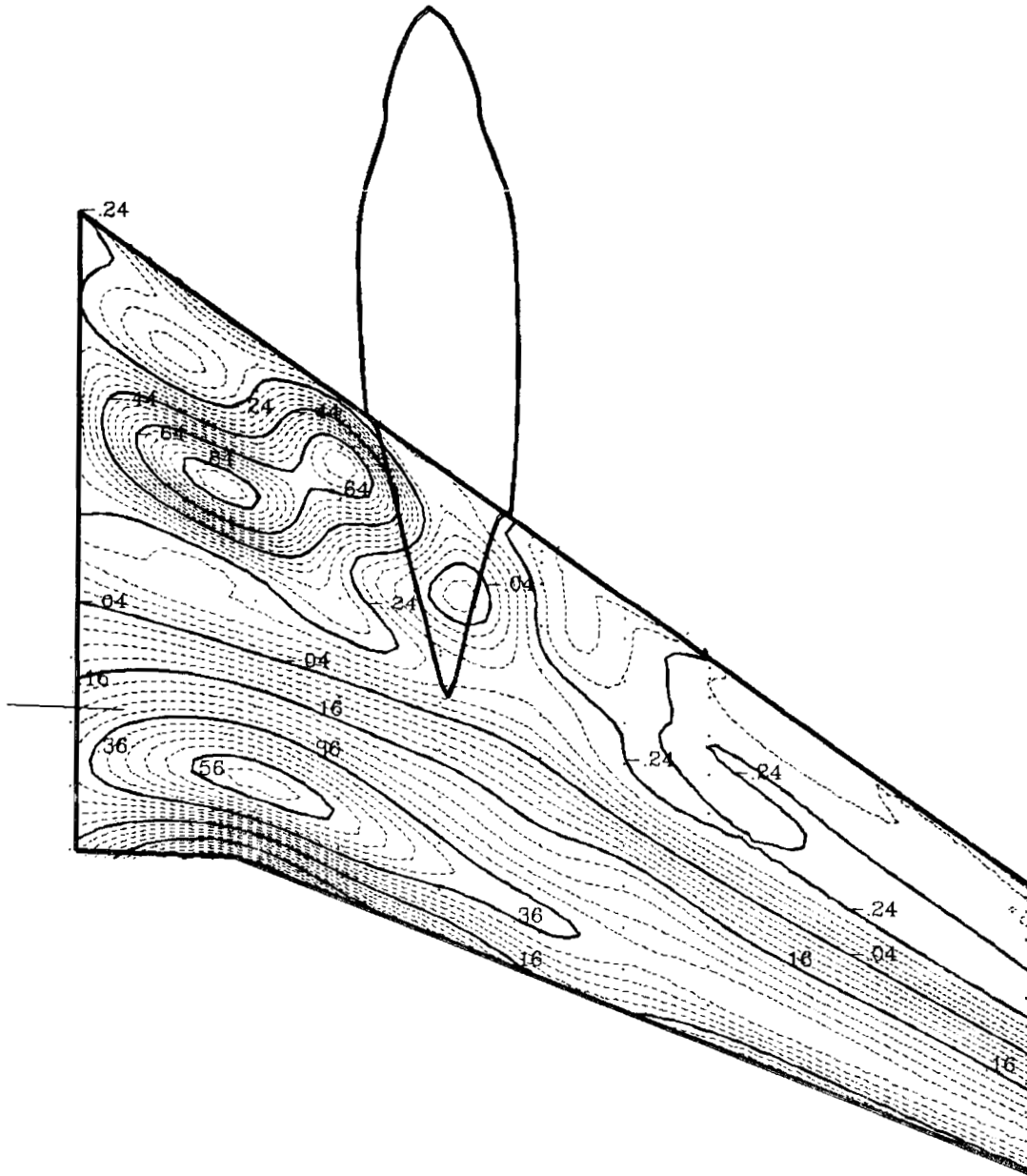
(f) Wing-body-nacelle-LEX, lower surface; $M = 0.80$, $\alpha = 1.96^\circ$, $EPR = 1.73$.

Figure 17.- Concluded.



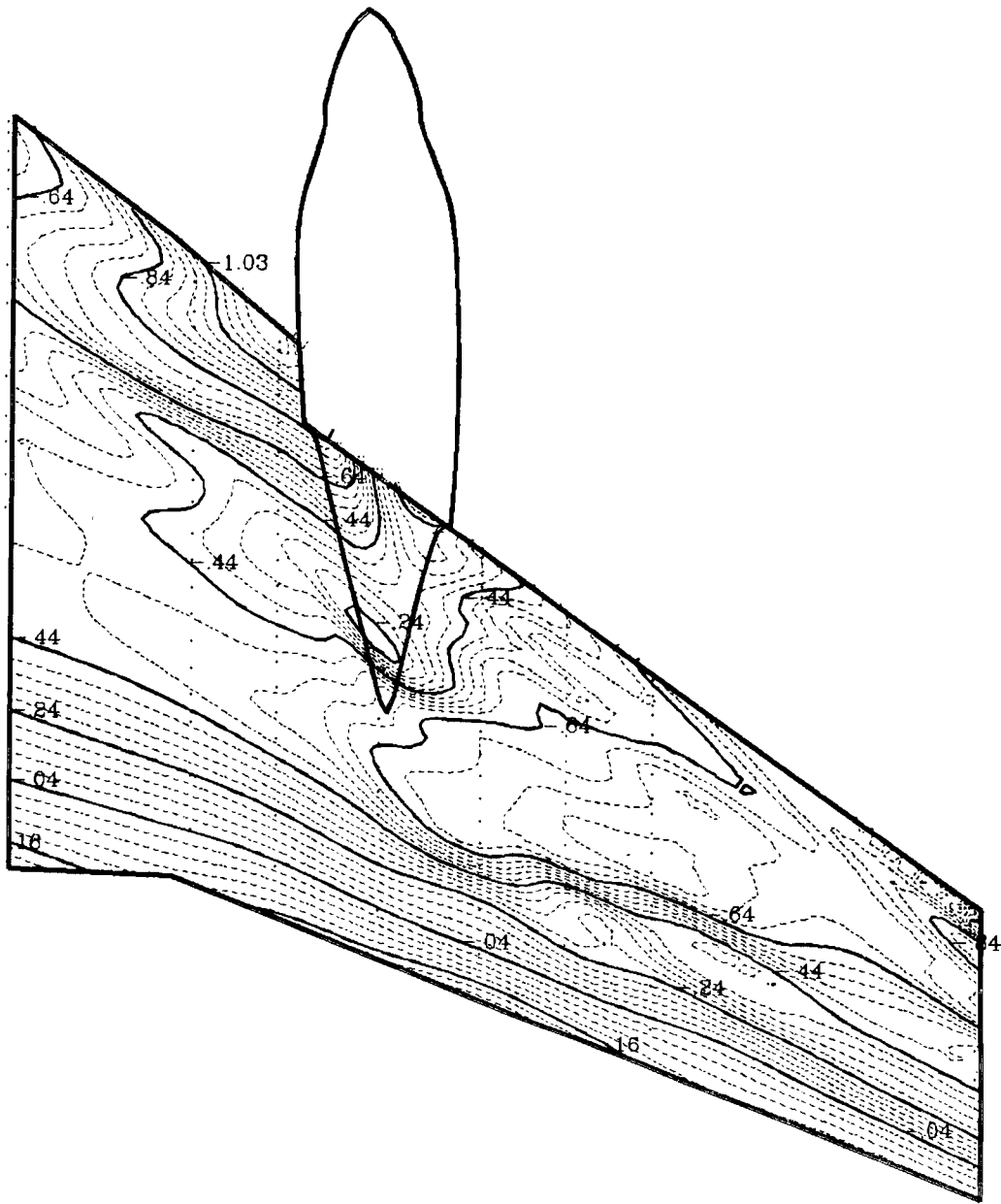
(a) Baseline configuration, upper surface; $M = 0.81$, $\alpha = 1.94^\circ$, $EPR = 1.77$,
rpm = 8471.

Figure 18.- Propeller-on pressure isobars.



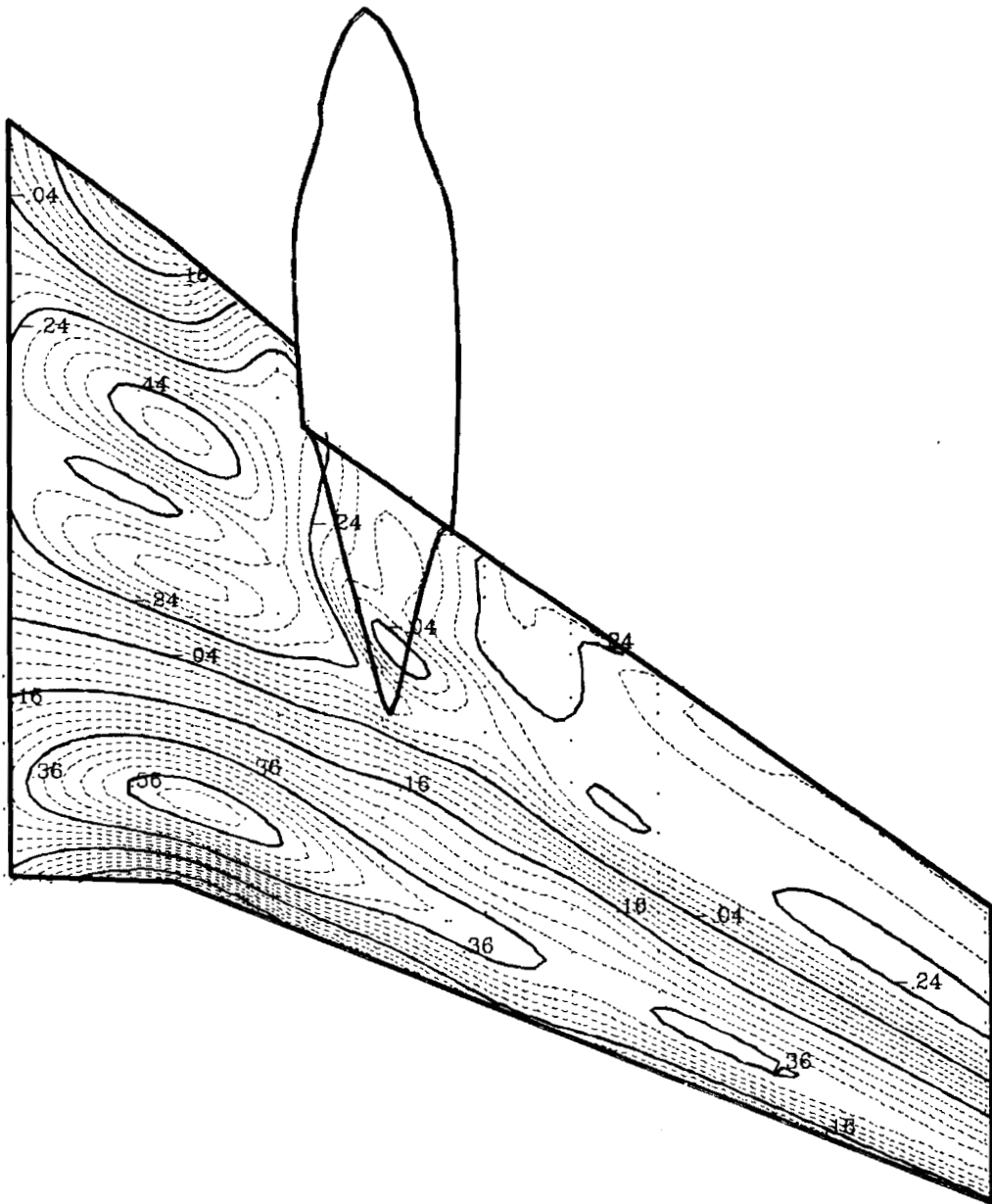
(b) Baseline configuration, lower surface; $M = 0.81$, $\alpha = 1.94^\circ$, $EPR = 1.77$,
 $rpm = 8471$.

Figure 18.- Continued.



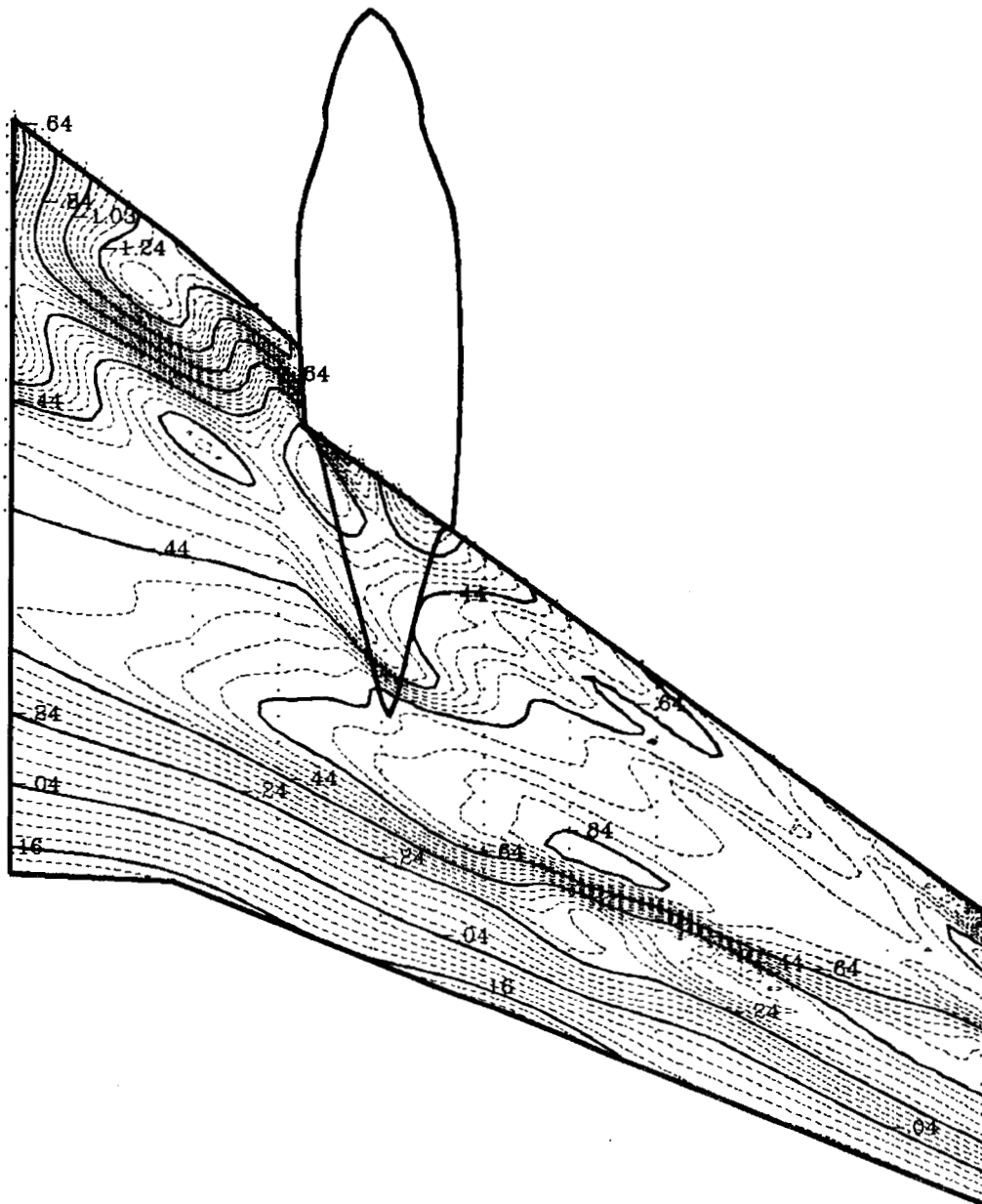
(c) Baseline + LEX, upper surface; $M = 0.80$, $\alpha = 1.96^\circ$, $EPR = 1.77$,
 $rpm = 8494$.

Figure 18.- Continued.



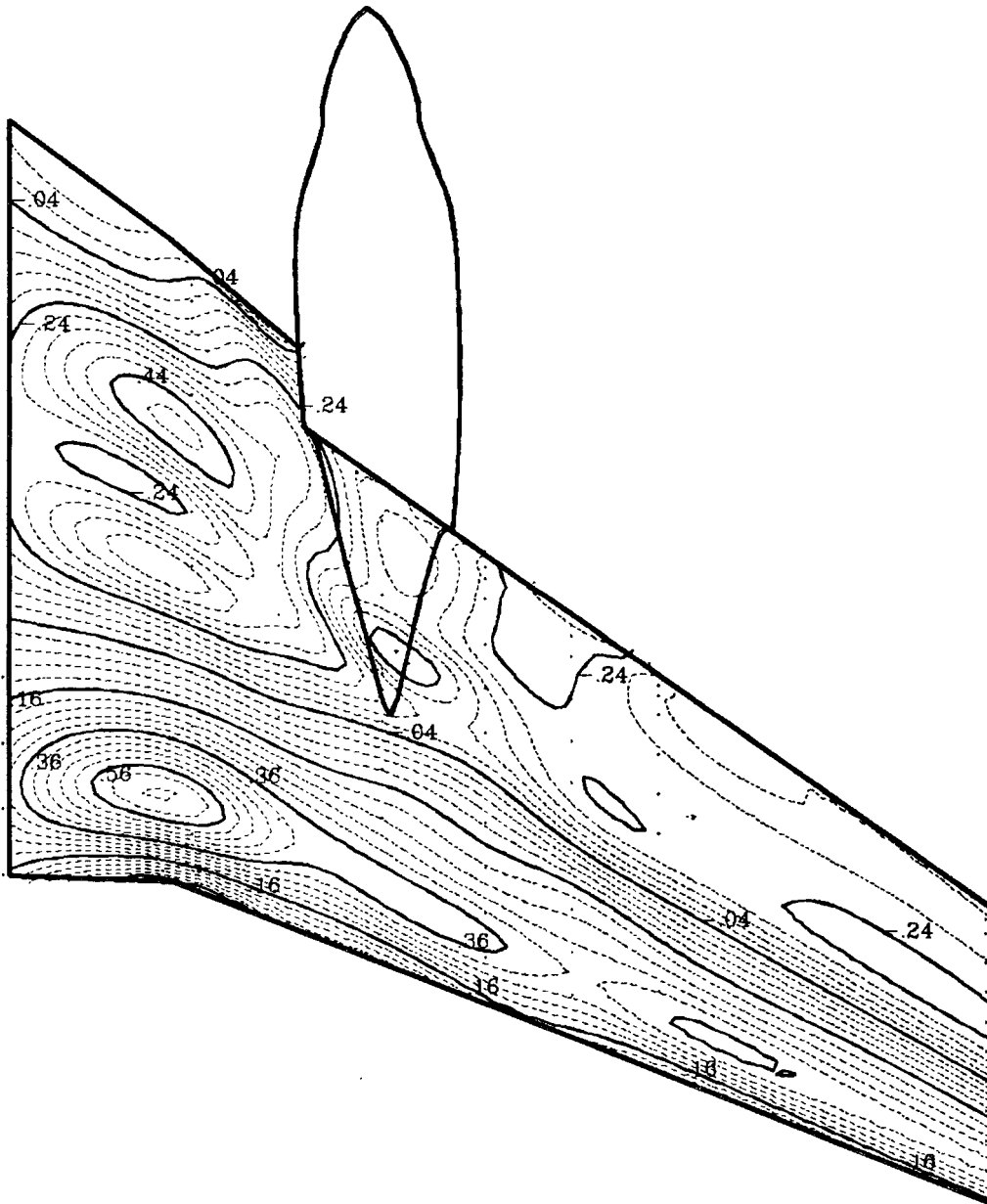
(d) Baseline + LEX, lower surface; $M = 0.80$, $\alpha = 1.96^\circ$, $EPR = 1.77$,
 $rpm = 8494$.

Figure 18.- Concluded.



(a) Upper surface; $M = 0.80$, $\alpha = 1.94^\circ$, $EPR = 1.73$, $rpm = 8486$.

Figure 19.- Wing-body-nacelle-LEX-fillet-strake pressure isobars, propeller on.



(b) Lower surface; $M = 0.80$, $\alpha = 1.94^\circ$, $EPR = 1.73$, $rpm = 8486$.

Figure 19.- Concluded.

SYMBOL CONFIGURATION

-
-
- ◇

- RN
- 5.132
 - 8.106
 - 11.165

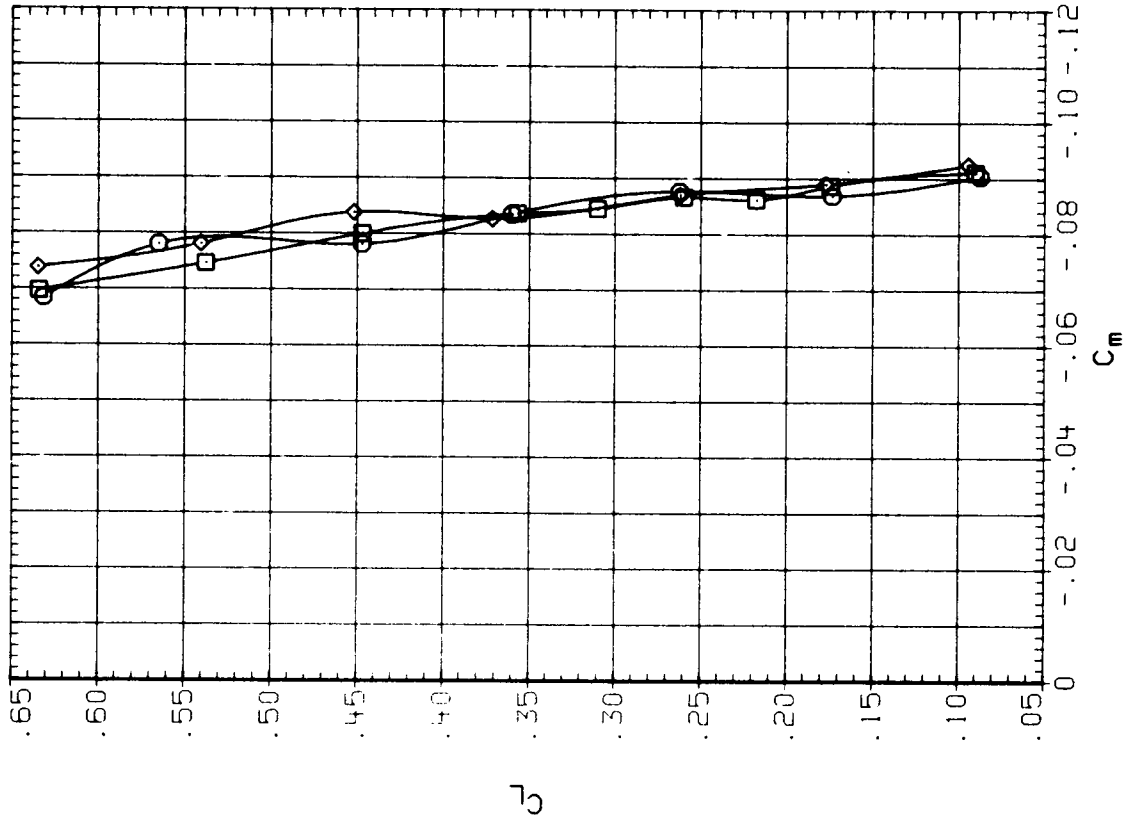
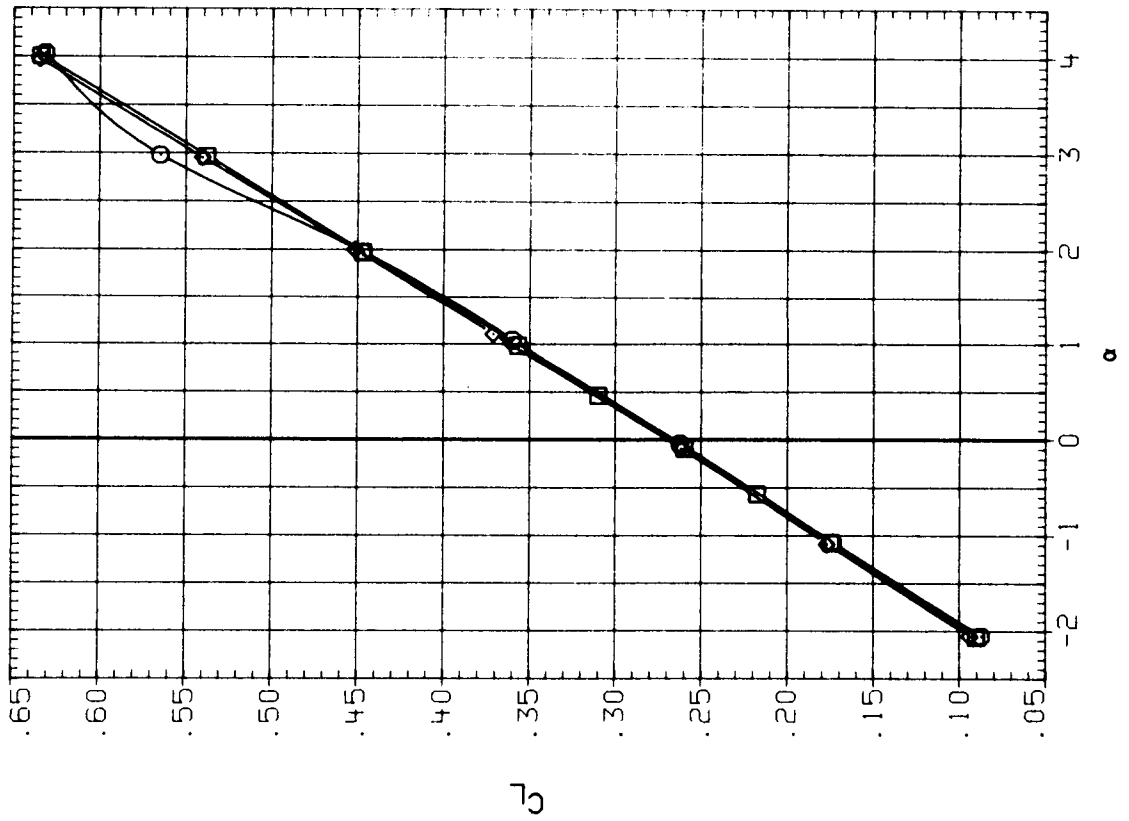


Figure 20.- Effect of Reynolds number on the longitudinal characteristics;
M = 0.60.

SYMBOL CONFIGURATION

WB
○
WB
◇

RN
5.132
8.106
11.165

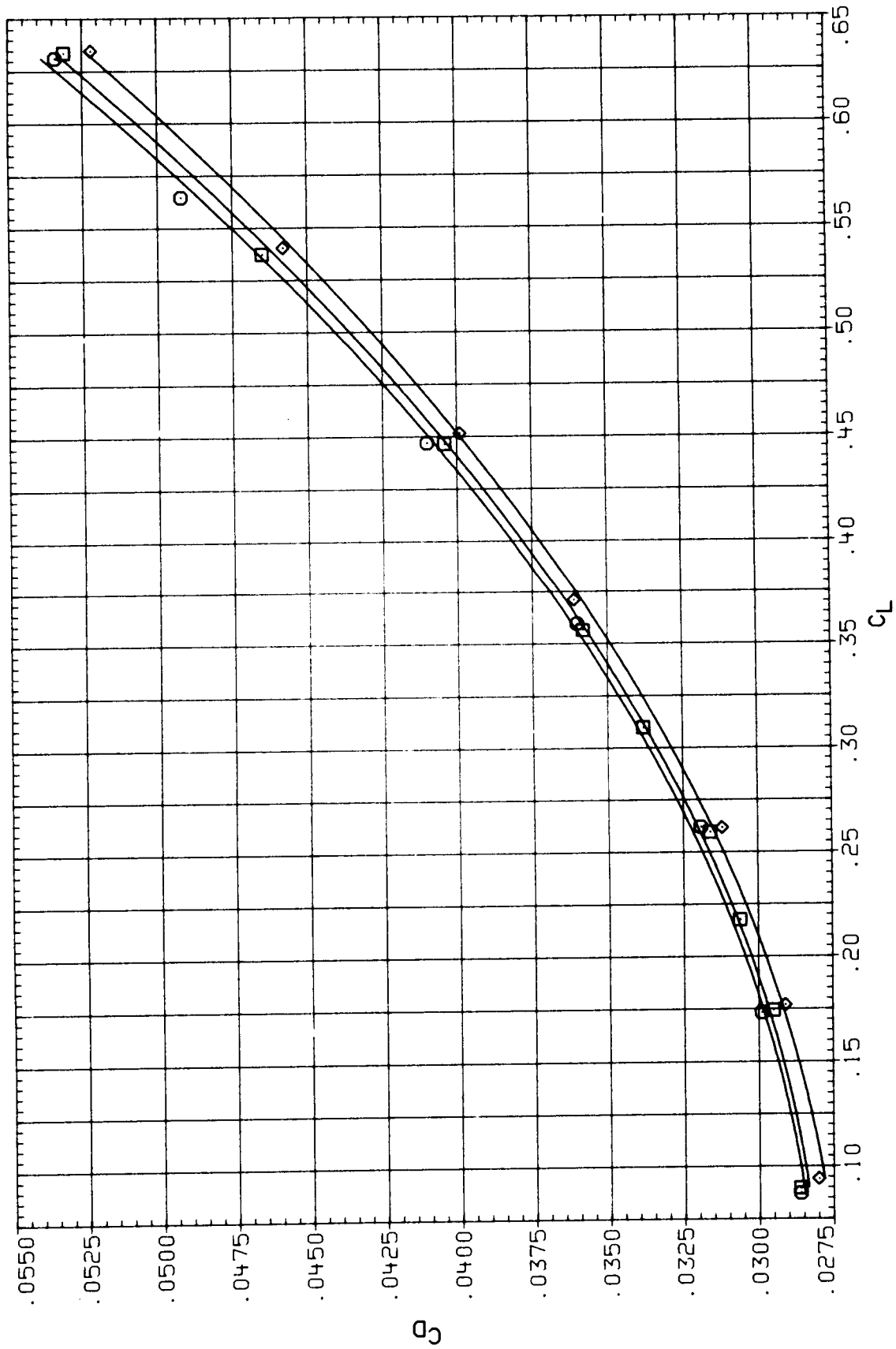


Figure 20.- Continued.

SYMBOL CONFIGURATION

- WB
- WB
- ◇ WB

RN

- 5.132
- 8.106
- 11.165

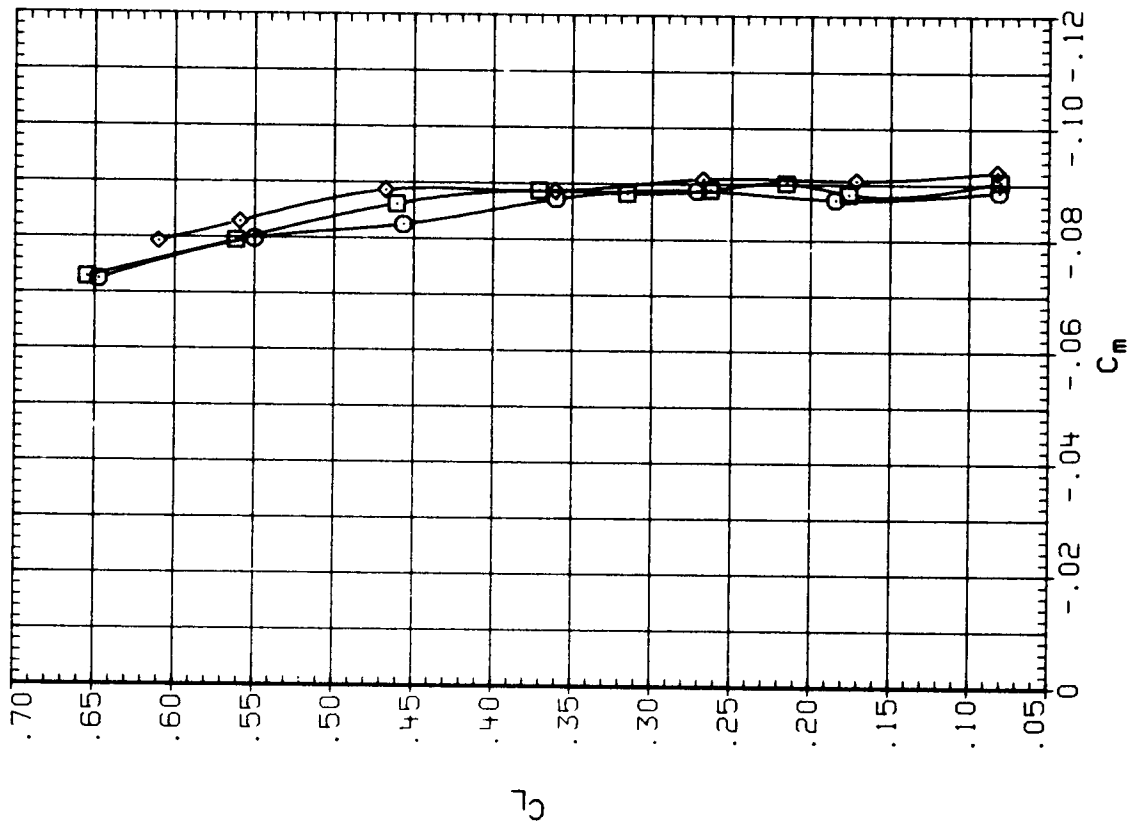
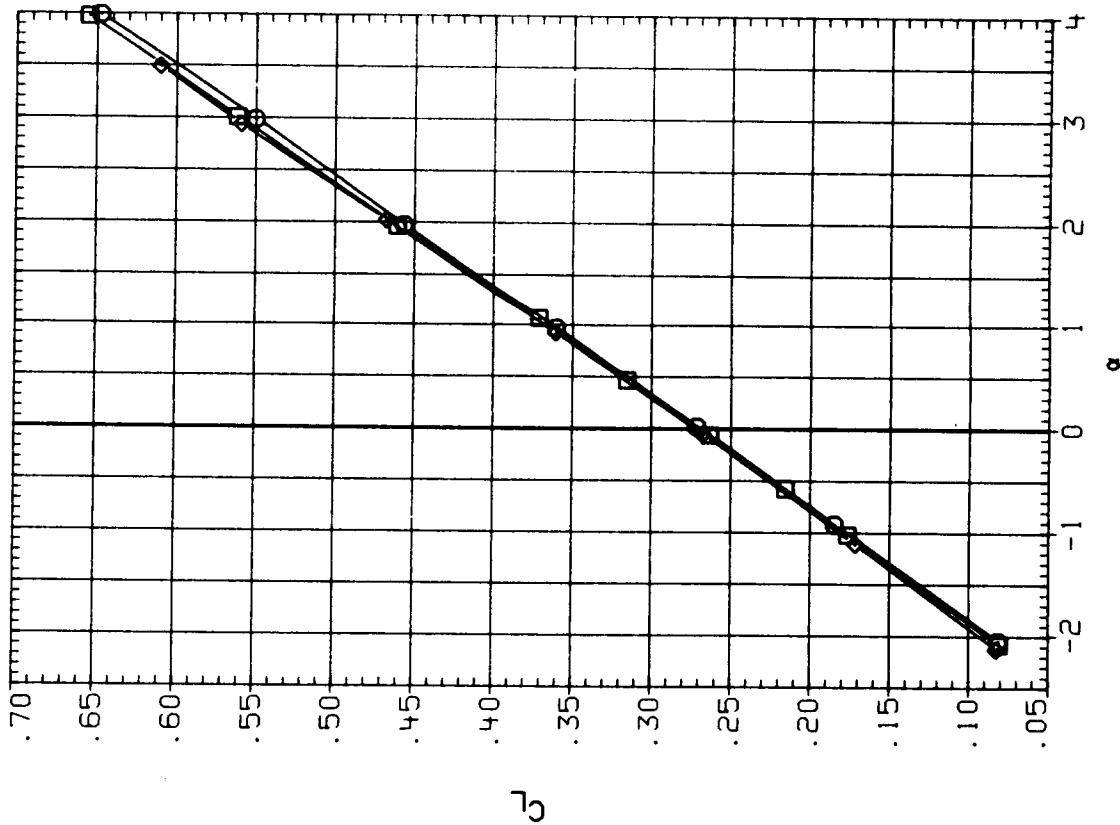


Figure 20.- Continued; M = 0.70.

RN
 5.132
 8.106
 11.165

SYMBOL CONFIGURATION
 ○ WB
 □ WB
 ◇ WB

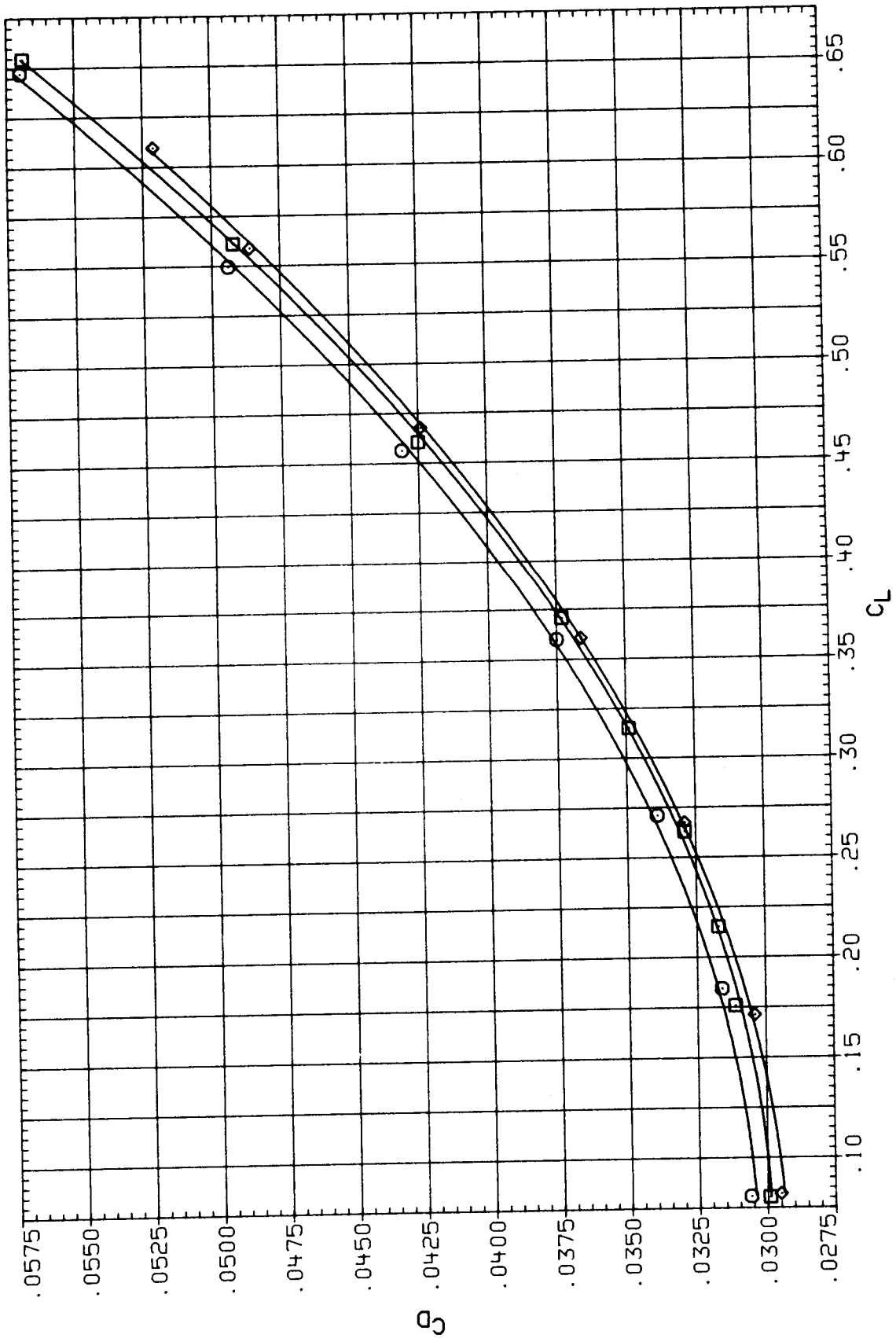


Figure 20.- Continued.

SYMBOL CONFIGURATION

- HB
- HB
- ◇ HB

RN
5.132
8.106
11.165

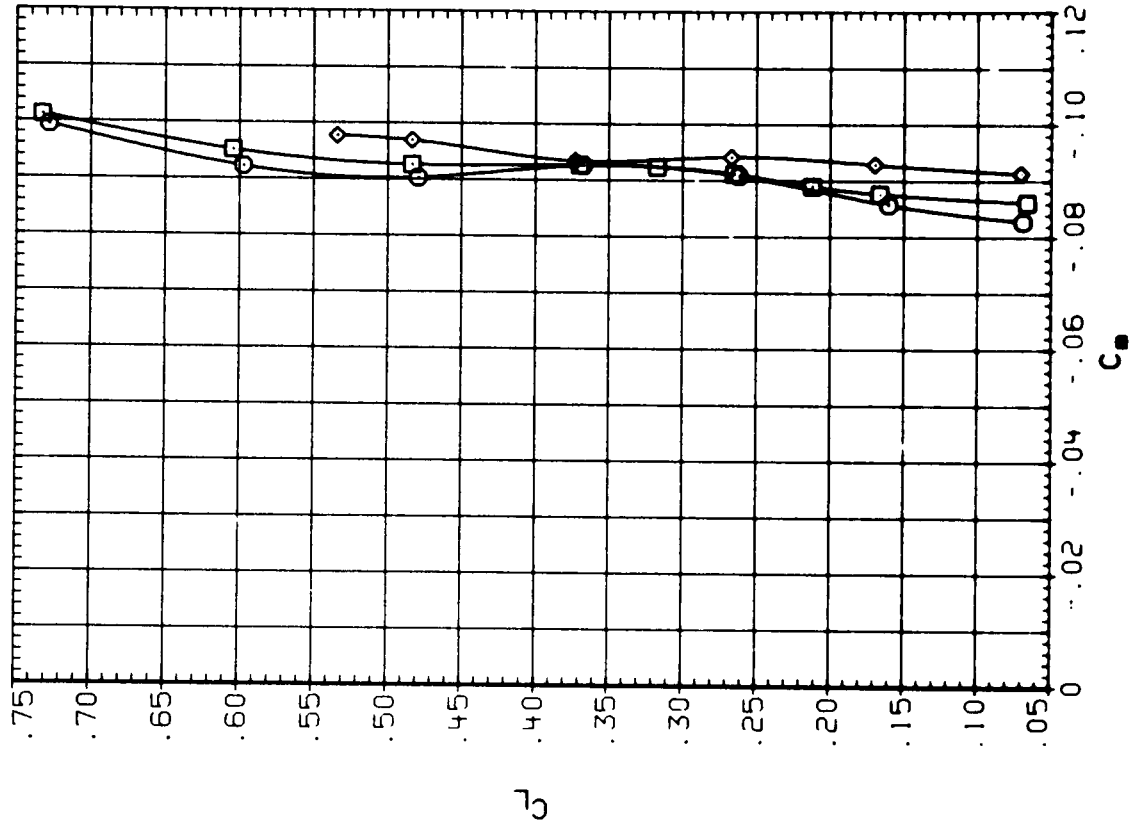
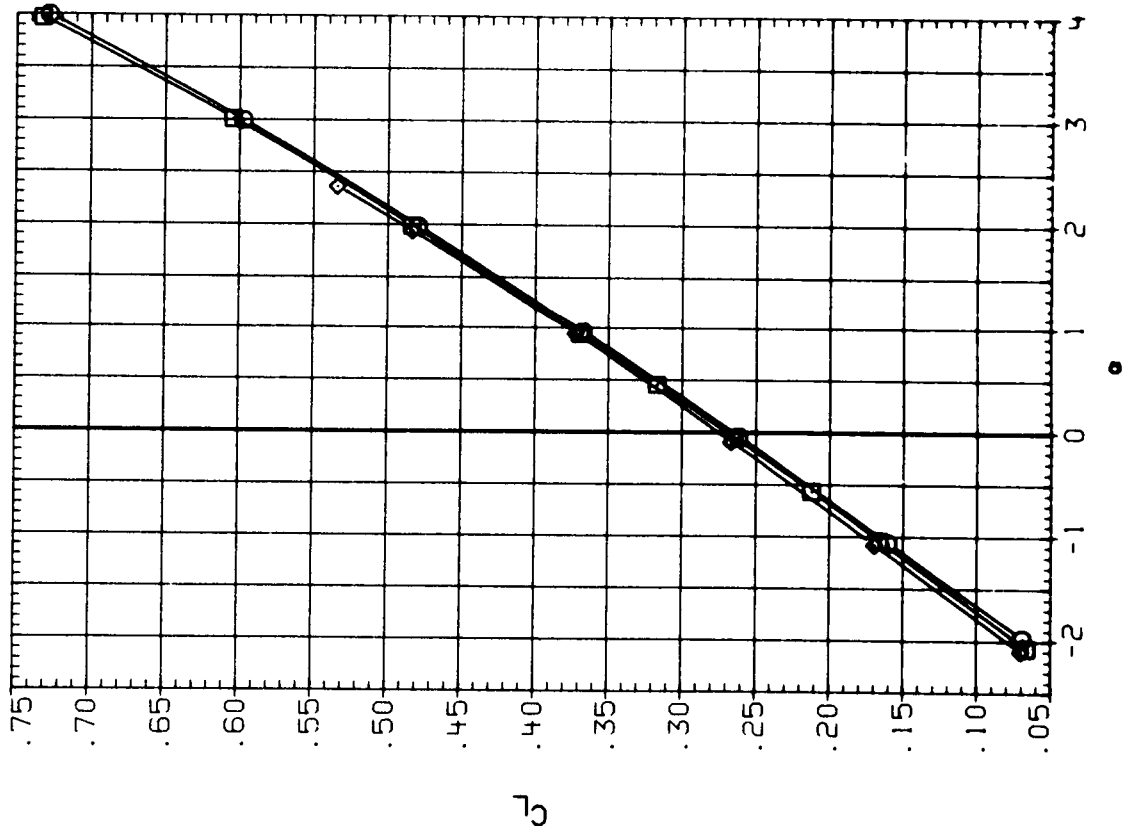


Figure 20.- Continued; M = 0.80.

SYMBOL CONFIGURATION
 MB
 □ MB
 ◇ MB

RN
 5.132
 8.106
 11.165

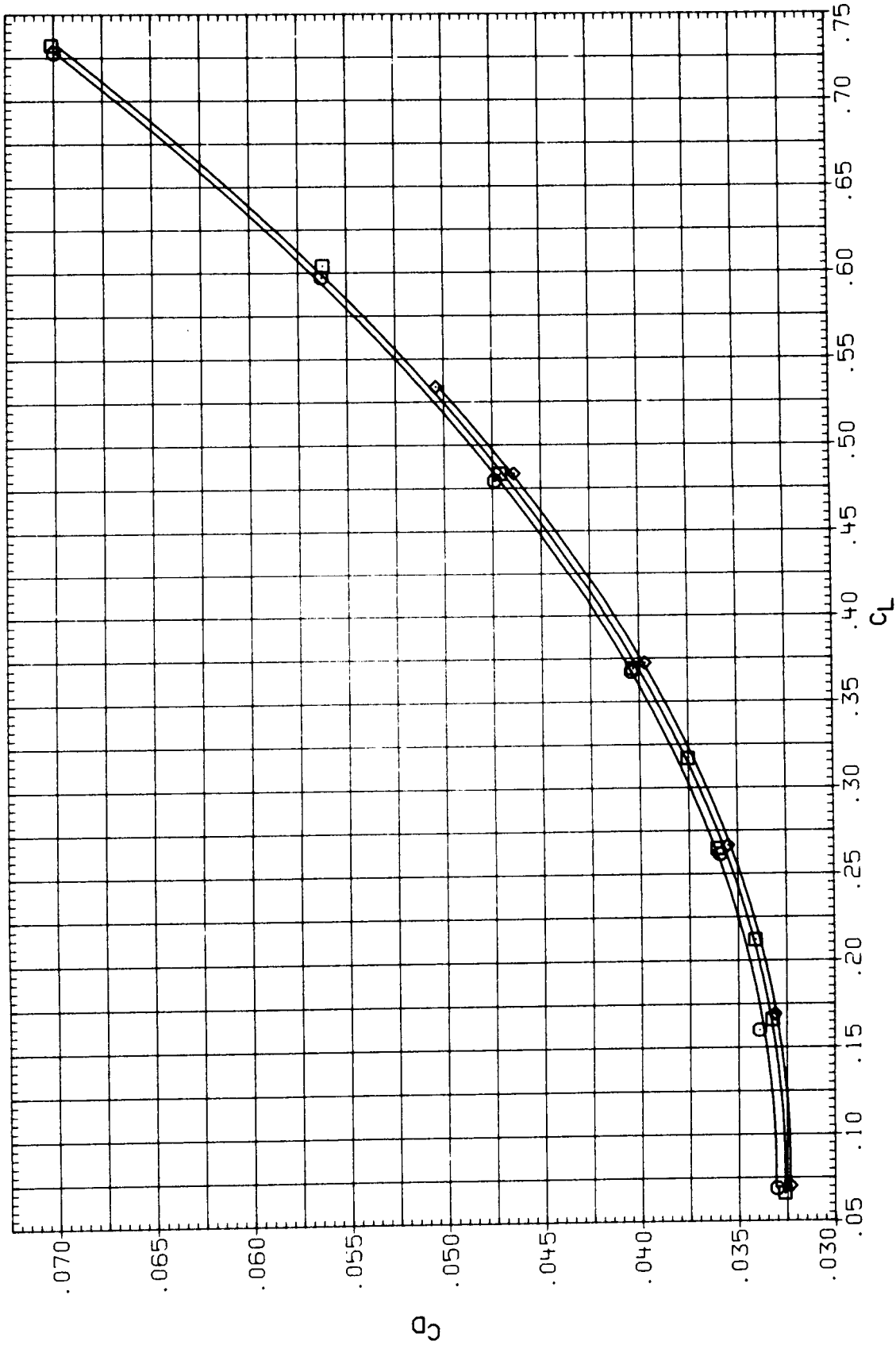


Figure 20.- Concluded.

SYMBOL CONFIGURATION

○ MB
 □ MBN
 ◇ MBN

EPR

1.000
 1.000
 1.750

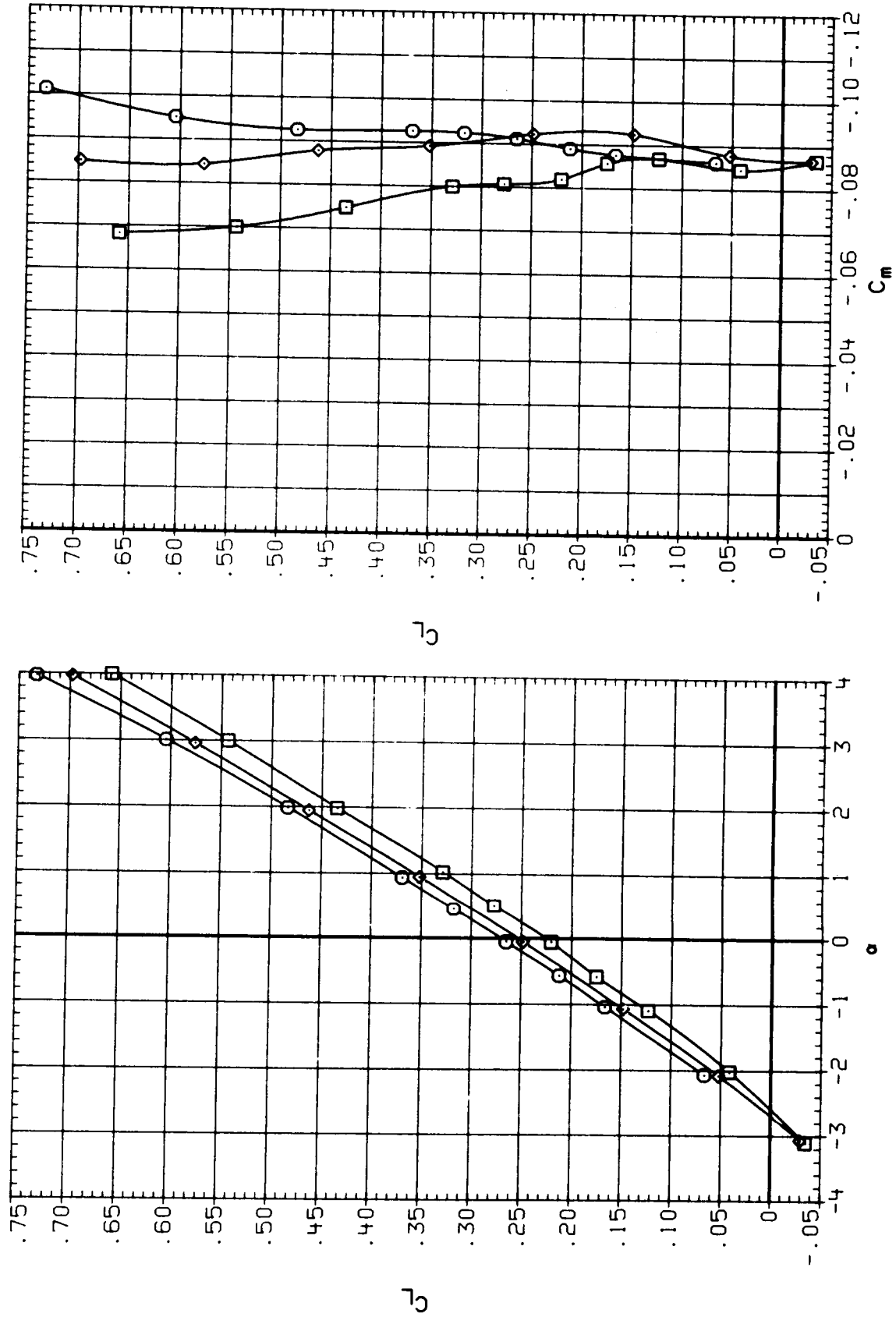


Figure 21.- Effect of nacelle and jet on the aerodynamic characteristics;
 $M = 0.80$.

EPR
 1.000
 1.000
 1.750

SYMBOL CONFIGURATION
 ○ HB
 □ HBN
 ◇ HBN

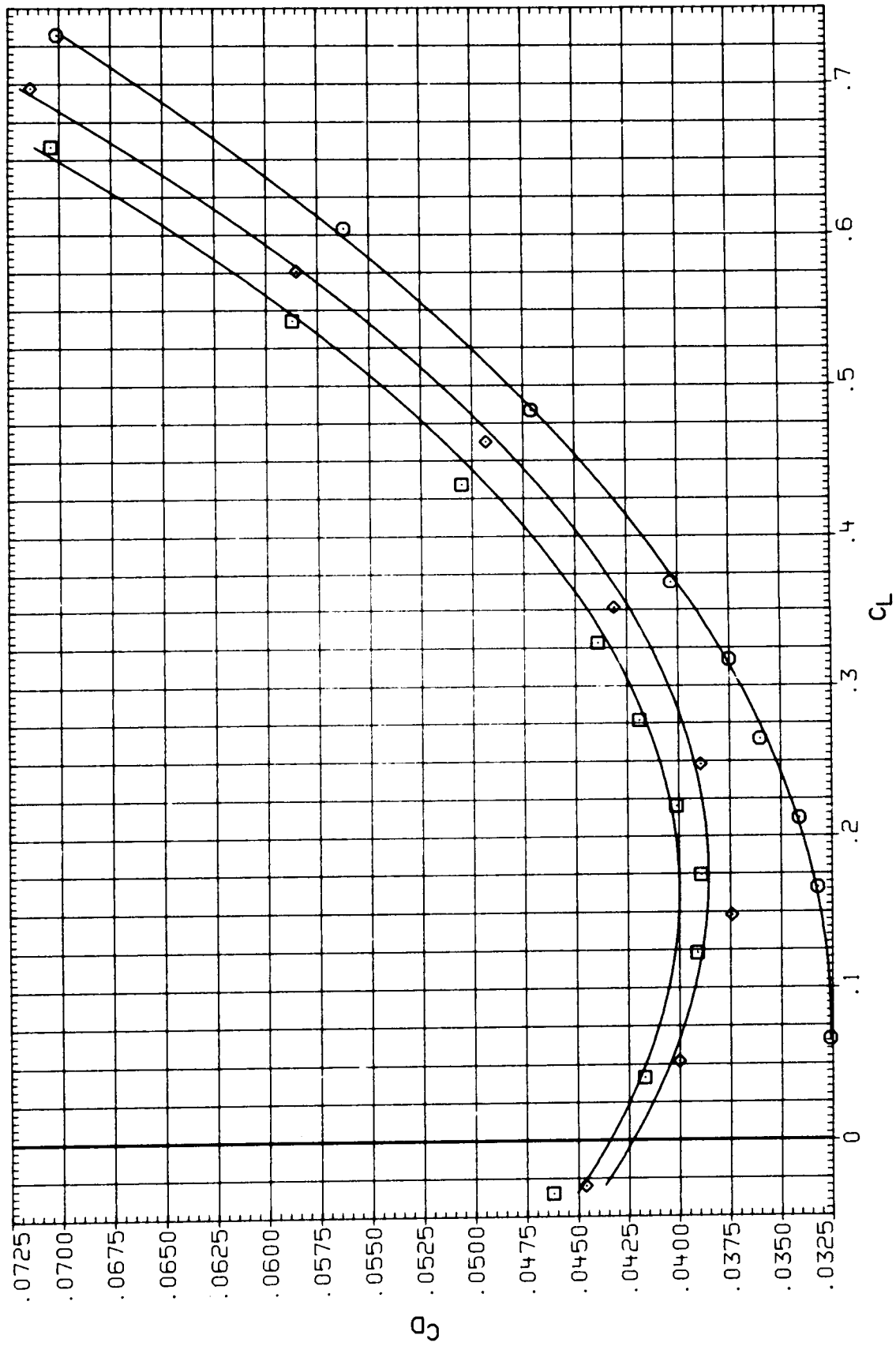


Figure 21.- Concluded.

EPR
 1.000
 1.750
 1.750

SYMBOL CONFIGURATION
 ○ HB
 □ MBN
 ◇ MBNL

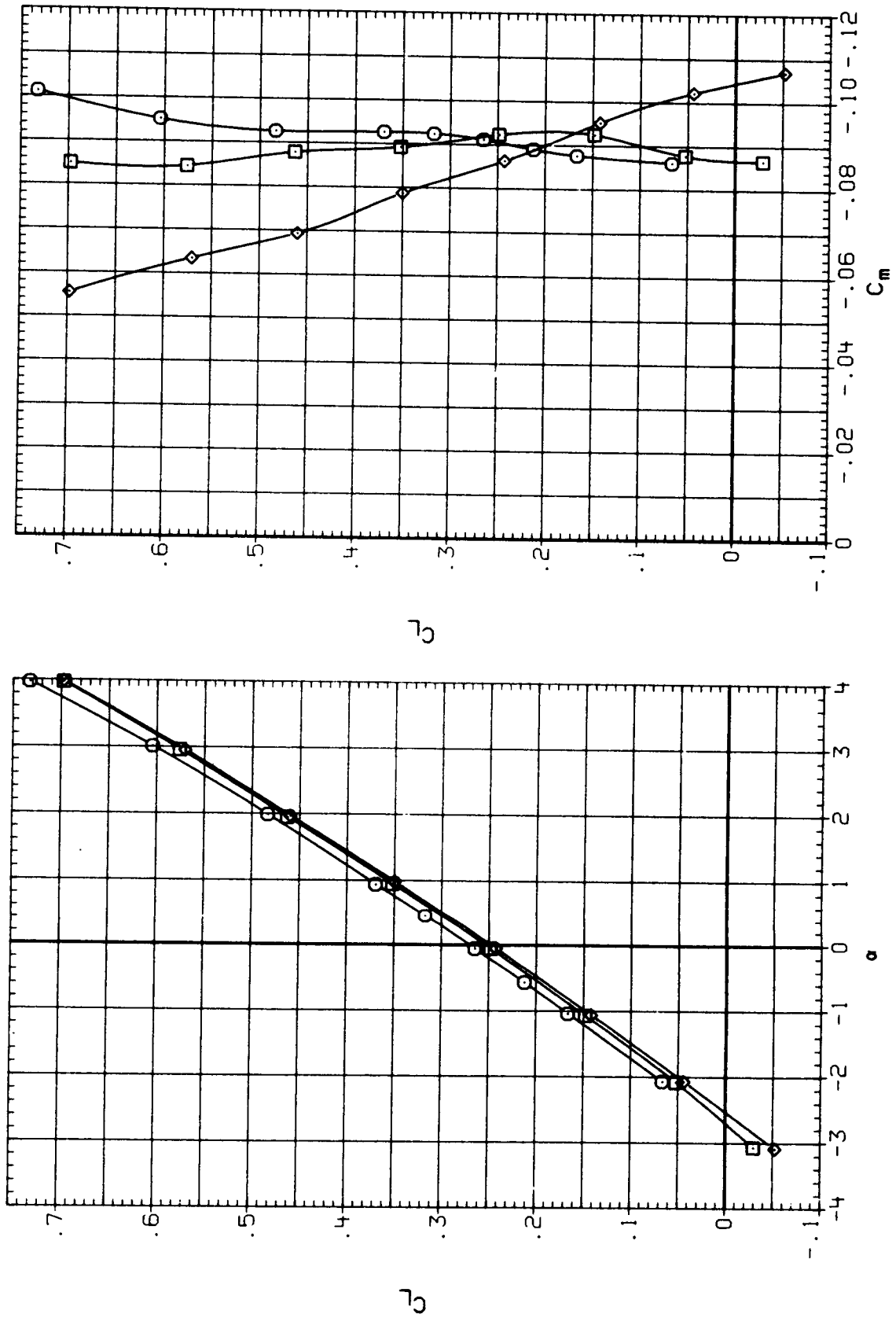


Figure 22.- Comparison of LEX-on and LEX-off at cruise EPR; M = 0.80.

EPR
 1.000
 1.750
 1.750

SYMBOL CONFIGURATION
 ○ HB
 □ HBN
 ◇ HBNL

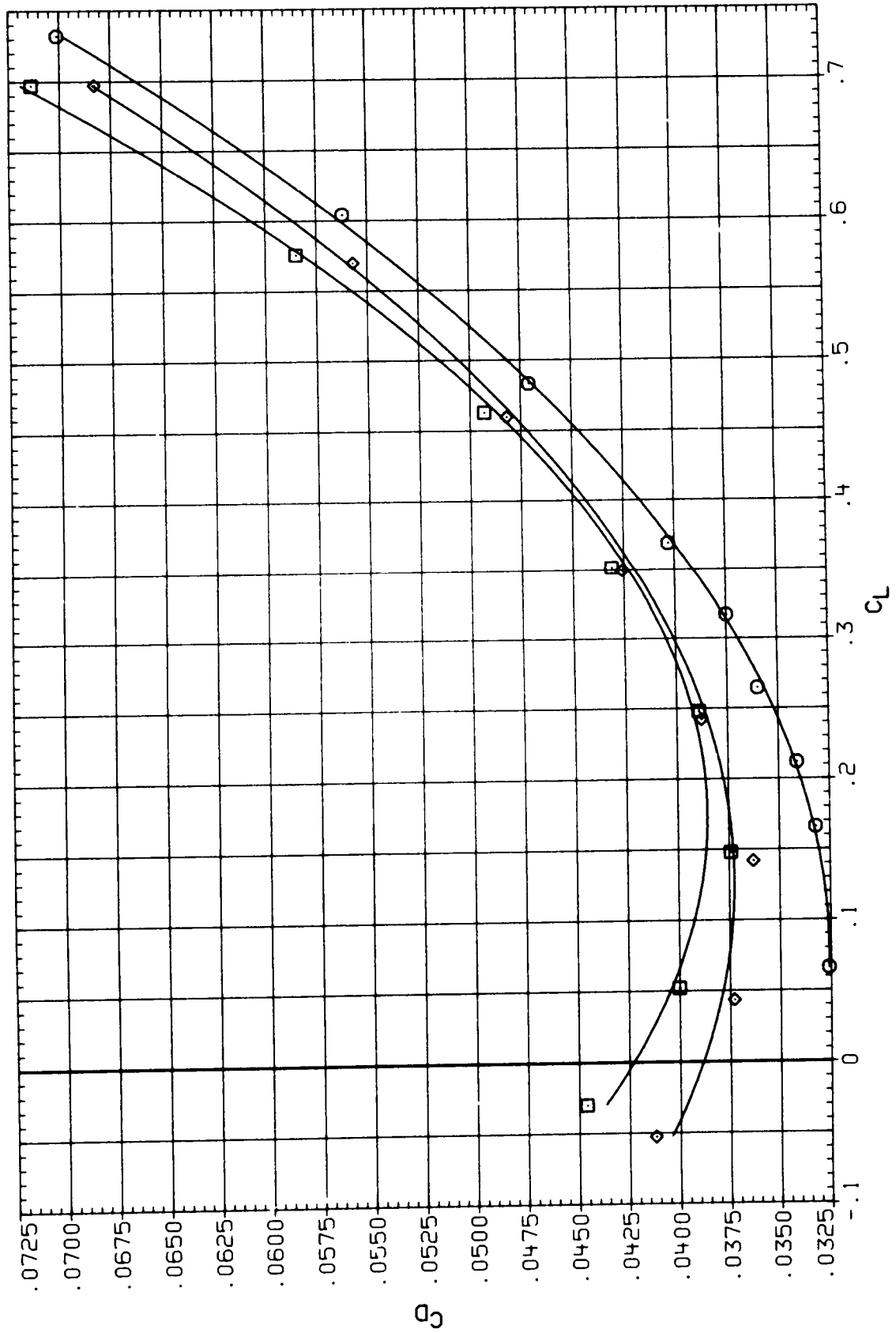
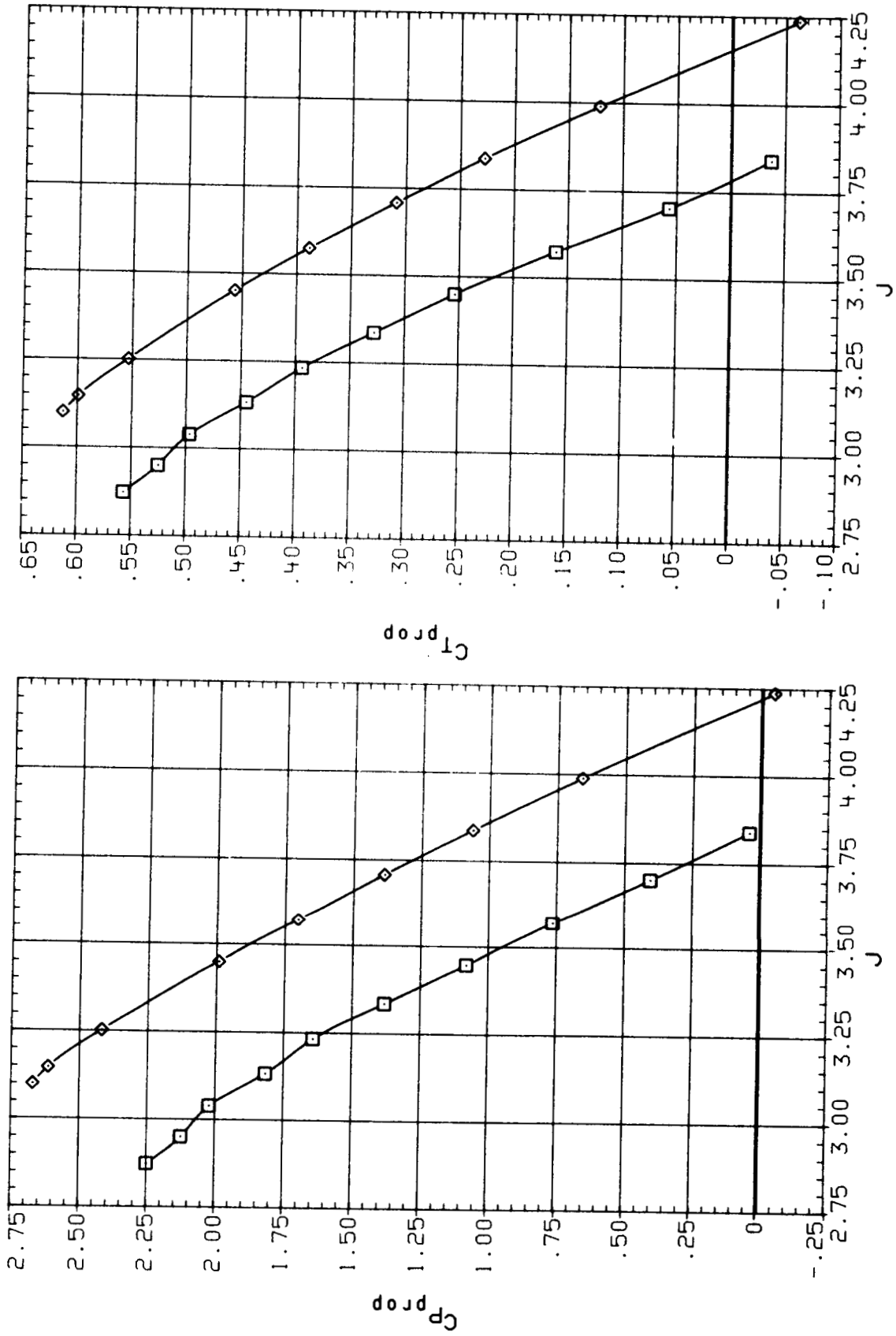


Figure 22.- Concluded.

SYMBOL CONFIGURATION

□ WBNLP
 ◇ WBNLP

PITCH
 57.200
 59.200

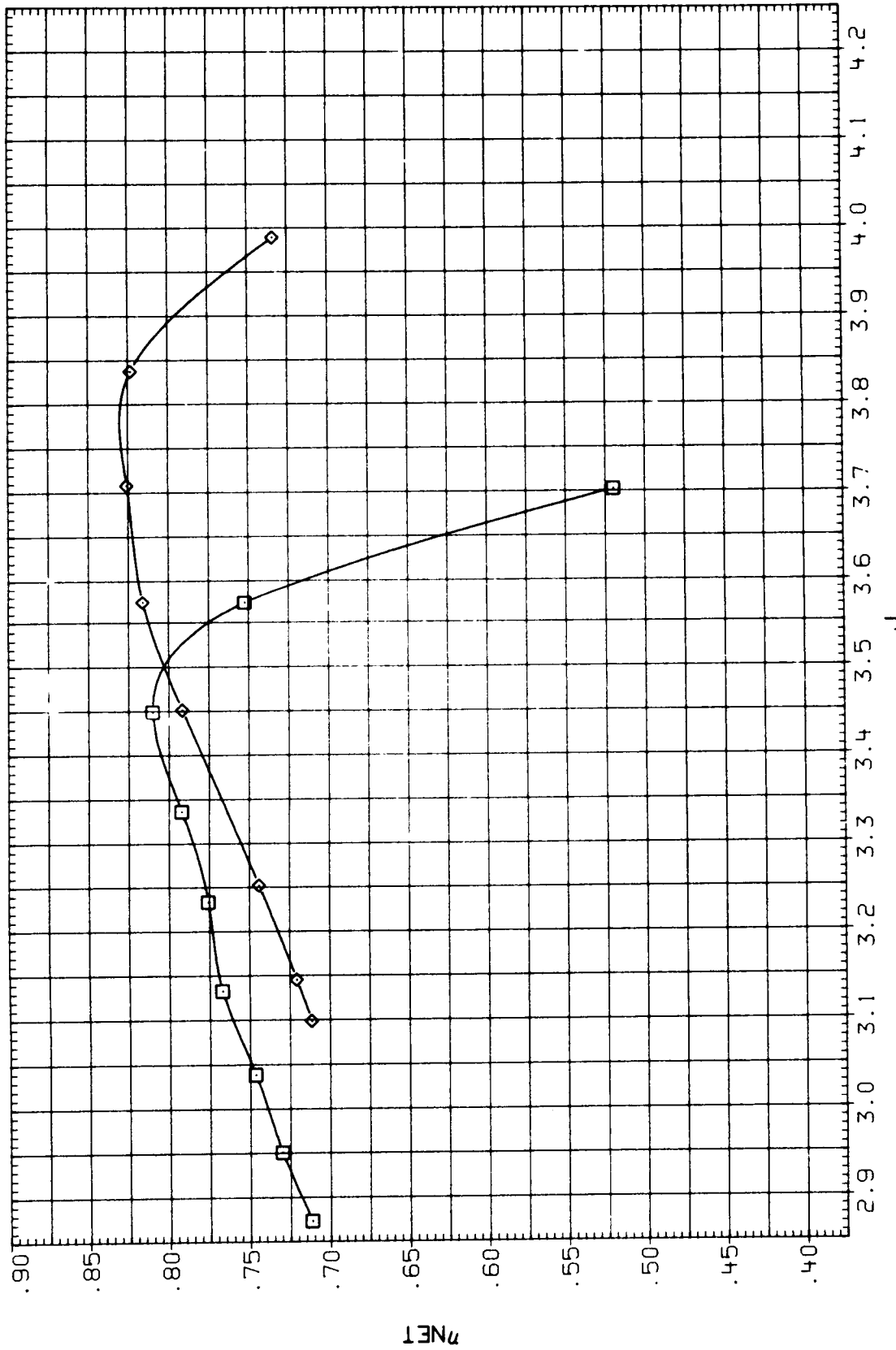


(a) $\alpha = 0^\circ$, $M = 0.80$.

Figure 23.- Propeller performance.

PITCH
57.20
59.200

SYMBOL CONFIGURATION
□ MBNLP
◇ MBNLP

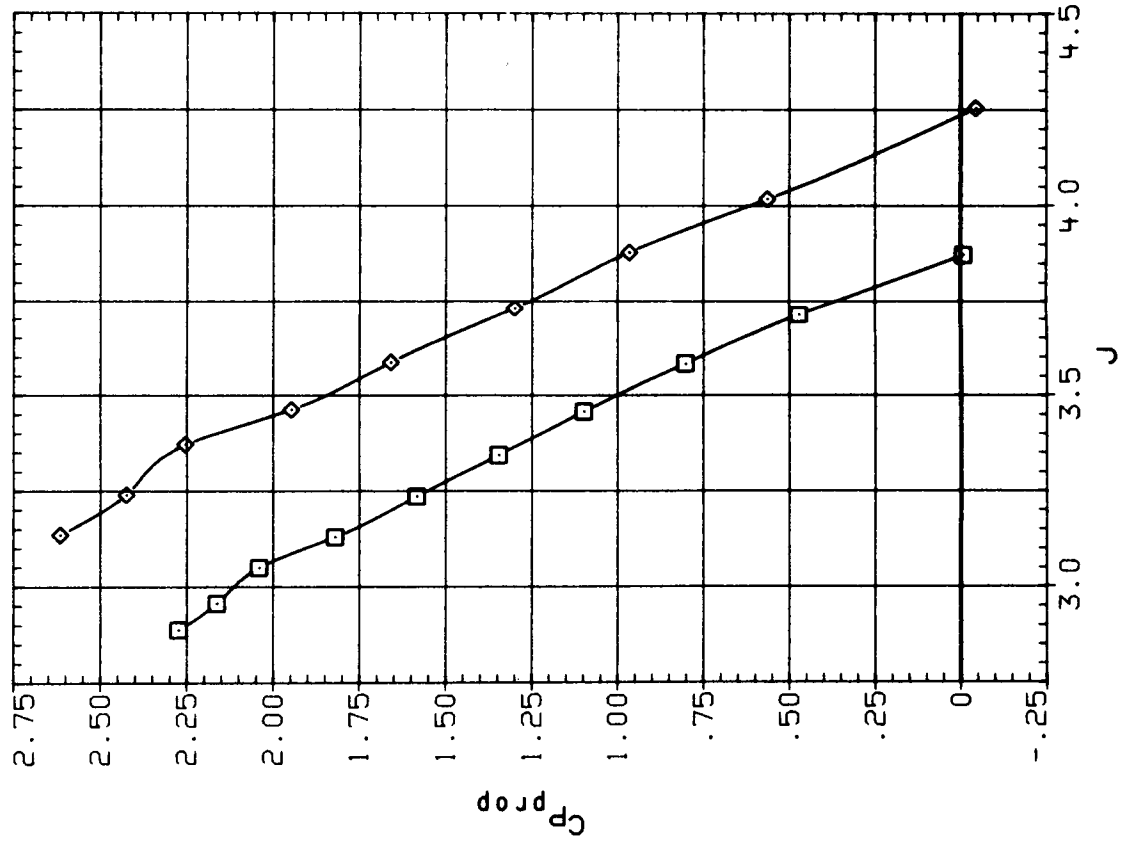
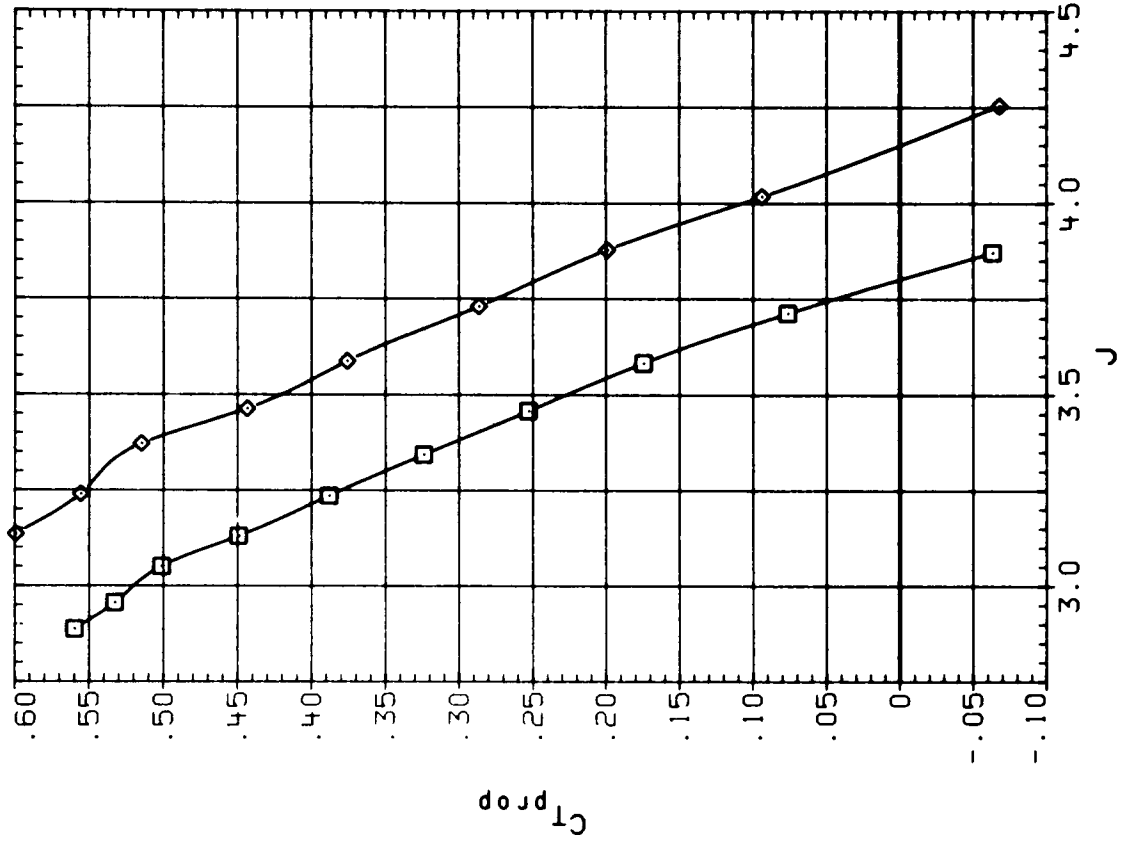


(a) Concluded.

Figure 23.- Continued.

PITCH
57.200
59.200

SYMBOL CONFIGURATION
□ HB/NLP
◇ HB/NLP



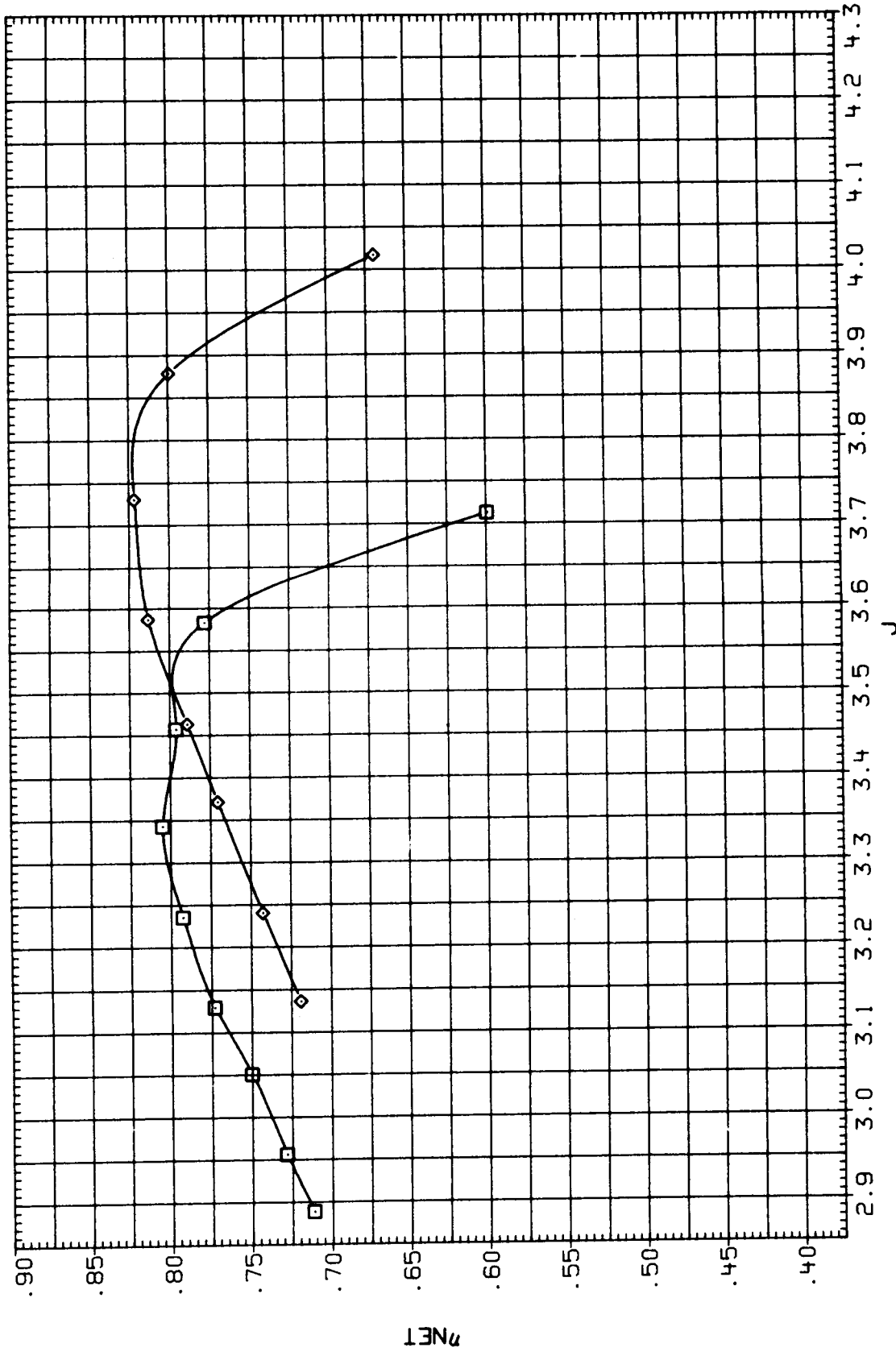
(b) $\alpha = 1^\circ$, $M = 0.80$.

Figure 23.- Continued.

SYMBOL CONFIGURATION

-
- ◇

PITCH
57.200
59.200

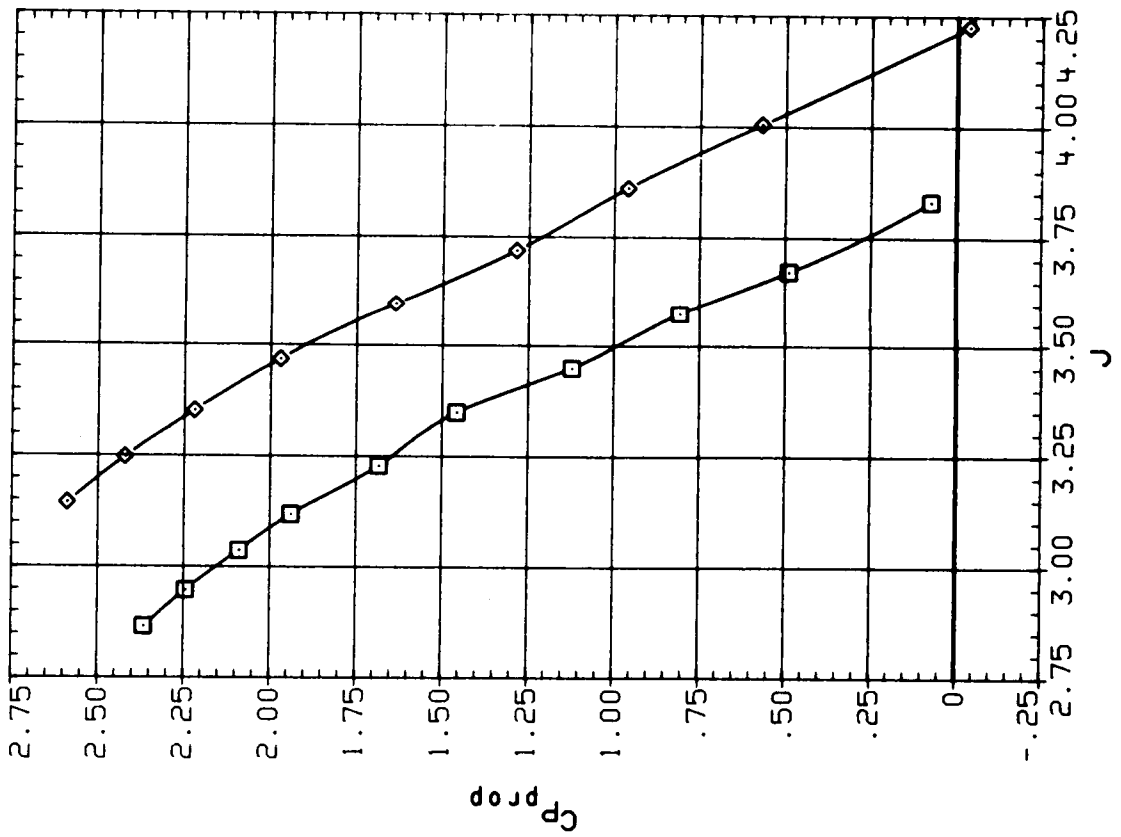
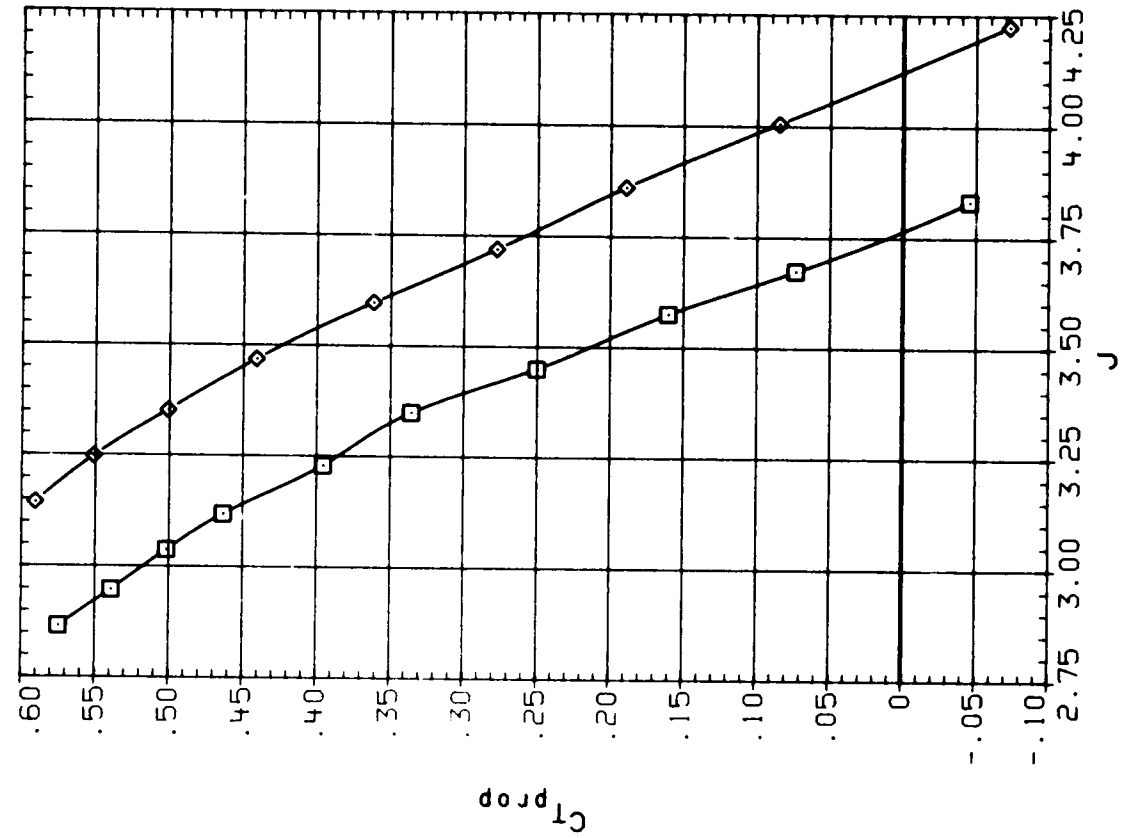


(b) Concluded.

Figure 23.- Continued.

PITCH
57.200
59.200

SYMBOL CONFIGURATION
□ HB/NLP
◇ HB/NLP

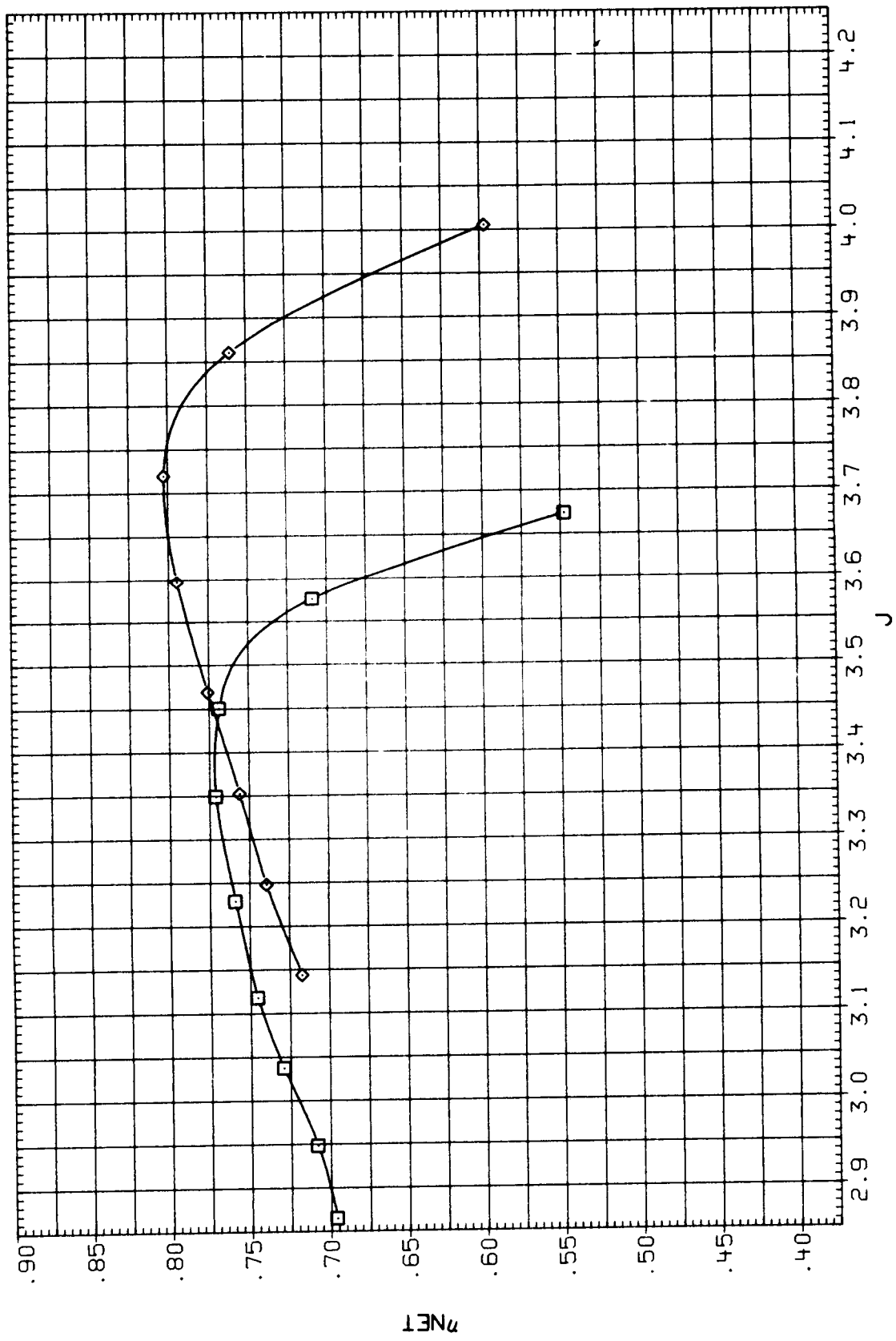


(c) $\alpha = 2^\circ$, $M = 0.80$.

Figure 23.- Continued.

PITCH
57.200
59.200

SYMBOL CONFIGURATION
□ HB/NLP
◇ HB/NLP

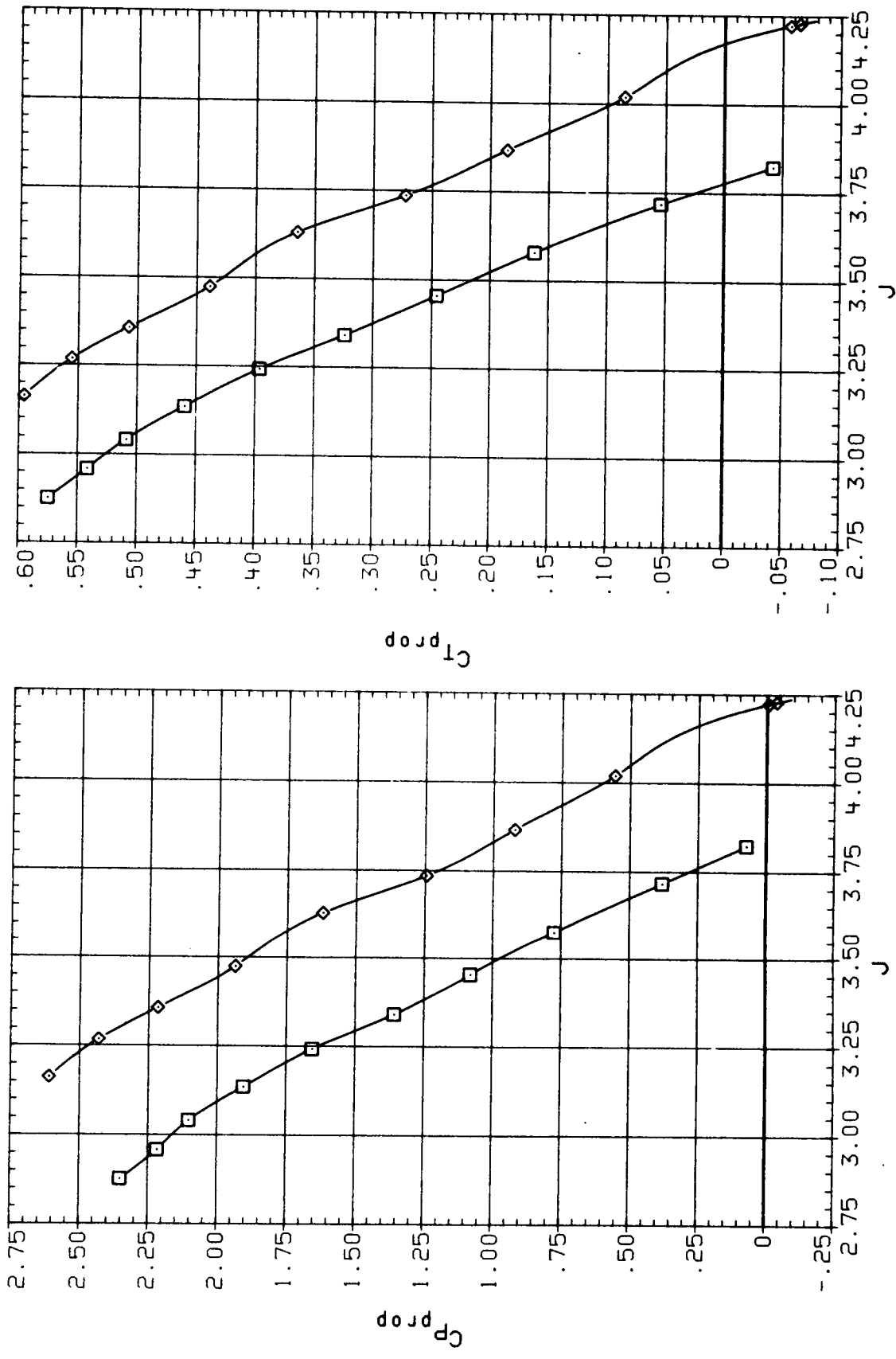


(c) Concluded.

Figure 23.- Continued.

SYMBOL CONFIGURATION
 □ HB/NLP
 ◇ HB/NLP

PITCH
 57.200
 59.200

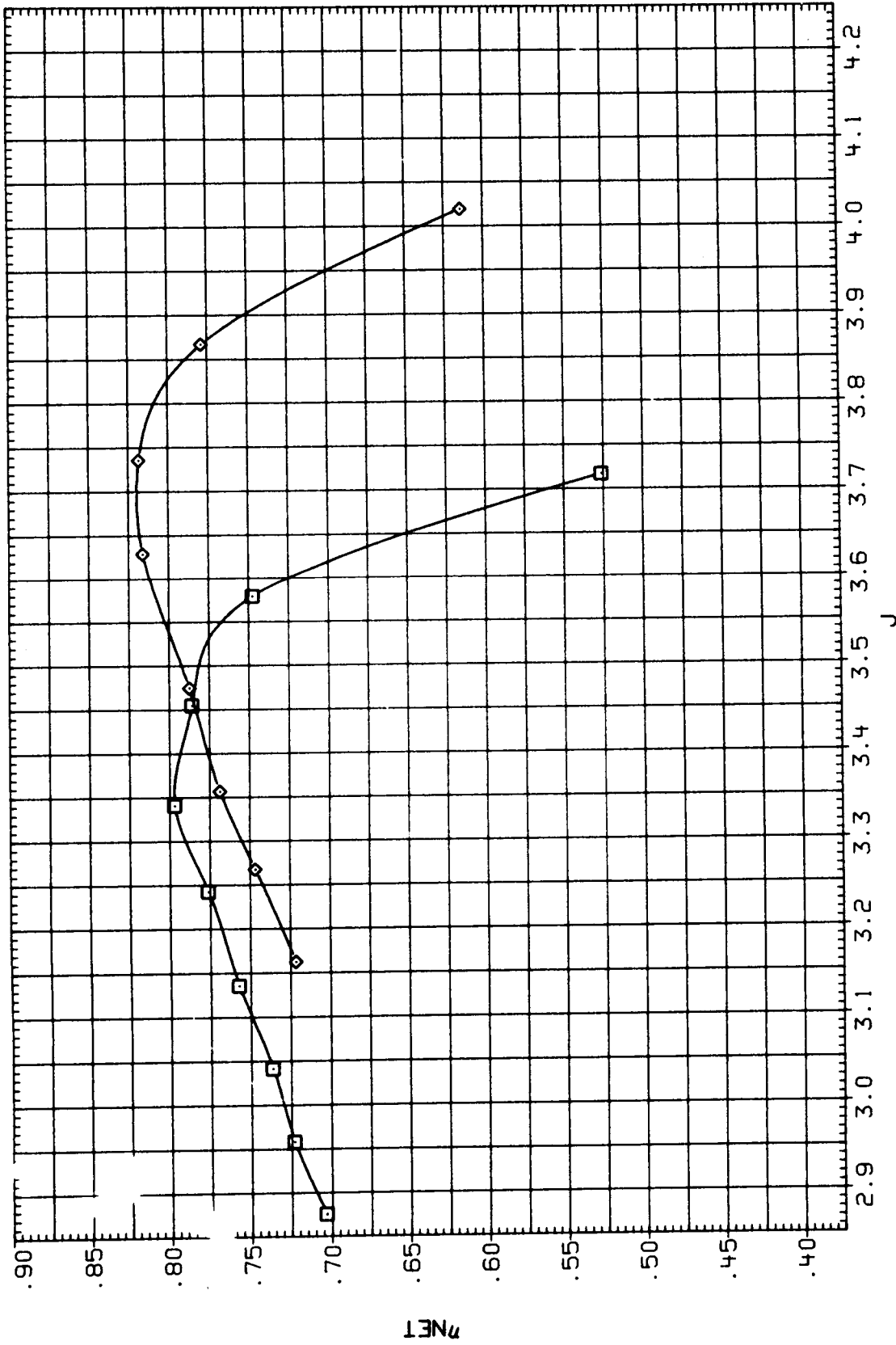


(d) $\alpha = 3^\circ$, $M = 0.80$.

Figure 23. - Continued.

SYMBOL CONFIGURATION
□ HB/LP
◇ HB/HP

PITCH
57.200
59.200

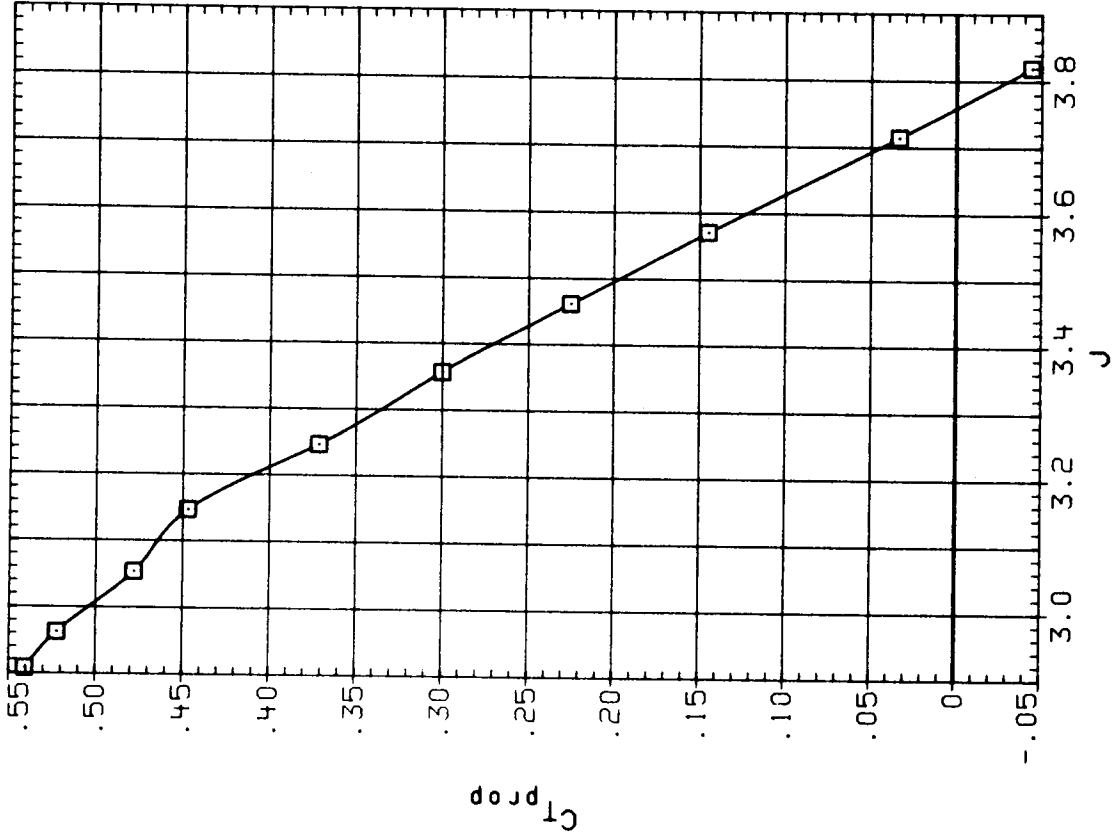
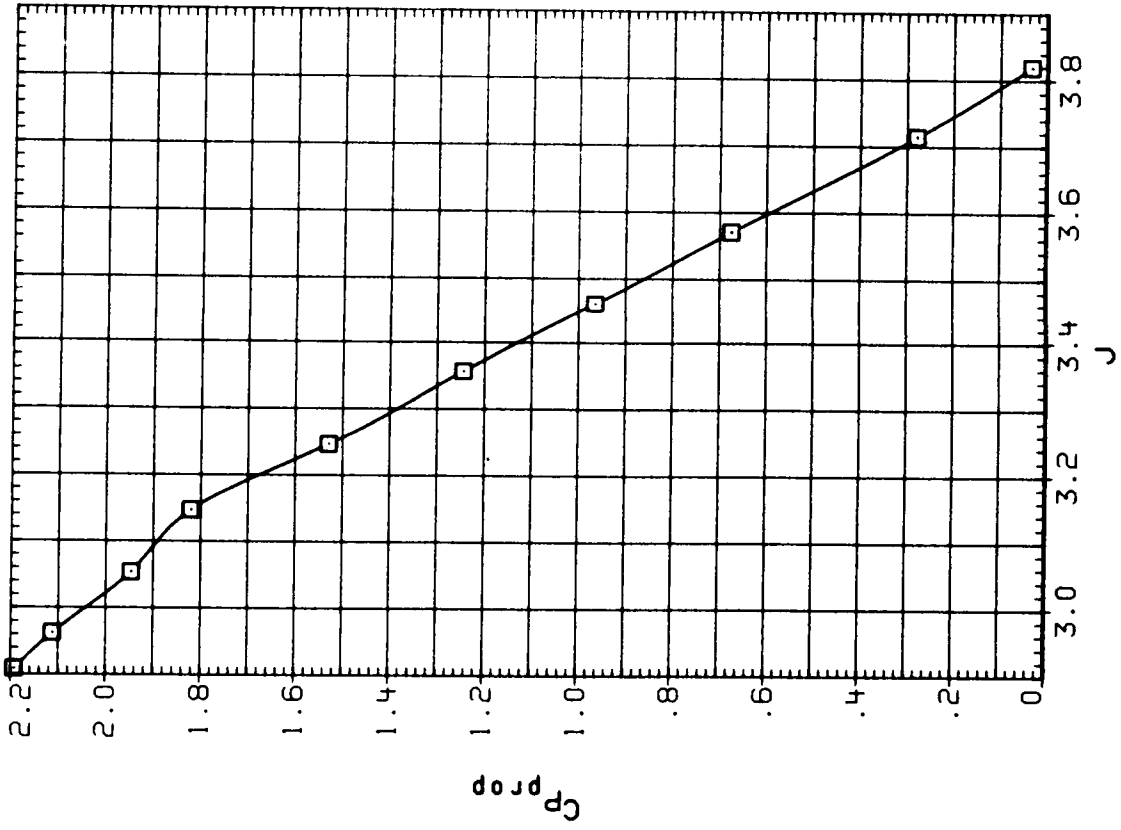


(d) Concluded.

Figure 23.- Continued.

PITCH
57.200

SYMBOL CONFIGURATION
□ HB/NLP

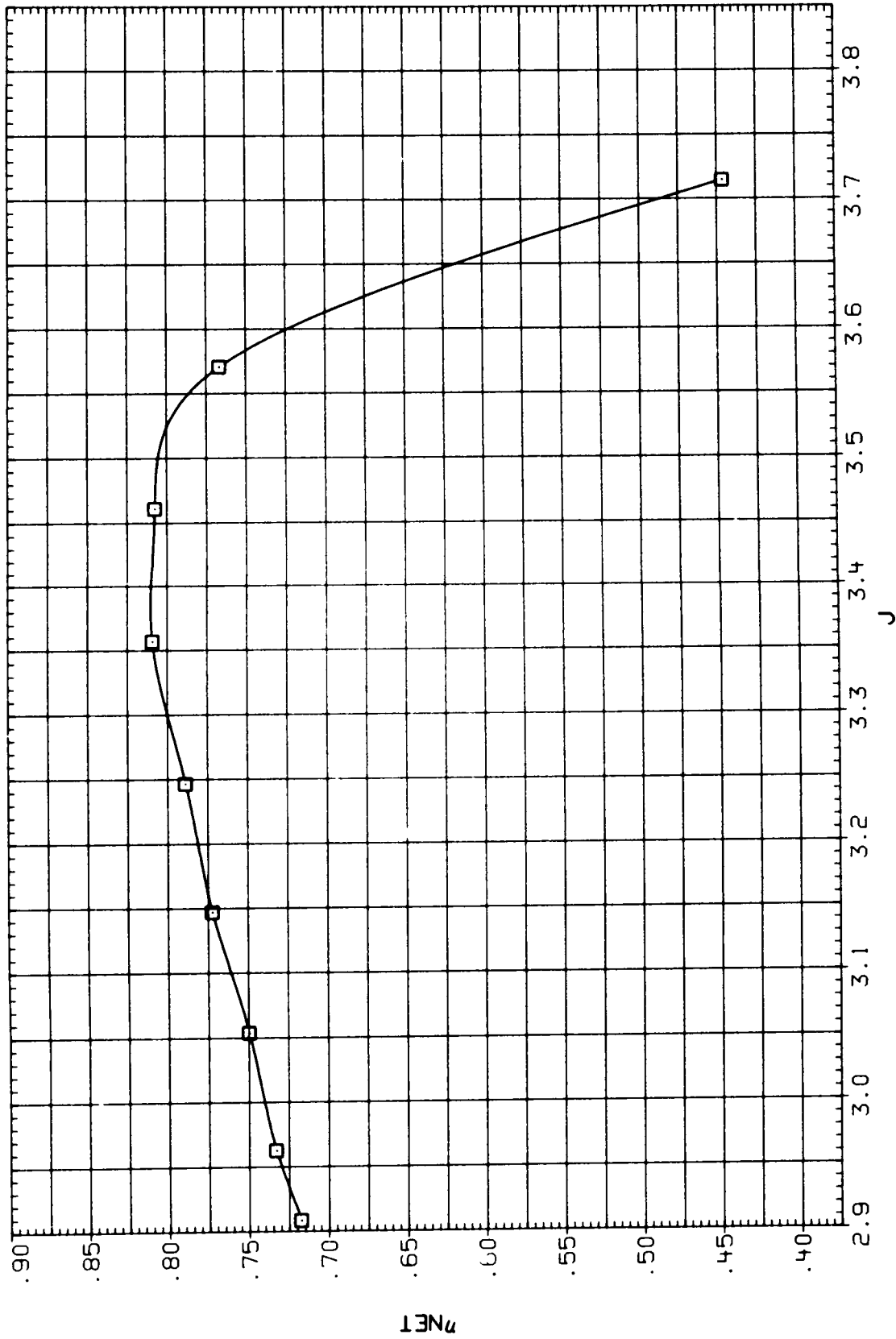


(e) $\alpha = 4^\circ$, $M = 0.80$.

Figure 23.- Continued.

PITCH
57.200

SYMBOL CONFIGURATION
□ HB/NLP



(e) Concluded.

Figure 23.- Concluded.

SYMBOL CONFIGURATION

- MBNP
- MBNLP
- ◇ MBNLF 3SP

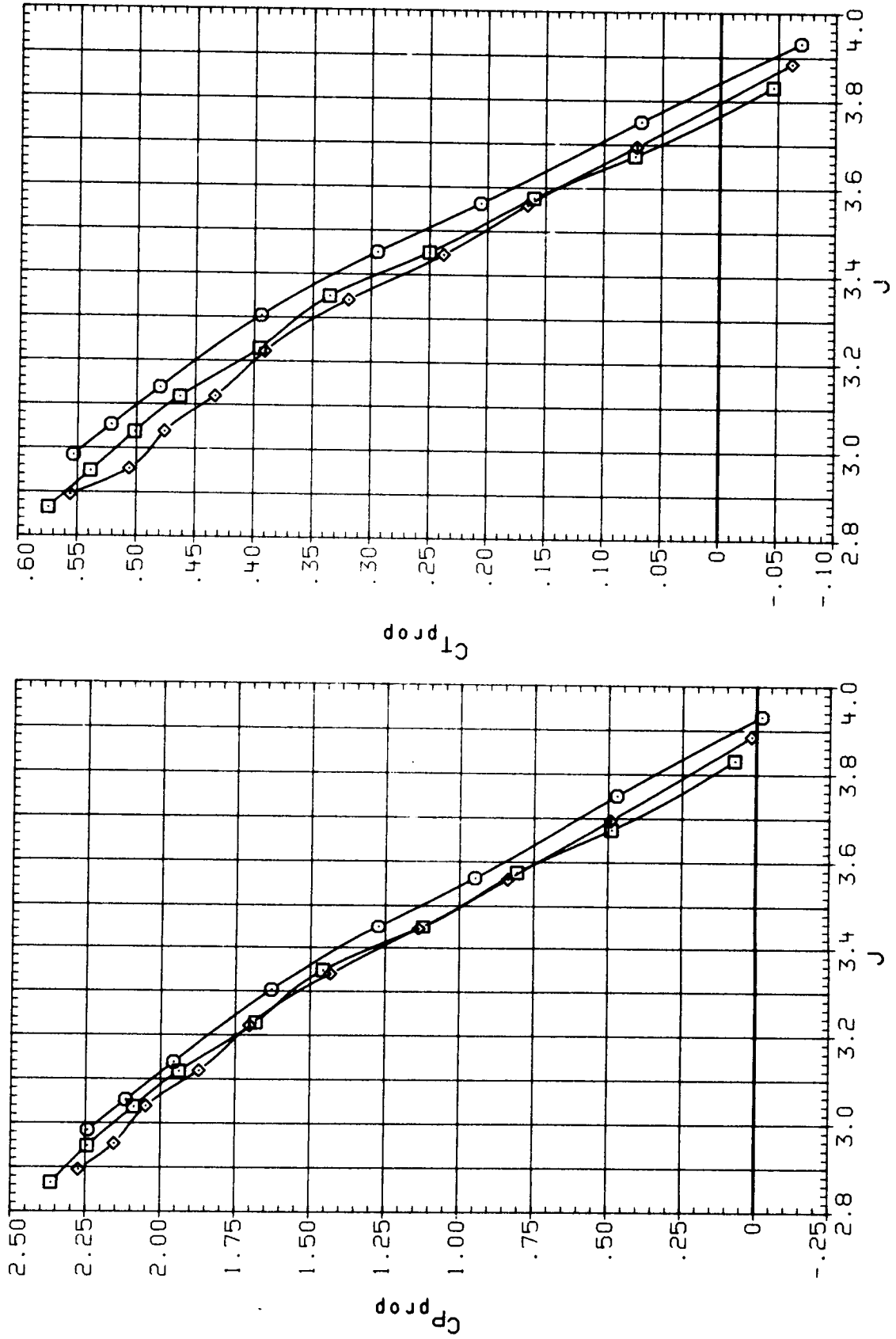


Figure 24.- Effect of LEX, fillet and strake on propeller performance;
 $\beta_p = 57.2^\circ$, $\alpha = 2^\circ$, $M = 0.80$.

SYMBOL CONFIGURATION

- HBMP
- HBMLP
- ◇ HBMLF3SP

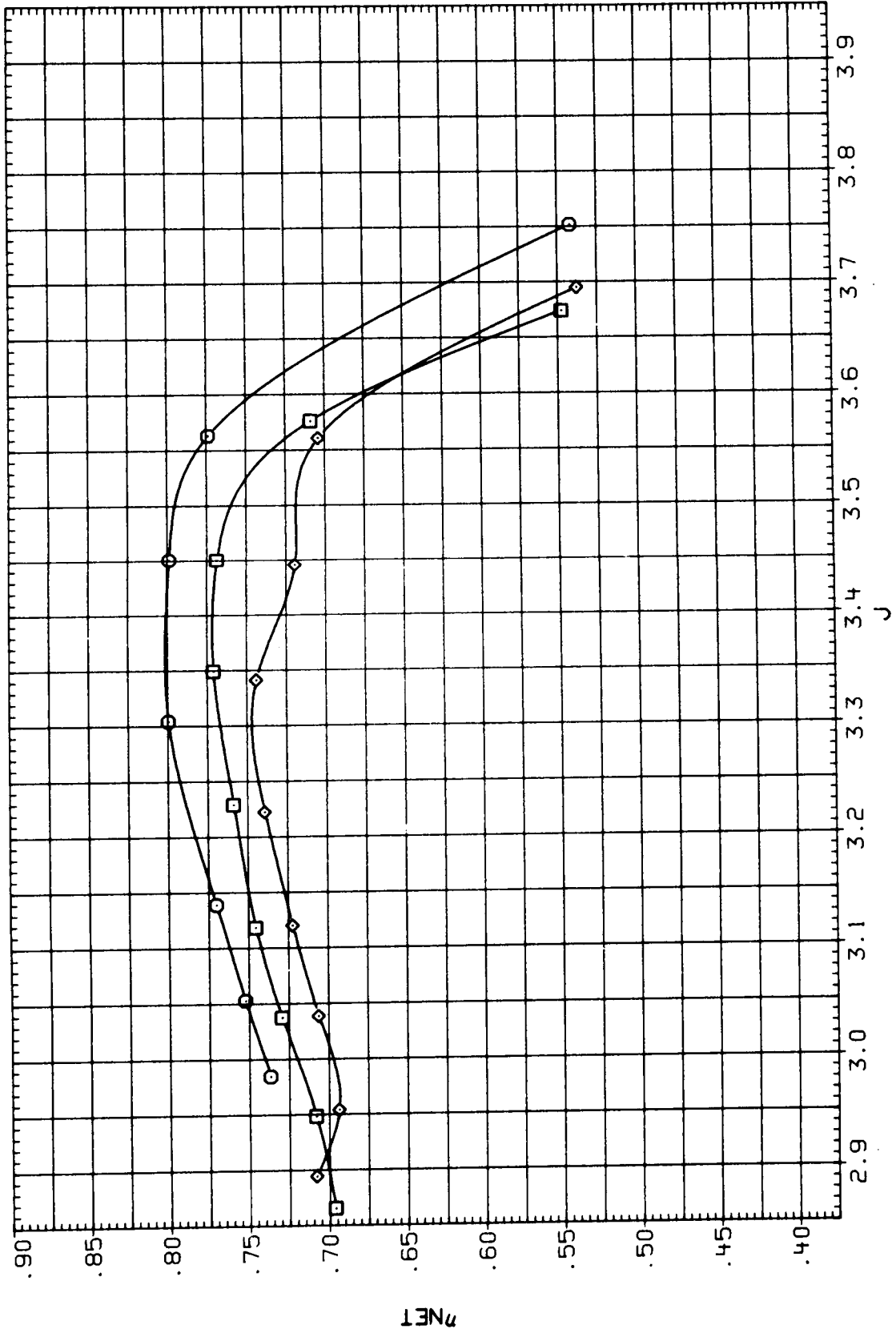


Figure 24.- Concluded.

SYMBOL CONFIGURATION

- HBNP
- HBNP

RN

- 9.562
- 5.698

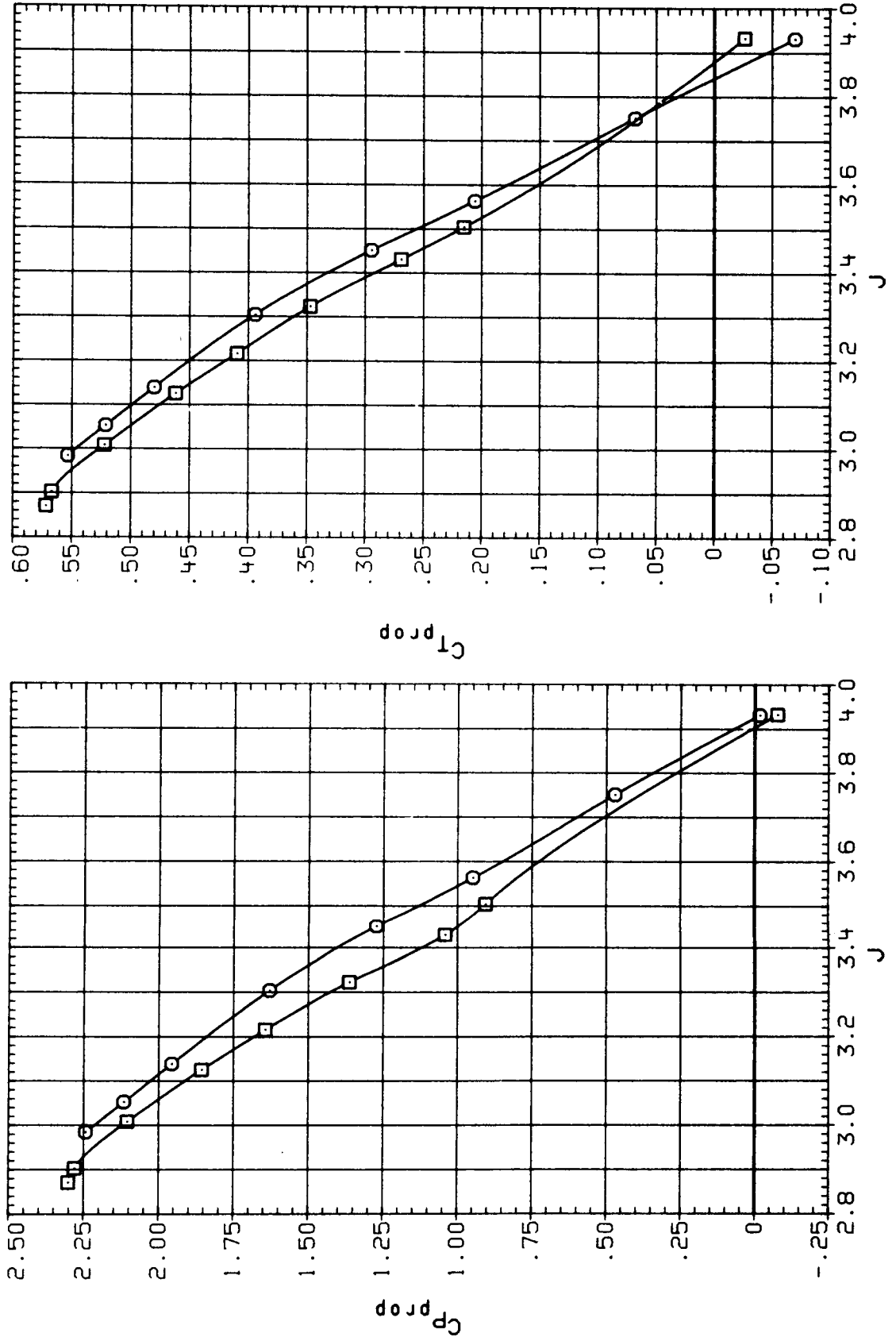


Figure 25.- Reynolds number effect on propeller performance; $M = 0.80$.

SYMBOL CONFIGURATION

○ MBNP
□ MBNP

RN
9.562
5.698

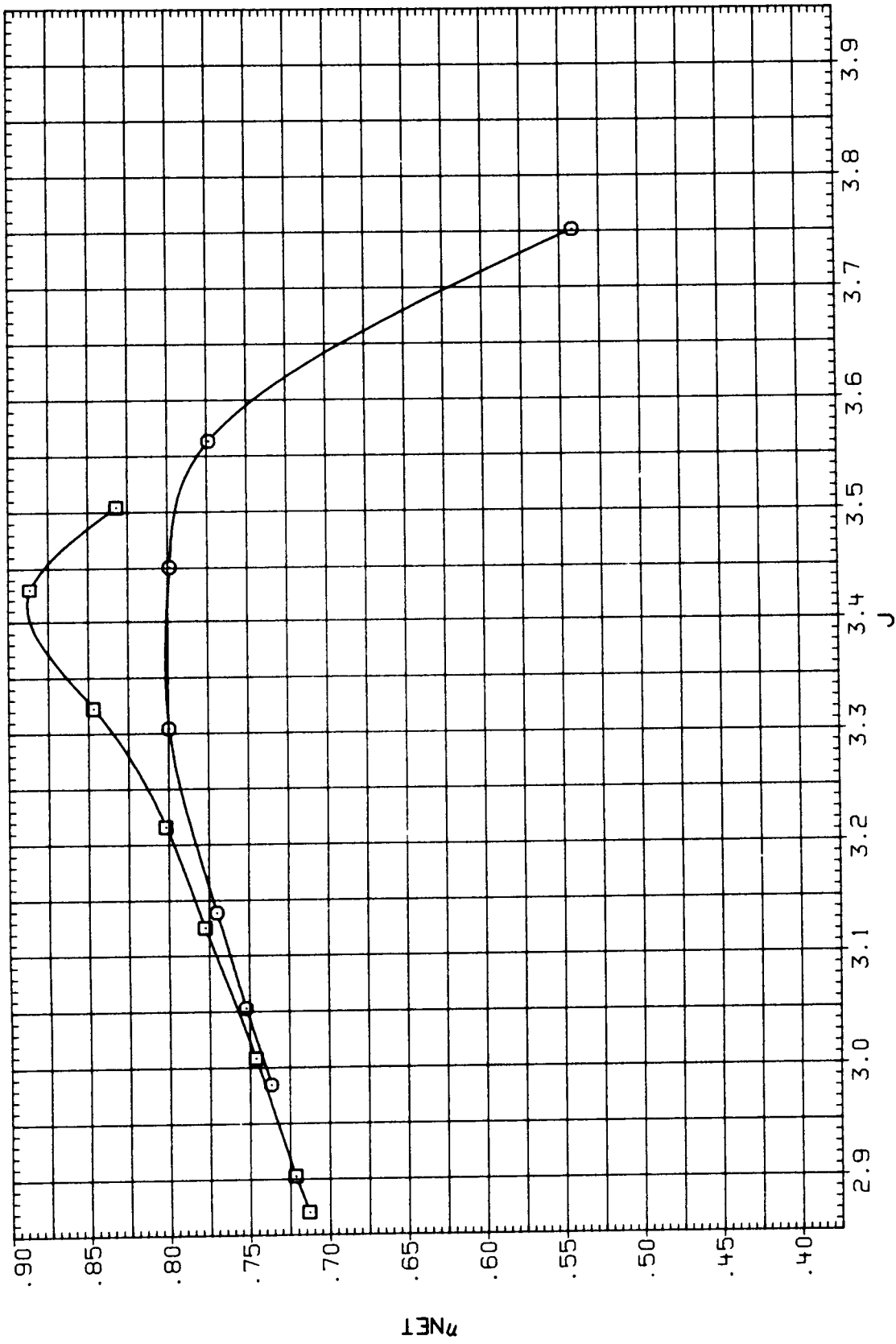


Figure 25.- Concluded.

SYMBOL CONFIGURATION

- MBNP
- MBNP
- ◇ MBNP
- △ MBNP

PITCH ALPHA

55.200	-.072
55.200	.975
55.200	1.968
55.200	2.964
55.200	3.959

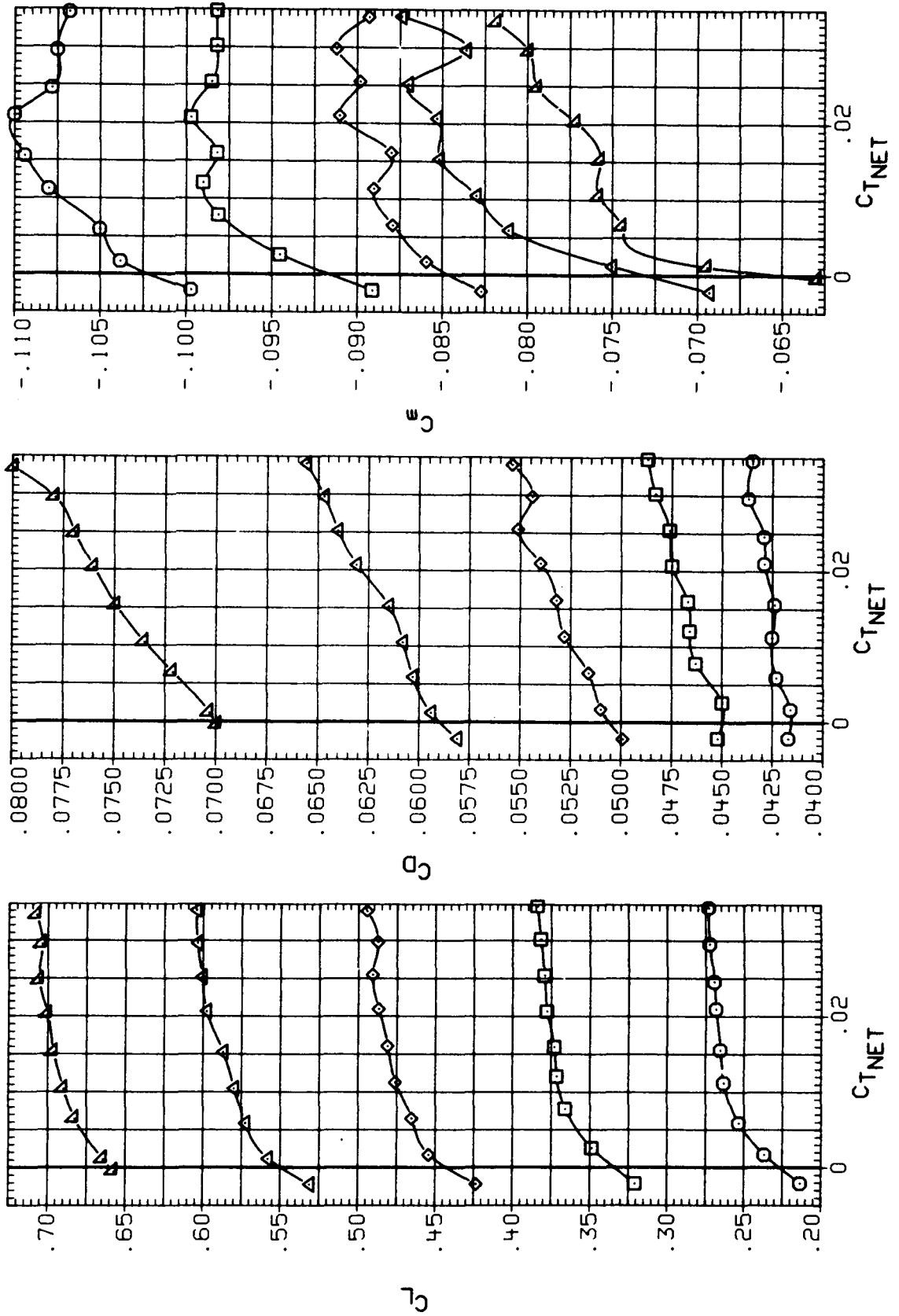


Figure 26.- Effect of thrust on the aerodynamic characteristics--LEX off; M = 0.80.

SYMBOL CONFIGURATION

- MBNP
- MBNP
- ◇ MBNP
- △ MBNP

PITCH	ALPHA
59.200	-.908
59.200	.950
59.200	1.936
59.200	2.950
59.200	3.975

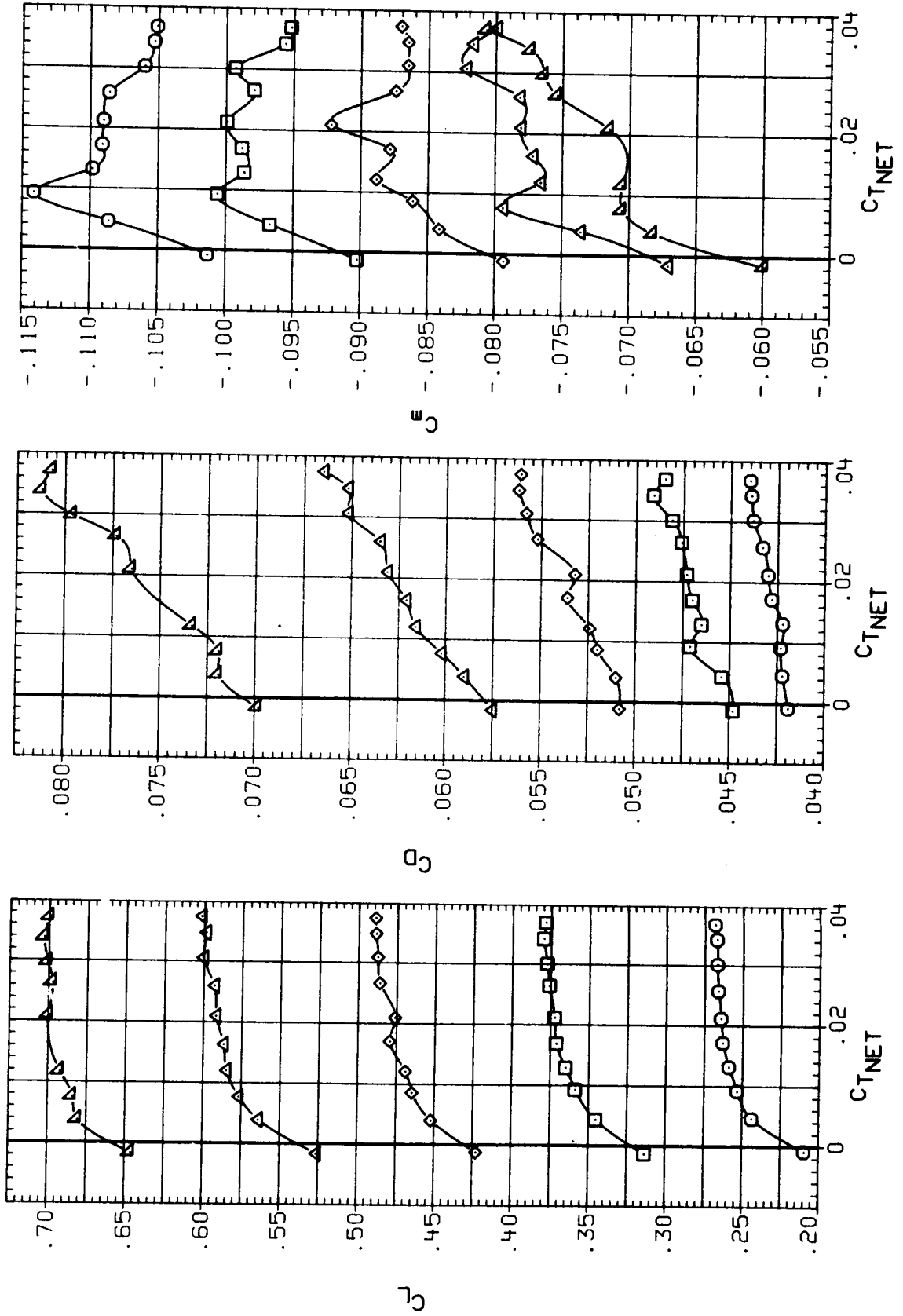


Figure 26.- Concluded.

SYMBOL CONFIGURATION
 ○ HBNLP
 □ HBNLP
 △ HBNLP

PITCH ALPHA
 57.200 .046
 57.200 1.003
 57.200 1.974
 57.200 2.941
 57.200 3.988

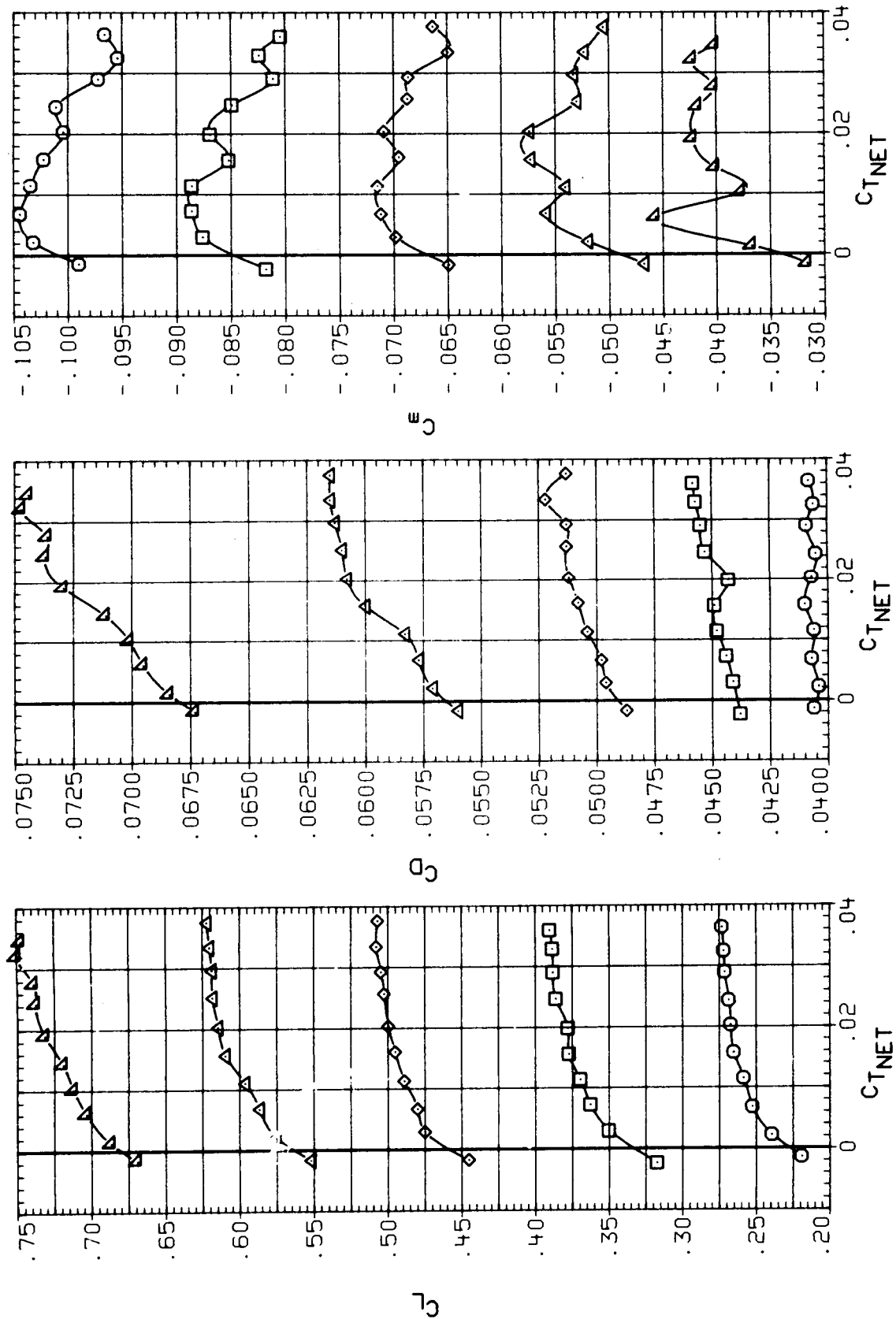


Figure 27.- Effect of thrust on the aerodynamic characteristics--LEX on;
 M = 0.80.

SYMBOL CONFIGURATION

-
-
- ◇
- △

PITCH ALPHA
 59.200 -.093
 59.200 .931
 59.200 2.037
 59.200 2.949

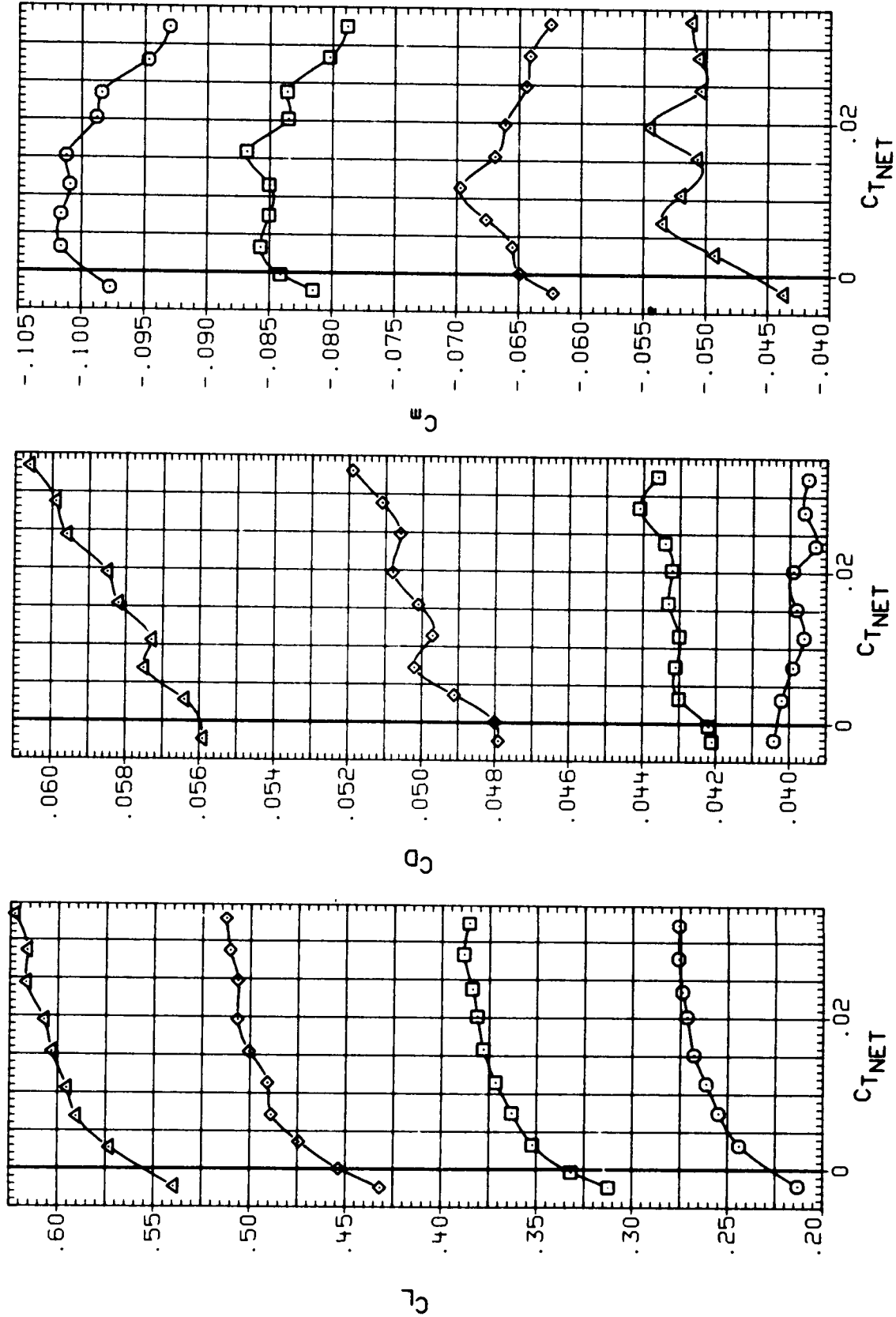


Figure 27.- Concluded.

SYMBOL CONFIGURATION
 ○ MBNP
 □ MBNLP
 ◇ MBNLF 3SP

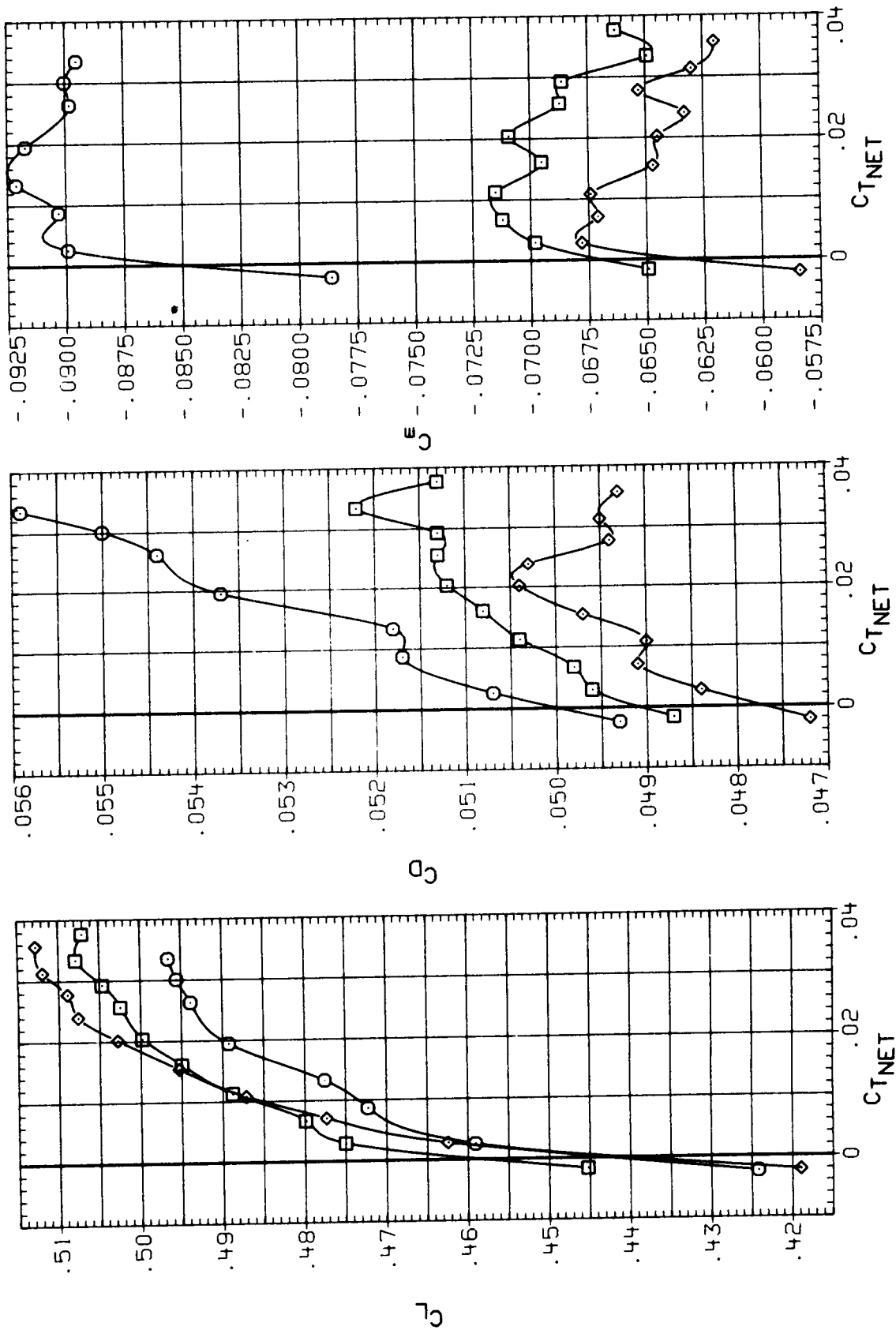
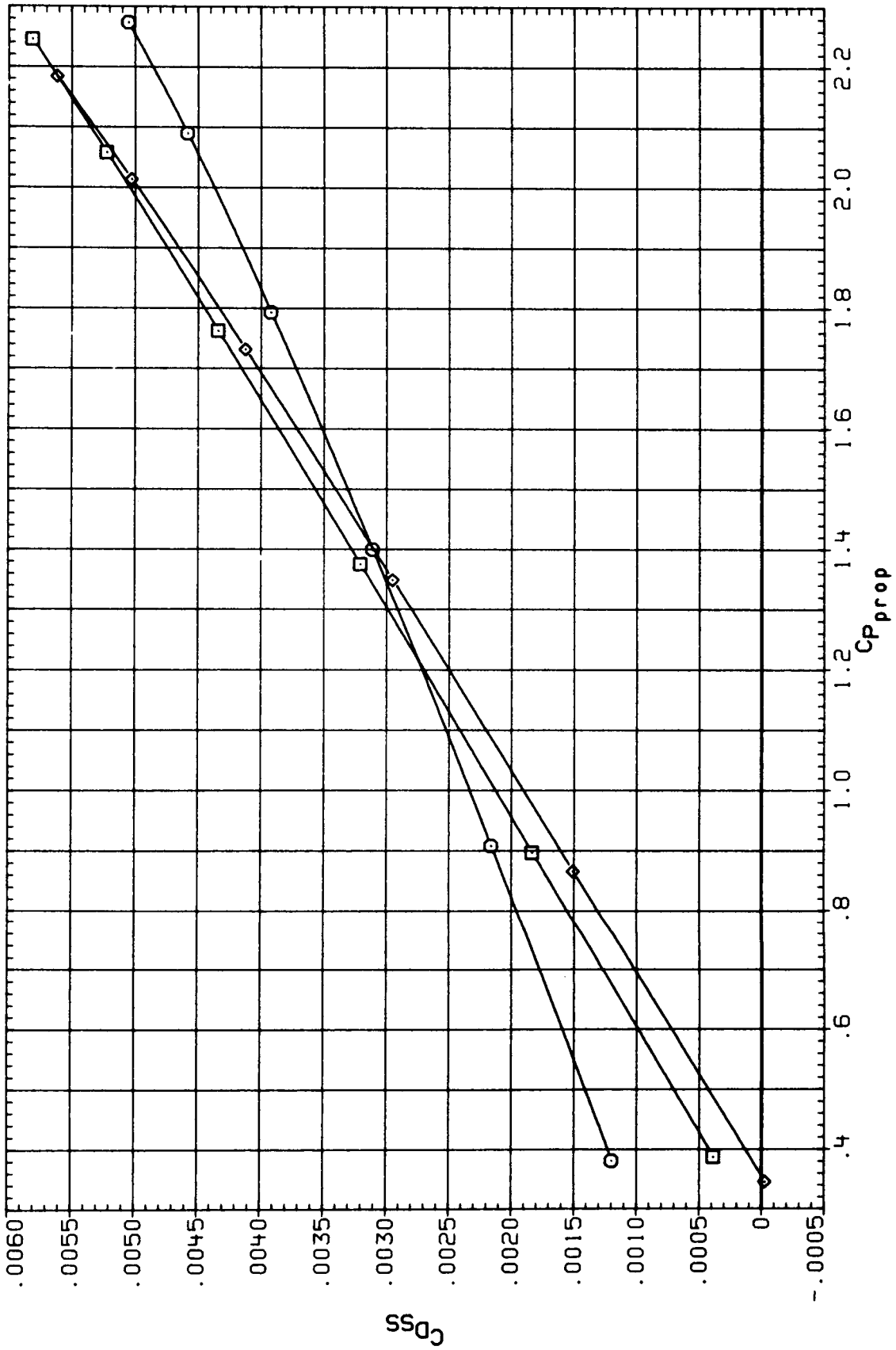


Figure 28.- Configuration effect on the thrust-removed characteristics;
 $\beta_p = 57.2^\circ$, $\alpha = 2^\circ$, $M = 0.80$.

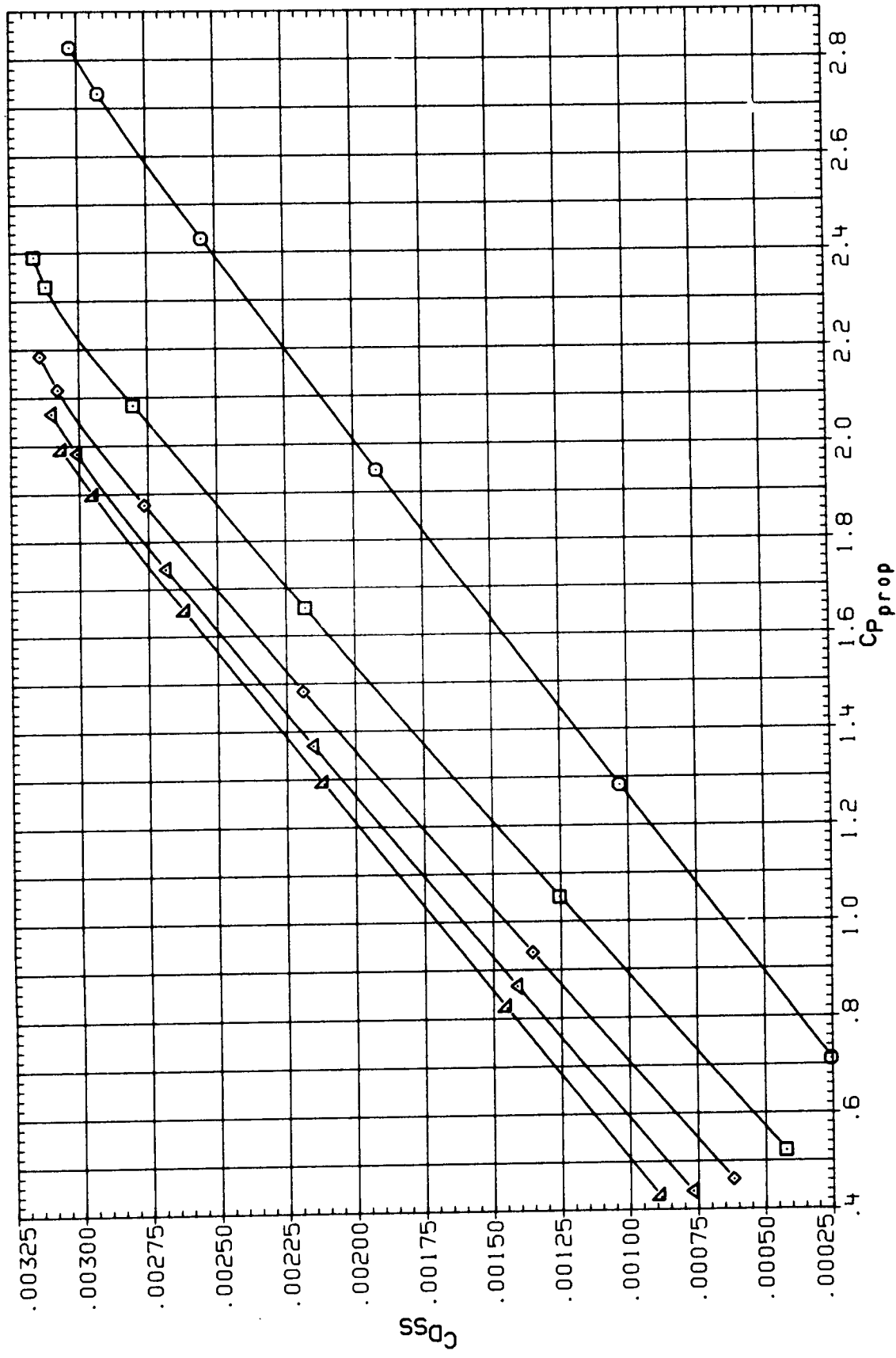
CONFIGURATION HENP
 MACH .750 PITCH 57.200
 .780 ALPHA 2.016
 .800



(a) LEX off.

Figure 29.- Variation of slipstream interference drag with power.

CONFIGURATION HERNLP
 MACH PARAMETRIC VALUES
 .600 PITCH 57.200
 .700 ALPHA 2.000
 .750
 .780
 .800

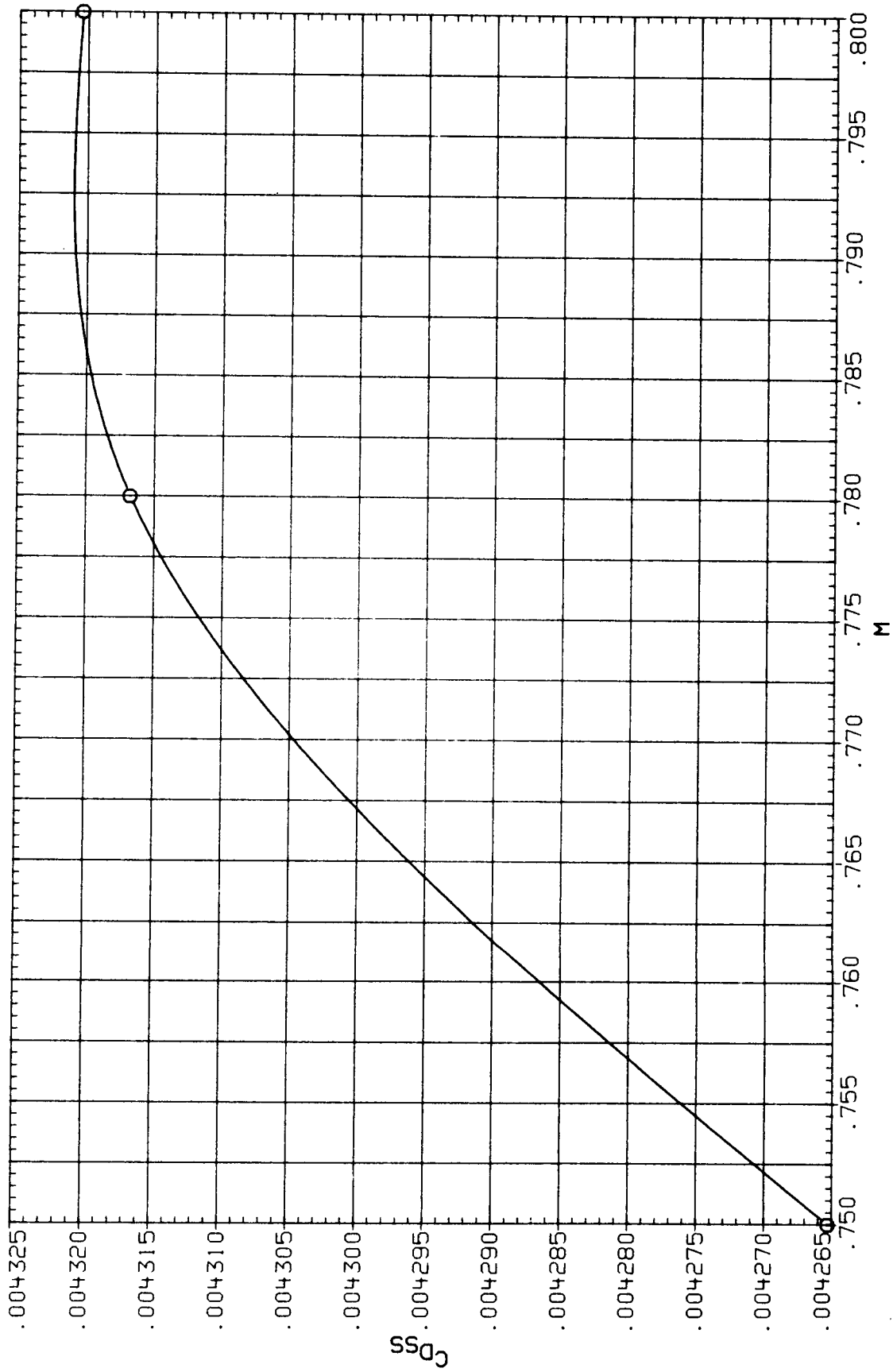


(b) LEX on.

Figure 29.- Concluded.

SYMBOL CONFIGURATION
O MBNP

PITCH CTNET
57.200 .032

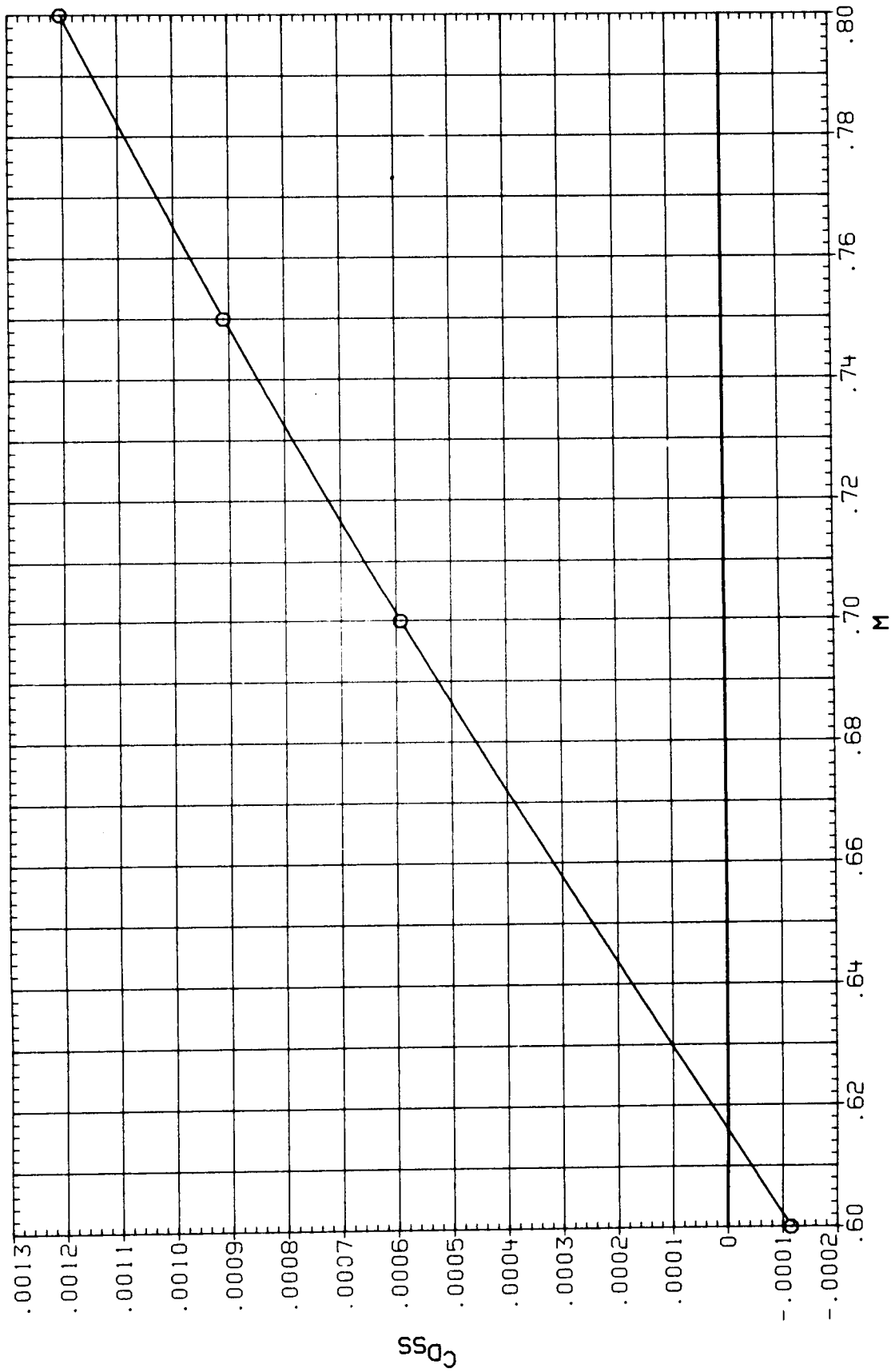


(a) LEX off.

Figure 30.- Variation of slipstream interference drag with Mach number at $C_L = 0.5$.

SYMBOL CONFIGURATION
O WBNLP

PITCH CTNET
57.200 .032

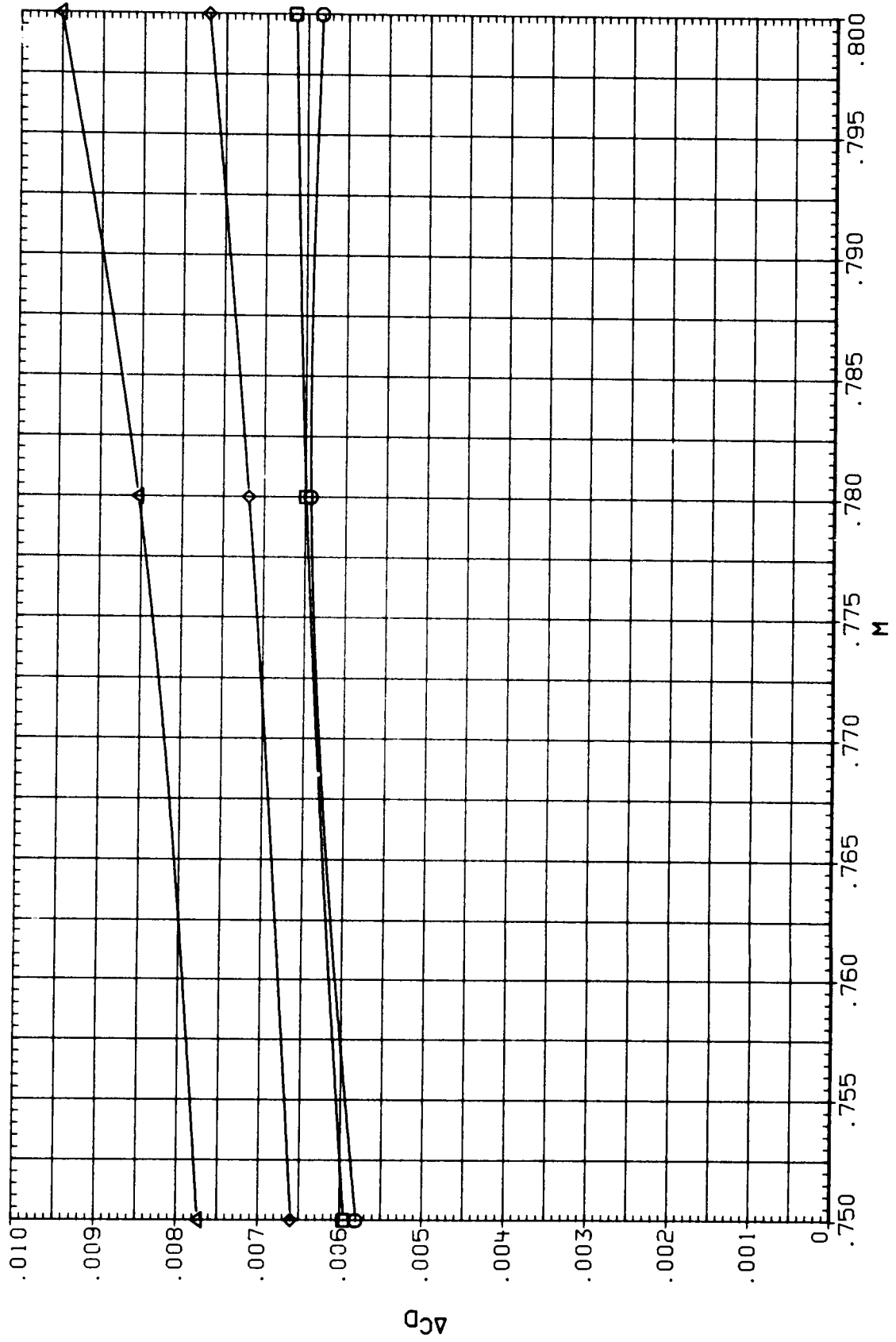


(b) LEX on.

Figure 30.- Concluded.

CONFIGURATION WBNP
 CL PARAMETRIC VALUES
 PITCH 57.200
 .300
 .400
 .500
 .600

SYMBOL
 ◊ ◊ ◊ ◊

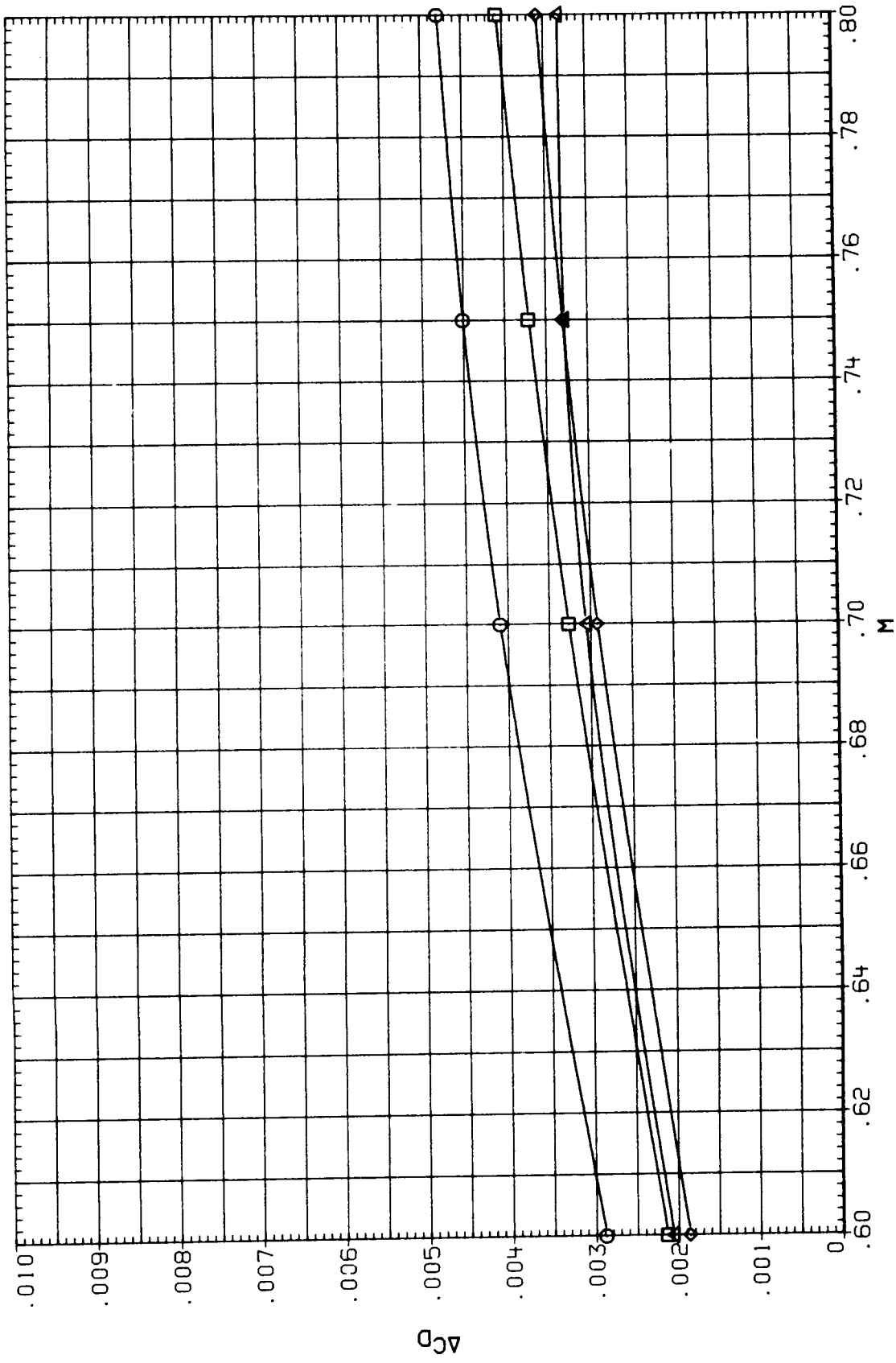


(a) LEX off.

Figure 31.- Total installation drag as a function of Mach number.

CONFIGURATION WBNLP
 CL PARAMETRIC VALUES
 PITCH 57.200
 .300
 .400
 .500
 .600

SYMBOL
 ○ □ ◇

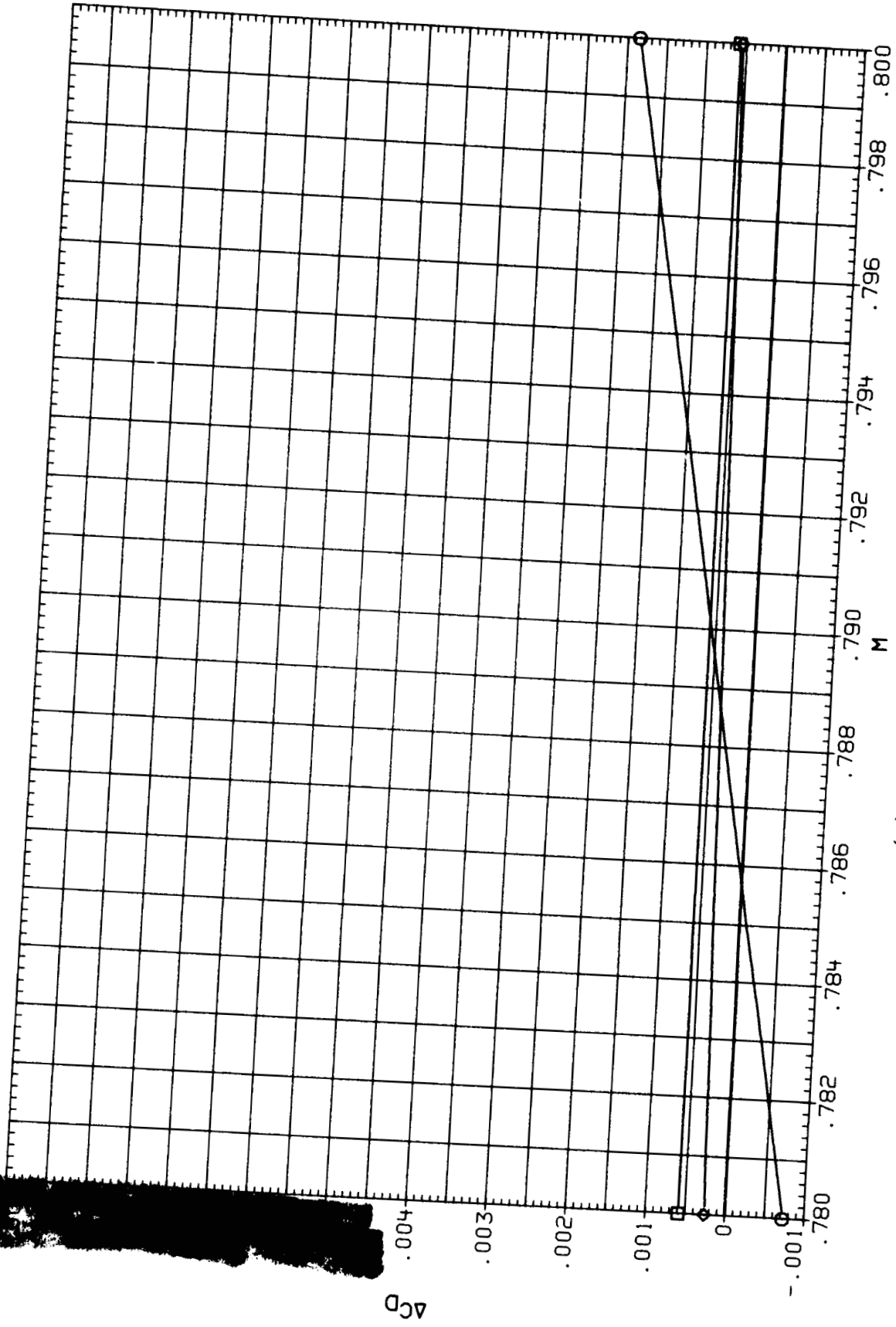


(b) LEX on.

Figure 31.- Continued.

SYMBOL □ ◇

CONFIGURATION HENLF3SP
CL [REDACTED]
PARAMETRIC VALUES
PITCH 57.200



(c) LEX, fillet, strake.

Figure 31.- Concluded.

1. Report No. NASA TM-86705	2. Government Accession No.	3. Recipient's Catalog No.	
4. Title and Subtitle AERODYNAMIC AND PROPELLER PERFORMANCE CHARACTERISTICS OF A PROPFAN-POWERED, SEMISPAN MODEL		5. Report Date December 1985	6. Performing Organization Code
		8. Performing Organization Report No. A-85175	10. Work Unit No.
7. Author(s) Alan D. Levin, Ronald C. Smith, and Richard D. Wood		11. Contract or Grant No.	
		13. Type of Report and Period Covered Technical Memorandum	
9. Performing Organization Name and Address Ames Research Center Moffett Field, CA 94035		14. Sponsoring Agency Code 535-03-11	
		12. Sponsoring Agency Name and Address National Aeronautics and Space Administration Washington, DC 20546	
15. Supplementary Notes Point of Contact: Alan D. Levin, Ames Research Center, MS 227-6, Moffett Field, CA 94035, (415)694-5858 or FTS 464-5858			
16. Abstract A semispan wing/body model with a powered propeller has been tested to provide data on the total powerplant installation drag penalty of advanced propfan-powered aircraft. The supercritical wing, with under-the-wing nacelle, was tested in the Ames Research Center's 11-Foot Transonic Wind Tunnel. The test was conducted at angles of attack from -3° to 4° over the Mach number range 0.6 to 0.8. Tunnel total pressure was held constant at one atmosphere. The test objectives were to determine propeller performance, jet effects, propeller slipstream interference drag, total powerplant installation drag, and the effect of configuration modifications on the installation drag. Test results indicated that the total powerplant installation drag can be as high as 77 drag counts (0.0077) at a Mach number 0.8 and a lift coefficient of 0.5. Adding a wing leading edge extension (LEX) between the nacelle and fuselage reduced the installation drag to 36 drag counts. The best configuration, however, was the LEX in combination with a fillet and strake at the wing-nacelle intersections. For this configuration, the total powerplant installation drag was reduced to 18 drag counts.			
17. Key Words (Suggested by Author(s)) Turboprop Powerplant integration Drag reduction		18. Distribution Statement  Subject category - 05	
19. Security Classif. (of this report) Unclassified	20. Security Classif. (of this page) Unclassified	21. No. of Pages 145	22. Price* A07